AD-A064 148 KAMAN AVIDYNE BURLINGTON MASS F/G 1/3
MEASUREMENTS OF BLAST PRESSURES ON A RIGID 65 DEG SWEPTBACK WIN--ETC(U)
DEC 77 G ZARTARIAN, J R RUETENIK, R F SMILEY DNA001-76-C-0106
UNCLASSIFIED KA-TR-137-VOL-3 DNA-4400F-3 NL

1 OF 2
AD A064148

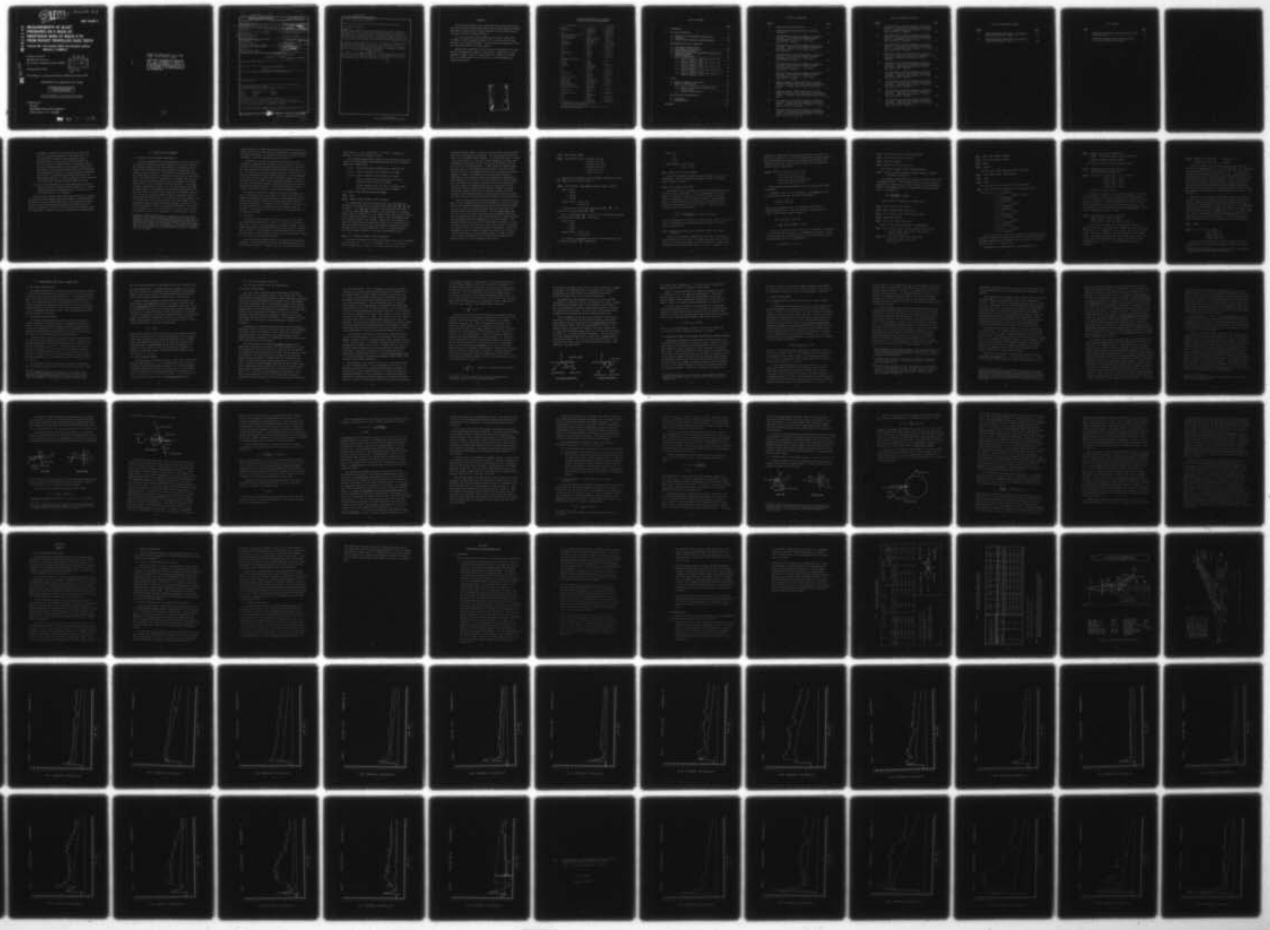

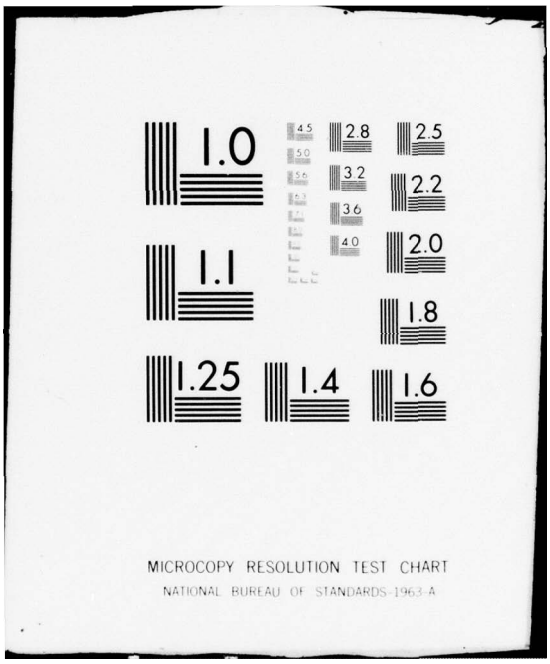
1.0
1.1
1.25
1.4
1.6
1.8
2.0
2.2
2.5
2.8
3.2
3.6
4.0
4.5
5.0
5.6
6.3
MICROCOPY RESOLUTION TEST CHART
NATIONAL BUREAU OF STANDARDS-1963-A

(12) LEVEL II AD-E300 413
NW AD62365

DNA 4400F-3

AD A064148

# MEASUREMENTS OF BLAST PRESSURES ON A RIGID 65° SWEPTBACK WING AT MACH 0.76 FROM ROCKET PROPELLED SLED TESTS

## Volume III—Correlation With the Doublet-Lattice Method in VIBRA-6

Kaman AviDyne
83 Second Avenue
Burlington, Massachusetts 01803

DDC
RECEIVED
FEB 5 1979
B

DDC FILE COPY

20 December 1977

Final Report for Period October 1975—November 1977

CONTRACT No. DNA 001-76-C-0106

APPROVED FOR PUBLIC RELEASE;
DISTRIBUTION UNLIMITED.

THIS WORK SPONSORED BY THE DEFENSE NUCLEAR AGENCY
UNDER RDT&E RMSS CODE B342077464 N99QAXAE50101 H2590D.

Prepared for
Director
DEFENSE NUCLEAR AGENCY
Washington, D. C. 20305

78 11 28 019

Destroy this report when it is no longer needed. Do not return to sender.

PLEASE NOTIFY THE DEFENSE NUCLEAR AGENCY, ATTN: TISI, WASHINGTON, D.C. 20305, IF YOUR ADDRESS IS INCORRECT, IF YOU WISH TO BE DELETED FROM THE DISTRIBUTION LIST, OR IF THE ADDRESSEE IS NO LONGER EMPLOYED BY YOUR ORGANIZATION.

DNA PRINTING PLANT

(18) DNA, SRIE (19) 4400F-3, AD-E300 413

UNCLASSIFIED

SECURITY CLASSIFICATION OF THIS PAGE *(When Data Entered)*

## REPORT DOCUMENTATION PAGE

READ INSTRUCTIONS BEFORE COMPLETING FORM

| 1. REPORT NUMBER | 2. GOVT ACCESSION NO. | 3. RECIPIENT'S CATALOG NUMBER |
|---|---|---|
| DNA 4400F-3 | | (9) |

(6) 4. TITLE (and Subtitle)

MEASUREMENTS OF BLAST PRESSURES ON A RIGID 65° Deg SWEPTBACK WING AT MACH 0.76 FROM ROCKET PROPELLED SLED TESTS. Volume III. Correlation with Doublet-Lattice Method in VIBRA-6.

5. TYPE OF REPORT & PERIOD COVERED
Final Report for Period October 1975—November 1977.

6. PERFORMING ORG. REPORT NUMBER
KA TR-137 Volume III

(10) 7. AUTHOR(s)
Garabed Zartarian
J. Ray Ruetenik
Robert F. Smiley

(15) 8. CONTRACT OR GRANT NUMBER(s)
DNA 001-76-C-0106

9. PERFORMING ORGANIZATION NAME AND ADDRESS
Kaman AviDyne
83 Second Avenue
Burlington, Massachusetts 01803

(16) 10. PROGRAM ELEMENT, PROJECT, TASK AREA & WORK UNIT NUMBERS
NWED Subtask (17) E501
N99QAXAE501-01

(11) 11. CONTROLLING OFFICE NAME AND ADDRESS
Director
Defense Nuclear Agency
Washington, D.C. 20305

12. REPORT DATE
20 December 1977

13. NUMBER OF PAGES
190

14. MONITORING AGENCY NAME & ADDRESS *(if different from Controlling Office)*
(12) 190p

15. SECURITY CLASS *(of this report)*
UNCLASSIFIED

15a. DECLASSIFICATION DOWNGRADING SCHEDULE

16. DISTRIBUTION STATEMENT *(of this Report)*

Approved for public release; distribution unlimited.

(14) KA-TR-137-Vol-3

17. DISTRIBUTION STATEMENT *(of the abstract entered in Block 20, if different from Report)*

18. SUPPLEMENTARY NOTES

This work sponsored by the Defense Nuclear Agency under RDT&E RMSS Code B342077464 N99QAXAE50101 H2590D.

19. KEY WORDS *(Continue on reverse side if necessary and identify by block number)*

| | | |
|---|---|---|
| Blast | Experimental Test | Vortex |
| Shock | Explosives | Sweptback |
| Sled Test | Aircraft | Subsonic |
| Pressure | Wing | |

20. ABSTRACT *(Continue on reverse side if necessary and identify by block number)*

Interaction of a blast wave with a highly sweptback wing model was measured in a series of three sled tests performed on the 50,788-foot track at Holloman Air Force Base in July and August of 1976.

The sled, traveling at Mach 0.76, was intercepted progressively by blast waves produced from the sequential detonation of three charges of TNT. (over)

DD FORM 1 JAN 73 1473 EDITION OF 1 NOV 65 IS OBSOLETE

11-20-019

UNCLASSIFIED

SECURITY CLASSIFICATION OF THIS PAGE *(When Data Entered)*

194 970

4. TITLE (and Subtitle) (Continued)

Volume III—Correlation With the Doublet-Lattice Method in VIBRA-6

20. ABSTRACT (Continued)

The model consisted of a sting-mounted wing and fuselage combination. Wing properties were: 46.80-in span, 18.95-in mean chord, 2.47 aspect ratio, 0.29 taper ratio, 67-deg leading edge sweepback, 64.8-deg quarter-chord sweepback, and a 64A012 wing section. Blast-induced loadings were measured at 20 locations on the wing for blast intercept overpressures of about 2 and 4 psi for blast intercept angles of about 20, 90, and 135 degrees from head-on.

Pressure response predictions based on the Doublet-Lattice Method (DLM) in VIBRA-6 are correlated with the test data. The comparisons indicate the existence of some non-linear blast-induced loads on the model. The experimental loadings are considerably greater than the corresponding predictions based on the linearized Doublet-Lattice Method.

(AD-A062 365)

Volume 1 of this report describes the test, and presents and discusses the reduced test data. Volume 2 presents a complete set of the wing differential pressure time histories in working size plots; and Volume 3 covers the experimental-analytical correlation phase of this study.

# PREFACE

This work was performed by the AviDyne Division of the Kaman Sciences Corporation for the Defense Nuclear Agency under Contract DNA-001-76-C-0106. MAJ David W. Garrison and CAPT Michael Rafferty of the DNA Shock Physics Directorate served as technical monitors.

Dr. J. Ray Ruetenik of Kaman AviDyne was the project leader under Dr. Norman P. Hobbs, Technical Director of KA. The analytical work was conducted by Mr. Garabed Zartarian. The correlation and evaluation efforts were performed jointly by the three authors.

Appreciation is expressed to MAJ Garrison and CAPT Rafferty for their interest and significant support of this program. Appreciation is also expressed to Messrs. Alfred L. Sharp and Gerry M. Campbell of the AFWL and to Mr. Michael Tomayko of the KA staff for their programming and computational support.

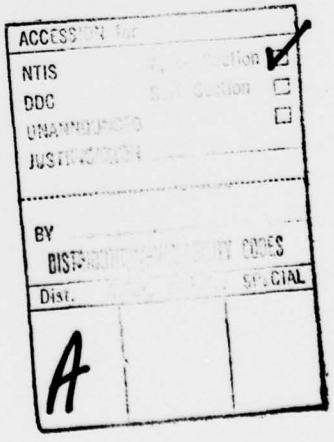

## Conversion factors for U.S. customary to metric (SI) units of measurement.

| To Convert From | To | Multiply By |
|---|---|---|
| angstrom | meters (m) | 1.000 000 X E -10 |
| atmosphere (normal) | kilo pascal (kPa) | 1.013 25 X E +2 |
| bar | kilo pascal (kPa) | 1.000 000 X E +2 |
| barn | meter$^2$ ($m^2$) | 1.000 000 X E -28 |
| British thermal unit (thermochemical) | joule (J) | 1.054 350 X E +3 |
| calorie (thermochemical) | joule (J) | 4.184 000 |
| cal (thermochemical)/$cm^2$ | mega joule/$m^2$ ($MJ/m^2$) | 4.184 000 X E -2 |
| curie | *giga becquerel (GBq) | 3.700 000 X E +1 |
| degree (angle) | radian (rad) | 1.745 329 X E -2 |
| degree Fahrenheit | degree kelvin (K) | $t_K = (t°f + 459.67)/1.8$ |
| electron volt | joule (J) | 1.602 19 X E -19 |
| erg | joule (J) | 1.000 000 X E -7 |
| erg/second | watt (W) | 1.000 000 X E -7 |
| foot | meter (m) | 3.048 000 X E -1 |
| foot-pound-force | joule (J) | 1.355 818 |
| gallon (U.S. liquid) | meter$^3$ ($m^3$) | 3.785 412 X E -3 |
| inch | meter (m) | 2.540 000 X E -2 |
| jerk | joule (J) | 1.000 000 X E +9 |
| joule/kilogram (J/kg) (radiation dose absorbed) | Gray (Gy) | 1.000 000 |
| kilotons | terajoules | 4.183 |
| kip (1000 lbf) | newton (N) | 4.448 222 X E +3 |
| kip/inch$^2$ (ksi) | kilo pascal (kPa) | 6.894 757 X E +3 |
| ktap | newton-second/$m^2$ ($N-s/m^2$) | 1.000 000 X E +2 |
| micron | meter (m) | 1.000 000 X E -6 |
| mil | meter (m) | 2.540 000 X E -5 |
| mile (international) | meter (m) | 1.609 344 X E +3 |
| ounce | kilogram (kg) | 2.834 952 X E -2 |
| pound-force (lbs avoirdupois) | newton (N) | 4.448 222 |
| pound-force inch | newton-meter (N·m) | 1.129 848 X E -1 |
| pound-force/inch | newton/meter (N/m) | 1.751 268 X E +2 |
| pound-force/foot$^2$ | kilo pascal (kPa) | 4.788 026 X E -2 |
| pound-force/inch$^2$ (psi) | kilo pascal (kPa) | 6.894 757 |
| pound-mass (lbm avoirdupois) | kilogram (kg) | 4.535 924 X E -1 |
| pound-mass-foot$^2$ (moment of inertia) | kilogram-meter$^2$ ($kg·m^2$) | 4.214 011 X E -2 |
| pound-mass/foot$^3$ | kilogram/meter$^3$ ($kg/m^3$) | 1.601 846 X E +1 |
| rad (radiation dose absorbed) | **Gray (Gy) | 1.000 000 X E -2 |
| roentgen | coulomb/kilogram (C/kg) | 2.579 760 X E -4 |
| shake | second (s) | 1.000 000 X E -8 |
| slug | kilogram (kg) | 1.459 390 X E +1 |
| torr (mm Hg, 0° C) | kilo pascal (kPa) | 1.333 22 X E -1 |

*The becquerel (Bq) is the SI unit of radioactivity; 1 Bq = 1 event/s.
**The Gray (Gy) is the SI unit of absorbed radiation.

A more complete listing of conversions may be found in "Metric Practice Guide E 380-74," American Society for Testing and Materials.

TABLE OF CONTENTS


| | | Page |
|---|---|---|
| 1. | INTRODUCTION | 9 |
| 2. | ANALYTICAL PROCEDURES | 12 |
| | 2.1 MODELING OF THE AERODYNAMIC CONFIGURATION | 12 |
| | 2.2 INPUT DATA | 13 |
| | 2.3 LISTING OF DATA DECK AND CLARIFYING REMARKS | 14 |
| 3. | EXPERIMENTAL-ANALYTICAL CORRELATION | 25 |
| | 3.1 THE VIBRA-6 PROGRAM OUTPUT | 25 |
| | 3.2 THE EXTERNAL PLOTTING ROUTINE | 25 |
| | 3.3 SOME PRELIMINARY REMARKS | 26 |
| | 3.4 PRESENTATION FORMATS OF EXPERIMENTAL AND ANALYTICAL PRESSURE RESPONSES | 31 |
| | 3.5 DETAILED CORRELATIONS | 32 |
| | 3.5.1 Intercept 9B-A1-2; $\phi$=87.6 deg, $\Delta p_s$=2.1 psi. (Case 1, Figures 3, 16) | 32 |
| | 3.5.2 Intercept 9B-A2-2; $\phi$=90.3 deg, $\Delta p_s$=4.0 psi. (Case 3, Figures 5, 18) | 37 |
| | 3.5.3 Intercept 9B-A2-1; $\phi$=20.1 deg, $\Delta p_s$=2.0 psi. (Case 2, Figures 4, 17.) | 39 |
| | 3.5.4 Intercept 9B-A4-1; $\phi$ = 20.1 deg, $\Delta p_s$=3.6 psi. (Case 5, Figures 7, 20) | 44 |
| | 3.5.5 Intercept 9B-A2-3; $\phi$=134.9 deg, $\Delta p_s$=2 psi. (Case 4, Figures 6, 19.) | 46 |
| 4. | SUMMARY | 53 |
| | 4.1 SCOPE OF COVERAGE IN THIS VOLUME | 53 |
| | 4.2 SUMMARY OF OBSERVATIONS | 54 |
| | 4.2.1 Effects of Blast-Induced Angle of Attack | 54 |
| | 4.2.2 Relative Importance of the Diffractive Period Loading | 54 |
| | 4.2.3 Nonlinear Vortex Effects | 55 |
| 5. | CONCLUSIONS AND RECOMMENDATIONS | 57 |
| | 5.1 CONCLUSIONS | 57 |
| | 5.2 RECOMMENDATIONS | 59 |
| REFERENCES | | 185 |

LIST OF ILLUSTRATIONS


| Figure | | Page |
|---|---|---|
| 1. | Experimental Model Configuration . . . . . | 63 |
| 2. | Simplified Wing Planform and Grid System Used in Analysis. . . . . | 64 |
| 3. | Time-Variations of Pressure Loadings at Transducer Locations. Predictions From VIBRA-6 Compared With Experiment. Case 1 - $\phi$ = 87.6 deg, $\Delta p_s$=2.07 psi. (9B-A1-2) . . . . . | 65 |
| 4. | Time-Variations of Pressure Loadings at Transducer Locations. Predictions From VIBRA-6 Compared with Experiment. Case 3 - $\phi$ = 90.3 deg, $\Delta p_s$=4.02 psi. (9B-A2-2). . . . . | 86 |
| 5. | Time-Variations of Pressure Loadings at Transducer Locations. Predictions From VIBRA-6 Compared With Experiment. Case 2 - $\phi$ = 20.1 deg, $\Delta p_s$=2.01 psi. (9B-A2-1) . . . . . | 107 |
| 6. | Time-Variations of Pressure Loadings at Transducer Locations. Predictions From VIBRA-6 Compared With Experiment. Case 5 - $\phi$ = 20.1 deg, $\Delta p_s$=3.56 psi. (9B-A3-1) . . . . . | 128 |
| 7. | Time-Variations of Pressure Loadings at Transducer Locations. Predictions From VIBRA-6 Compared With Experiment. Case 4 - $\phi$ = 134.9 deg, $\Delta p_s$=1.97 psi. (9B-A2-3) . . . . . | 149 |
| 8. | Comparison Between VIBRA-6 (DLM) and Quasi-Steady (V6QS) Predictions for Time-Variations of Differential Pressure. Spanwise Along the Quarter-Chord Line. Case 4 . . . . . | 170 |
| 9. | Comparison Between VIBRA-6 (DLM) and Quasi-Steady (V6QS) Predictions for Time-Variations of Differential Pressure. Chordwise Along the 60 Percent Span Station. Case 4 . . . . . | 171 |
| 10. | Time-Variations of Pressure Loadings at Transducer Locations. Predictions From Linearized Quasi-Steady Theory. Long Duration Traces for Case 1 - $\phi$ = 87.6 deg, $\Delta p_s$=2.07 psi. (9B-A1-2) . . . . . | 172 |
| 11. | Time-Variations of Pressure Loadings at Transducer Locations. Predictions From Linearized Quasi-Steady Theory. Long-Duration Traces for Case 3 - $\phi$ = 90.3 deg, $\Delta p_s$=4.02 psi. (9B-A2-2) . . . . . | 173 |

LIST OF ILLUSTRATIONS (CONT'D)


| Figure | | Page |
|---|---|---|
| 12. | Time-Variations of Pressure Loadings at Transducer Locations. Predictions From Linearized Quasi-Steady Theory. Long-Duration Traces for Case 2 - $\phi$ = 20.1 deg, $\Delta p_s$=2.01 psi. (9B-A2-1) . . . . . | 174 |
| 13. | Time-Variations of Pressure Loadings at Transducer Locations. Predictions From Linearized Quasi-Steady Theory. Long-Duration Traces for Case 5 - $\phi$ = 20.1 deg, $\Delta p_s$=3.56 psi. (9B-A3-1) . . . . . | 175 |
| 14. | Time-Variations of Pressure Loadings at Transducer Locations. Predictions From Linearized Quasi-Steady Theory. Long-Duration Traces for Case 4 - $\phi$ = 134.9 deg, $\Delta p_s$=1.97 psi. (9B-A2-3) . . . . . | 176 |
| 15. | Reflection Factor Versus Shock Incidence Angle For Two Values of Shock Strength Ratio. (From Figure 11.12, Reference 4, Modified to Conform With Present Notation.) . . . . . | 177 |
| 16. | Time-Variations of Pressure Loadings at Transducer Locations. Predictions From VIBRA-6 Compared With Experiment. Composite Plots for Case 1 - $\phi$=87.6 deg, $\Delta p_s$=2.07 psi. (9B-A1-2) . . . . . | 178 |
| 17. | Time-Variations of Pressure Loadings at Transducer Locations. Predictions From VIBRA-6 Compared With Experiment. Composite Plots for Case 3 - $\phi$ = 90.3 deg, $\Delta p_s$=4.02 psi. (9B-A2-2) . . . . . | 179 |
| 18. | Time-Variations of Pressure Loadings at Transducer Locations. Predictions From VIBRA-6 Compared With Experiment. Composite Plots for Case 2 - $\phi$ = 20.1 deg, $\Delta p_s$=2.01 psi. (9B-A2-1) . . . . . | 180 |
| 19. | Time-Variations of Pressure Loadings at Transducer Locations. Predictions From VIBRA-6 Compared With Experiment. Composite Plots for Case 5 - $\phi$=20.1 deg, $\Delta p_s$=3.56 psi. (9B-A4-1) . . . . . | 181 |
| 20. | Time-Variations of Pressure Loadings at Transducer Locations. Predictions From VIBRA-6 Compared With Experiment. Composite Plots for Case 4 - $\phi$ = 134.9 deg, $\Delta p_s$=1.97 psi. (9B-A2-3) . . . . . | 182 |

LIST OF ILLUSTRATIONS (CONCL'D)


| Figure | | Page |
|---|---|---|
| 21. | Comparisons Between Experimental and Predicted Initial Pressure Rises - Case 1. . . . . | 183 |
| 22. | Comparisons Between Experimental and Predicted Initial Pressure Rises - Case 3. . . . . | 184 |

LIST OF TABLES


| Table | | Page |
|---|---|---|
| 1. | Ambient and Operational Conditions During the Five Experimental Runs . . . . . | 61 |
| 2. | Local Shock Incidence Angles and Expected Peak Reflected Overpressure at Intercept . . . . . | 62 |

# 1. INTRODUCTION

VIBRA-6 is the latest in a series of nuclear vulnerability codes for predicting the blast-induced responses of aircraft flying at subsonic speeds (Reference 1). Previous versions of the VIBRA series (e.g., the subsonic option in VIBRA-4 of Reference 2) rely on empirically-derived aerodynamic results, based in part on two-dimensional transient loadings measured in a shock tube, for estimating the transient airloads at subsonic speeds. The objective in developing the new program was to incorporate a three-dimensional aerodynamic subroutine based on the so-called doublet-lattice method (DLM) which is expected to be more accurate for small induced angles of attack. The DLM had shown considerable promise in an earlier feasibility study (Reference 3). To include the new aerodynamic subroutine, the authors of Reference 1 found it more convenient to rewrite essentially the entire response code than to effect major modifications to the preceding VIBRA-4 code. However, they did make an effort to retain, as much as possible, certain "blocks" and terminologies adopted in the earlier versions.

In its normal modes of operation, VIBRA-6 does not output time histories of the pressure loadings. However, it does include an auxiliary subroutine, called RIGD, which provides the means for calculating the pressure loadings on rigid configurations, i.e., omitting the motion-dependent forces resulting from elastic deformations. RIGD was written specifically for the present analytical-experimental correlation effort. All the pressure loading predictions presented in this report are outputs from this subroutine.

One point should be made clear. RIGD extracts from the normal aerodynamic subroutine in VIBRA-6 the calculated pressures associated with sinusoidal gusts from an arbitrary orientation. It then proceeds to calculate the transient pressure loadings for bursts from the same orientation. Comparisons of the RIGD pressure loadings with experiment should therefore be indicative of the accuracy with which VIBRA-6 estimates the aerodynamic forcing functions to arrive at the predicted structural and motion responses during its application in a vulnerability study.

The end results from all the VIBRA codes are of course the time histories of the various structural and motion responses. However, there is a marked and important difference between the approaches of the earlier VIBRA versions and VIBRA-6. In the earlier versions, the equations of motion are integrated in the time domain and, as such, the aerodynamic loads are calculated at each time step using "transient aerodynamics". In contrast, VIBRA-6 determines the airloads for sinusoidal (or harmonic) gusts and sinusoidal motions and utilizes them to calculate all sinusoidal responses to harmonic gusts at a large number of gust wave lengths (or equivalently, reduced frequencies). The sinusoidal responses (structural and motion) are then synthesized through Fourier transform techniques to obtain the transient responses for the given blast encounter condition. The responses of interest here are the pressure differences at selected points on the instrumented wing, specifically at the pressure transducer locations. In RIGD, these transient loadings are obtained by Fourier inverting the product of the Fourier transform of the appropriate blast input and the sinusoidal pressure loadings (or pressure loading transfer functions).

There is yet another difference which should be pointed out. The VIBRA-6 formulation is a linear one, i.e., it utilizes linearized equations of motion, the DLM which is derived from linearized aerodynamics, and the linearized version of piston theory. With VIBRA-4, in contrast, the equations of motion are "quasi non-linear" and, depending on the aerodynamic subroutine used, the aerodynamics may be either from linearized theory or derived from test data.

In the present application, the VIBRA-6 program is exercised in two steps:

(1) An aerodynamic tape (designated as Tape 19) is prepared. It includes the sinusoidal pressure loads for a number of reduced frequencies $k_r$ and several gust orientations. $k_r$ is defined as $\omega c_r/2V$ where $c_r$ is the reference chord, V is the flight speed, and $\omega$ is the circular frequency associated with the gust wavelength. This step utilizes the so-called AERO subroutine. Due to inherent limitations in the DLM, the

aerodynamic calculations are carried out according to DLM only at "low reduced frequencies". The upper limit of $k_r$ (for which DLM is expected to give reasonably accurate results) depends on the box size of the grid system used. This point will be discussed further in a subsequent section. Since the transfer functions are also needed at high reduced frequencies to effect accurate inverse Fourier transformations, the calculations for high $k_r$'s are done according to linearized piston theory. The results from DLM and piston theory are then merged internally. If needed, results for other frequencies may be added later through the special MERGE subroutine.

(2) Utilizing the AERO Tape 19, the RIGD subroutine is then exercised to obtain the transient pressure loadings (i.e., pressure differences between corresponding points on the two sides of the wing) which are to be correlated.

The above rather general remarks should prove sufficient to acquaint the reader with the aerodynamic approach in VIBRA-6. Additional details are deferred to later sections which present the analytical procedures (Section 2) and the analytical-experimental correlation (Section 3). Section 4 summarizes the scope of the effort and the observations during the correlations. Section 5 offers the conclusions and recommendations.

# 2. ANALYTICAL PROCEDURES

## 2.1 MODELING OF THE AERODYNAMIC CONFIGURATION

The 65-deg sweptback model configuration which was built and tested to provide the experimental pressure loading data is shown in Figure 1. The "exposed" semispans of the wing planform are approximated for the VIBRA-6 code by quadrilateral surfaces which are overlaid with grid systems as shown in Figure 2.* The grid splits the right wing surface into eight strips, with each strip divided in turn into five equal-chord boxes. The curved wing tip is replaced by a streamwise edge, with the result that this analytical model has a 22.23 in semispan as compared with the actual 23.4 in semispan as depicted in Figure 1. The streamwise edge of the analytical model, i.e., the chord between points ③ and ④ in Figure 2, corresponds to the 95 percent semispan station of the actual model. The widths of the strips and the chordwise divisions of the strips into boxes are chosen so that the transducer locations coincide with the "load points" of the boxes in which they happen to fall. A box "load point" is at the quarter-chord of the box midspan station. The VIBRA-6 program computes the pressure loadings at selected (or even all) box load points. There is one unavoidable exception: The center of the innermost strip is at 21.05 percent of the actual span, whereas the transducer in box 2 is at 20 percent of the actual span. For this

*In Figure 2, only the right semispan is depicted. The grid system is specified for the right semispan; the program assumes the same grid system for the left wing. The experimental data were obtained from the instrumented left wing. The analysis is conducted for the right wing which is the one illustrated in the figure. This should pose no problem since the blast loadings at corresponding points on the left and right wings are the same with the burst point being in the plane of symmetry, i.e., the x-z plane.

single transducer, the difference between its location and that of its nearest load point is small and may be ignored when correlating measured and predicted loadings. The program is instructed to compute and print differences only at the circled load points in Figure 2.

The body is of circular cross-section, with the x-axis as its centerline. Being circular, the aspect ratios are unity at all cross-sections. The body has an ogive nose with the apex at Sta 0 (x=-32.24 in) and terminates at Sta 32.014 (x=-0.226 in) with a base radius of 4 in. It continues as a circular cylinder to Sta 64.4 (x=32.16 in). The cross-sections beyond Sta 64.4 become rectangular. Since the loadings on the body are not of interest here, the body is modeled to Sta 85.7 (x=53.46 in) as a cylinder. As per program instructions, the model of the body is divided into segments, with shorter divisions near the nose and near the wing-body juncture. Fourteen body segments are taken. In Figure 2, dashed lines are used to show the body segmentation.

To include the wing-body interference effects, the program calls for an "interference body", specifically a circular tube, which spans between the longitudinal stations about one chord length ahead and one chord length behind the foremost and aftmost wing-fuselage juncture stations, respectively. Accordingly, the 8-in diameter cylindrical tube is taken between Sta 6.01 and 56.31, and it is segmented into four sections. The interference effects are expected to be appreciable for the innermost stations.

## 2.2 INPUT DATA

The VIBRA-6 input requirements call for two decks of data: FIXED data and RUN data (Reference 1). Each deck is split into a number of groups and, in turn, each group consists of a number of items. For the present application, several FIXED and RUN data groups are not pertinent and are omitted. In what follows, all the necessary data are listed in the same format as that outlined in Reference 1, with discussions confined only to those items needing clarification.

Some of the input parameters depend on the ambient and operational conditions. These conditions for the five experimental encounter cases are summarized in Table 1. Note that Case 1 is the second intercept of

Run 1; Cases 2, 3, 4 are intercepts 1, 2, 3 of Run 2, respectively; and Case 5 is the first intercept of Run 3.

The following coding system is used to relate the entries with those called for in the DATA DECK INPUT DESCRIPTIONS (pp. 88-116 of Reference 1, updated as of August 1977):

| | |
|---|---|
| F or R | First letter denotes FIXED data (F) or RUN data (R). |
| G1, G2,.. | Letter G indicates group followed by its number. |
| I1, I2,.. | Letter I indicates item followed by its number. |
| V | Letter V indicates that the particular item varies generally from one run case to another |
| T | Letter T indicates that the input is a lengthy tabular entry which varies from one run case to another. |

## 2.3 LISTING OF DATA DECK AND CLARIFYING REMARKS

FG1I1: AERO

FG1I2: NODES=6, NSYM=2, NASYM=1, MFIX1=1, MFIX2=2

The quadrilateral surface representing the rigid wing planform is defined by four aerodynamic nodal points, namely points ①, ②, ③, ④ in Figure 2. The rigid body is defined by two aerodynamic nodal points on its axis, points ⑤, ⑥ in Figure 2. The total number of aerodynamic points, NODES, is therefore six. Two symmetric modes (pitch and translation in the z-direction, labelled as Modes 1 and 2) and one antisymmetric mode (yaw, labelled as Mode 3) are included. Modes 1 and 2 are monitored to check the harmonic pressure coefficients outputted by the AERO subroutine. Mode 1 also furnishes the necessary calculations to include the pre-blast (initial) angle of attack contributions. Mode 3 is considered because the program requires inclusion of at least one antisymmetric mode.

FG1I3: NP=1, NSTRIP=8, NSMAX=8, NCMAX=5, NBOXES=40

The wing is represented by a single panel (NP=1), since it has no dihedral or control surfaces. The rest of the parameter values are appropriate for the grid system shown in Figure 2. The doublet-lattice method, being

a numerical scheme, imposes a restriction on the highest reduced frequency which may be considered in the analysis. The finer the grid system, the higher is this maximum reduced frequency. See item FG1I10 below. Although a finer grid system (i.e., more than 5 boxes chordwise) would have been preferrable to increase the accuracy of the DLM calculations, this was not done for the following reasons. A larger number of chordwise boxes per strip calls for more spanwise strips in order to keep the "aspect ratios" of boxes in the neighborhood of unity as required by the program. Doubling the number of chordwise boxes per strip means essentially quadrupling the total number of boxes and increasing the computational times drastically. If one were to go from 5 boxes to say 11 boxes chordwise, the boxes within a given strip would have to be of unequal chords in order to make the transducer points and the load points coincide. Unequal box chords are undesirable because they introduce fictitious and sizeable pressure fluctations in a numerical scheme such as DLM. Choosing 25 boxes chordwise with 40 spanwise strips would overcome this objection; but then the computation time requirements would be prohibitive.

During the wing design and construction phase, a decision had to be made as to the chordwise locations of the transducers. Based on recommendations from McDonnell-Douglas personnel who were developing the VIBRA-6 code at the time, it was mutually decided that an analyses with five chordwise boxes should prove sufficient. With five equal-chord boxes, the 5, 25, 45, 65, 85 percent chord stations coincide with load points; and the predicted loadings at these points could then be compared directly with experimental data from transducers at the same locations. Later findings indicated that five boxes chordwise may be sufficient for forces and moments per unit span; but such a coarse grid system is not adequate for present purposes of correlating pressure differentials. Rather than attempting to cover the complete frequency spectrum by the DLM using a very fine grid system, a more reasonable approach is taken: the lower range of reduced frequencies ($k_r$) is covered by the doublet-lattice method and the rest by the linearized piston theory.

FG1I4: NB=1, MSBE=14, MBE=4

FG1I5: (ELXIA, ELYIA, ELZIA) = (-2.817, 4.0, 0.0)
= (24.072, 4.0, 0.0)
= (40.131, 22.23, 0.0)
= (50.108, 22.23, 0.0)
= (-32.24, 0.0, 0.0)
= (53.46, 0.0, 0.0)

These are the coordinates of the aerodynamic nodal points, points ① - ⑥, which are listed in Figure 2.

FG1I6: For Pitch Mode 1, per radian in positive angle of attack:

PHINA = 2.817
= -24.072
= -40.131
= -50.108

(PHIZA, PHIYA) = (32.24, 0.0)
= (-53.46, 0.0)

The first four of these are for nodal points ① - ④ . The last two are for nodal points ⑤ - ⑥.

For z - Translational Mode 2, per 9.217 in. translational amplitude, and for nodal points ① - ⑥ , respectively:

PHINA = -9.217
= -9.217
= -9.217
= -9.217

(PHIZA, PHIYA) = (-9.217, 0.0)
= (-9.217, 0.0)

For Yaw Mode 3, per radian in positive yaw angle amplitude, again for nodal points ① to ⑥ , respectively:

PHINA = 0.0
= 0.0
= 0.0
= 0.0
(PHIZA, PHIYA) = (0.0, 32.24)
= (0.0, - 53.46)

FG1I7: IPR1=0, IPR2=0, IPR3=0, NGUST=5

The first five standard orientations are overriden by a new set of orientations. The new orientations correspond to those for intercept cases 1 through 5 in Table 1.

FG1I8: NKD=8, NKP=21, MK1=0, MK2=0

NKD and NKP refer to the number of reduced frequencies using the DLM and piston theory, respectively. This is a requirement from a recent update of the program. Eight values of reduced frequency (including $k_r$=0) cover adequately the DLM $k_r$-range of validity. Together with 21 values of reduced frequency for piston theory, the pressure harmonic response calculations span the interval $0 \leq k_r \leq 50$. (See FG1I10 below.) The upper limit $k_r$=50 corresponds to

$$\omega = \frac{2Vk_r}{\bar{c}} \cong \frac{(2)(862)(50)(12)}{18.433} = 56117 \text{ rad} \cong 8930 \text{ Hz}$$

since the minimum velocity V=862 ft/s and the reference chord $\bar{c}$ = 18.433 in. This is the maximum cut-off frequency that can be used in the inverse Fourier transformations.

FG1I9: FMACH=0.760, REFA=672.0673, REFS=22.23, REFC=18.433, XM=0.0, SCALAR=2.0

Although the Mach number (FMACH) varies from case to case (Table 1), the differences are rather small. By taking the average value of 0.760, only one aero tape need be prepared, saving a good deal of computer time. The moments are taken about the y-axis, i.e., XM=0.0. SCALAR is a new

parameter for identifying the wing region interfered by the body. It should be at least 2.0, i.e., the body interference is assumed negligible only for wing spanwise stations two or more body radii away from the centerline of the body. The inclusion of SCALAR is a requirement from a recent update of the program.

FG1I10: FREQ = 0.0, 0.1, 0.2, 0.4, 0.6, 0.8
= 1.0, 1.2, 1.6, 2.0, 2.5, 3.0
= 4.0, 5.0, 6.0, 7.0, 8.0, 9.0
= 10.0, 12.0, 14.0, 16.0, 20.0, 25.0
= 30.0, 35.0, 40.0, 45.0, 50.0

These include reduced frequencies $k_r$ for the DLM and piston theory calculations.

According to Vol. 2, p. 26 of Reference 1, the maximum box chord one should have for accuracy in the DLM calculations is

$$(c_{box})_{max} \leq \frac{\bar{c}}{6k_r} = \frac{V}{3\omega}$$

where $\bar{c}$ is the reference chord. The reference chord $\bar{c}$=1.536 ft (FG1I9, REFC=18.433 in. = 1.536 ft); and since the maximum chord is 0.438 ft with the grid system of Figure 2,

$$\frac{V}{3\omega} \geq 0.438, \quad \frac{3\omega}{V} \leq 2.283, \text{ and}$$

$$k_r = \frac{\bar{c}\omega}{2V} = \frac{\bar{c}}{6} \frac{3\omega}{V} \leq \frac{2.283}{6} \bar{c} = 0.585$$

However, the stated criterion on box size is admittedly a conservative one. With some loss in accuracy, it is permissible to go twice as high as this $k_r$-value with the DLM-calculations. Thus the highest $k_r$ which is considered above for the DLM calculations is

$$k_r = (2)(0.585) = 1.17 \approx 1.2$$

FG2I1: X1=-2.817, X2=24.072, X3=40.131, X4=50.108

FG2I2: Y1=4.0, Y2=22.23, Z1=0.0, Z2=0.0

FG2I3: NC=5, NS=8, IGRUP=1

FG2I4: THI=0.0, 0.2, 0.4, 0.6, 0.8, 1.0

Each strip is divided into five equal-chord boxes.

FG2I5: TAU=0.0, 0.101481, 0.229841, 0.358201, 0.486561, 0.614920
=0.743280, 0.871640, 1.0

The wing-body juncture which is at (100)(4.0/23.4)=17.094% of span corresponds to TAU=0.0. The streamwise edge at y = 22.23 in, which approximates the wing tip and is at the 95 percent span, corresponds to TAU=1.0. The innermost strip has its outer edge at 25 percent span; thus, it corresponds to

$$\text{TAU} = \frac{25-17.094}{95-17.094} = 0.101481,$$

The other TAU's are obtained in a similar fashion.

FG3I1: ZC=0.0, YC=0.0, AO=4.0, AR=1.0

FG3I2: NBE=4, NSBE=14, NRI=0, NRS=1, NT1=4

FG3I3: XII = -26.226, -2.817, 8.745, 24.072, 50.108

FG3I4: Omitted since NRI=0

FG3I5: TH1 = 45.0, 135.0, 225.0, 315.0

Choice of TH1's based on Reference 1 recommendations.

FG3I6: XIS = -32.24, -26.226, -20.226, -16.226, -12.226, -8.226
= -4.226, -0.226, 4.774, 9.774, 14.774, 19.774
= 29.774, 39.774, 53.46

FG3I7: RS = 0.0, 1.445, 2.569, 3.138, 3.564, 3.846
= 3.985, 4.0, 4.0, 4.0, 4.0, 4.0
= 4.0, 4.0, 4.0

FG4I1: NSB=1, NSP=1, NMAX=4, KPRINT=0

FG4I2: IF1=1, NXQ=2, NSUP=1, IXCON=0

FG4I3: ISUP=1

FG4I4: NODE=5, 6

The above FG4I2, FG4I3, FG4I4 are for the "superbody".

FG4I2: IF1=0, NXQ=4, NSUP=1, IXCON (Omitted)

FG4I3: ISUP=1

FG4I4: NODE=1, 2, 3, 4

The above FG4I2, FG4I3, FG4I4 are for the "superpanel".

FG5I1: Arrays of NN, MM (Orientation No.), CR (Direction cosines)

| | | |
|---|---|---|
| (NN, MM, CR) = 1, 1, 0.041492015 | | |
| = 2, 1, 0.0 | Case 1 of Table 1 | |
| = 3, 1, 0.999138836 | | |
| = 1, 2, 0.939106248 | | |
| = 2, 2, 0.0 | Case 2 | |
| = 3, 2, 0.343626914 | | |
| = 1, 3, -0.004712372 | | |
| = 2, 3, 0.0 | Case 3 | |
| = 3, 3, 0.999988897 | | |
| = 1, 4, -0.705747932 | | |
| = 2, 4, 0.0 | Case 4 | |
| = 3, 4, 0.708463025 | | |
| = 1, 5, 0.939238122 | | |
| = 2, 5, 0.0 | Case 5 | |
| = 3, 5, 0.343266298 | | |

Since the blast center lies in the x-z plane of the model in all the test runs, the direction cosines CR1, CR2, and CR3 (of angles alpha, beta, and gamma, respectively) are dependent only on $\phi$, where $\phi$ is the angle defined in Table 1. It turns out that

CR1=CR(NN=1)=cos$\phi$, CR2=CR(NN=2)=0.0, and CR3=CR(NN=3)=sin$\phi$

RG1I1V: IDENT=13 When preparing AERO Tape 19

IDENT=n Where n=case number, when exercising RIGD

KPRCXQ=0, KPRCHQ=0, KPRCXL=0, KPRCHL=0

The value n is the same as the index NOR in RG6I1V.

RG1I2V: OPCD=4H AERO When preparing AERO Tape 19

OPCD=4H RIGD When exercising RIGD

RG1I3V: (ALT, VKEAS) = 7630.0, 459.5 Case 1 of Table 1

= 6170.0, 472.4 Case 2

= 6170.0, 465.6 Case 3

= 6170.0, 468.9 Case 4

= 6750.0, 467.1 Case 5

SIZFCT=1.0, PLQ=0.0, PLL=0.0

The program is set to accept only standard atmospheric conditions. To input the correct density, ALT is taken as the "density altitude", i.e., the altitude in the standard atmosphere where the density is equal to the actual density. A slight inconsistency is expected since the ambient temperatures and thus sound speeds (actual versus the values at standard density altitude) cannot be matched simultaneously. SIZFCT=1.0 since all dimensions are given in inches.

RG6I1V: NTMGST=number of cards in entry RG6I8T

NBOX=20, NSBE=1, IPLOT=1, IPREQ=0

NOR=n, where n is the case number from Table 1.

Each card in entry RG6I8T contains overpressure, density, and material velocity for a specified time. NTMGST varies from case to case. For Cases 1, 2, 3, 5, NTMGST=101, as tabulations are on time t=0(0.001) 0.100s. For Case 4, NTMGST=121, with the tabulations on t=0 (0.001) 0.120s. (The entire table given under entry RG6I8T is not used in any of the cases since the solutions are carried out to shorter times TIMEMX=0.025s for cases 1, 2, 3, 5 and TIMEMX=0.050s for Case 4. See RG6I2V.)

RG6I2V: TIMEMX=0.025, DELT=0.0001 for Cases 1, 2, 3, 5

TIMEMX=0.050, DELT=0.0001 for Case 4

Time t=0 is taken as that time when the blast reaches the "first point" on the configuration, i.e., t is "intercept time". The calculations are conducted for $0 \leq t \leq$ 25 ms* for Cases 1, 2, 3, 5. For Case 4, which involves a shock overtaking the wing from the rear, a longer duration is considered ($0 \leq t \leq$ 50 ms). These time spans are sufficiently long to cover the significant levels of pressure response. In fact, it will be shown later that the responses reach "quasi-steady" conditions before these maximum solution times; and the results from the VIBRA-6 calculations agree with the so-called linearized quasi-steady theory which has already been compared with experiment in a preceding volume of this report. (See Section 3.3.)

The choice of time increment DELT=0.0001s (0.1 ms) is a compromise. The smaller the value for DELT, the better are the sharp pressure rises defined. However, the required computer times increase since they are proportional to (TIMEMX/DELT). Two trial runs were made with TIMEMX=0.005, and for two values of DELT, DELT=0.0001 and 0.000025s. As expected, the results from both runs agree at common times, i.e., at t=0, 0.001, 0.0002, etc. However, "spike-like" peaks occurring between time steps 0.1 ms apart are lost with the coarser DELT=0.1 ms. Slight inaccuracies in defining the peak values (by taking DELT=0.1 ms) are not objectionable.

RG6I3: NFRGR=4

RG6I4: (F1, F2, DF) = 0.0, 199.0, 1.0
= 200.0, 598.0, 2.0
= 600.0, 1196.0, 4.0
= 1200.0, 4000.0, 8.0

The above four cards define the frequency range for the Fourier transformations. The frequency f runs from 0 to 4 kHz. The cut-off

*Note that in the program the unit of time is seconds. For discussion purposes times are usually given in milliseconds.

frequency $f_c$ is therefore 4 kHz. This is a reasonable value for $f_c$, inasmuch as the experimental data is estimated to be limited to frequencies up to a maximum of about 4 kHz because of telemetering. Trial computer runs were made varying the cutoff frequency: $f_c$= 2kHz, 4kHz, and 8kHz. The $f_c$=8kHz calculations showed slightly shorter rise times and slightly higher initial peaks when compared with the corresponding calculations with $f_c$= 4kHz. Lowering $f_c$ from 4kHz to 2kHz increased somewhat more the rise times and lowered the initial peaks. In this respect, taking $f_c$=4kHz is also a reasonable compromise.

DF=$\Delta f=\Delta(\omega/2\pi)$ is the specified frequency <u>increment</u> to be used in the Fourier transformations. It should be small enough to avoid inaccurate (or even erratic) results for times near t=TIMEMX. With a high cutoff frequency (4kHz), it should not be made too small, for it is known that small DF's can overload the program. Taking too high a value for DF is known to also affect the results at low t's. For higher t's, i.e., $0.010 \leq t \leq$ TIMEMX, the lower frequency effects are predominant, and a DF=1Hz or less is called for. Larger DF's may introduce some errors since the sin $\omega t$ - term in the inverse Fourier transformations (see p.80, Vol. 1, Reference 1) varies very rapidly with high t's. To clarify this point, one should note that for t=TIMEMX=0.050s (limit for Case 4), and with DF=1Hz

$$\Delta\omega t=(1)(2\pi)(0.05) \cong 0.31 \text{ rad}$$

indicating that consecutive points in the numerical integrations have sin $\omega t$ factors which are 0.31 rad apart. If DF were 8Hz, consecutive points would have arguments ($\omega t$) separated by 2.5 rad which is intolerable. The frequency $0 \leq f \leq f_c$ is specified in four ranges, as seen above, with the lower and predominating range $0 \leq f \leq$ 200 Hz split by increments DF=1 Hz. (Although it is desirable to run the whole range 0 to 4 kHz with DF=1Hz, this is not possible because of program overloading.)

RG6I5: IBOX = 2, 7, 11, 12, 13, 14
= 15, 17, 21, 22, 23, 24
= 25, 27, 31, 32, 33, 34
= 35, 37

RG6I6: ISBE=1, IDIR=1, ISBE=1, IDIR=2

The z- and y-direction forces are monitored for the first (nose) segment of the slender body through these inputs. Actually, the forces on the body are of no interest here; but at least one such set appears to be required by the program.

RG6I7: Q=0.055851, 0.000001, 0.000001

The initial angle of attack, $\alpha_o$, is 3.2 deg = 0.055851 rad for all five cases. No yaw and steady translation in the z-direction are involved, and thus $\tilde{Q}$=0.0 for Modes 2 and 3.

RG6I7T: (TIME, DP, RHO, VG)

From baseline pressure data, the overpressure (DP, in psi), the total density (RHO = $\rho_\infty+\Delta\rho_s$, in slugs/ft$^3$), and the material velocity (VG = gust velocity in ft/s) for the datum point (origin) are prepared in tabular form for times starting at 0.s. TIME=0. for this tabulation corresponds to the time when the shock front reaches the datum point. The tabular form covers TIME=0.0(0.001)TIMEMAX where TIMEMAX depends on the particular case. For Case 4, for example,

(TIME, DP, RHO,VG) = 0.0, 2.017600, 0.002194, 119.99000
= 0.001, 1.965700, 0.002189, 117.71000
= 0.002, 1.914801, 0.002184, 115.48000
= . . . .
= . . . .
= 0.120, 0.00000, 0.001977, 0.00000

This completes the input deck description.

# 3. EXPERIMENTAL-ANALYTICAL CORRELATION

## 3.1 THE VIBRA-6 PROGRAM OUTPUT

The VIBRA-6 program outputs on tape the differential pressure responses at the specified load points for a period of up to t= TIMEMX at intervals of $\Delta t$=DELT. (See item under RG6I2, Section 2.3.) It also provides on-line plots of the same results for quick-look purposes and tabulations of the same. For correlation purposes, the program output tape is processed through a separate (and external) plotting routine to give the analytical pressure loading vs time traces which have the same plotting scale factors as the corresponding experimental traces. This allows direct comparisons between experiment and analyses.

## 3.2 THE EXTERNAL PLOTTING ROUTINE

The separate plotting routine referred to above was developed to process and prepare superimposed plots of experimental and analytical results. This routine performs a number of preparatory functions prior to plotting, including the origin alignment of the experimental data so that both the experimental and analytical results start at the same time and reflect the same pre-intercept pressure differentials.

A few words need be said about the pre-blast levels since they are also pertinent to the alignment task referred to above. Consider first the analytical results. The VIBRA-6 output tape has no values for the pressure differential, $\delta_p$, for $t<0$.* To show the pre-blast $\delta_p$-level, the plot is started at t=-1 ms; and the plotting routine is instructed to use for the VIBRA-6 curve the value of $\delta_p$ at t=0 for all t's less than zero. $\delta_p(t=0)$ is truly the predicted pre-blast loading associated with the steady-state (i.e., $k_r=0$) initial angle of attack $\alpha_o=3.2$ deg., i.e., Mode 1.

The experimental $\delta_p$-traces contain noise, masking to some degree their low pre-blast levels; and they are also known to experience some

*The time origin for the analytical results is the instant of shock arrival at the intercept point, defined as the first point on the wing-body configuration intercepted by the shock. In this volume, time t is referenced to this origin and is termed "intercept time."

drift attributed principally to aerodynamic heating and a possible offset due to data processing. A reasonable approach to negate the zero drift and offset effects is to circumvent them by translating the experimental levels so that their means for a few milliseconds before shock arrival align with the constant analytical values for $t \leq 0$. This was done.

Another alignment problem is one associated with the abscissa. As stated earlier, the analytical results are in terms of intercept time; but the experimental results on tape are referenced to IRIG time. Let $t_d$ be IRIG time for shock arrival at the datum point (the datum point being the origin of the spatial coordinates fixed to the model). Let further $\tau$=time for the shock to travel from the intercept point to the datum point. $t_d$ may be estimated from experimental data and $\tau$ is available from the VIBRA-6 output printout. Both $t_d$ and $\tau$ vary from case to case. With t = intercept time and $t_b$ = IRIG time, the expression

$$t = t_b - (t_d - \tau)$$

should effect conversion of the time scale on the experimental tape from IRIG time to intercept time. The shift, amounting to $(t_d-\tau)$ according to the above expression, did not align satisfactorily all the channels. Slight misalignments were detected in the various data channels; they were attributed to instrumentation and data playback problems. Consequently, it was decided to carry out the time scale alignment on a channel to channel basis rather than by shifting all channels by the same amount, i.e., by $(t_d-\tau)$.

### 3.3 SOME PRELIMINARY REMARKS

The experimental and analytical results, in the form of differential pressure time histories (i.e., $\delta_p$ vs intercept time t) for the twenty transducer locations, are presented in Figures 3-7. Before proceeding to detailed comparisons with each of the five cases, it is worthwhile to discuss in general terms some important features of the results which deserve consideration in this correlation effort. For convenience, the response period may be split into two arbitrarily-defined phases:

(a) The lift development phase, and

(b) The quasi-steady or the late response phase.

These will be defined below.

As in the case of an aircraft wing encountering a "step gust", it takes time for the loading to develop. The situation with a wing intercepted by a blast wave presents other aspects which need be described. During the so-called diffraction period, which occurs at the beginning of the lift development phase, the differential pressure rises sharply due to shock reflection; this is followed by adjustments resulting from generated waves as the shock engulfs the configuration. This diffraction period is short compared with the duration of the lift (or load) development phase and depends on configuration shape and size, blast orientation, and location of the load point. It is estimated to be less than 3 msecs for all intercept cases and transducer locations to be considered.

Concurrently, the material velocity behind the shock establishes a "moving gust field". This field initiates a "gust type" load development which takes several chord lengths of travel before the flow reaches a quasi-steady state. As pointed out later and discussed in detail, experiment shows the formation of a leading-edge- attached vortex system which complicates the load development.

From the viewpoint of the VIBRA-6 aerodynamic analysis, which neglects the non-linear vortex effects, the quasi-steady state is taken to be reached when the load variations are slow and follow essentially the variations in gust-induced angles of attack. One can identify roughly the beginning of the quasi-steady phase by comparing the calculated pressure loadings according to VIBRA-6 (DLM) with corresponding ones based on the quasi-steady theory (V6QS) described in Vol. 1 of this report. Figures 8-9 present typical comparisons between VIBRA-6 results and corresponding predictions based on the so-called "linearized quasi-steady theory" (labelled the V6QS results in Section 6.3, Vol. 1 of this report.) For brevity, the illustrations are confined to Case 4 and for seven transducer locations covering partially the spanwise distribution along the quarter-chord line and the chordwise distribution

at the 60% span station. Case 4 is deemed to be the worst intercept situation, in the sense that the load buildup period is expected to be the longest because the blast catches up with the wing from the rear. It is clear from these figures that beyond a certain time (say $t=t_{1d}$), the VIBRA-6 results and the quasi-steady (V6QS) results are the same for all practical purposes. For the illustrated Case 4, $t_{1d}$ may be taken roughly as 20 ms which happens to be about half the overpressure positive phase duration, $t_p^+$, "as seen by the wing." For the other four cases, the lift development phase durations are shorter. It is estimated that they are roughly 10 ms for Cases 1 and 3 (where $\phi \cong 90$ deg) and 7 ms for Cases 2 and 5 (where $\phi \cong 20$ deg). Thus, the first 20 ms of response covers more than the entire load development phases in all cases to be discussed. (The 20 ms value should not be interpreted as a general result. The lift development phase durations depend on chord lengths of travel, orientation, and decay characteristics of the blast field; and for full-scale configurations, they will be considerably longer than 20 ms.)

In what follows, the detailed correlations are addressed mainly to the lift development phase, i.e., for $t \leq 20$ ms based on the preceding remarks, inasmuch as the late response phase has been adequately covered in Vol. 1 of this report. It suffices to present Figures 10-14 which are reproductions of Figures 27-31 of Vol. 1. Figures 10-14 give the comparisons between experiment and the "linearized" quasi-steady (V6QS) predictions. They are also indicative of the comparisons between experiment and VIBRA-6 (DLM) results for the late response phase, based on the above discussions concerning the relations between VIBRA-6 (DLM) and quasi-steady (V6QS) predictions.

How important are the "details" of the $\delta_p$ vs t variations during the lift development phase? From an aerodynamics point of view it is desirable of course to have an analysis which predicts accurately not only the actual "average load levels" but also "peaks and valleys" of appreciable magnitude. From the viewpoint of a structural dynamicist interested in estimating structural responses in aircraft blast vulnerability, the answer to this question depends on the specific application.

If the pressure loading is to be applied to a structural component with a "high" natural frequency (high in the sense that the period of the highest structural mode is of the order or less than $t_{ld}$, where $t_{ld}$ is the duration of the lift development) then certain types of details will be important. If on the other hand, the structural component has a "low" natural frequency for the highest contributing elastic mode, i.e., $t_{ld}$ is much less (say one tenth or less) of the period of that structural mode, then the details per se are not important. What is important in the latter case, however, is the loading impulse defined by*

$$I = \int_o^{t_{ld}} \delta_p \, dt$$

Consider first the so-called "overpressure type problems" where the structural responses of high frequency components are of interest. These include wing and fuselage panels, local structures such as frames, longerons, stringers, etc. There, the magnitudes and shapes of the diffractive phase loadings are very important because even peaks of short durations induce early maximum responses. In contrast, "gust type problems" are those associated with low-frequency modes of major components, e.g., wing bending modes. There, the structural responses of interest are peak bending moments, torsional moments, etc. With full-scale configurations, the wing structural mode periods are typically of the same order of magnitude as the durations of the lift development phases. This means that certain details of the $\delta_p$ vs. t variations during $0 \leq t \leq t_{ld}$ may be important; others may not. Extremely high frequency contents in these variations are not important. The peaks during the short diffractive periods (referred to above) need not be predicted accurately for wing bending moment responses. More specifically, as long as the impulses over $0 \leq t_{ld}$, i.e.,

$$I_d = \int_o^{t_d} \delta_p dt \qquad \text{(where } t_d = \text{diffractive phase duration)},$$

*Of course, if the details and overall levels are predicted with reasonable accuracy, so will the computed impulses.

are predicted "reasonably well", there is no need to duplicate the shapes of the peaks. By "reasonably well", it is implied that the error in predicting $I_d$ is a small fraction of the impulse for the period $0 \leq t \leq \frac{1}{4}(1/f_s)$ where $(1/f_s)$ is the structural mode period.

The VIBRA-6 code was developed to be used in gust type problems. Accordingly, its evaluation is directed primarily on this basis. However, the doublet-lattice method, which is the aerodynamic tool in VIBRA-6, does yield information on pressure response which should be of interest in overpressure type problems. For this reason, the diffraction phase responses are also assessed during the correlation discussions.

Table 2 summarizes the results of some preliminary calculations to be used in the correlations for the diffractive phase. They pertain specifically to the so-called peak reflected overpressures according to shock reflection theory. When the shock impinges on a surface, the pressure jumps by an amount which depends on the shock strength ratio $\xi = \Delta p_s / p_\infty$ and the incidence angle, where $\Delta p_s$ is the pressure jump across the shock, i.e., the peak free-field overpressure. The incidence angle, $\theta_i$, is that between the shock velocity vector and the inward normal to the reflecting surface. For $\theta_i$'s less than the critical angle $\theta_i^*$ the reflection is a regular one; for $\theta_i$'s above $\theta_i^*$ the reflection is a Mach reflection. See sketch below.

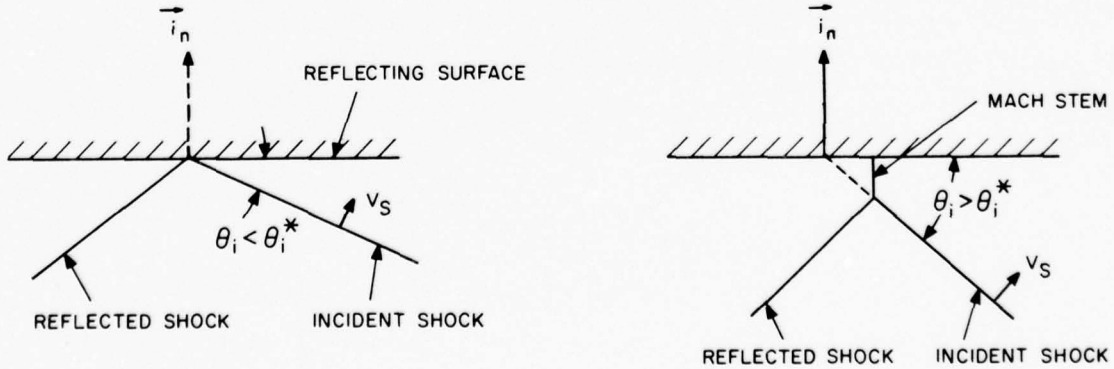


(a) REGULAR REFLECTION

(b) MACH REFLECTION

The critical angle $\theta_i^*$ depends on $\xi$. For very high $\xi_s'$, the angle $\theta_i^*$ is around 40 deg; for low $\xi$'s, $\theta_i^*$ tends to higher values.

Figure 15, taken from Reference 4, depicts the reflection factor r as a function of $\theta_i$ for two values of the parameter $\xi$.* The initial pressure rise is $r\Delta p_s$. The solid and dashed portions of the curves indicate regular and Mach reflections, respectively. The initial rises given in Table 2 were computed using interpolations of these curves.

The results given in Figure 15 are appropriate for a planar shock intercepting a planar surface, i.e., $\theta_i$ is constant for a given encounter condition. When the shock strikes the "lower" (i.e., windward) curved surface of the wing, the incidence angle changes while the shock traverses over the wing. The local shock incidence angle can be shown to be

$$\theta_i = |90-\phi-\alpha_o-\varepsilon_i| \text{ degrees}$$

where $\alpha_o$ is the initial angle of attack (= 3.2 deg in all cases) and $\varepsilon_i$ is the local surface inclination angle due to thickness.

## 3.4 PRESENTATION FORMATS OF EXPERIMENTAL AND ANALYTICAL PRESSURE RESPONSES

Superimposed experimental and analytical differential pressure ($\delta_p$) time histories are presented in two sets of figures. Figures 3-7, introduced earlier, are "full-scale" and individual plots for Cases 1-5 which show clearly the details, especially at early times when the pressures vary rapidly. Figure 16-20 present the same results on a "reduced scale". In the latter set, each figure covers one case and is a composite of plots for all twenty transducer locations, with the horizontal arrays showing the chordwise $\delta_p$-variations at the 40, 60, and 80 percent span stations and the vertical array showing the spanwise variation along the quarter-chord line. The composite figures are useful for detecting trends and for discussion purposes. In both sets of figures, the ordinate scale

*In duplicating Figure 11.12 of Reference 4 some changes were made to conform to the present notation. The two curves cover the $\xi$-range of interest here.

runs from - 2 psi to + 14 psi with 1 psi/div, except for Case 2 where the scale runs from - 2 psi to + 6 psi with 0.5 psi/div. The time scale is 1 msec/div, starting at t=-1 msec. and terminating at t=20 msecs.

## 3.5 DETAILED CORRELATIONS

### 3.5.1 Intercept 9B-A1-2; $\phi$=87.6 deg, $\Delta p_s$=2.1 psi. (Case 1, Figures 3, 16)

The configuration was mounted on the sled so that the plane of the wing was perpendicular to the ground and set at an angle of attack of 3.2 deg. (See Vol. 1 of this report.) For Case 1, the shock is directly from the left side of the sled track ($\phi$=87.6 deg $\simeq$ 90 deg). This shock orientation corresponds to an aircraft receiving a blast directly from below while in level flight at $\alpha$=3.2 deg. The shock front intercept point with the wing plane traverses in the body x-axis direction and relative to the wing at extremely high speeds; and for present purposes one may assume that all points on the blast side (or windward side) of the wing surface receive the shock front at the same time. According to shock reflection theory, the pressure differential $\delta_p$ at any wing station should increase instantaneously by an amount $r\Delta p_s$ at the instant the shock reaches the station, i.e.,

$$\delta_p(t_a)-(\delta_p)_{\text{pre-blast}} = r\Delta p_s$$

where $\Delta p_s$ is the peak free-field overpressure at intercept (= 2.07 psi for Case 1, see Table 1) and r is the reflection factor. According to the calculated results shown in Table 2, this increase should amount to 4.43 psi at all wing points (with r being constant for the range of shock incidence angles and $\xi$ = 0.166).

For near normally incident and very weak shocks (i.e., $\xi$ and $\theta_i$ small), the reflection factor is 2.0 according to acoustic theory, indicating a peak reflected overpressure of about $r\Delta p_s$ = 4.14 psi. The acoustic value is given here also because the VIBRA-6 approach is a linearized one (up to a point) and hence utilizes approximations which are closely related to those in acoustic theory. However, the VIBRA-6 analysis internally adjusts its linearized results by a factor $f_a$. This

factor is equal to $(\rho_s/\rho_\infty)(\bar{V}/V)$ where $(\rho_s/\rho_\infty)$ is the density ratio across the shock and $\bar{V}$ is the relative wind speed which accounts for the material velocity behind the shock.* For Case 1, $f_a$ is found to be 1.127 at the instant of shock reflection. If one applies the factor 1.127 to the 4.14 psi value, one obtains the adjusted value of 4.67 psi for the initial pressure rise. This value can be used as a side check on the VIBRA-6 calculations since it should be the limit for the predicted initial pressure rises from all channels.

The initial pressure rises according to the VIBRA-6 predictions are compared with experiment in Figure 21. The curves are for the chordwise variations at the 40, 60, and 80 percent span stations and for the spanwise variation along the quarter-chord line. (Note the suppressed zeros in the ordinate scales.) The solid curves are the analytical results with the cutoff frequency $f_c$ equal to 4 kHz and the frequency increment $\Delta f$ = 1 to 10 Hz depending on frequency range. The VIBRA-6 predictions fall below 4.67 psi, the limit derived earlier. With a cut-off frequency much higher than 4 kHz and a smaller frequency increment $\Delta f$, the predictions would have been closer to the 4.67 psi value.** One should expect reduced peaks with a finite cut-off frequency; and this was partially confirmed by additional short calculations with $f_c$ = 8 kHz. The peaks with $f_c$ = 8 kHz were found to be as much as 0.3 psi higher and thus closer to the 4.67 psi value.*** "Peak clippings" of 0.3 psi

---

*Past experience in correlating experimental and analytical blast-induced loads on airfoil sections indicates that a correction factor which accounts for "density jumps and q-effects", such as $f_a$ above, improves the predictions significantly.

**As pointed out in Section 2.3, data entry item RG6I4, the choices of $f_c$ and $\Delta f$ affect the VIBRA-6 calculations because they control the Fourier transformations.

***The calculations referred to here were performed with $f_c$=4 kHz and 8 kHz for a response period of 2 ms. In both cases, the results were printed at 25 μs intervals to define the peaks accurately. The 0.3 psi value was derived from these calculations. See also remarks under item RG6I2V, Section 2.3.

magnitude are insignificant because (a) they are very small compared with the peak magnitudes, and (b) they give negligible contributions to the impulses.

The experimental data in Figure 21 show initial pressure rises which are always higher than the predicted, except at the 5 percent chord locations. There is a spread in the experimental peak values of as much as 1 psi. One definite trend is noted in the spanwise variation along the quarter-chord line. As may be seen in Figure 21, the experimental peak values tend to rise appreciably toward the inboard transducer locations, with the level at the innermost station (20/25)* being 30-40 percent higher than those at 50 percent station and beyond. This is probably the well-known "corner effect" due to a Mach stem which forms following shock reflection from the body and which propagates and influences the wing pressures particularly at the inboard stations.

According to shock reflection theory, the rises are instantaneous as stated earlier. In the VIBRA-6 predictions, the rise times to peak are from 0.1 to 0.2 ms. This is expected, inasmuch as the cutoff frequency is 4 kHz. Experimentally, the rise times are observed to be around 0.2 to 0.4 ms depending on transducer channel. These are deemed a little high in view of the nominal 4 kHz frequency response of the telemetry system. Rise times of 0.2-0.4 ms suggest experimental lower cutoff frequency, and perhaps as low as about 2 kHz, apparently caused by excessive filtering by the data reduction system.

Consider next the sequence of events following shock reflection. If the wing were stationary (i.e., V=0), the pressures on the two sides of the wing would nearly equalize in a short time, resulting in small

*In all figures presenting time histories of sled transducer pressures, transducer locations are identified by a four digit code, e.g., 20/25, where the first two digits (20) give the spanwise distance from the model centerline as a percent of the semi-span (e.g., 20%) and the last two digits (25) give the percentage chordwise distance from the leading edge of the wing.

pressure differentials; thereafter the loading would be much like the drag force on a plate exposed to a stream normal to its surface with the stream velocity equal to the material velocity in the shock field. The magnitude of this $\delta_p$ would be $\leq$ 0.2 psi. But with the wing traveling at V$\tilde{=}$870 ft/s, the gust field results in an angle of attack which develops a pressure differential far in excess of 0.2 psi. Referring specifically to the prediction curve for the 80/05 station (Figure 3), one notes that the initial rise to the peak value of $\delta_p \tilde{=}$ 6.5 psi is followed by a decay for a short time until the lift buildup takes over and increases $\delta_p$ to a second and higher peak $\delta_p$ = 6.95 psi at t$\tilde{=}$3.5 ms. Being at the 5% chord station where the $\delta_p$'s are high due to angle of attack, this buildup to a higher $\delta_p$-level is not surprising. The experimental pressure loading, on the other hand, shows a rise to near 10.0 psi at t$\tilde{=}$1.2 ms followed by a reduction significantly below the predicted level. This large experimental peak is attributed to a vortex system which starts at the leading edge and develops over the leeside surface. Vortex-induced peaks are also noted on the traces for the 80/25 and 80/45 stations at the later times t=1.8 and 2.9 ms, respectively. The corresponding peaks at stations 80/65 and 80/85 are not as clear.

The vortex behavior need be described further. Experimentally, it is known that highly swept wings, such as the tested wing, set at angles of attack above a few degrees (say 3 or 4 degs) develop such vortices. In steady flight, the vortex location is stationary, with its core swept back more than the wing, i.e., starting near the leading edge at inboard stations and drifting downstream relative to the chord at outboard stations. With increasing angle of attack, the vortex strengthens and sweeps further downstream. This type of wind tunnel information is helpful in explaining qualitatively the flow behavior during blast encounter. Consider Case 1, and assume for the time being that the blast field does not decay, i.e., a step jump is sustained following shock arrival. When the shock arrives, the angle of attack jumps from its initial pre-blast level of 3.2 deg to about 11.4 deg. The vortex forms and first travels rapidly downstream toward the position it would occupy for $\alpha$=11.4 deg. in steady flow; then it slows down and stops since the blast field is sustained. In the actual

situation, the angle of attack starts decreasing as a result of the decaying material velocity field; and given sufficient time, one would expect a trend to return to forward positions. The blast decay has the net effect of slowing down the rearward movement to a position ahead of that associated with $\alpha$=11.4 deg (in steady flow) and of a slow return to its pre-blast position after the shock field has passed through. This sort of vortex behavior may be noted in the present test if one examines simultaneously the time histories of $\delta_p$ for the five chordwise locations at the 80 percent span station in Figure 16.

At a given instant of time, the pressure differentials just below the vortex center are high. Somewhat upstream of that point, the flow is separated on the vortex side of the wing, giving higher pressures on the leeward side of the wing and thus reducing the $\delta_p$'s; and downstream of that point, the differential pressures are higher than they would be in the absence of the vortex system.

A similar trend may be observed from the 60%-span station traces shown in Figure 16. There the vortex movement is not as far downstream chordwise. Also, the vortex effects are not too distinct in the 60/45 and 60/65 traces. Except possibly with the 90/25 channel, which appears to have malfunctioned, is it clear from the composite response curves in Figure 16 that the vortex-induced effects on the loadings are quite large, and perhaps of even greater significance than one would expect based on steady-state data for 65-deg sweptback wings set at moderate angles of attack (between 3.2 and 11.4 deg). The doublet-lattice analysis, which is essentially a linear one* and neglects the leading edge vortex effects, generally underpredicts the loadings. The percentages by which the predicted $\delta_p$'s are lower than the experimental $\delta_p$'s depend on time and location, thus affecting not only sectional lifts but even to greater extents the sectional pitching (or torsional) moments.

---

*Except for the adjustment factor $f_a$ discussed earlier to account for the "density jump and q-effects".

In view of the above observations, it is appropriate to raise the question: For highly-swept wings, how seriously are the predictions for structural responses of low-frequency components (e.g., peak wing bending moments) affected by the severe VIBRA-6 loading underestimations? With no detailed analysis on a typical configuration and for various encounter conditions, one can only give an "order of magnitude" estimate as to the accuracy of structural response predictions. Experimental-analytical comparisons of the loadings are also indicative of those associated with their respective impulses over a time period comparable with the structural mode period (and also of the first half of the blast field positive phase duration). Looking at the comparisons in Figure 16, it would not be surprising if one predicted peak root bending moments which are only half of what they are actually. These observations and conclusions are further substantiated by the results from the next case to be discussed, namely Case 3. In the latter, the shock is essentially from the same orientation ($\tilde{\phi}$=90 deg) but its strength is at a higher level.

Commenting generally on the comparisons shown in Figure 16, some major predicted trends agree roughly with observations, but the neglect of the vortex system in the analysis imposes serious limitations as to the accuracy of the doublet-lattice method. These limitations are expected to be more and more significant with increasing wing sweep angles and shock strengths. Because they are nonlinear, vortex-induced effects cannot be estimated separately and added to the pressure loads predicted by the DLM. No simple means can be offered at this time to overcome the DLM underpredictions.

3.5.2 Intercept 9B-A2-2; $\phi$=90.3 deg; $\Delta p_s$=4.0 psi. (Case 3, Figures 5, 18)

Case 3 is discussed next because it is most clearly related to Case 1 above. Here the shock is also almost directly from "below", i.e., $\phi$=90.3 deg $\cong$ 90 deg; but the shock strength is nearly twice that in Case 1, i.e., $\Delta p_s$=4.02 psi vs. 2.07 psi. (See Table 1.)

The initial pressure rises obtained from the VIBRA-6 predictions are compared with experiment in Figure 22. The curves are once more for the chordwise variations at the 40, 60, and 80 percent span stations

and for the spanwise variation along the quarter-chord line. (Note that the ordinate scales have suppressed zeros.) The initial pressure rises should have the limiting value of

$$r\Delta p_s = (2)(4.02)(1.256) = 10.1 \text{ psi}$$

with the adjustment factor $f_a$ (defined and justified in Section 3.5.1) for this case turning out to be 1.256. The comparisons are similar to those in Figure 21 for Case 1. Generally, the experimental results have about a 1 psi scatter and are in some cases below the VIBRA-6 prediction curves, especially from the transducers along the 80 percent span station.

Compared with Case 1, the leading-edge vortex system is stronger as the angle of attack reaches the 18 deg. level at intercept. Its action is clearly defined in this case, as may be seen even in the traces for the 40 and 60 percent stations. Vortex-induced peaks are easily identifiable: 12.6 psi at $t \tilde{=} 1.2$ ms for 40/05 and 13.7 psi at $t \tilde{=} 1.0$ ms for 60/06, for example. (See Figures 5, 18.) Looking at the spanwise variation along the quarter-chord line in Figure 18, the vortex-induced peaks are distinct for the 40, 50, 70, and 80 percent span stations and are substantially above the initial shock reflection peaks. No similar peak is seen for the 60 percent span quarter-chord station. This <u>may</u> be due to possible failure of the leeward side of the pressure transducer pair during the test run, so that the vortex effect would not be a contributing factor to the observed signal. As noted in Table 7 of Volume 1, this leeward transducer was definitely inoperative <u>after</u> completion of this test run.

On a relative basis, examinations of Figures 16 and 18 show the Case 3 vortex-induced effects to be more pronounced, of longer durations, and over a larger outboard portion of the wing than those for Case 1.

Compare next the VIBRA-6 predictions with experiment (Figures 5 and 18). In Case 1, VIBRA-6 underestimated the loadings except at Sta. 80/05 for times roughly between 1.5 to 10.5 msecs; for Case 3, however, overestimations are noted at the 5 percent chordwise locations of the 60 and 80 percent span stations (and even at station 80/25). <u>Overall,</u> however, the VIBRA-6 predictions are again substantially lower.

The important conclusion drawn from the results of Case 1 applies to this case also; namely, the VIBRA-6 analysis seriously underpredicts the pressure loadings with the consequence that the computed peak structural responses are expected to be very significantly lower than actual.

3.5.3 Intercept 9B-A2-1; $\phi$=20.1 deg, $\Delta p_s$=2.0 psi. (Case 2, Figures 4, 17)

The situation in this case (as well as in Case 5 to be discussed next) is quite different from the previous two in that the blast is from a "nearly head-on" direction. It corresponds to an aircraft flying level and encountering a blast from the direction indicated in the sketch below.

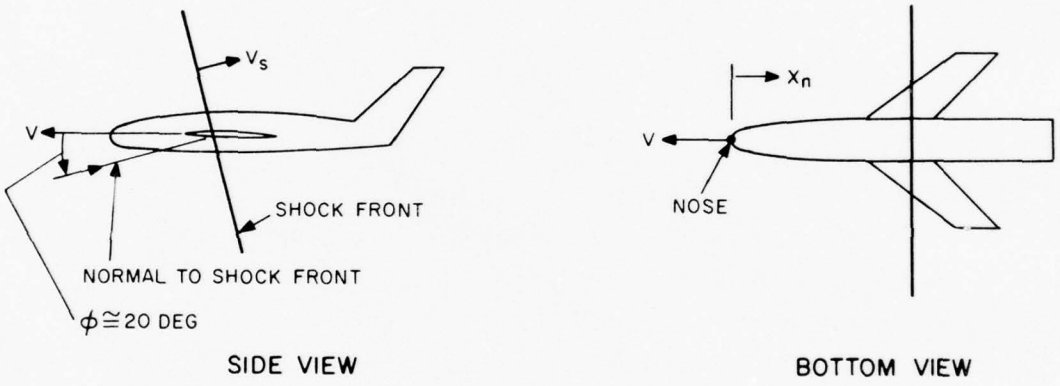


With the shock from this orientation, the blast-induced pressure loadings are, as expected, at lower overall levels than those with a normally incident shock (i.e., $\phi \simeq 90$ deg) of the same strength.*

The shock front traverses the wing chord line at a speed

$$V_t = V + \frac{V_s}{\cos\phi} = 2166 \text{ ft/s}$$

relative to the wing, since V≅874 ft/s, $V_s$=1213 ft/s, and cos$\phi$≅0.939.

*For Case 2, $\Delta p_s$=2.01 psi. Because the overall pressure differentials are low, the loading responses in Figures 4 and 17 are presented with an ordinate scale of 0.5 psi/div instead of 1 psi/div.

The situation is as depicted in the sketch below

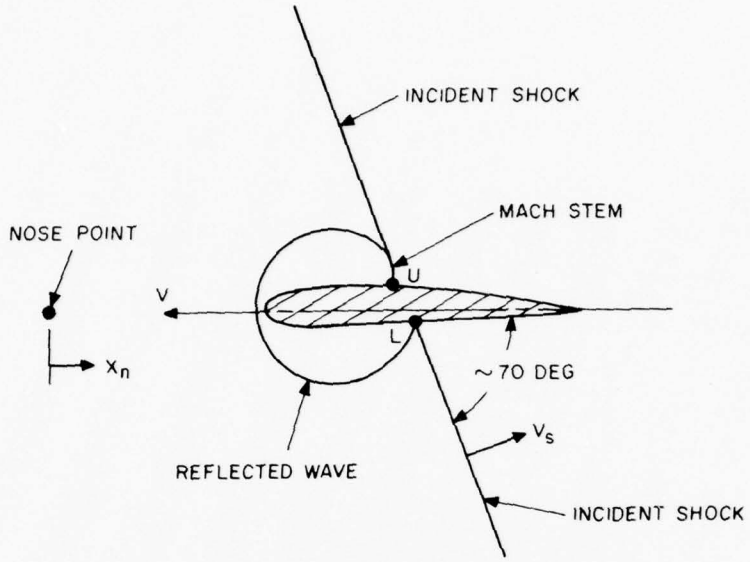


From the results given in Table 2 for Case 2, the shock incidence angles at the 25 percent chord station and aft are such that the reflection from the lower surface is a Mach reflection with a stem which traverses the surface at a speed slightly higher than 2166 ft/s. On the upper surface, the shock speed is slightly lower. At the instant the shock pattern is in the position indicated in the sketch, the small chord segment between points U and L experiences large pressure differentials. The chord segment between the leading edge and point U has much lower $\delta_p$'s inasmuch as some pressure equalization has been effected between the two sides of the wing. The large $\delta_p$'s along the short chordlength between points U and L translate into a sharp spike of very short duration at a fixed wing station. According to the results given in Table 2, the spike peaks should reach the values $(\delta_p)_{\text{pre-blast}} + r\Delta p_s$, where $r\Delta p_s$ varies from 4.26 psi (at the 85 percent chord stations) to as high as 5.69 psi (at the 25 percent chord stations); but the experimental and the VIBRA-6 peaks do not reflect such high levels. The duration of the spike at a given wing station is the difference in shock arrival times on the top and bottom surface points at that station. It amounts to a very small fraction of a millisecond. In fact, it is so short that one should not

expect to (a) be able to predict its shape with the VIBRA-6 analysis, and (b) see such spikes in the experimental traces because of the frequency limitations of the instrumentation. From a practical point of view, the inability of the VIBRA-6 to predict or the failure of the instrumentation to show the full extents of such spikes is immaterial. As far as structural responses are concerned, the spike contributions are through their impulses. Even though the spike peaks are high, their impulses are expected to be very low because of their very short durations. In any event, should the impulses be significant, they would be reflected in the measurements and also, hopefully, in the predictions.

From the discussions above, it should be clear that the shock arrival time $t_a$ (in intercept time) for a wing station $x_n$ inches aft of the nose is

$$t_a = \frac{x_n}{(12)(2166)} = 0.0385x_n \quad \text{ms}$$

The $x_n$'s range from 38 to 75 in. for the various transducer locations. Thus the shock arrival times vary from $t_a$=1.5 ms at Sta 20/25 to $t_a$=2.9 ms at Sta 80/85. The times to initial peaks as seen in the VIBRA-6 results (Figure 4) are slightly higher because (a) $V_s$ is taken to be equal to the speed of sound ($a_\infty$=1140 ft/s) instead of its true value of 1213 ft/s, and (b) there is a rise time due to the fact that the cutoff frequency $f_c$ in the Fourier transformations is only 4 kHz.

Following the very short duration initial spikes, the pressure differentials reach levels which are more in line with "lift type" loads. As a result of the downwash field

$$w = w_m \sin\phi$$

set up by the material velocity ($w_m$) field behind the shock, the lift starts to build up. The lift build-up masks to some extent the latter stages of the sharp peak decay.

With the peak material velocity behind the shock being about 118 ft/s, the angle of attack which is 3.2 deg. pre-blast increases to as high as

$$\alpha \cong 3.2 + 57.3 \left(\frac{118 \sin\phi}{874 + 118\cos\phi}\right)$$

$$\cong 5.6 \text{ deg.}$$

The maximum angle of attack being 5.6 deg, a level not too deep into the nonlinear range of lift versus $\alpha$, the leading edge vortex system is weak (compared with the previous two cases) and is not expected to influence as strongly and as large a portion of the outboard wing area as in the previous cases. Peaks associated with the vortex movement during the transient period, similar to those identified in Case 1 Figures 3 and 15, are not as distinct in this case. Examining Figures 4 and 17, one can detect lesser peaks at some of the stations which are anticipated to be affected most. For example the 4.8-5.0 psi peak at $t \cong 3.3$ ms for 60/05 and the 3.3 psi peak at $t \cong 3.5$ ms for 80/25 are attributed to the vortex system. Corresponding peaks for stations 60/25, 70/25, 80/05 are not as easily discernible.

Even though the aforementioned peaks are not clearly seen, the vortex-induced contributions to the pressure loadings appear to be still very large. From steady-state experimental data for a similar wing at M=0.85, one would not expect the vortex contributions to be appreciable inasmuch as the angle of attack reaches the modest value of 5.6 deg. But in a transient situation, the situation may be different. On an absolute basis, they are undoubtedly small; but so are the overall blast-induced levels. On a basis of percentages of the total blast-induced loads, the vortex contributions may still stay relatively high. This appears to be the case if one compares the VIBRA-6 prediction curves with the experimental data in Figure 17. Since the experimental pre-blast levels have been aligned with those according to the analysis and they are of the order of one third to one half of the average levels during the first 10 ms of response, one can only compare the blast-induced parts, i.e., $\Delta\delta_p(t) = \delta_p(t) - (\delta_p)_{\text{pre-blast}}$. From analytical-experimental comparisons, one sees that the analytical $\Delta\delta_p$'s over a period of several milliseconds are very

roughly half as large as the experimental $\Delta\delta_p(t)$'s. The implication here is that the structural responses according to VIBRA-6 for nearly head-on orientations are also expected to be very significantly lower than the actual ones.

There are two other factors which should be mentioned in connection with the experimental-analytical comparisons. The first stems from changes in Mach number during the transient period and the second pertains to thickness effects, both of which are unaccounted for in the aerodynamics routine in VIBRA-6. The analysis assumes a constant Mach number and zero thickness. The Mach number change stems from two sources: the speed of sound behind the shock being different from the pre-blast ambient speed of sound, and more importantly, the change in the relative wind speed due to the component of the material velocity behind the shock parallel to the sled velocity V.

For Cases 1 and 3, the component of material velocity in the direction of V is nearly zero, and changes in M are small. For Case 2, however, the maximum material velocity is 118 ft/s, which means that its "x-component" adds 111 ft/s to the relative wind speed. Effectively then, the relative wind speed is 985 ft/s. With the speed of sound behind the shock being 1164 ft/s, the Mach number turns out to be about 0.85 as compared with the pre-blast value of 0.76, an increase of over 10%.

With the experimental wing model being 12 percent thick in the stream direction, the Mach number reaching 0.85 (and even higher in Case 5 to be discussed), and with significant increments in angle of attack due to the blast, questions arise as to how important are these two effects. Some calculations using linearized theory indicate that the M-effect is small, even though M tends towards unity, because of the high sweep angle and low aspect ratio conditions. With a fairly thick wing at high angles of attack, one cannot overlook the possibility of some transonic flow regions. If such regions emerge, the question is to what degree they affect the pressure loadings.

To answer these questions, it would have been useful to have some wind tunnel steady-state pressure measurements on the present configuration for ranges of high subsonic Mach numbers and angles of attack. Unfortunately, such data are not available. However, an examination of experimental data on a similar, highly-swept, low-aspect-ratio wing configuration (Ref. 5) indicates that the Mach number and thickness effects may be relatively small on sectional lift coefficients and on chordwise center of pressure locations. This suggests that the same effects are probably small also on local pressure loadings.

Before concluding the coverage for Case 2, the following two additional points may be of interest to the reader:

(a) No experimental data are available for Stations 20/25 and 90/25.

(b) The character of the 50/25 trace is not in line with those for 40/25 and 60/25: whereas the latter two traces show sharp rises at shock arrival times, the 50/25 trace does not. In contrast, the same channel (50/25) falls in line with the two adjoining quarter-chord channels (40/25 and 60/25) in Case 5, the case which has essentially the same blast orientation as Case 2, but a higher overpressure level ($\Delta p_s \tilde{=} 3.6$ psi). No explanation can be offered for this apparent "odd behavior" from the 50/25 channel.

3.5.4 Intercept 9B-A3-1, $\phi$ = 20.1 deg, $\Delta p_s$=3.6 psi. (Case 5, Figures 7, 20)

As in the preceding case, the blast is from a nearly head-on direction ($\phi \tilde{=} 20.1$ deg); but the shock strength and the velocity positive phase duration are $\Delta p_s$= 3.56 psi and $t_v^+ > 17$ ms, respectively, as compared with $\Delta p_s$=2.01 psi and $t_v^+$= 13.8 ms for Case 2.* The two sketches in Section 3.5.3 depicting the encounter geometry and the shock pattern during engulfment apply also to this case. Here the shock speed along the wing chordline and relative to the wing is approximately

$$V_t = V + \frac{V_s}{\cos\phi} = 2228 \text{ ft/s}$$

*For Case 5, $t_v^+$ was not determined for reasons discussed in Vol. 1 of this report.

since V=872 ft/s, $V_s$ = 1273 ft/s, and $\cos\phi \cong 0.939$. The shock arrival times $t_a$ (in intercept time) are slightly earlier in this case, ranging from about 1.4 ms (Sta 20/25) to 2.8 ms (Sta 80/85). The initial peaks, as predicted by VIBRA-6 calculations (Figure 7), occur at slightly later times for reasons discussed in Section 3.5.3.

Refer to the calculated results in Table 2 for Case 5. With the shock strength ratio $\xi$=0.282, the reflection from the lower surface is a Mach reflection aft of the 5 percent chord station; and the corresponding reflection factors are such that the expected peak overpressures for the initial spikes range from about 9.5 psi (at 5 percent chord) to 6.0 psi (at 85 percent chord). These spikes are once more of very short durations; and their shapes are not predicted by VIBRA-6 nor observed experimentally for reasons stated in Section 3.5.3.

With the peak material velocity behind the shock being about 204 ft/s, the angle of attack which is 3.2 deg pre-blast increases to as high as

$$\alpha \cong 3.2 + 57.3 \left(\frac{203\sin\phi}{872+203\cos\phi}\right)$$

$$\cong 7.0 \text{ deg.}$$

The maximum angle of attack being 7.0 deg (and somewhat higher than in Case 2 where $\alpha_{max}$ = 5.6 deg), the leading edge vortex system is stronger. The associated peaks are easily identifiable in the 60/25, 60/45, 80/05, 80/25 traces. (See Figures 7 and 20.) The noise in the records for 60/05, 80/25, 80/65 and 80/85, attributed to the telemetry is of sufficient magnitude to mask the vortex-induced peaks.

Experimental-analytical comparisons in Figures 7 and 20 show once more that the blast-induced pressure loadings during the first 10 msecs or so are underpredicted by VIBRA-6, and by percentages in excess of those in Case 2. On an absolute basis, the underpredictions are particularly severe at stations where the loading levels are highest, namely, at the 5, 25, and 45 percent chords of the outboard stations. It suffices

to look at the comparisons shown by the traces for stations 50/25, 60/25, 60/45, 80/05, 80/25.* Since the loads at such stations are the major contributors to the bending moments, these comparisons are also indicative of the sort of accuracy one should expect from a VIBRA-6 structural analysis for highly swept configurations and for near head-on blast encounters.

For Case 5, the maximum material velocity behind the shock is 203 ft/s. With the speed of sound and the adjusted relative wind speed equal to 1186 and 1065 ft/s, respectively, the peak Mach number turns out to be 0.90 as compared with the constant value of M=0.76 used in the VIBRA-6 calculations. Although this Mach number increase amounts to 18 percent and the wing is 12 percent thick, the Mach number change and thickness effects are still believed to be relatively minor contributing factors for reasons discussed in the previous section.

3.5.5 Intercept 9B-A2-3; $\phi$=134.9 deg, $\Delta p_s$=2 psi. (Case 4, Figures 6, 19.)

The blast encounter in this case corresponds to the situation of an aircraft flying level and being overtaken by a shock from the "rear lower quadrant" as shown in the next sketch

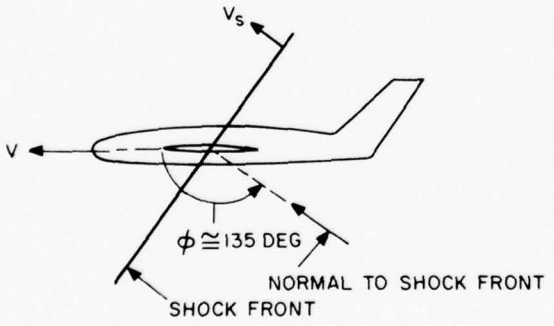


SIDE VIEW

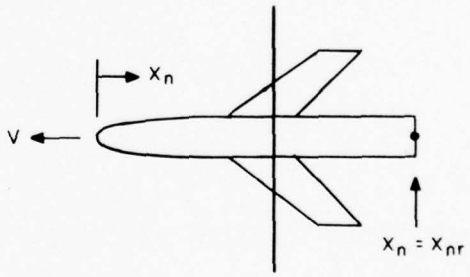


BOTTOM VIEW

*The 60/05, 70/25, 80/65 and 80/85 traces indicate channel malfunctions. Although included in Figures 7 and 20 for the sake of completeness of experimental data, these traces add no additional information for present purposes.

The shock front traverses the wing chord line, from the trailing edge towards the leading edge (i.e., overtaking the wing) at a speed

$$V_t = - V - \frac{V_s}{\cos\phi} = 854 \ ft/s$$

relative to the wing, since V=868 ft/s, $V_s$=1215 ft/s, and $\cos\phi$=- 0.706. Recall that $V_t$ for the nearly head-on Case 2 (at the same overpressure level) was 2166 ft/s in the opposite direction. With the shock overtaking the wing at a relatively low speed (854 ft/s), the wing remains in the blast field for a longer period of time. More specifically, the velocity positive phase duration, $t_v^+$, as seen by a wing point is about 56.5 ms, a duration twice as long as that seen by a point fixed in space.

Referring to the calculated results in Table 2, the shock incidence on the lower (reflecting) surface varies from 41 to 63 deg. With the shock strength ratio $\xi$ = 0.155, this means that the reflection is a regular one for points aft of the 20 percent chord station. The situation is as sketched below

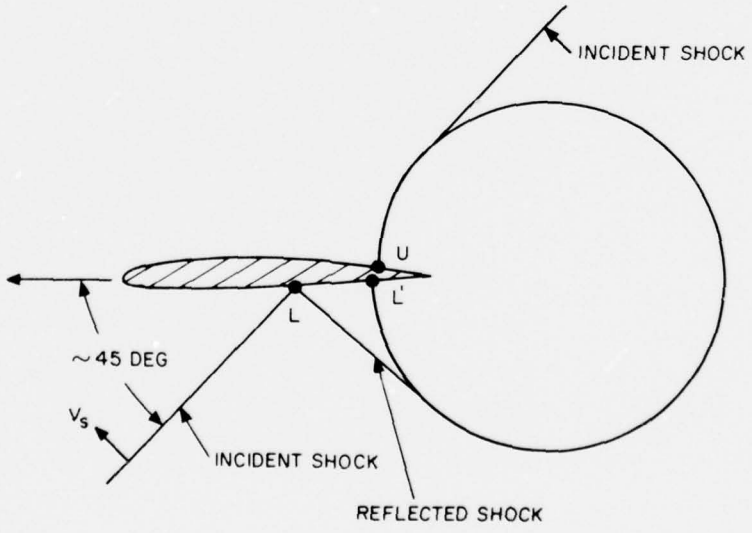

On the lower surface the shock traverses at a speed of 854 ft/s relative to the wing as calculated earlier (i.e., speed of point L = $V_L$ = 854 ft/s). The corresponding shock speed over the upper surface is estimated to be very roughly 300 ft/s (i.e., speed of point U=$V_U$ = 300 ft/s). The 300 ft/s value is arrived at assuming two-dimensionality and no sweep. If one accounts for the trailing edge sweep, the speed $V_U$ would increase somewhat. Because of the difference $V_L$-$V_U$ $\approx$ 500 ft/s, the separation distance between points L and U may become sizeable fractions of the chord when L approaches the leading edge. (The segment of the chord between L and U is important because of its very high loading.) Coupled with the slower speeds $V_t$ (slower when compared with the speeds $V_t$ for near head-on Cases 2, 5), this separation should reflect in "wider" diffraction peaks. To see how "wide" these peaks may be, consider the responses for the 40 percent span stations where the chord is 21.92 in. = 1.83 ft. Station 40/45 is 1.01 ft. from its trailing edge. Utilizing the values of $V_L$ and $V_U$ given above, one finds that the 40/45 trace should have a diffraction peak width of the order of 2 ms. Similarily for the 40/85 station, which is 0.27 ft. away from the trailing edge, the width should be 0.6 ms. The peaks are sufficiently wide to be clearly seen in the measurements. These expectations are confirmed by the 40/45 and 40/85 experimental traces in Figure 6.

A few words need be said about shock arrival times, $t_a$, at various stations to point out a source of error in estimating $t_a$ using VIBRA-6, an error which is not apparent in the comparisons of Figures 6 and 19. Based on the $V_t$-value of 854 ft/s derived above, the shock arrival times $t_a$ (intercept time) are given by

$$t_a = \frac{x_{nr}-x_n}{(12)(854)} = 0.0976\ (x_{nr}-x_n)\ \text{ms}$$

where $(x_{nr}-x_n)$ is the distance in inches from intercept point to point in question. For this case, the intercept point is the most rearward point in the analysis configuration (see sketch at beginning of this section). With $x_{nr}$=85.7 in. and $x_n$ varying from 38 to 75 in., the shock arrival times range from 1.0 to 4.7 ms, depending on station. The VIBRA-6 response curves in Figure 6 show peaks at later times than those estimated according to the above formula, varying from about 1.8 to 6.0 ms. The two reasons

stated earlier in connection with Case 2 (Section 3.5.3) apply here also; namely, the rise time due to a finite cut off frequency and, more importantly in this case, the fact that the speed of sound is used in VIBRA-6 instead of the shock speed. Note that if $a_\infty$=1140 ft/s had been used instead of $V_s$=1215 ft/sec in the formula for $V_t$, the resultant value for $V_t$ would have been 747 ft/s, thus increasing the estimated $t_a$ values by a factor (854/747) = 1.14. Therefore the predicted shock arrival times at forward stations may be off by as much as 0.6 ms. This error is not apparent in the experimental-analytical comparisons of Figure 6 because the time scales of the experimental traces have been arbitrarily aligned on a channel to channel basis with those of the analytical traces. (See Section 3.2).

Case 4 has other features which differentiate it from the other cases and which deserve some comments. First of all, the Mach number decreases from its pre-blast value of 0.76 following shock engulfment, in contrast to Cases 2 and 5 where it increases. With the maximum material velocity being 120 ft/s and the speed of sound behind the shock estimated at 1164 ft/s, the lowest Mach number during the transient state turns out to be 0.67. (It is recalled that the analysis retains the 0.76 value for M at all times.) This decrease in M is expected to have an even lesser effect and in a direction opposite to that in Cases 2 and 5. Secondly, the angle of attack increases from 3.2 deg to about 9.4 deg following intercept. The $\alpha$-rise is of sufficient magnitude to portend the formation of a fairly strong leading edge vortex system in this case also. However, its development is delayed until the shock engulfs the leading edge. This delay affects the strength and the movement of the vortex core, and thus also the loadings; and as such, the characteristic signature of the vortex on the loads may be expected to be not as distinct as for intercepts near 90 degrees (Cases 1, 3).

Consider first the diffractive period and refer once more to the calculated results in Table 2 for Case 4. At a given station on the wing,

the loading should jump by an amount $r\Delta p_s$ when point L reaches the point directly below the station. With the shock strength ratio $\xi$=0.155 and the shock incidence angle on the reflecting lower surface varying between 41 and 63 deg., the initial rise $r\Delta p_s$ should amount to 4.3-4.6 psi for chord stations 25 percent and aft and nearly 6.0 psi at the 5 percent chord station. The total loading is then $\delta_p = (\delta_p)_{\text{pre-blast}} + r\Delta p_s$. This level should be maintained nearly until point L' reaches the station. Thereafter the pressure differential should drop, and fall substantially faster when point U reaches the point above the station. As pointed out earlier, this duration may be quite appreciable, depending on chordwise location, amounting to as much as 3 msecs in some cases. With wide diffraction peak widths and fairly high $r\Delta p_s$-values, the associated impulses could be quite significant, especially if post diffractive load levels are relatively low. This would be the situation with shocks from the rear as in Case 4.

Compare next the initial rises: the expected values $r\Delta p_s$ from Table 2 with the corresponding ones from experiment $[(\delta_p)_{\text{peak diff.}} - (\delta_p)_{\text{pre-blast}}]$. The experimental results are generally higher for the 25, 45, and 65 percent chord stations, with the worst comparison being at the 40/65 station where $r\Delta p_s$ = 4.34 psi versus $[(\delta_p)_{\text{peak diff}} - (\delta_p)_{\text{pre-blast}}]$ = 6.8 psi from experiment. The comparisons are good, within a few tenths of a psi, for the 85 percent chord stations, except that for station 60/85 which gives an initial rise of 2.5 psi versus the expected 4.26 psi (for reasons which cannot be explained). The expected rise at the 5 percent chord station is ~ 6.0 psi, whereas experimentally they amount to 3.3 psi at 40/05 and 60/05 and to the much lower value of 1.5 psi at 80/05. (more will be said about the 80/05 channel later.) No reasonable explanations can be offered why the initial rises at the 25, 45, and 65 percent chord stations are for the most part significantly higher than the predicted values in Table 2. Those at the 5 percent chord station are much lower than expected according to Table 2, presumably due to the proximity to the loading edge from which relieving signals emanate.

The VIBRA-6 predictions in Figure 6 show gradual initial rises to peaks which are less than 4.3 psi at all stations. And even though they are wider and "tend to duplicate" the observed variations, the analytical diffraction period responses show lower impulses than the experimental ones. In some cases, the impulse differences are quite large amounting to as large as 50 to 100 percent at the 25, 45, and 65 percent chord stations. This is important because the diffraction period impulses are significant portions of the total impulses (i.e., impulses during the lift development phase); and severe underestimations of the diffraction period impulses are expected to reflect as serious underestimations in structural responses (e.g., peak wing bending moments).

Beyond the diffraction periods, the prediction levels agree reasonably well on the average with experiment, but with some exceptions. For example, the loadings are underpredicted at stations 40/25, 50/25, 60/05, 60/25, 60/45, 80/45, 80/65, and this is likely to be due to the vortex effect. In contrast, the loading is overpredicted at station 80/05; the overall experimental levels seem to be far below one would expect by "extrapolating" the 40/05 and 60/05 results. First, the initial rise amounts to only 1.5 psi, even below the free-field peak overpressure. Secondly, the analysis predicts loading increments (due to blast) which are nearly double those indicated by experiment. The reason for the apparent odd behavior of the 80/05 channel is unknown.

Summarizing the assessments from comparisons for Case 4, which apply generally for intercepts from the rear, it is concluded that:

(1) Even though the VIBRA-6 predictions tend to follow the trends of the experimental $\delta_p$-variations during the diffraction period, their levels and hence their associated impulses are generally significantly lower.

(2) The VIBRA-6 overall $\delta_p$-levels during the entire lift development phase are lower for most outboard stations except those near the leading and trailing edges.

(3) As a consequence of (1) and (2), the VIBRA-6 analysis is expected to severly underpredict the peak structural responses induced by a 2-4 psi shock intercept from the "lower rear quadrant".

# SECTION 4

# SUMMARY

## 4.1 SCOPE OF COVERAGE IN THIS VOLUME

Blast-induced pressure loadings predicted by the doublet-lattice aerodynamic subroutine in VIBRA-6, hereafter referred to as the VIBRA-6 analysis, are correlated with experimental data from a highly-swept ($\Lambda_{c/4}$=64.8 deg) low aspect ratio (AR=2.47) wing configuration travelling at Mach 0.76. The comparisons and assessments are for five intercept conditions, including three blast orientations ($\phi\tilde{=}$20, 90, and 135 deg) and for two overpressure levels ($\Delta p_s\tilde{=}$2 and 4 psi).

In this volume, emphasis is placed on the pressure responses during the <u>early</u> phase, i.e., the so-called lift development phase, which includes the diffraction period, and which has a duration of 7 to 20 ms depending on intercept case. The VIBRA-6 analysis results for the <u>late</u> response phase have been found to essentially duplicate those from the quasi-steady analysis of Volume 1 (V6QS); hence, the comparisons and conclusions with V6QS already presented in Volume 1 of this report apply here also for the late response phase, and generally are not repeated below.

The three intercept angles of $\phi$=20, 90, and 135 deg correspond for an aircraft to a "near head-on" intercept, an intercept from "directly below", and an intercept from the "rear lower quadrant", respectively. Generally speaking, the characteristics of the pressure loadings for these orientations (and for a given overpressure level) are: relatively short duration and the lowest levels for the first, a longer duration and the highest levels for the second; and the longest duration and the "middle" levels for the third.

The VIBRA-6 aerodynamics is assessed with due consideration to its intended and primary use, viz that of predicting blast-induced structural responses on "low frequency" major components, i.e., "gust type" problems to which the VIBRA-6 code is addressed. However, some comments are also offered on the pressure loading variations during the early diffraction period; and they should be of interest in "overpressure type" problems, i.e., for responses of local structures such as panels, frames, longerons, etc.

## 4.2 SUMMARY OF OBSERVATIONS

The most significant features of the preceding discussions of the test results and of the comparisons of VIBRA-6 predictions with the test results are now summarized.

### 4.2.1 Effects of Blast-Induced Angle of Attack

For intercept Cases 2, 4, and 5, the peak angles of attack amount to 5.6, 9.4, and 7.0 deg, respectively. Even at these moderate angles of attack, the blast-induced incremental loadings predicted by VIBRA-6 are significantly lower than the corresponding measurements, generally by an amount as large as the jump in the prediction at shock arrival (c.f., observations for the late response phase and according to the quasi-steady analysis in Volume 1, Section 7.1). In intercept Cases 1 and 3, with peak angles of attack of 11.4 and 18.0 deg respectively, the under-predictions are even more severe, amounting in some cases to twice the predicted jump at shock arrival. With few exceptions, the largest differences between predicted and measured loadings are for the region of the wing between the leading edge and the 65-percent chordline from the 40-percent semispan outboard.

### 4.2.2 Relative Importance of the Diffractive Period Loading

With the blast intercept angle near 20 deg. from head-on (Cases 2, 5), shock-reflection theory predicts a large initial rise (of the order of 2 to 3 times $\Delta p_s$) at the instant of shock arrival. But the resulting spike is of such short duration that it was not fully sensed by the experimental instrumentation nor predicted by the VIBRA-6 analysis. Also, the measured peak loadings during the very early shock diffraction period are about at the same levels as those during the remainder of the lift development phase, except near the root and inner trailing-edge regions.

With the blast intercept directly from below ($\phi \tilde{=} 90$ deg, Cases 1 and 3), the sharp peak associated with the initial rise, which is of longer duration than in Case 2 or Case 5, is clearly seen in the experimental trace and predicted by the VIBRA-6 analysis; and its peak value

(observed or predicted by VIBRA-6) is closer to the value calculated according to shock-reflection theory, in contrast to the situations with Cases 2 and 5. In the $\phi$ = 90 deg-cases, the measured peak loadings during the diffractive period are also at about the same levels as those during the remainder of the lift development phase (for regions other than near the root and the inner trailing edge), except that the loading attributed to the leading-edge vortex has its highest peak during the diffraction period for most transducers near the leading edge.

With the blast intercept from the rear lower quadrant ($\phi \tilde{=} 135$ deg, Case 4), the peaks associated with the initial rises at shock arrival times are of much longer duration and they are significantly greater than the post-diffractive peaks (i.e., peaks during the remainder of the lift development phase) nearly everywhere on the wing. Whereas for 90 deg-intercept cases the initial diffractive peaks are of short durations and their impulses are relatively small when compared with the contributions of the post-diffractive period, this is not so with the 135 deg-intercept case. In the latter, the loading impulse during the diffraction phase constitutes a significant portion of the total impulse for the entire lift development phase.

### 4.2.3 Nonlinear Vortex Effects

The VIBRA-6 predictions of the pressure loadings during the lift development phase tend to follow roughly the trends observed in the experimental traces; but with few exceptions the predicted levels of these pressure loadings are significantly lower than those from experiment, particularly in the 90 deg-intercept cases (Cases 1, 3). The differences are attributed mainly to the formation of a vortex at the leading edge of the wing. With Cases 2, 4, and 5, where the maximum angles of attack are equal to or less than 9.4 deg, the peaks induced by the vortex are not very distinct. With the other two intercept cases (Cases 1 and 3, where the same angle is 11.4 and 18.0 deg, respectively), the loadings during the lift development phase show large peaks which are clear indications of strong, leading-edge generated vortices and

their movements. The high levels of the loadings resulting from the non-linear vortex effects are maintained during most of the lift development phase in a region ahead of a "sweptback line" on the wing extending from a position on the leading edge appreciably inboard of the wing tip to the outboard trailing edge, except regions very close to the leading edge.

# SECTION 5

# CONCLUSIONS AND RECOMMENDATIONS

## 5.1 CONCLUSIONS

This correlation effort has led to the following general conclusions:

1. For the nearly head-on intercept cases ($\phi \tilde{=} 20$ deg), the spike associated with the initial rise is of extremely short duration. It was not fully sensed by the experimental instrumentation and was not predicted by the VIBRA-6 analysis. The impulse associated with the spike is negligibly small. For $\phi \tilde{=} 20$ deg, the measured peak loadings during the diffractive period are generally at about the same levels as those during the remainder of the lift development phase, except near the root and inner trailing-edge region. The same conclusion is drawn for the $\phi \tilde{=} 90$ deg-cases, except (a) the initial rise peaks are of longer duration than in the $\phi = 20$ deg-cases, are clearly seen in the experimental traces and are predicted by VIBRA-6, and (b) the impulses associated with early-time peaks are no longer negligibly small for some local structural response problems. For the case with the intercept from the rear ($\phi \tilde{=} 135$ deg), the durations of the diffractive peaks are relatively long. Although the VIBRA-6 results tend to duplicate the observed trends of the diffraction loadings for rear intercepts, they underpredict the overall levels, and in most cases substantially. The diffractive pressure loadings for blast intercepts from the rear, being of sufficient durations and with magnitudes consistently higher than those during the post diffraction phase (i.e., during the remainder of the lift development period and beyond), become significant in both overpressure and gust type problems. They induce the early and maximum responses from local structural elements (overpressure type problems). They contribute appreciably through their impulses to the maximum structural responses in gust type problems. Note that the VIBRA-6 predictions fare much better in predicting observed trends than the quasi-steady analysis V6QS.

2. For the tested wing configuration, the VIBRA-6 analysis generally underpredicts the blast-induced loadings during the lift development phase, and by 50 percent or more in a number of instances. The same conclusion is drawn in Volume 1 of this report, following comparisons between results from the quasi-steady analysis with experiment for the pressure loadings over the lift development and late response phases. The major cause of the underpredictions is the nonlinear effect of a vortex system on the leeside of the wing which are unaccounted for in the linear analysis of VIBRA-6. With few exceptions, the area of the wing affected most is from the leading edge to the 65 percent chord stations at the outer 50-60 percent of wing semispan.

3. The code underpredictions referred to in (2) occur for all intercept cases investigated. They are particularly severe with the $\phi$=90 deg orientation (i.e., a blast directly from below) and with the higher shock strength; this is not surprising since the angle of attack reaches 18.0 deg and is the largest for this case. The exceptions worthy of note are the loadings at the 5 percent-chord stations outboard (at 80 percent span in Case 1 and at 60 and 80 percent span in Case 3) where large drops in pressure loadings are noted for several milliseconds shortly after shock arrival.

4. Increasing the total angle of attack (i.e., the sum of the initial and blast-induced angles of attack) accentuates the vortex-induced effects, resulting in poorer VIBRA-6 predictions for the pressure loadings. Increasing wing sweep is expected to have a similar effect. Conversely, with moderate sweep, say 30 to 45 deg, the VIBRA-6 predictions are expected to be in closer agreement with experiment, although this remains to be demonstrated.

5. The implication from conclusions under items (2) and (3) is that the peak structural response predictions based on the VIBRA-6 code for gust type problems are expected to be significantly lower than actual for highly swept wings such as the one tested here.

6. The vortex-induced effects, to which the major differences between experiment and analysis are attributed, are nonlinear in angle of attack; and as such, even if they can be estimated separately they cannot be simply added to the loadings predicted by a linear analysis which is the overall basis of the VIBRA-6 code. For VIBRA-6, a linear aerodynamic analysis is mandatory since the code synthesizes linearly the harmonic gust responses to arrive at the final transient responses. No simple means can be offered at this time to overcome the noted VIBRA-6 underpredictions.

7. Two other known effects are noted: those due to Mach number changes following shock arrival and those due to wing thickness, both of which are unaccounted for in the analysis. Their extents are believed to be small for reasons discussed in the text.

## 5.2 RECOMMENDATIONS

In view of these results from the correlation, three recommendations may be offered concerning future efforts in this area.

1. Additional tests and VIBRA-6 correlations are needed on a lower sweep (say 30-45 deg) wing configuration for which the vortex-induced effects are expected to be less dominant. The purpose here would be to ascertain if the DLM provides an adequate aerodynamic tool to justify using VIBRA-6 for predicting blast-induced structural responses of low to moderate sweep configurations.

2. For high sweep configurations, the need for a new aerodynamic approach is indicated. This approach would be a nonlinear one to properly account for the separated flow on the leeward side of the wing.

3. Steady-state wind tunnel data on candidate blast test configurations would be extremely useful in correlating predicted blast pressure loadings with experiment. The wind tunnel measurements would be for pressures at the same transducer locations as in the sled (blast) tests and covering sufficiently wide ranges in test Mach number and angle of attack to cover the pre-intercept and post-intercept conditions. Furthermore, one may speculate that these steady-state tests coupled with blast tests may still lead to some empirically derived correction factors which would improve significantly and by simple means the blast-induced loads predictions.

Table 1. Ambient and Operational Conditions
During The Five Experimental Runs

| Case No. | Test Run Identific. | Ambient Conditions | | Operational Conditions | | | | |
|---|---|---|---|---|---|---|---|---|
| | | Density, $\rho_\infty$, slugs/ft$^3$ | Speed of Sound, $a_\infty$, ft/s | Mach No., M | V ft/s | Equiv. V=$V_e$ $V_e$ in knots | Peak Free-Field Overpress., $\Delta p_s$, psi | Blast Orient. Angle, $\phi$, deg |
| 1 | 9B-A1-2 | 0.001890 | 1152 | 0.755 | 870 | 459.5 | 2.07 | 87.6 |
| 2 | 9B-A2-1 | 0.001977 | 1140 | 0.767 | 874 | 472.4 | 2.01 | 20.1 |
| 3 | 9B-A2-2 | 0.001977 | 1140 | 0.756 | 862 | 465.6 | 4.02 | 90.3 |
| 4 | 9B-A2-3 | 0.001977 | 1140 | 0.761 | 868 | 468.9 | 1.97 | 134.9 |
| 5 | 9B-A3-1 | 0.001942 | 1145 | 0.761 | 872 | 467.1 | 3.56 | 20.1 |

V = Sled Velocity at Intercept Time

B = Vector from Burst Point to Datum Point at Intercept Time

$\phi$ = Angle Between B and Positive x-Axis Burst Center in (x-z)-Plane of Vehicle

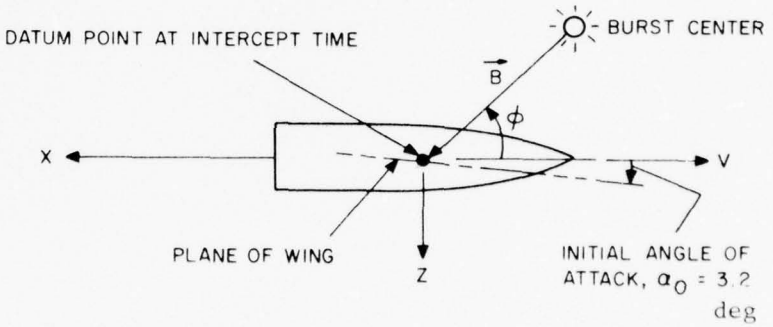

Table 2. Local Shock Incidence Angles and Expected Peak Reflected Overpressure at Intercept

| | | CASE 1 | | CASE 2 | | CASE 3 | | CASE 4 | | CASE 5 | |
|---|---|---|---|---|---|---|---|---|---|---|---|
| Ambient Pressure, $p_\infty$, psi | | 12.44 | | 12.75 | | 12.75 | | 12.75 | | 12.64 | |
| Shock Strength Ratio, $\xi=\Delta p_s/p_\infty$ | | 0.166 | | 0.158 | | 0.315 | | 0.155 | | 0.282 | |
| Chordwise Station (%) | $\varepsilon_i$ (deg) | $\theta_i$ (deg) | $r\Delta p_s$ (psi) | $\theta_i$ (deg) | $r\Delta p_s$ (psi) | $\theta_i$ (deg) | $r\Delta p_s$ (psi) | $\theta_i$ (deg) | $r\Delta p_s$ (psi) | $\theta_i$ (deg) | $r\Delta p_s$ (psi) |
| 5 | 15 | 15.8R | 4.43 | 51.7R | 4.46 | 15.3R | 8.78 | 63.1M | 5.95 | 51.7R | 9.51 |
| 25 | 3.9 | 4.7R | 4.43 | 62.8M | 5.69 | 4.2R | 8.96 | 52.0R | 4.54 | 62.8M | 9.10 |
| 45 | -2.1 | 1.3R | 4.43 | 68.8M | 5.24 | 1.8R | 9.08 | 46.0R | 4.34 | 68.8M | 7.26 |
| 65 | -6.1 | 5.3R | 4.43 | 72.8M | 4.32 | 5.8R | 8.93 | 42.0R | 4.28 | 72.8M | 6.23 |
| 85 | -7.1 | 6.3R | 4.43 | 73.8M | 4.26 | 6.8R | 8.92 | 41.0R | 4.26 | 73.8M | 6.05 |

R after $\theta_i$ value indicates regular reflection

M after $\theta_i$ value indicates Mach reflection

Note: Since they were obtained by interpolations of the $\xi$-curves in Figure 15, the given values of the peak overpressures ($r\Delta p_s$) are very approximate, especially for shock incidence angles near their critical values.

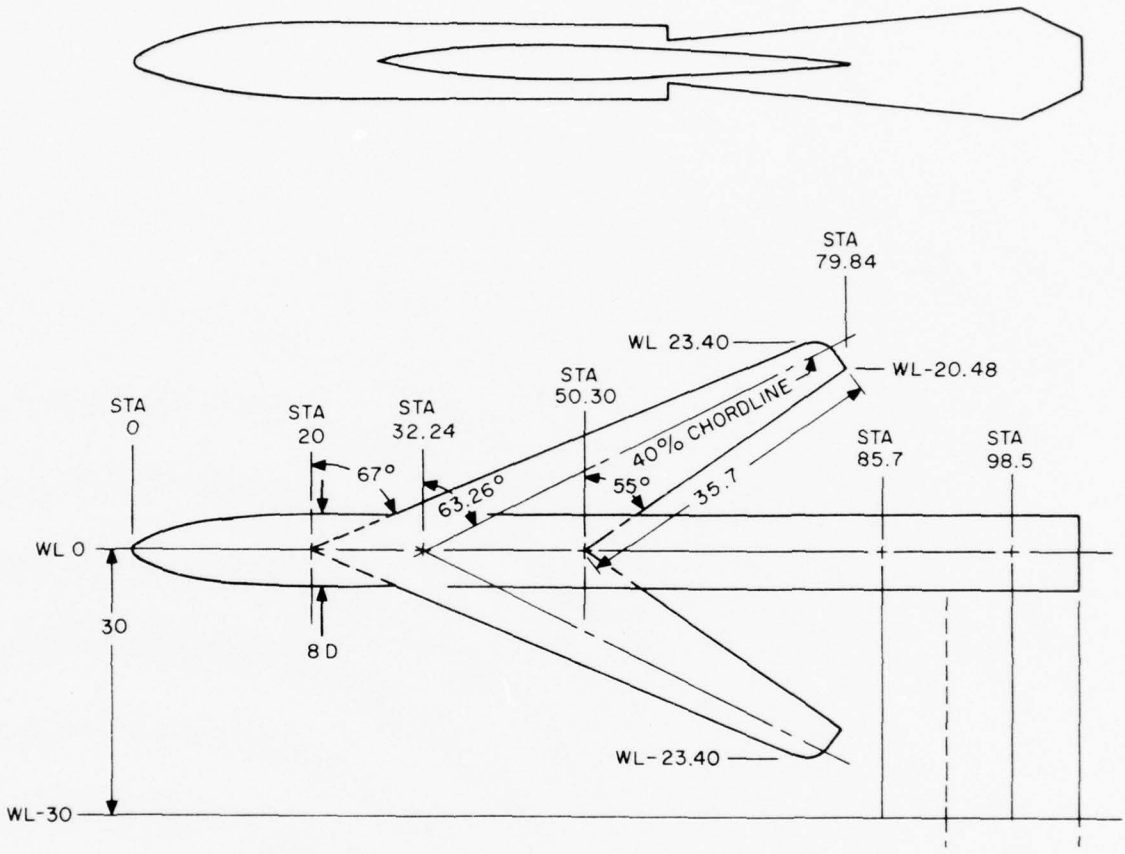


| | | | |
|---|---|---|---|
| Wing Span | 46.80 in | Fuselage Diameter | 8 in |
| Wing Aspect Ratio | 2.47 | Wing Section | 64A012 |
| Taper Ratio | 0.29 | Thickness Ratio | 12% |
| Centerline Chord | 30.60 in | (In Streamwise Sections) | |
| (At W.L.=0) | | Mean Chord | 18.95 in |
| Leading Edge Sweep | 67.0 deg | Wing Planform Area | 6.16 $ft^2$ |
| Quarter-Chord Sweep | 64.8 deg | (Including Portion | |
| Trailing Edge Sweep | 55.0 deg | Submerged Within | |
| | | Fuselage) | |

Figure 1. Experimental Model Configuration

| COORDINATES | | | |
|---|---|---|---|
| POINT | x | y | z |
| ① | -2.817 | 4.0 | 0.0 |
| ② | 24.072 | 4.0 | 0.0 |
| ③ | 40.131 | 22.23 | 0.0 |
| ④ | 50.108 | 22.23 | 0.0 |
| ⑤ | -32.24 | 0.0 | 0.0 |
| ⑥ | 53.46 | 0.0 | 0.0 |

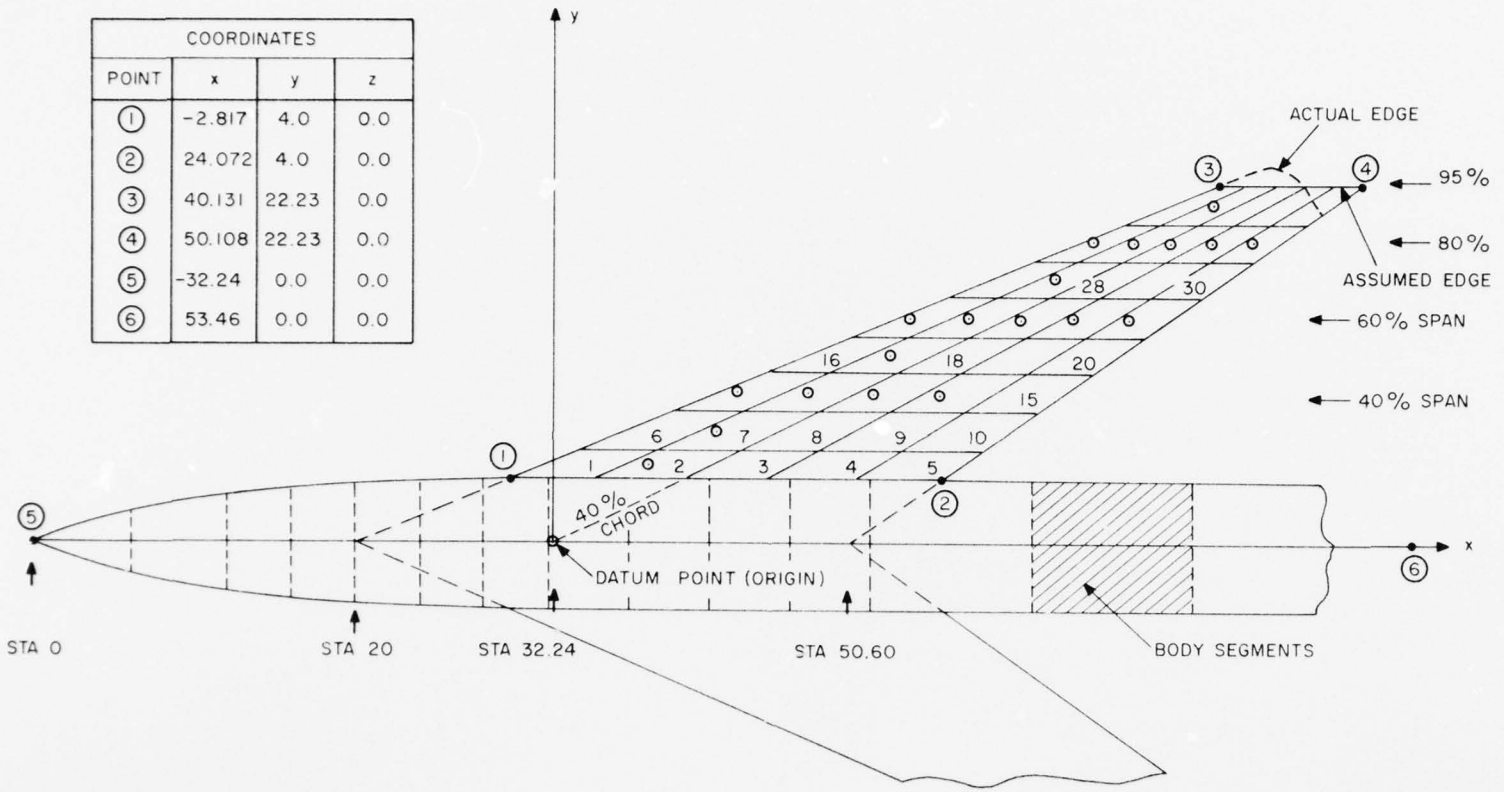


Figure 2. Simplified Wing Planform and Grid System Used in Analysis

Figure 3. Time-Variations of Pressure Loadings at Transducer Locations. Predictions From VIBRA-6 Compared With Experiment.

Case 1 - $\phi$ = 87.6 deg, $\Delta p_s$=2.07 psi. (9B-A1-2)

———— VIBRA-6

~~~~ Test Data
~~~~

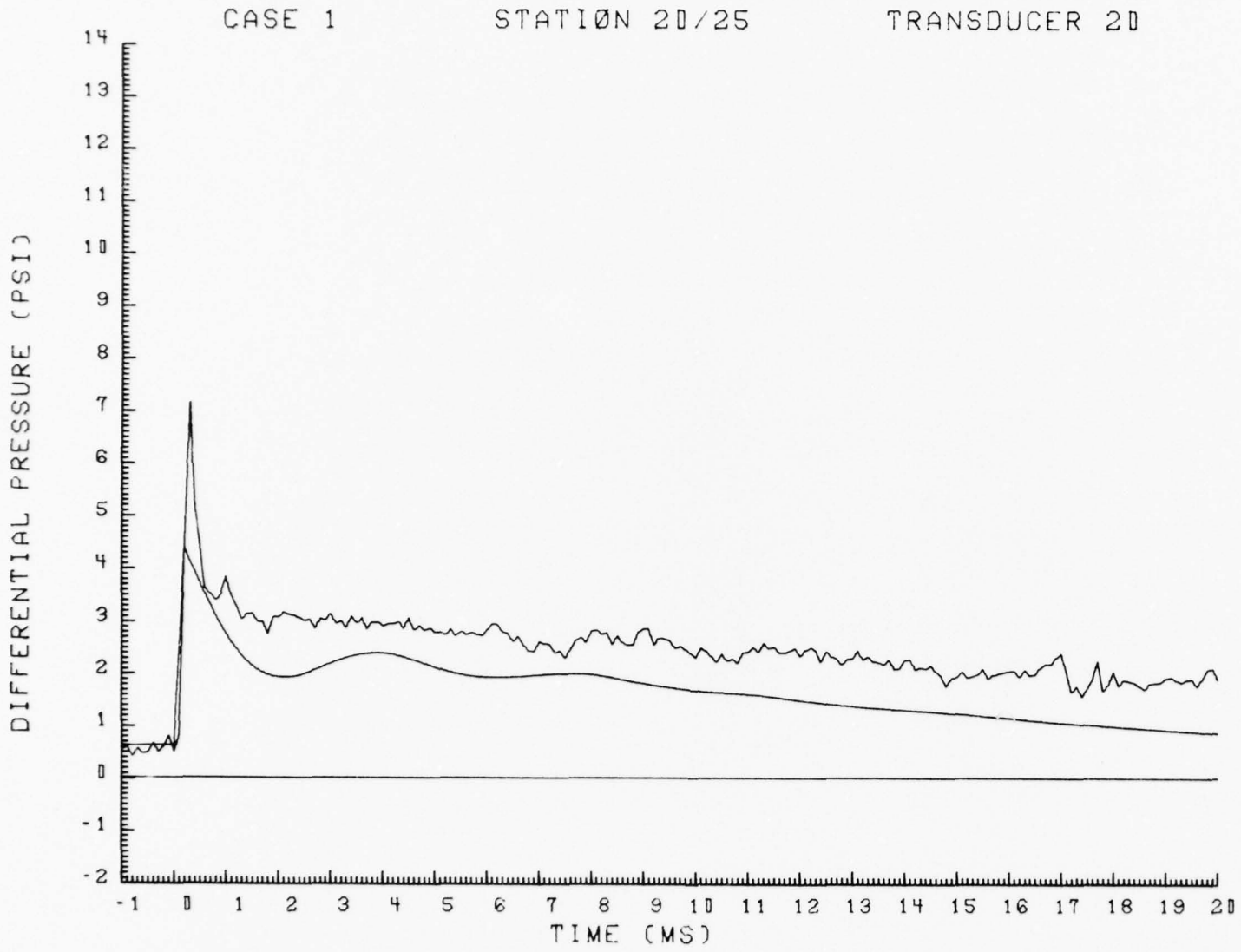
CASE 1
STATIØN 20/25
TRANSDUCER 20
DIFFERENTIAL PRESSURE (PSI)
14
13
12
11
10
9
8
7
6
5
4
3
2
1
0
-1
-2
-1 0 1 2 3 4 5 6 7 8 9 10 11 12 13 14 15 16 17 18 19 20
TIME (MS)

Figure 3

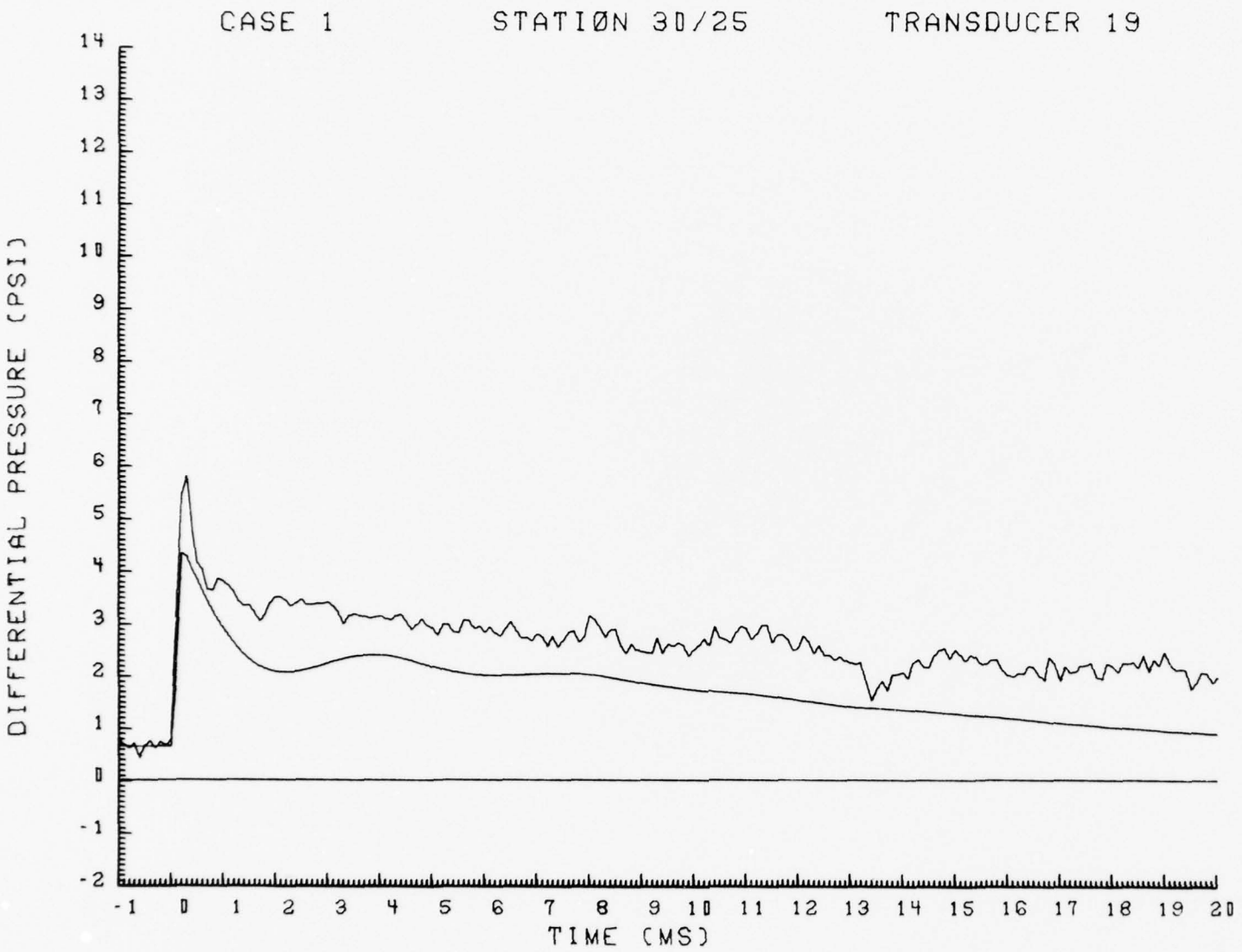


Figure 3. (Continued)

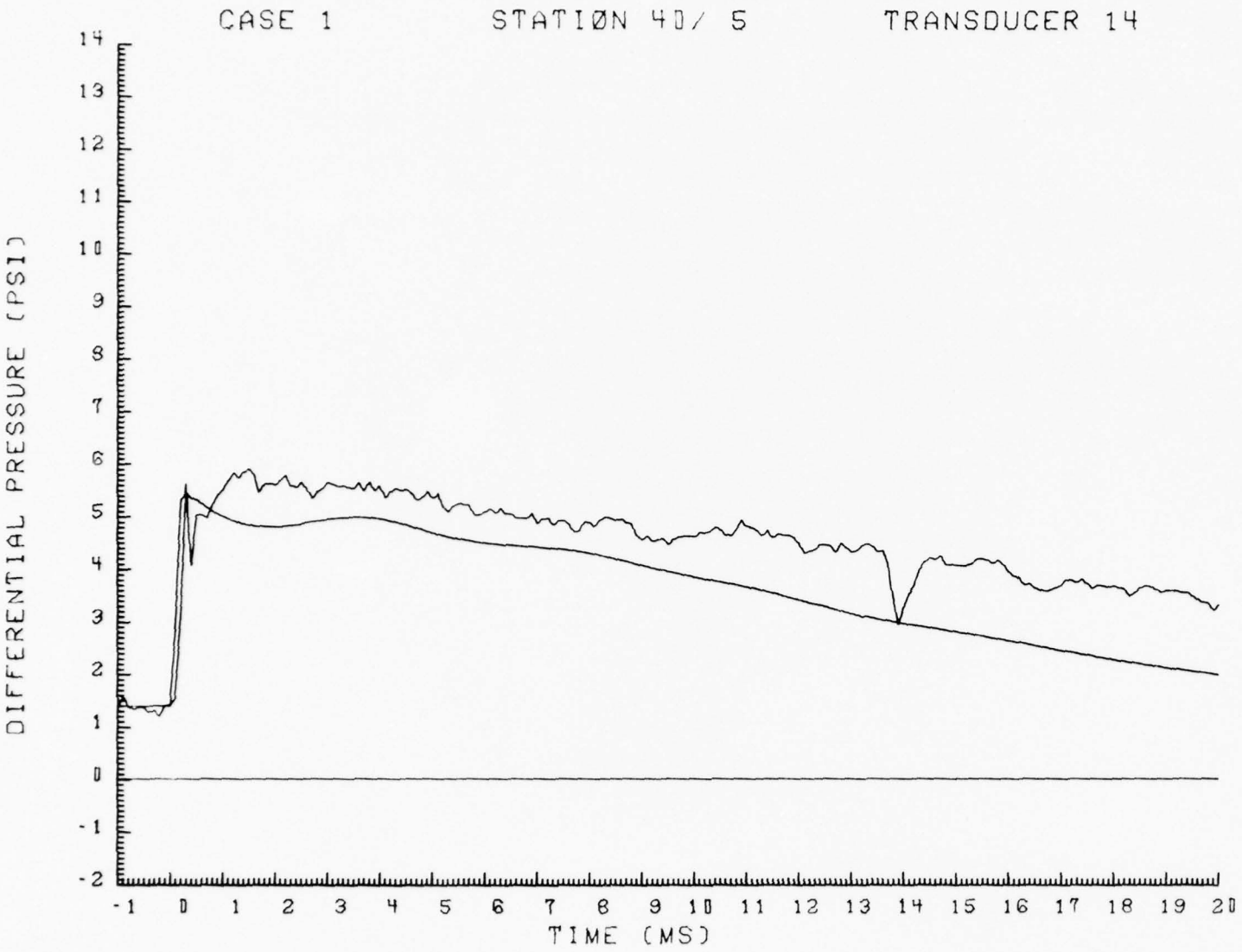


Figure 3. (Continued)

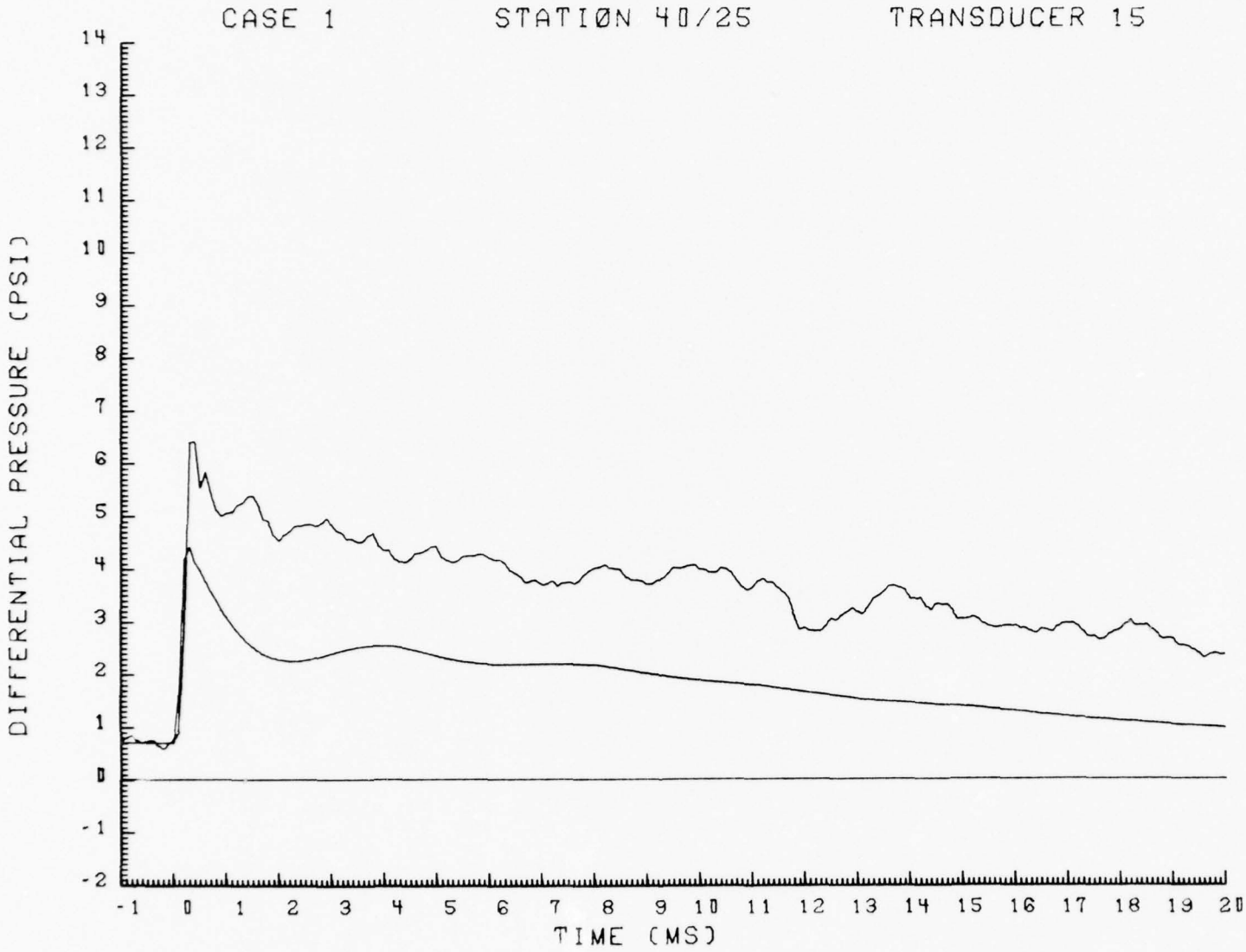


Figure 3. (Continued)

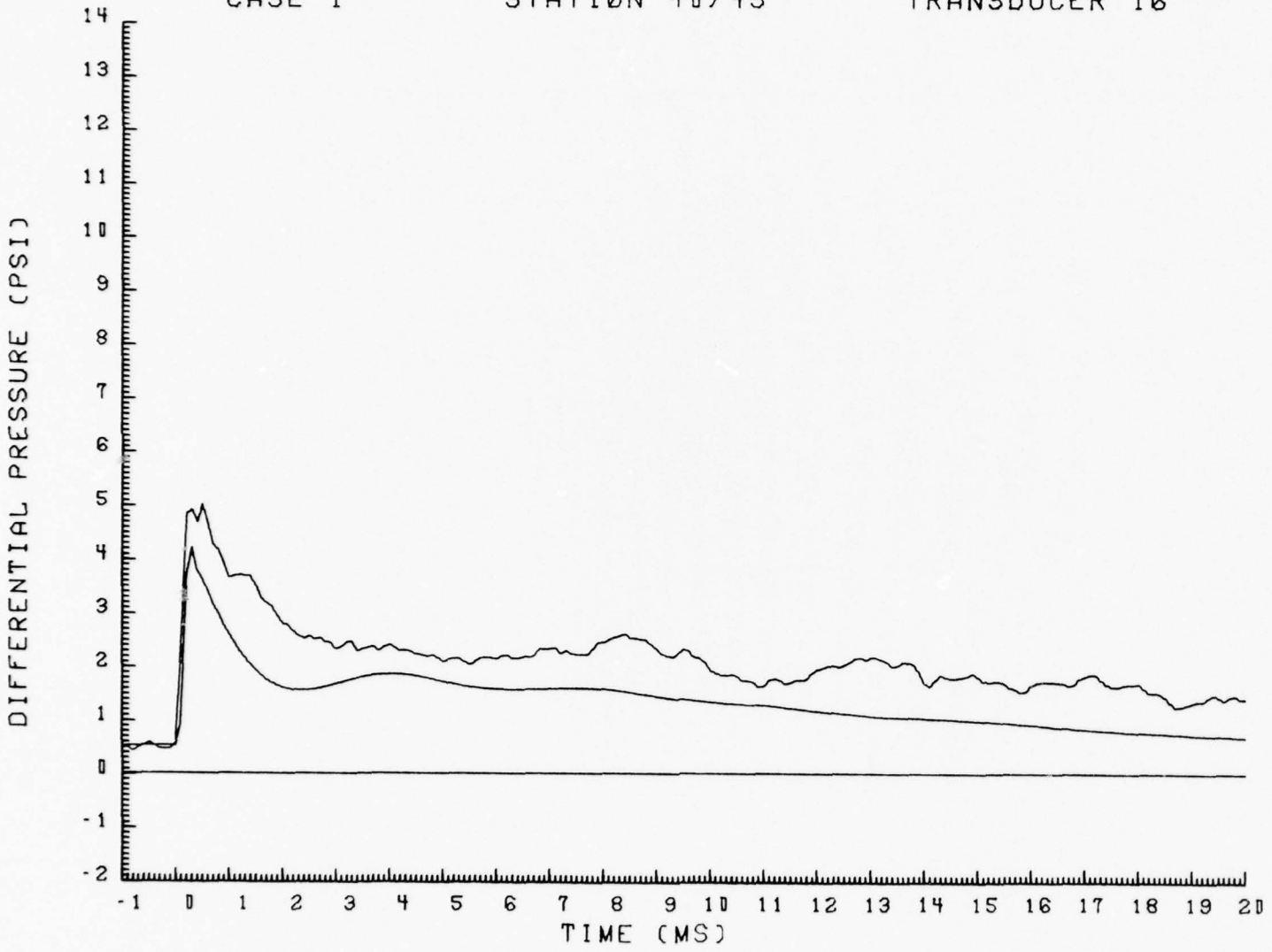


Figure 3. (Continued)

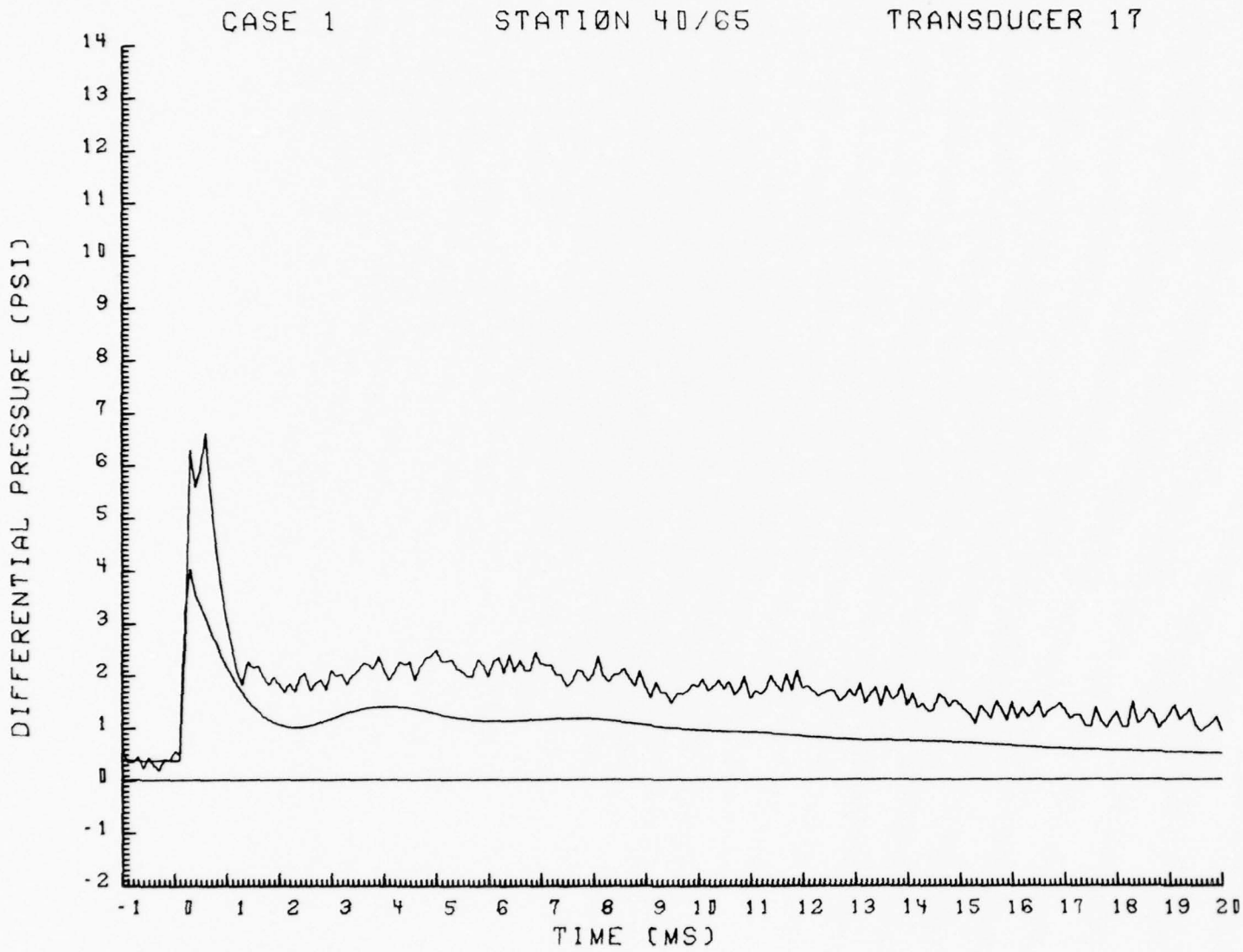


Figure 3. (Continued)

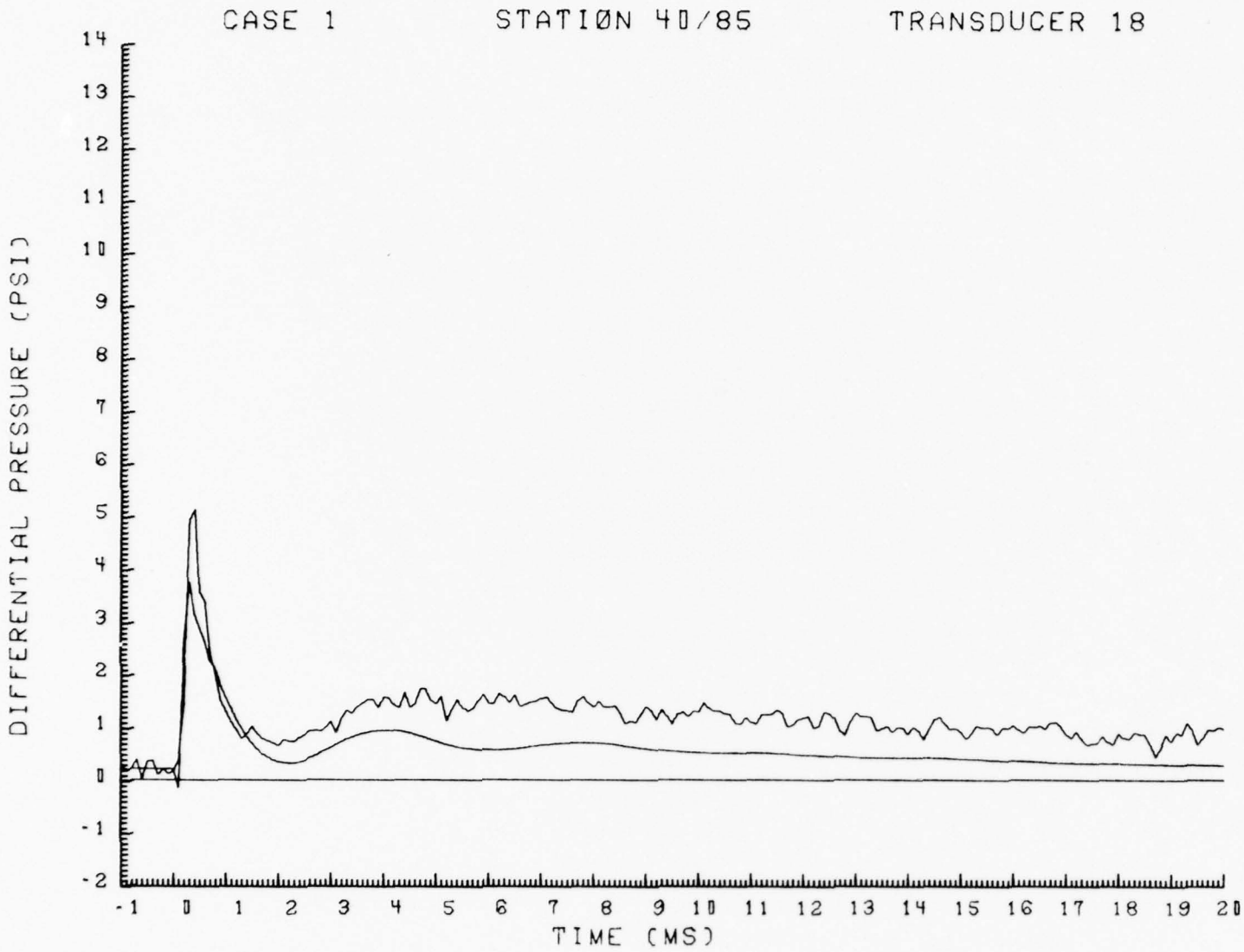


Figure 3. (Continued)

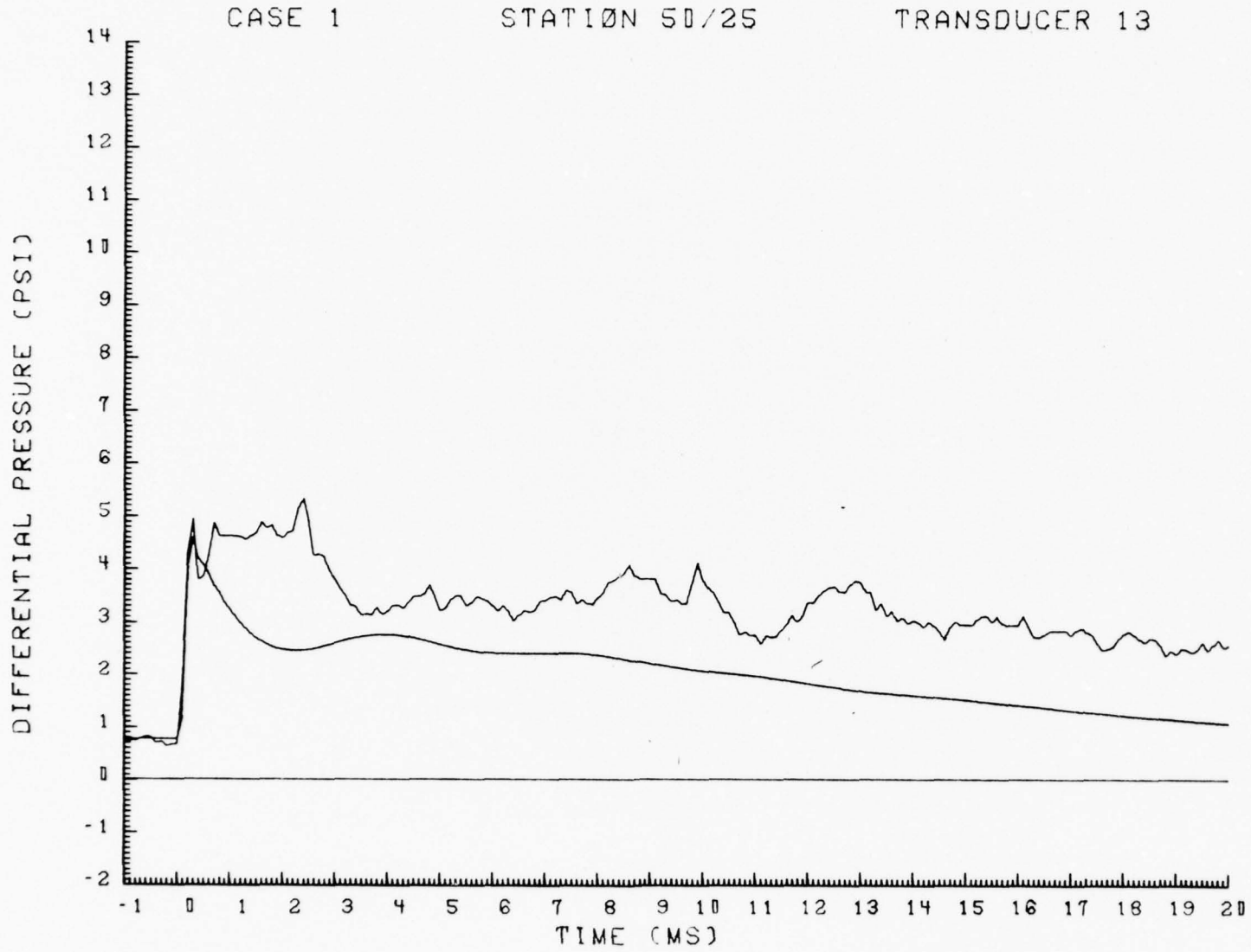


Figure 3. (Continued)

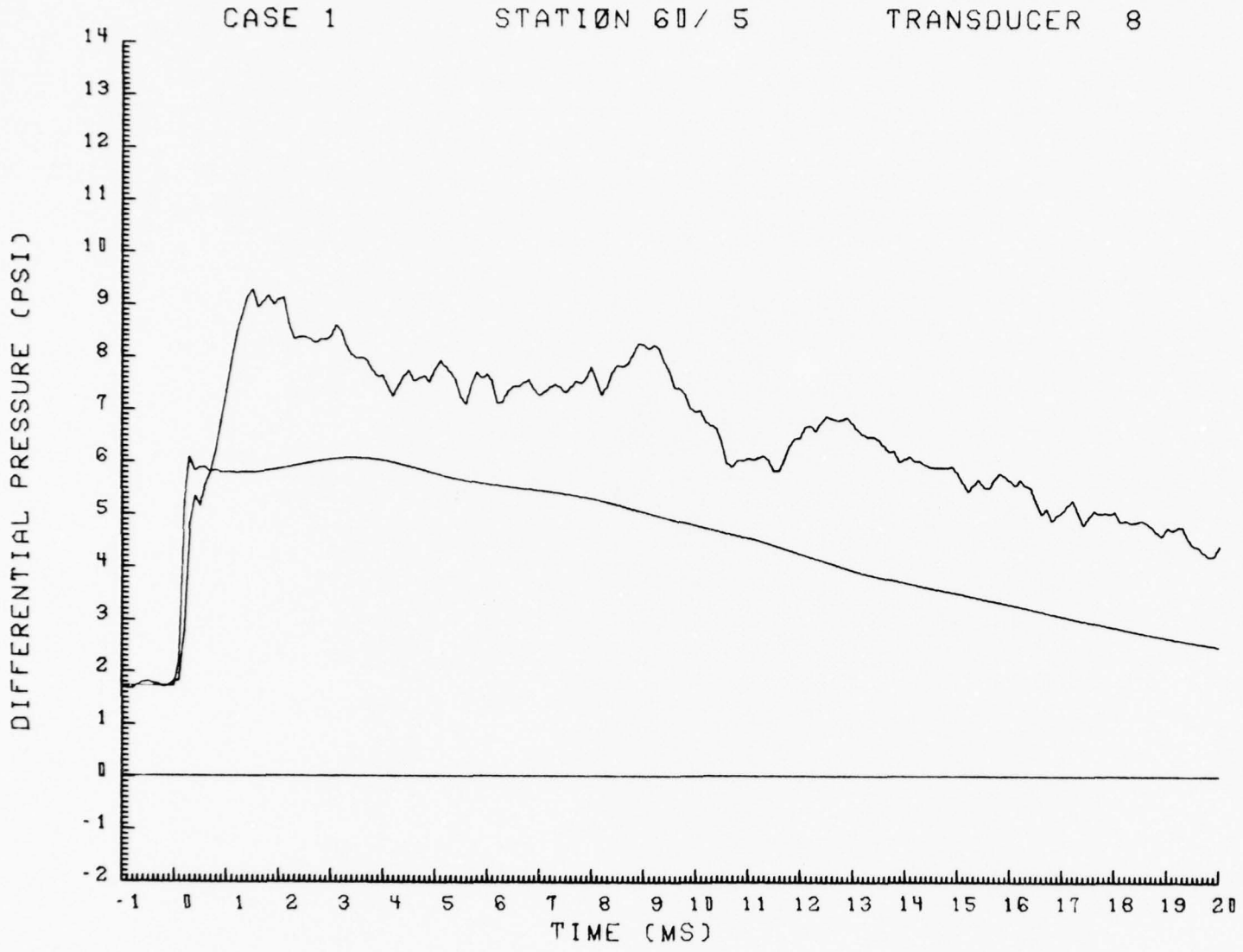


Figure 3. (Continued)

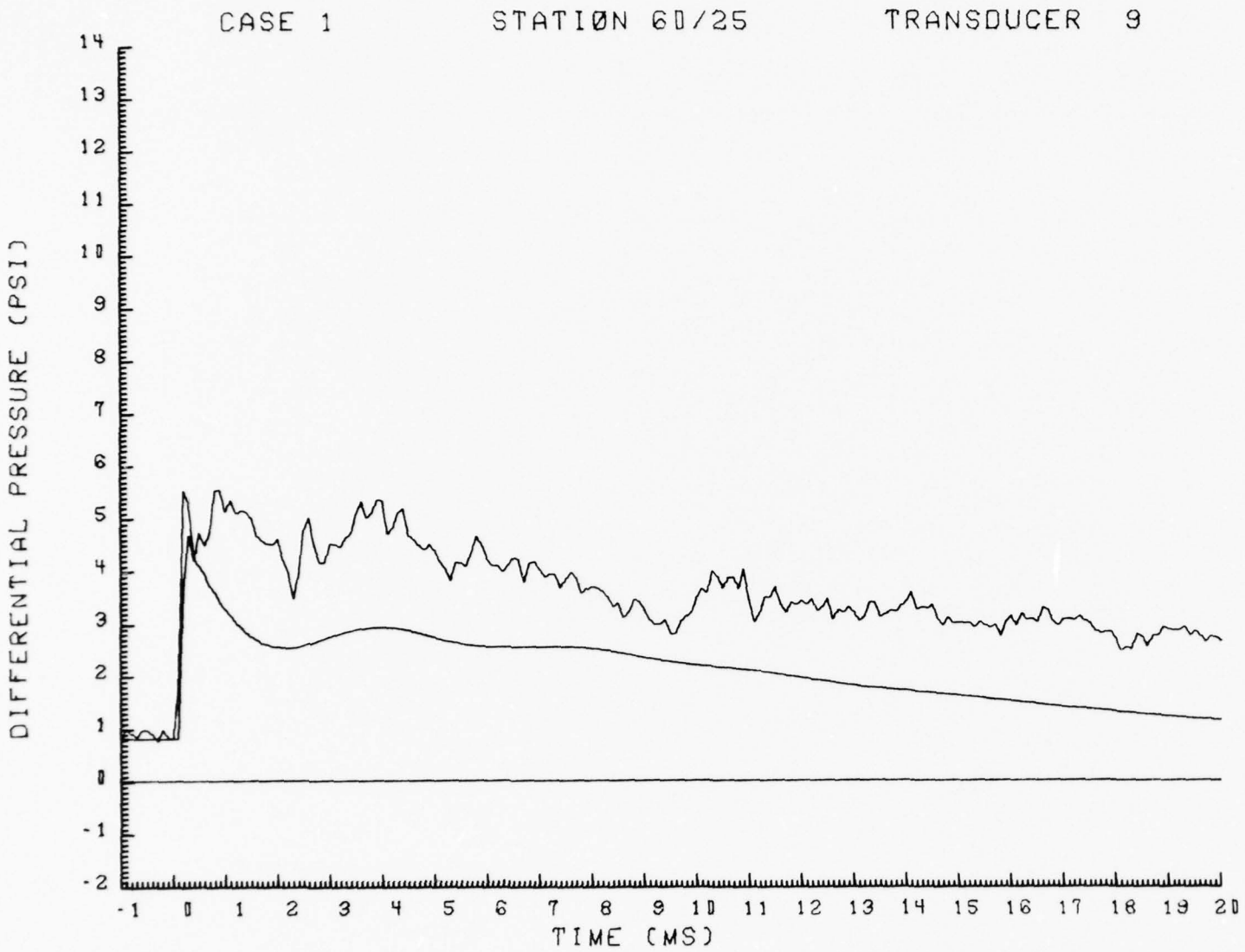


Figure 3. (Continued)

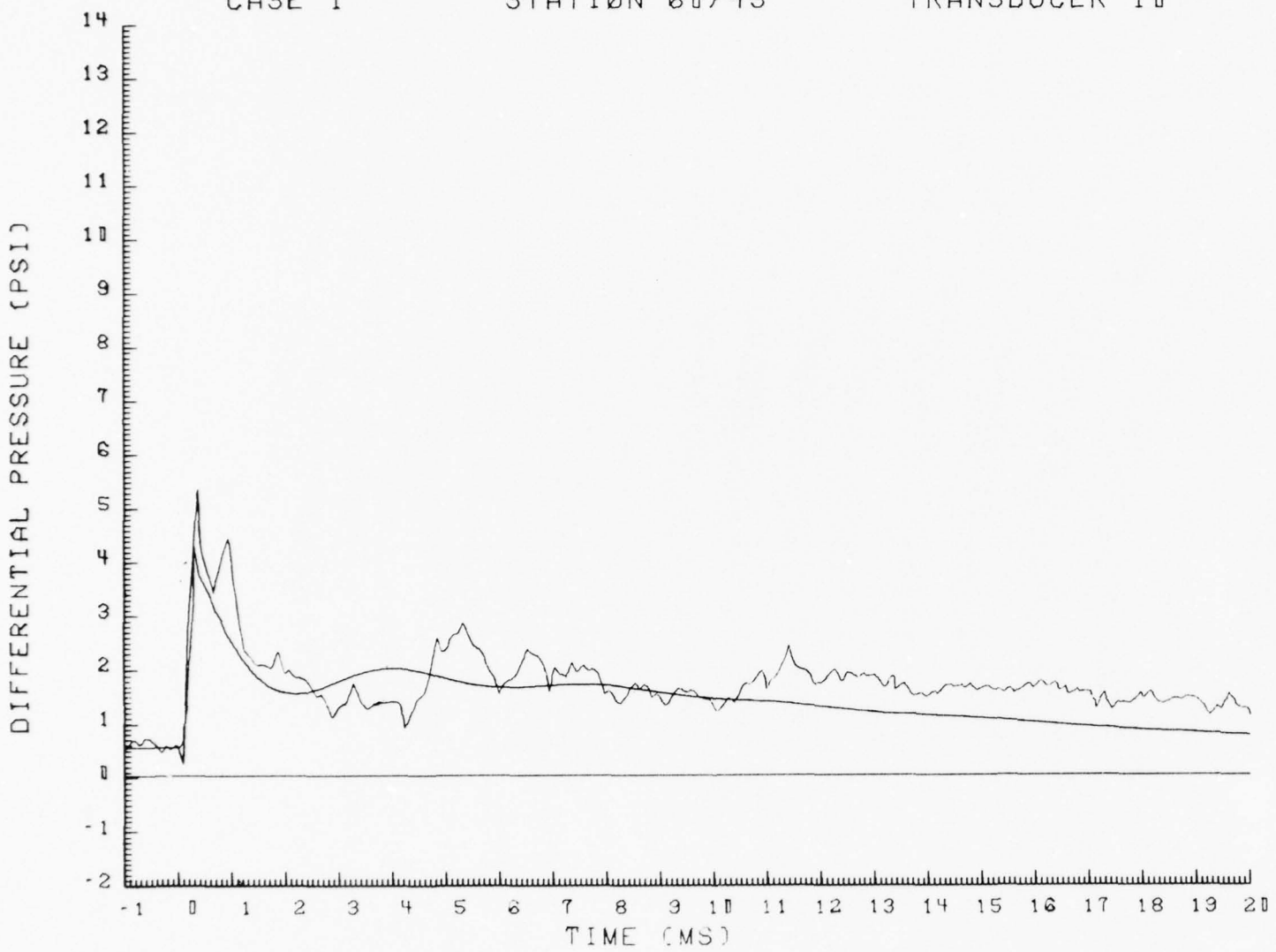


Figure 3. (Continued)

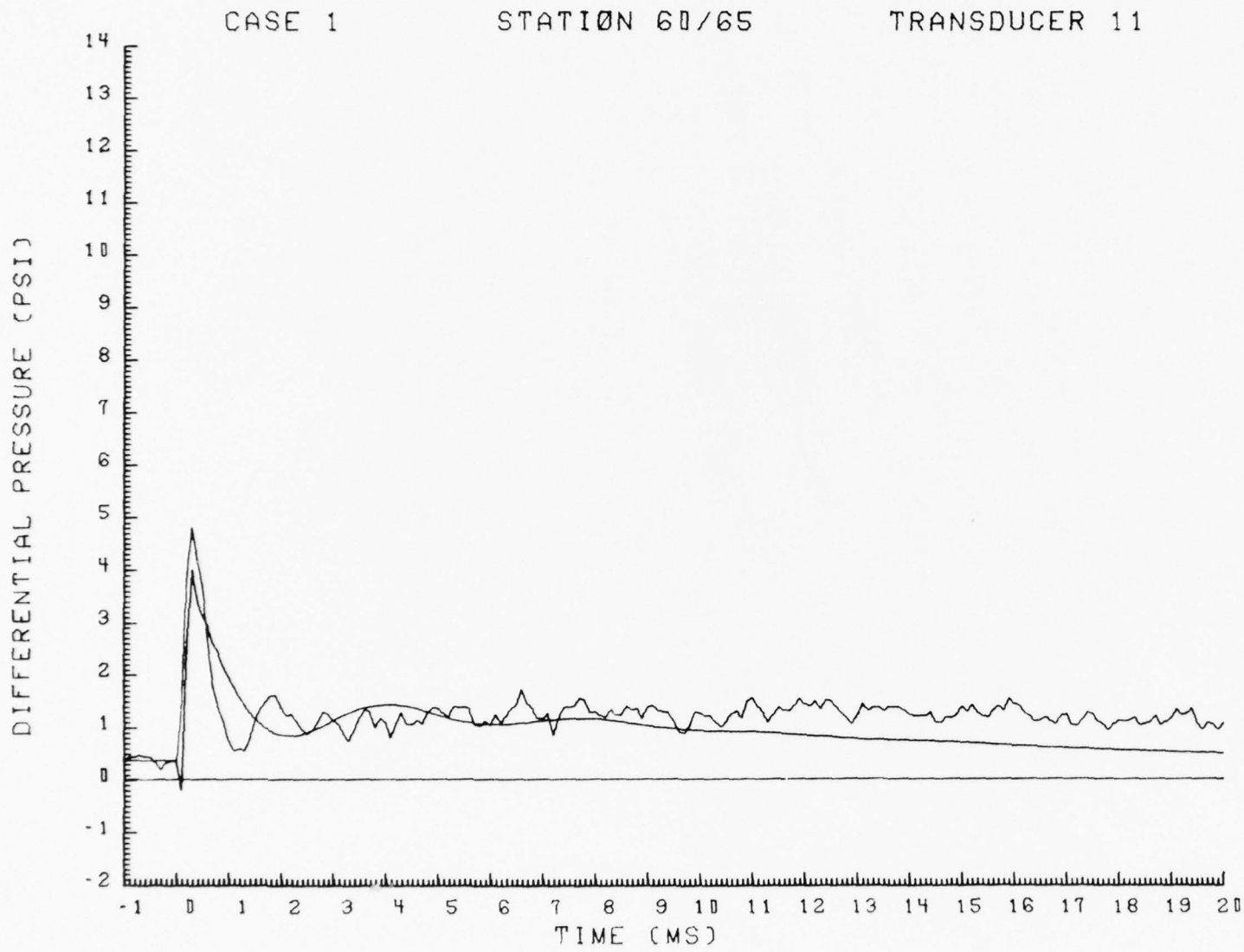


Figure 3. (Continued)

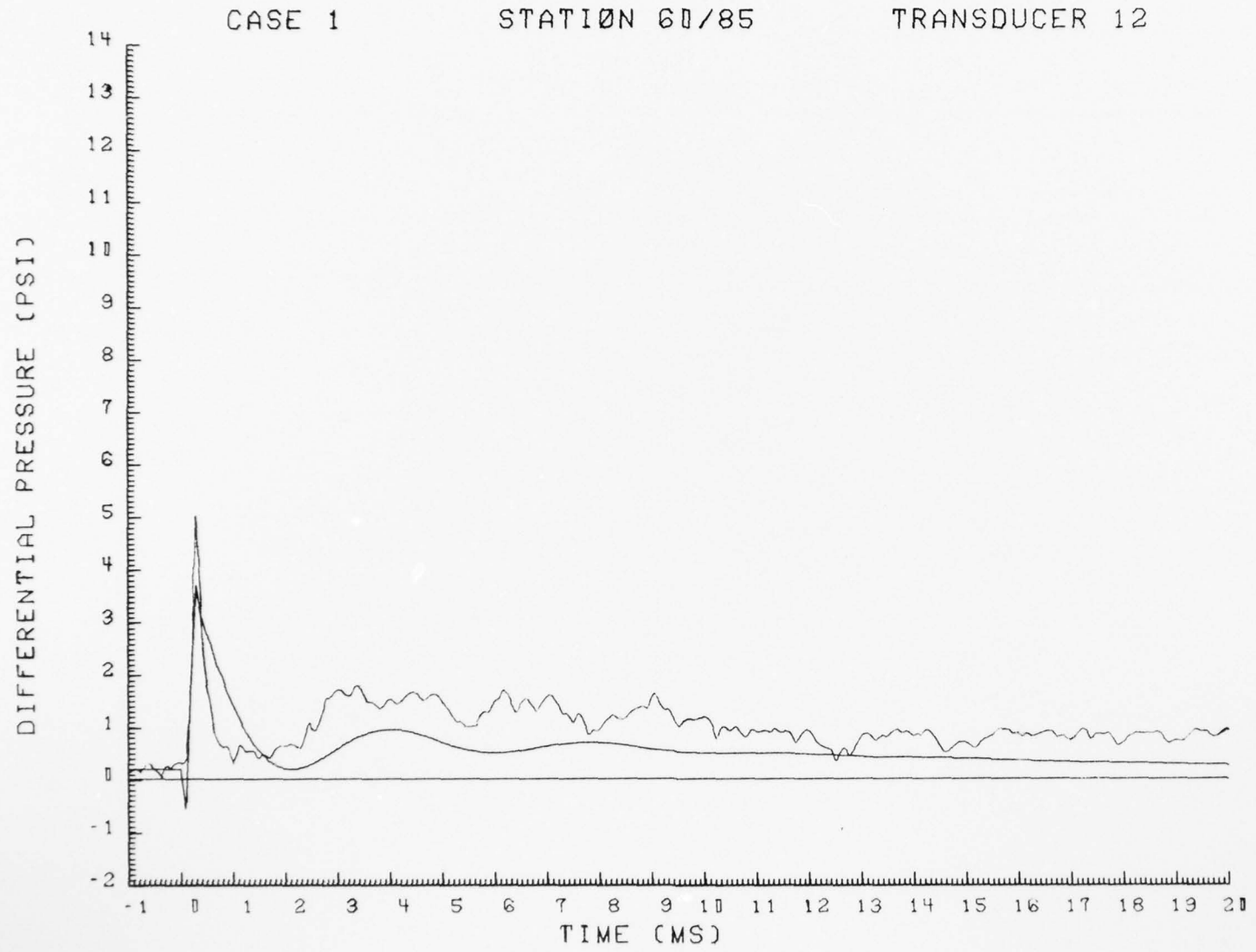


Figure 3. (Continued)

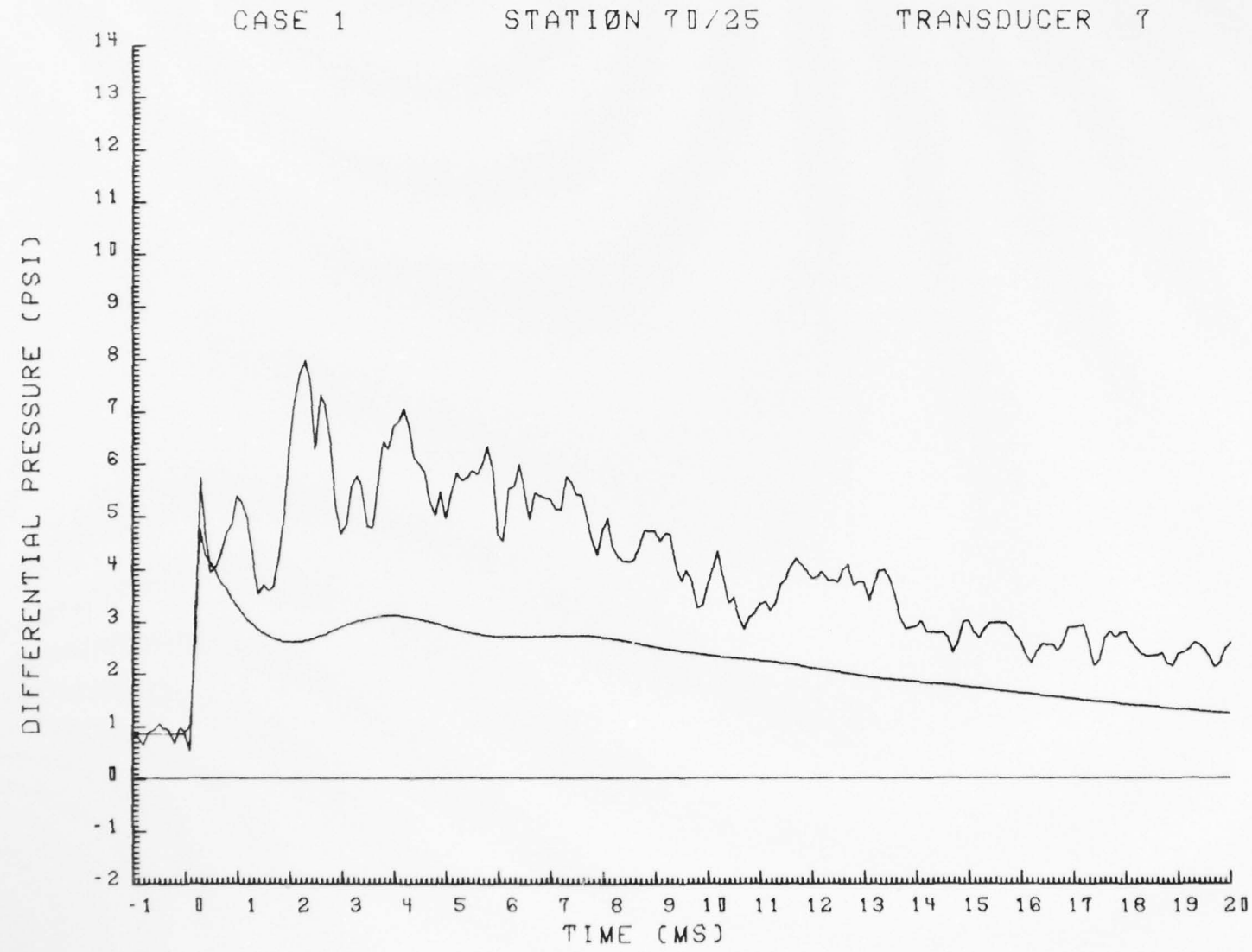


Figure 3. (Continued)

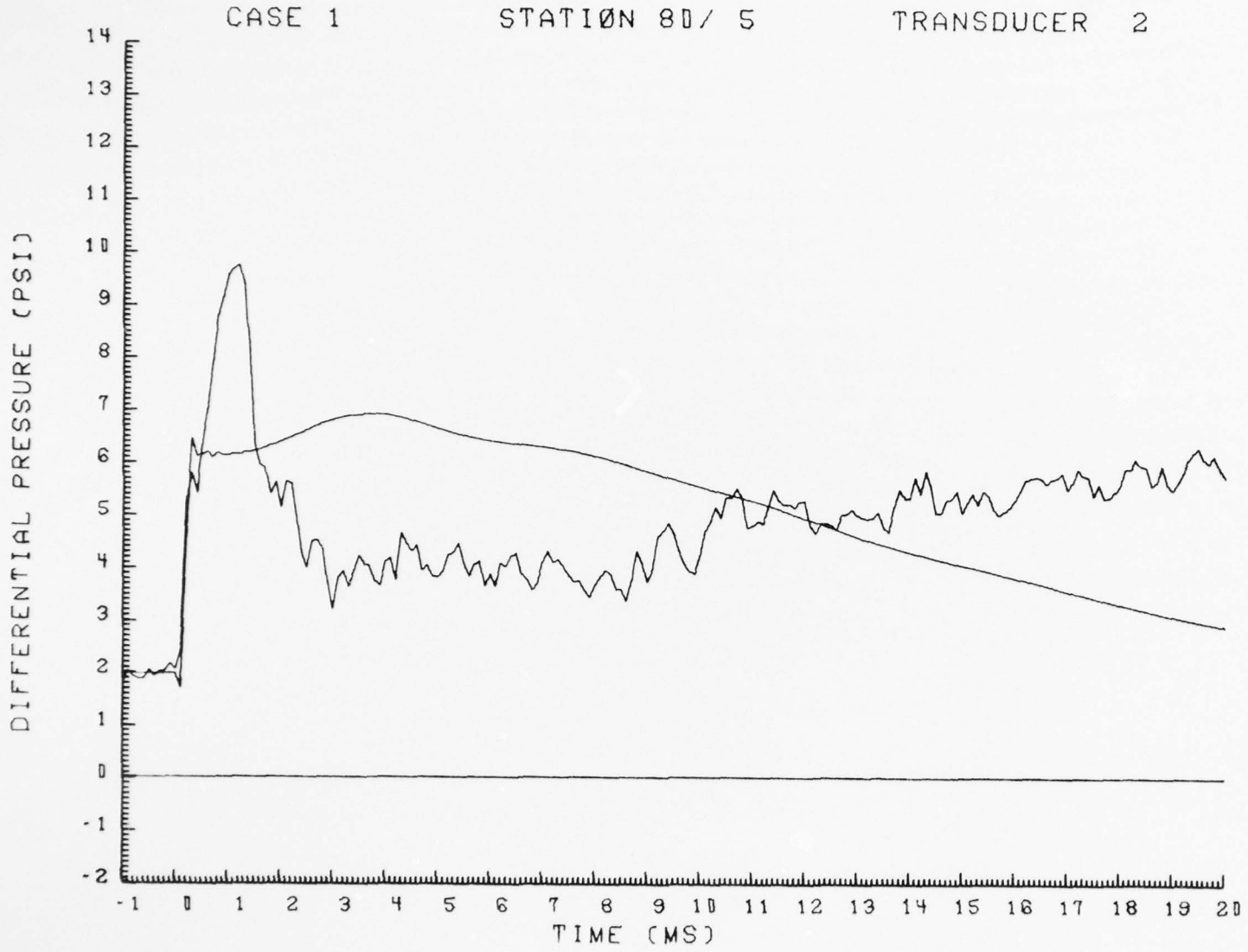


Figure 3. (Continued)

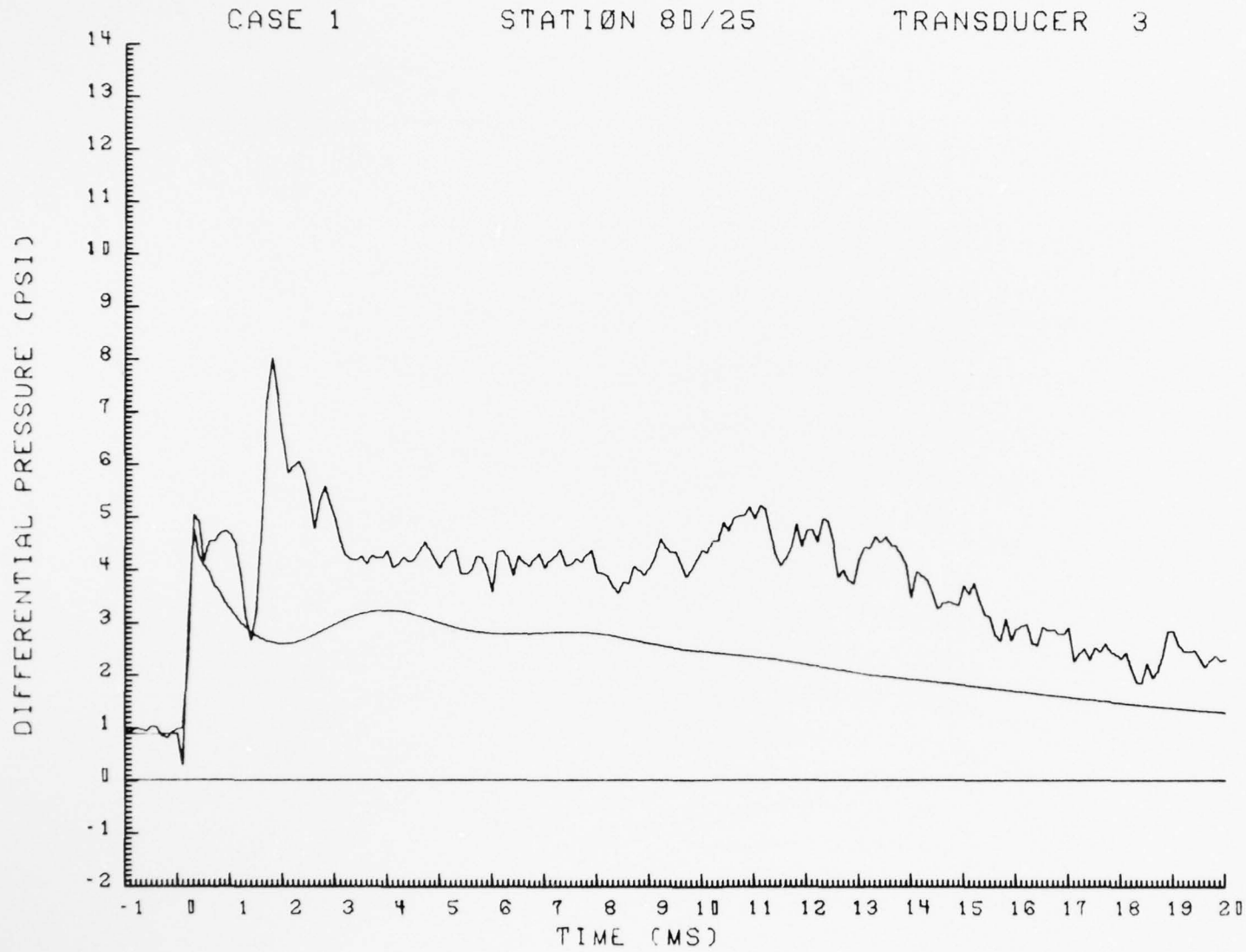


Figure 3. (Continued)

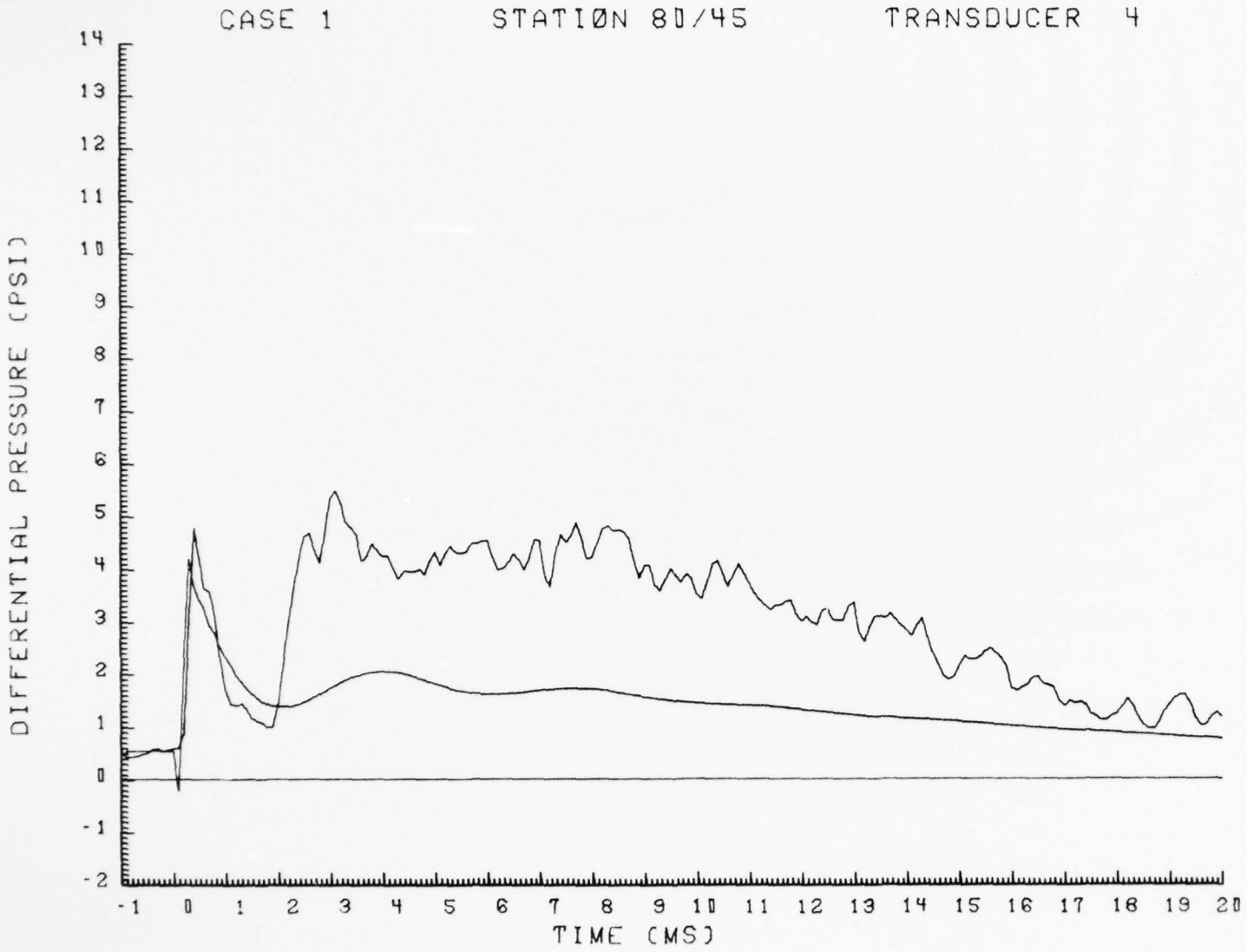


Figure 3. (Continued)

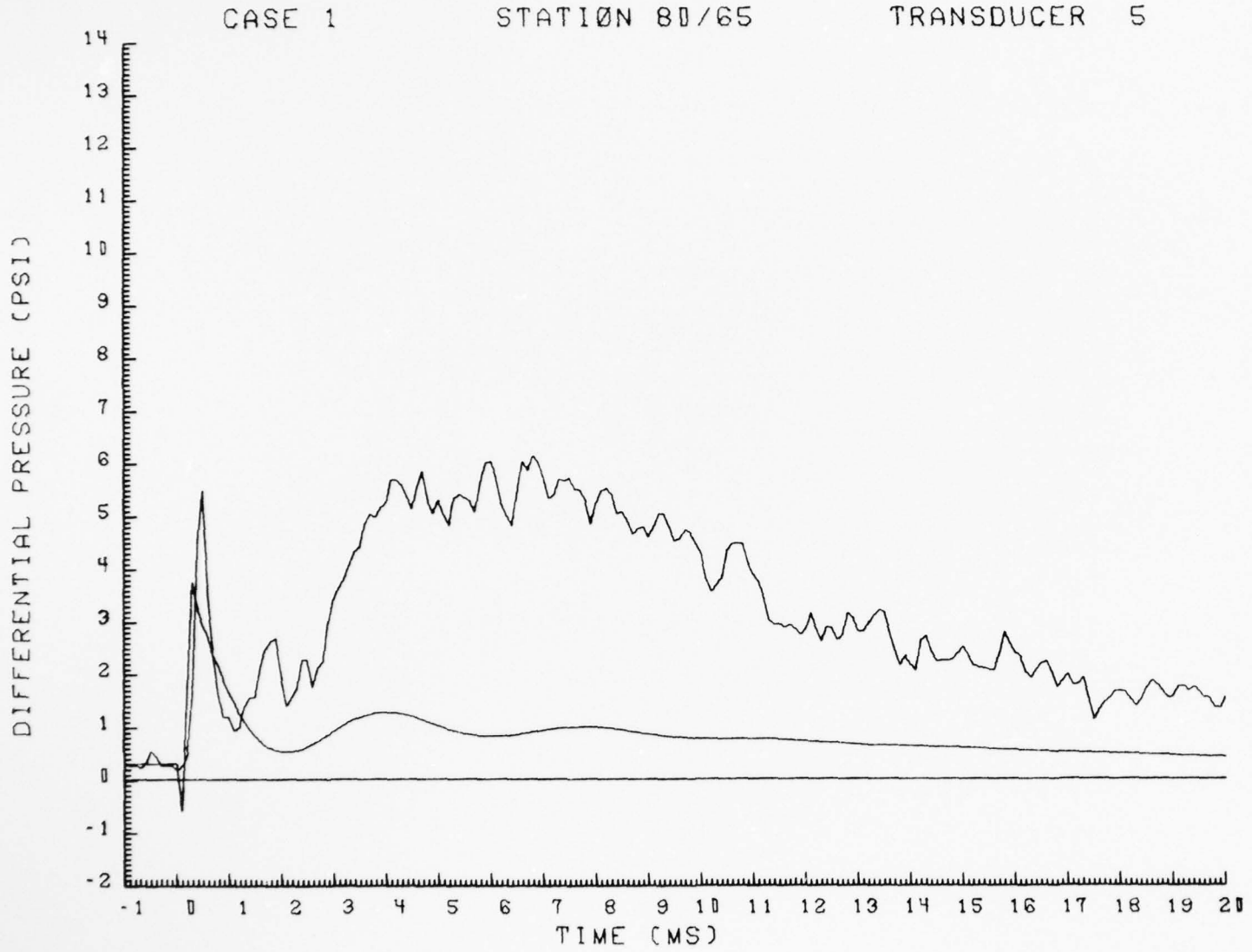


Figure 3. (Continued)

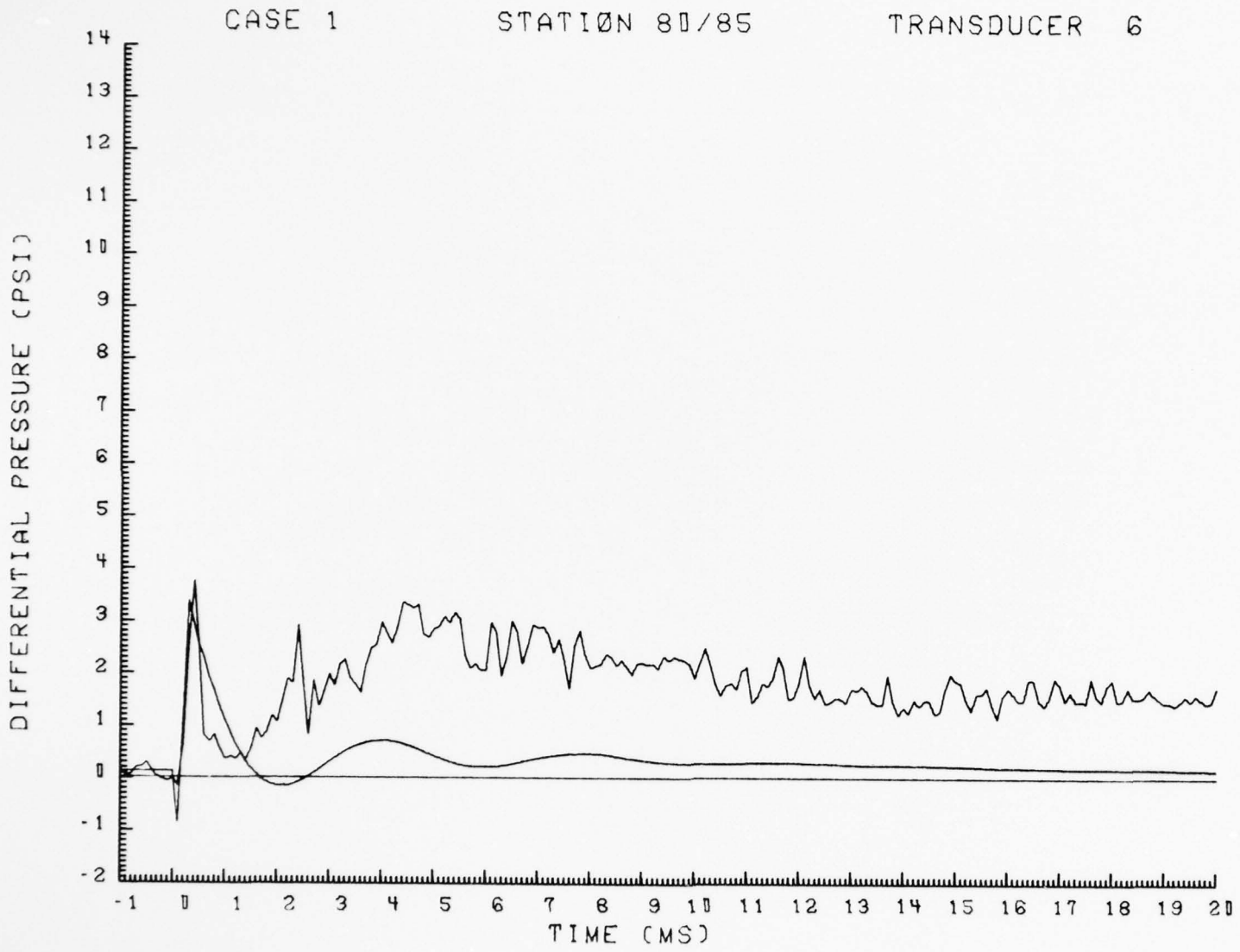


Figure 3. (Continued)

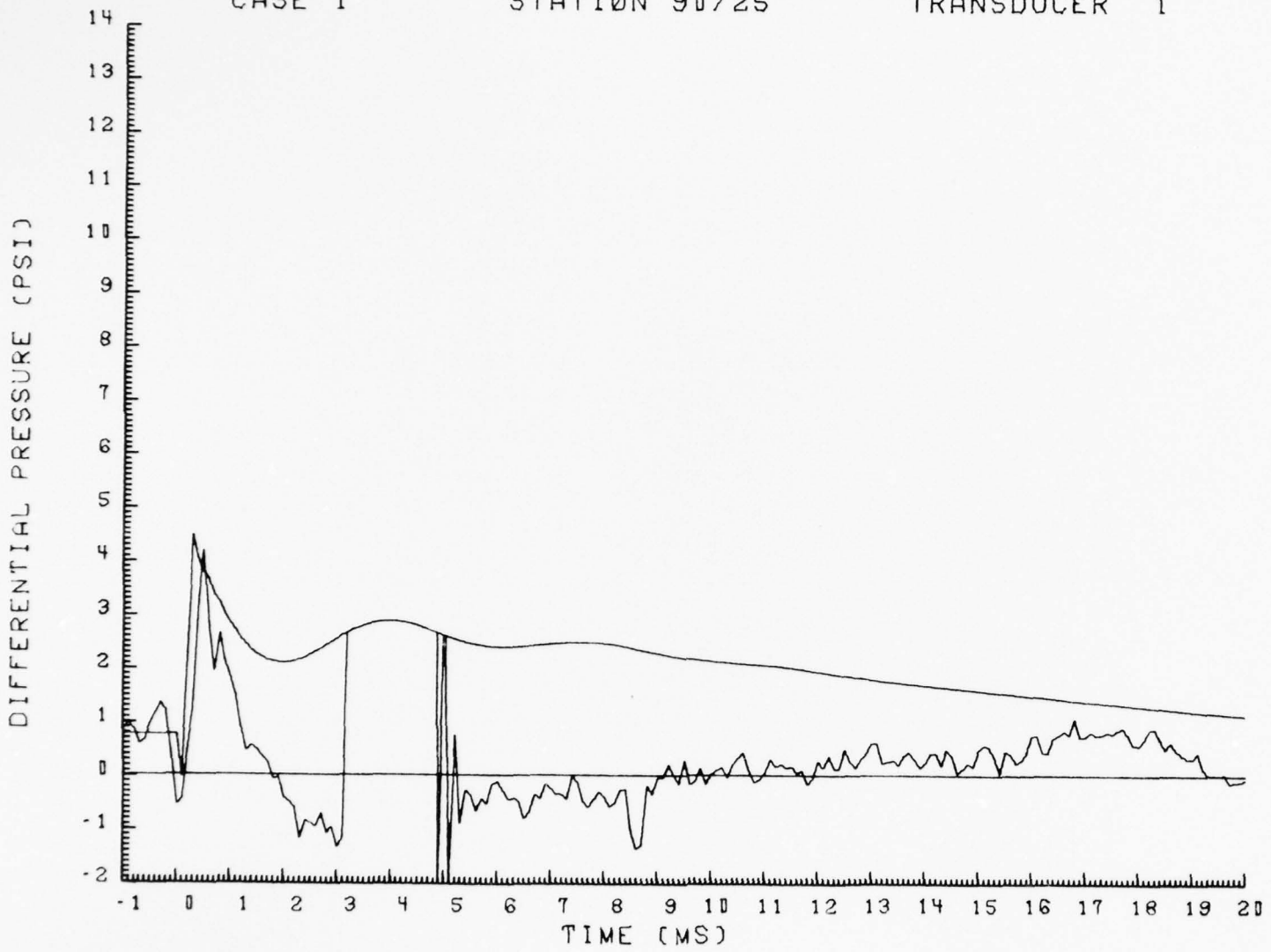


Figure 3. (Concluded)

Figure 4. Time-Variations of Pressure Loadings at Transducer Locations. Predictions From VIBRA-6 Compared With Experiment.

Case 3 - $\phi$ = 90.3 deg, $\Delta p_s$=4.02 psi. (9B-A2-2)

———— VIBRA-6

~~~~ Test Data
~~~~

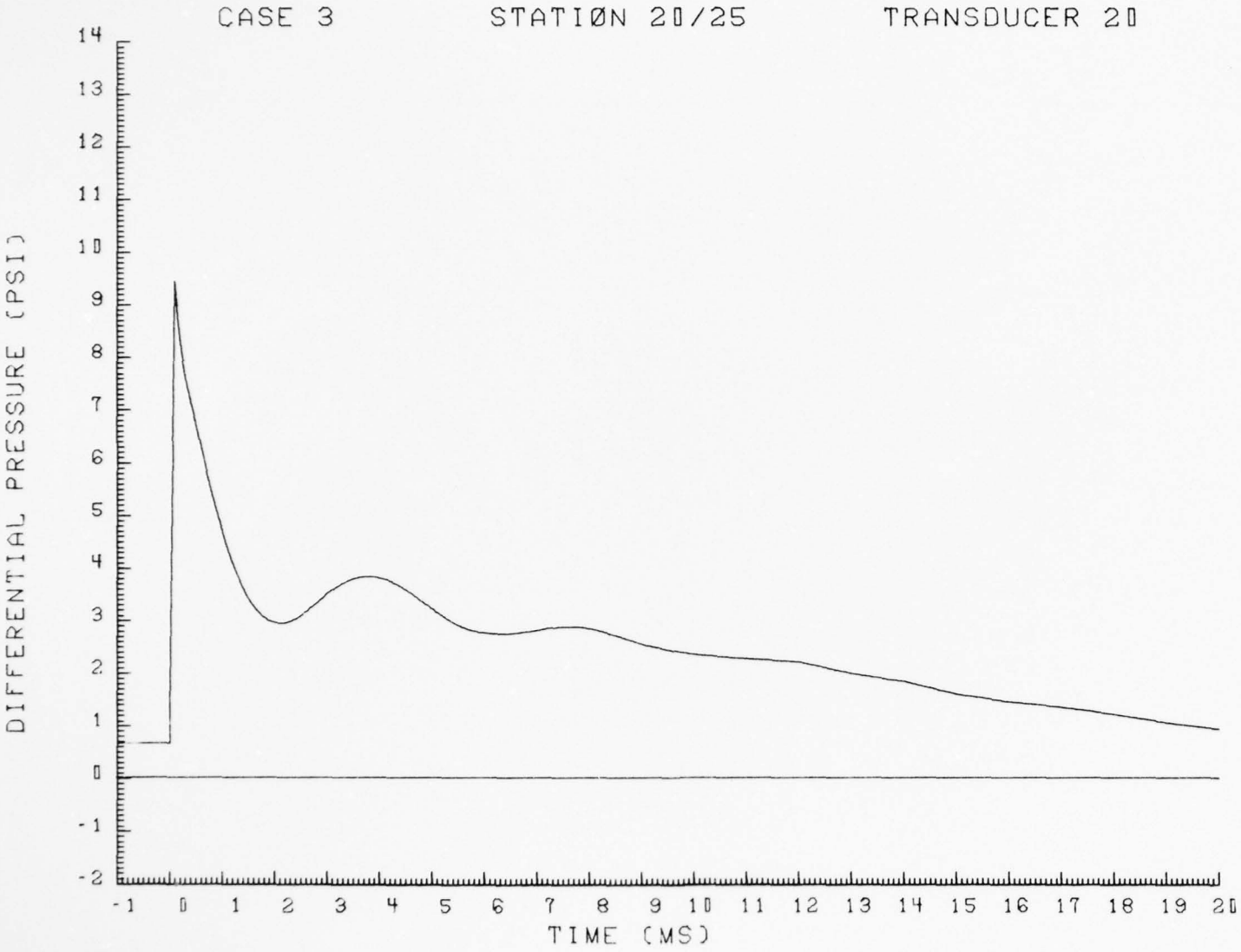
CASE 3
STATIØN 20/25
TRANSDUCER 20
DIFFERENTIAL PRESSURE (PSI)
14
13
12
11
10
9
8
7
6
5
4
3
2
1
0
-1
-2
-1 0 1 2 3 4 5 6 7 8 9 10 11 12 13 14 15 16 17 18 19 20
TIME (MS)

Figure 4

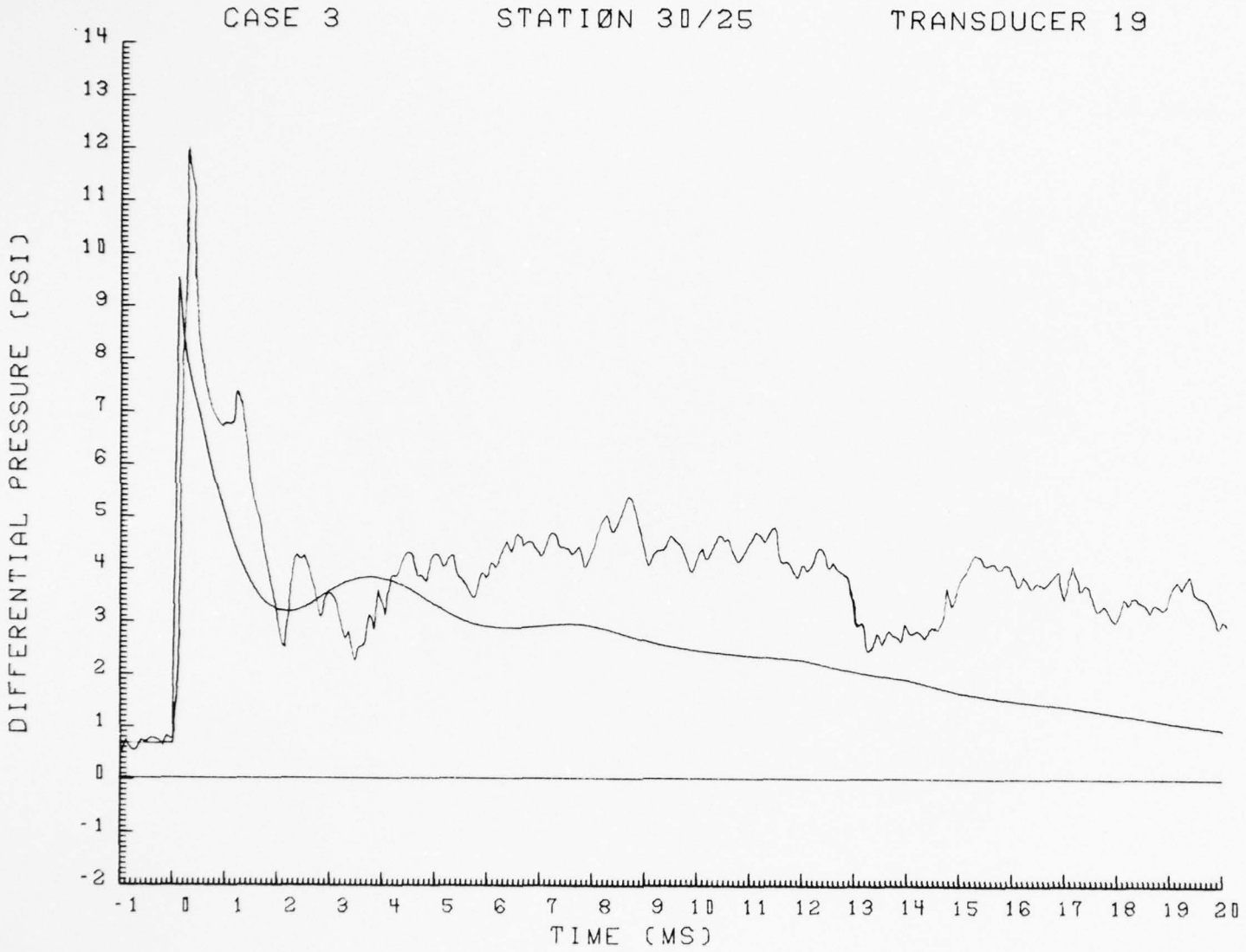


Figure 4. (Continued)

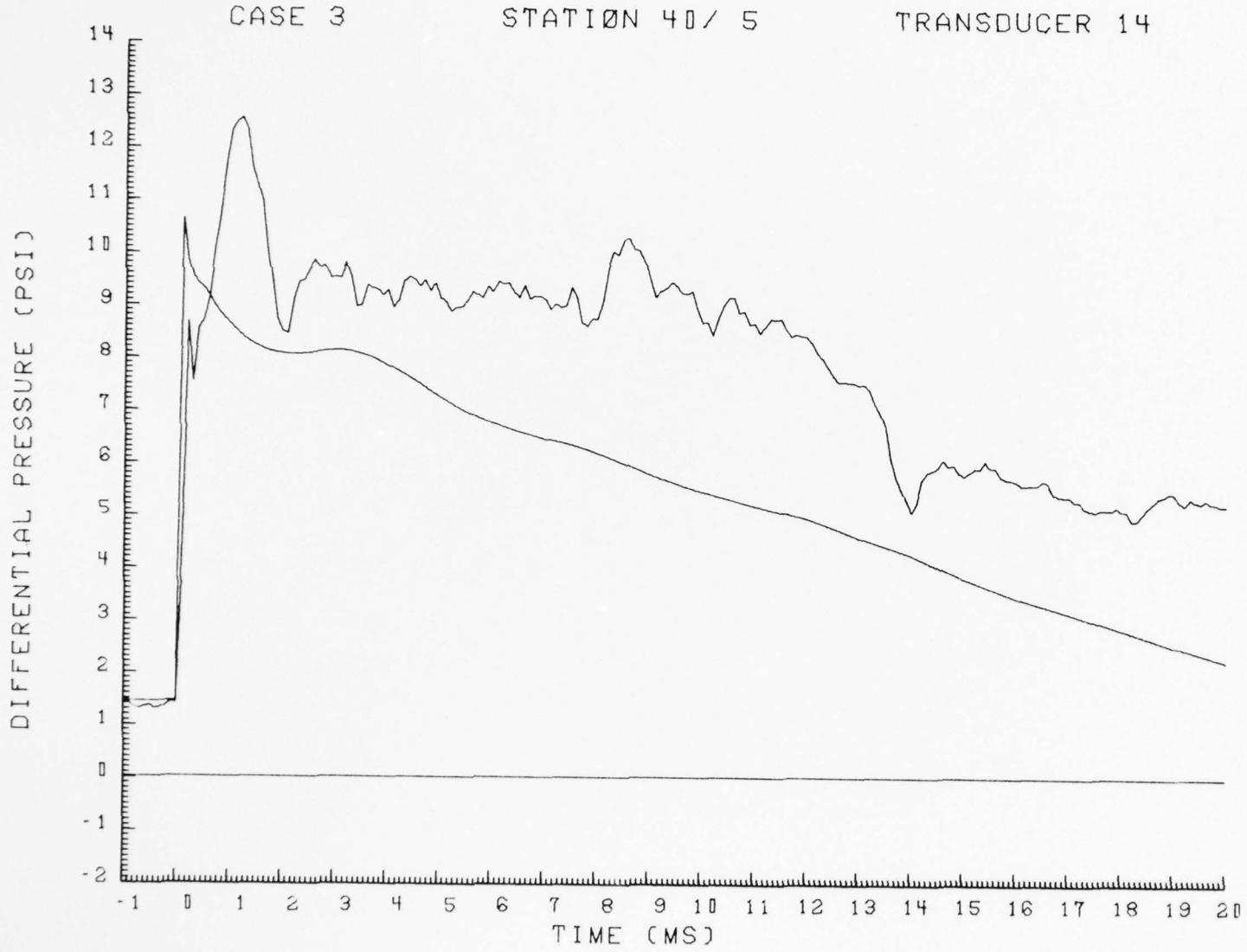


Figure 4. (Continued)

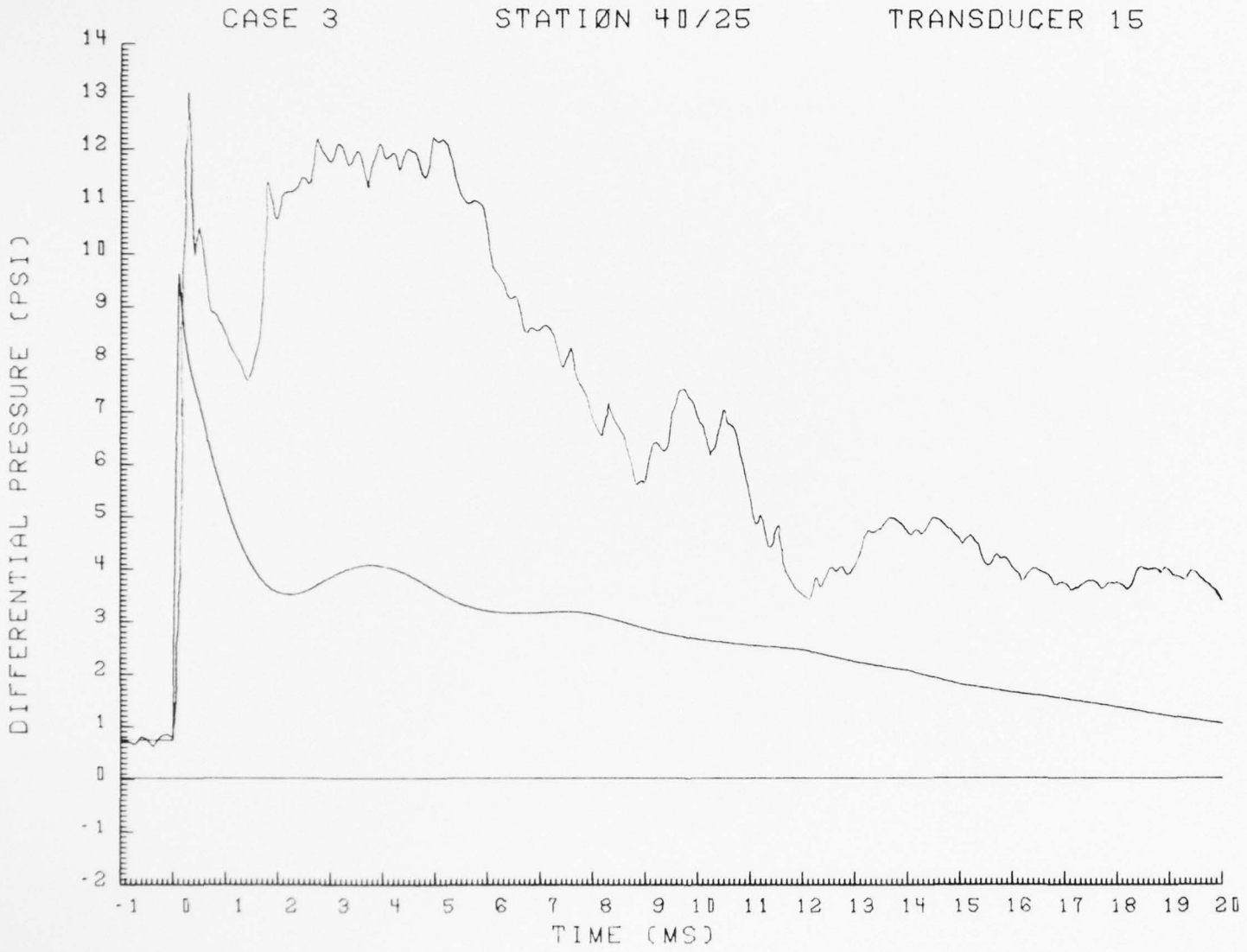


Figure 4. (Continued)

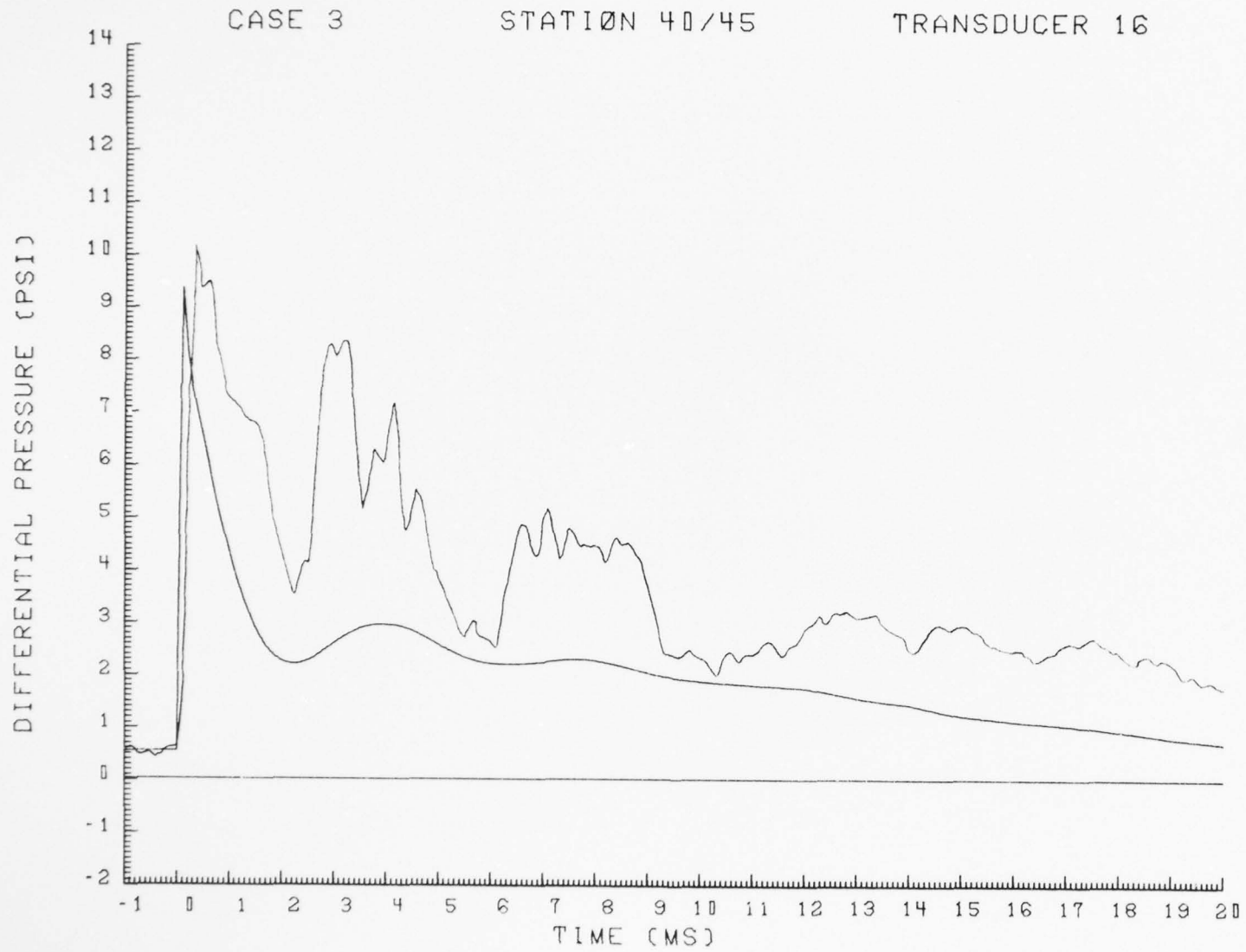


Figure 4. (Continued)

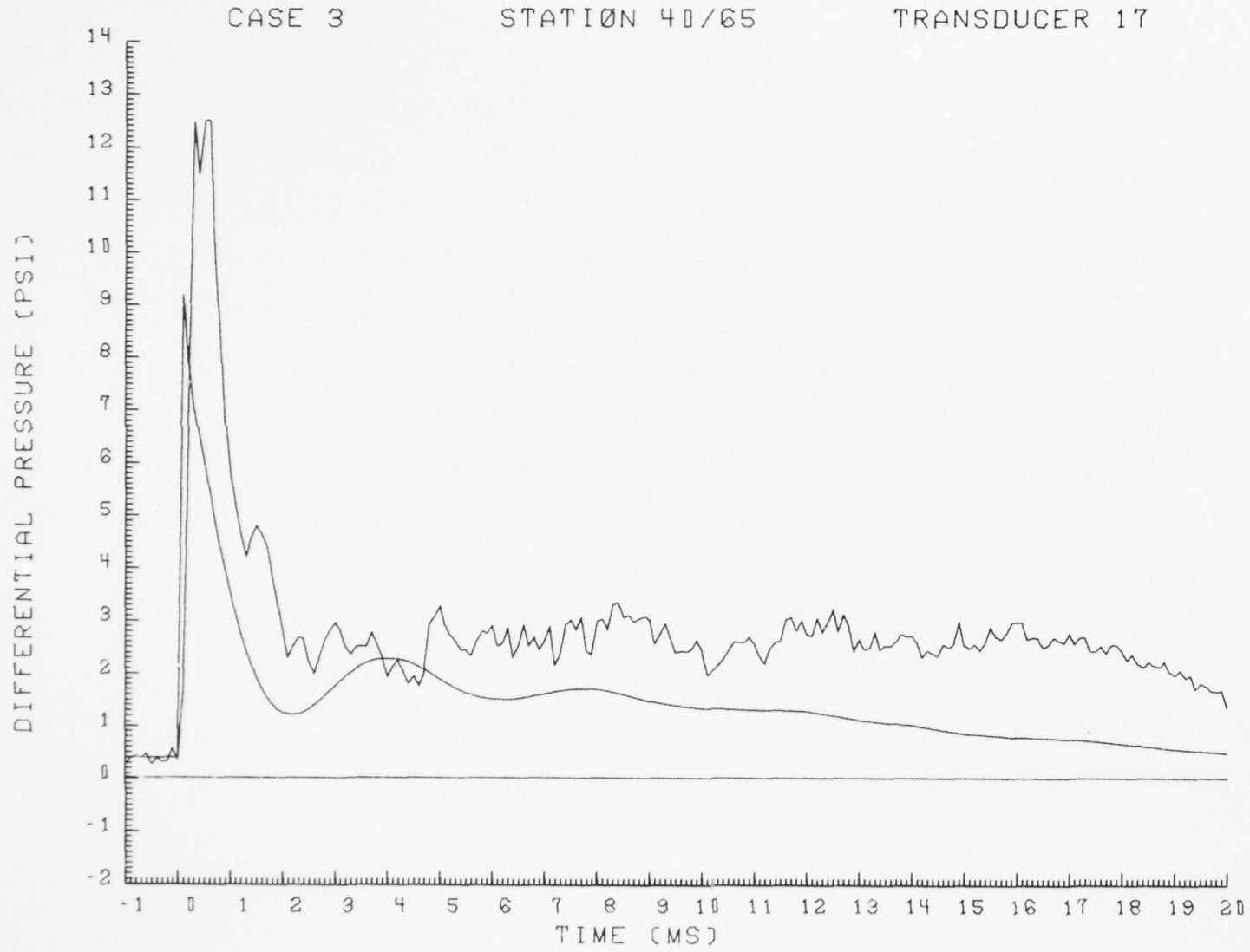


Figure 4. (Continued)

AD-A064 148 KAMAN AVIDYNE BURLINGTON MASS F/G 1/3
MEASUREMENTS OF BLAST PRESSURES ON A RIGID 65 DEG SWEPTBACK WIN--ETC(U)
DEC 77 G ZARTARIAN, J R RUETENIK, R F SMILEY DNA001-76-C-0106
UNCLASSIFIED KA-TR-137-VOL-3 DNA-4400F-3 NL

2 OF 2
AD A064148

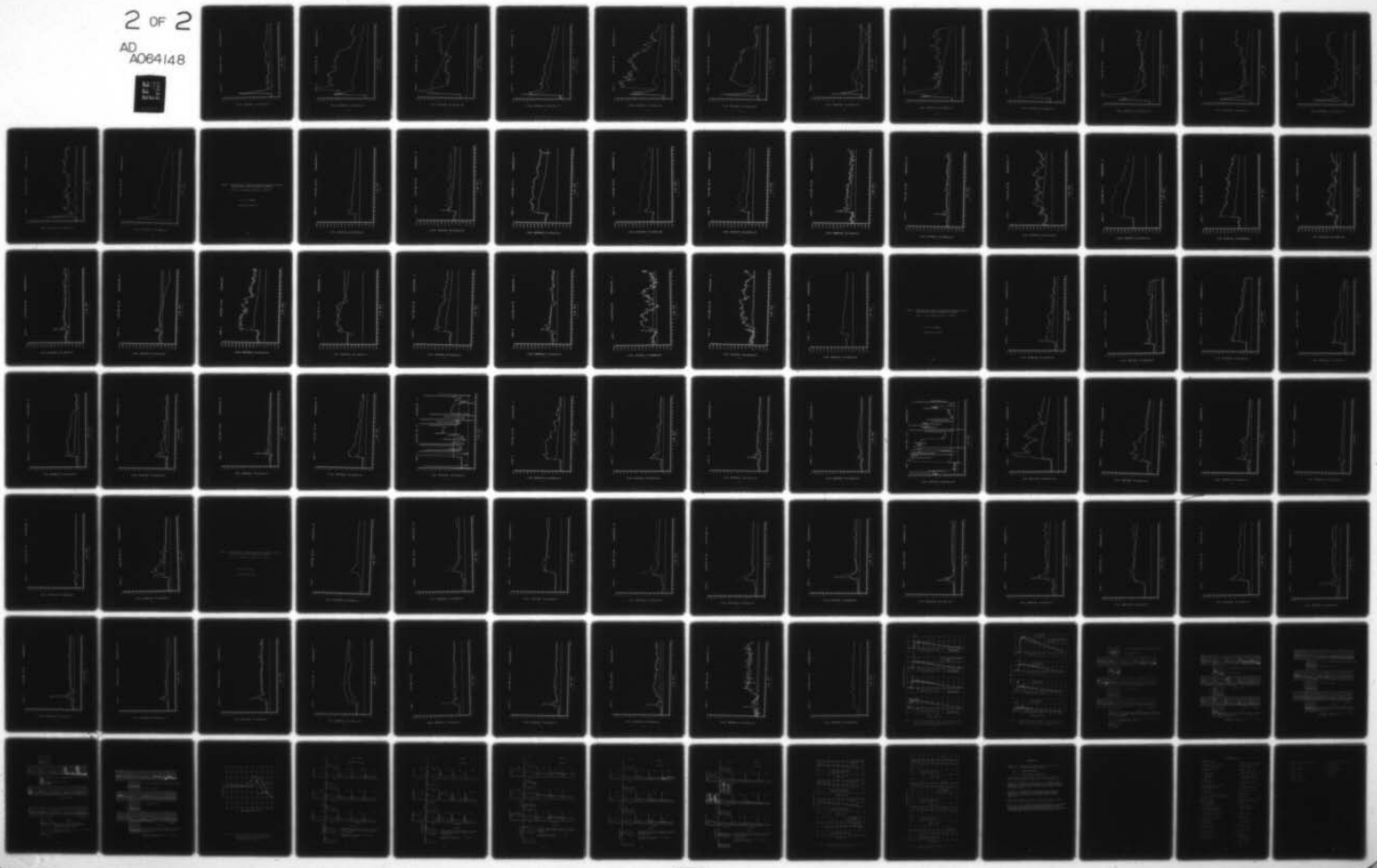

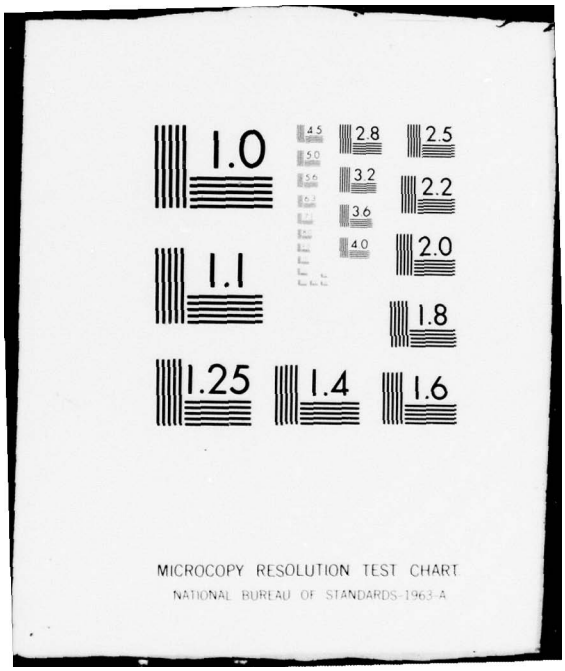
1.0
1.1
1.25
1.4
1.6
1.8
2.0
2.2
2.5
2.8
3.2
3.6
4.0
4.5
5.0
5.6
6.3
MICROCOPY RESOLUTION TEST CHART
NATIONAL BUREAU OF STANDARDS-1963-A

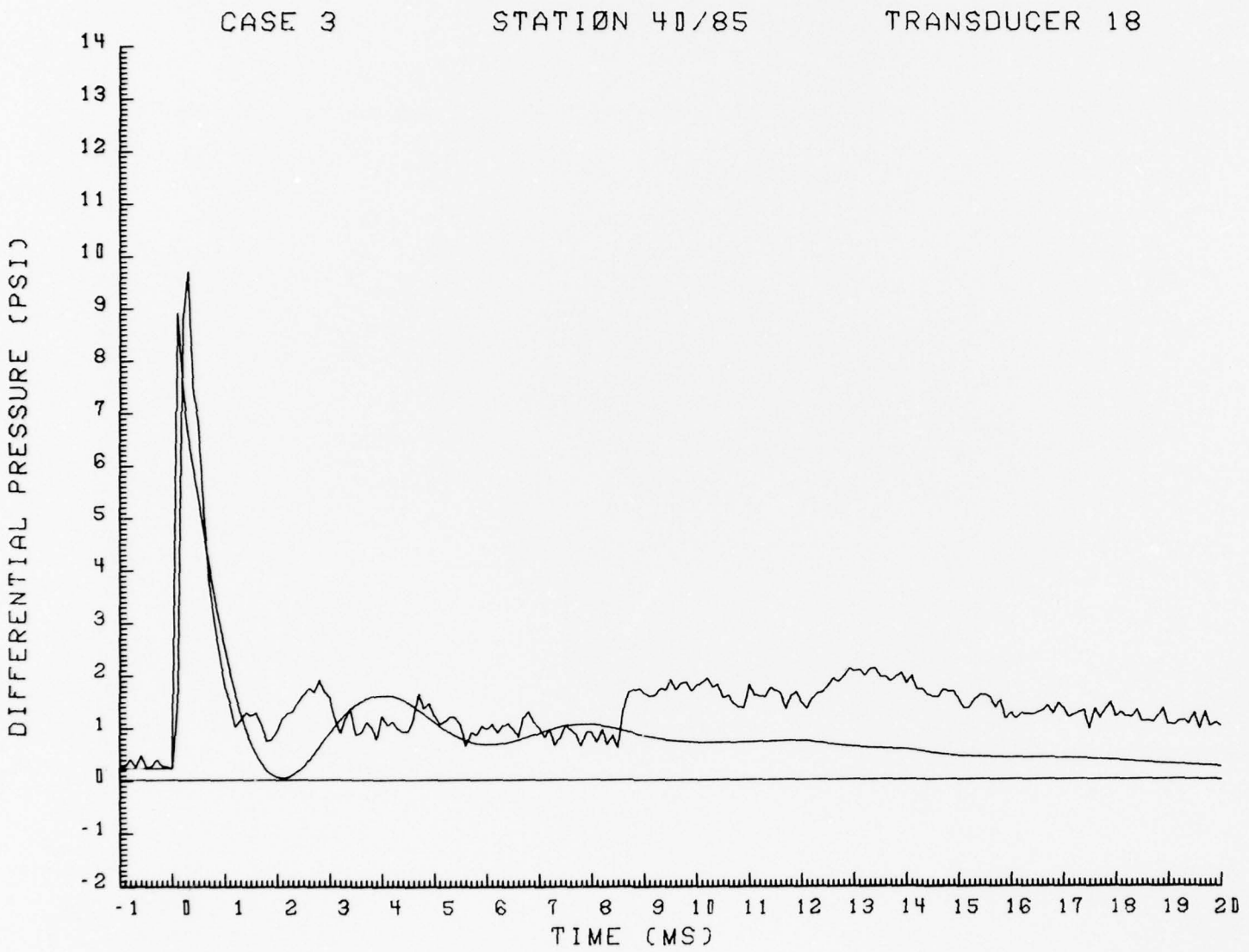


Figure 4. (Continued)

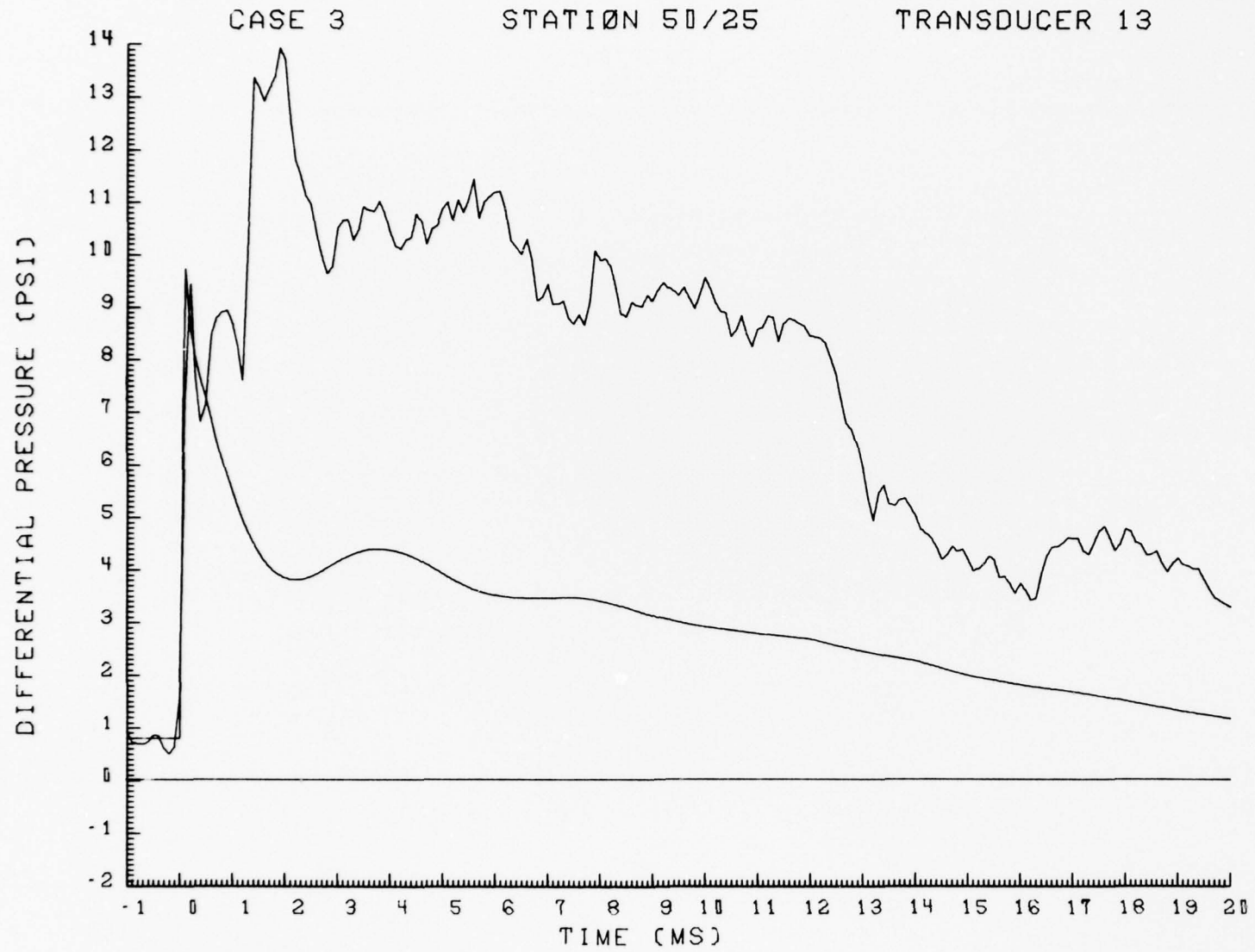


Figure 4. (Continued)

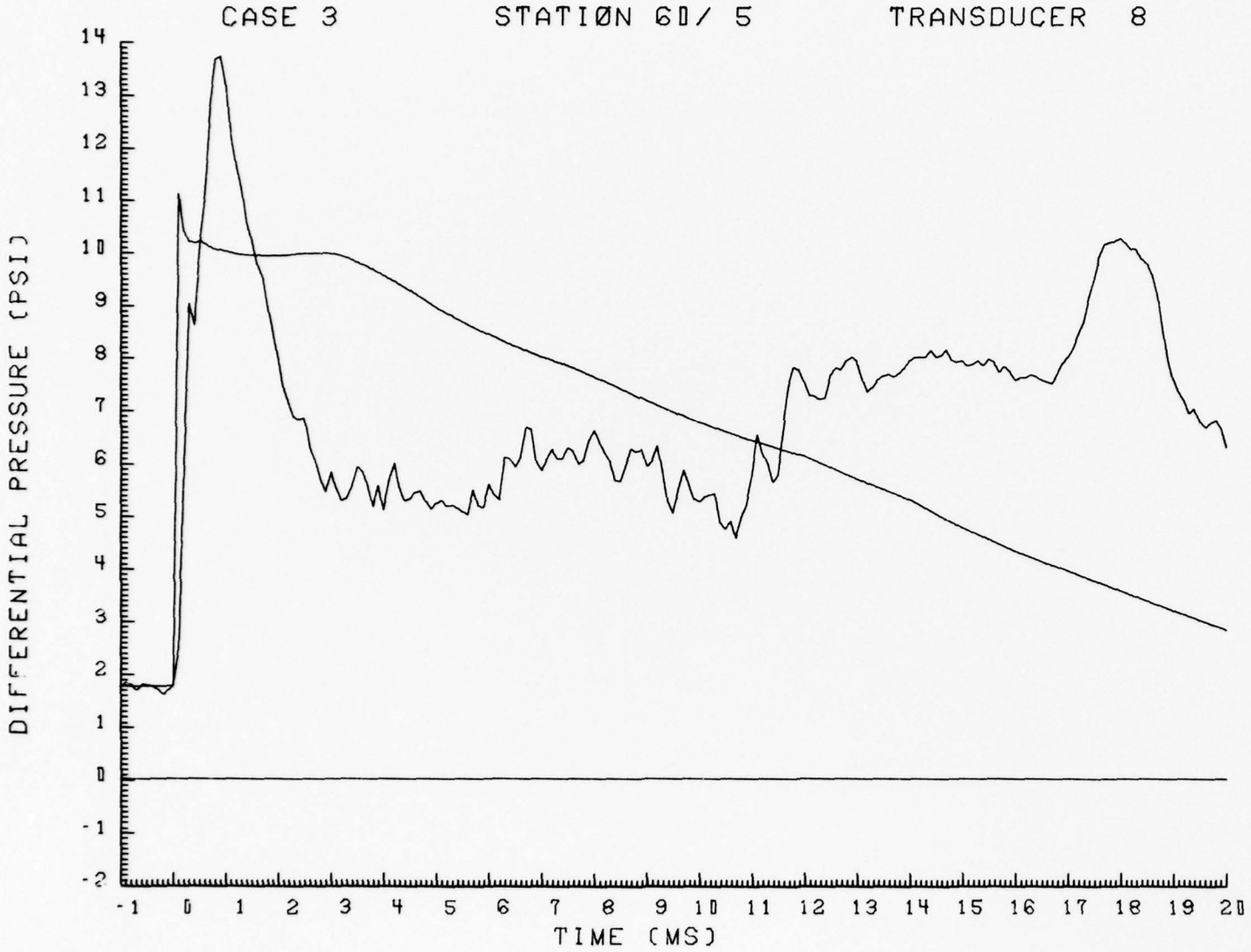


Figure 4. (Continued)

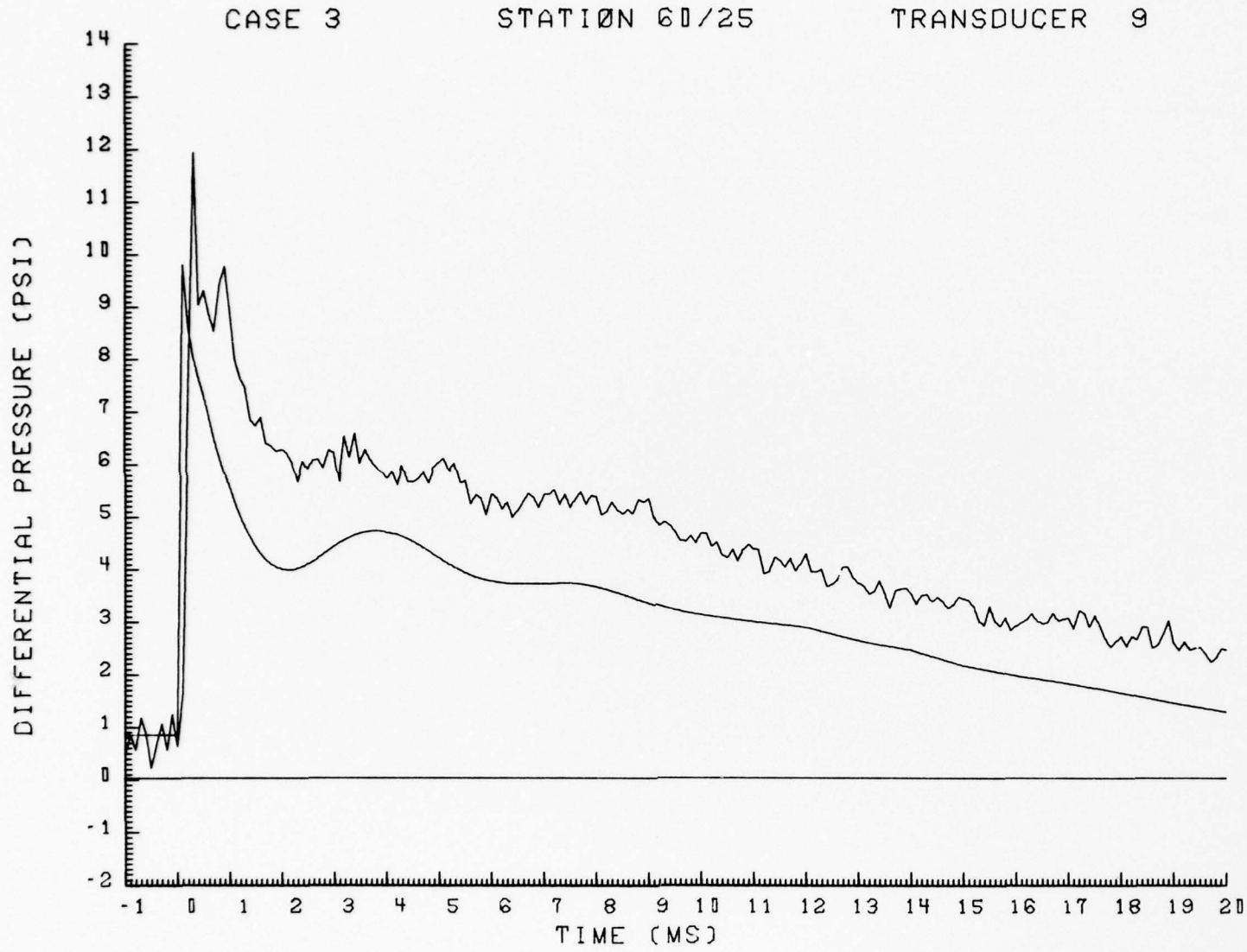


Figure 4. (Continued)

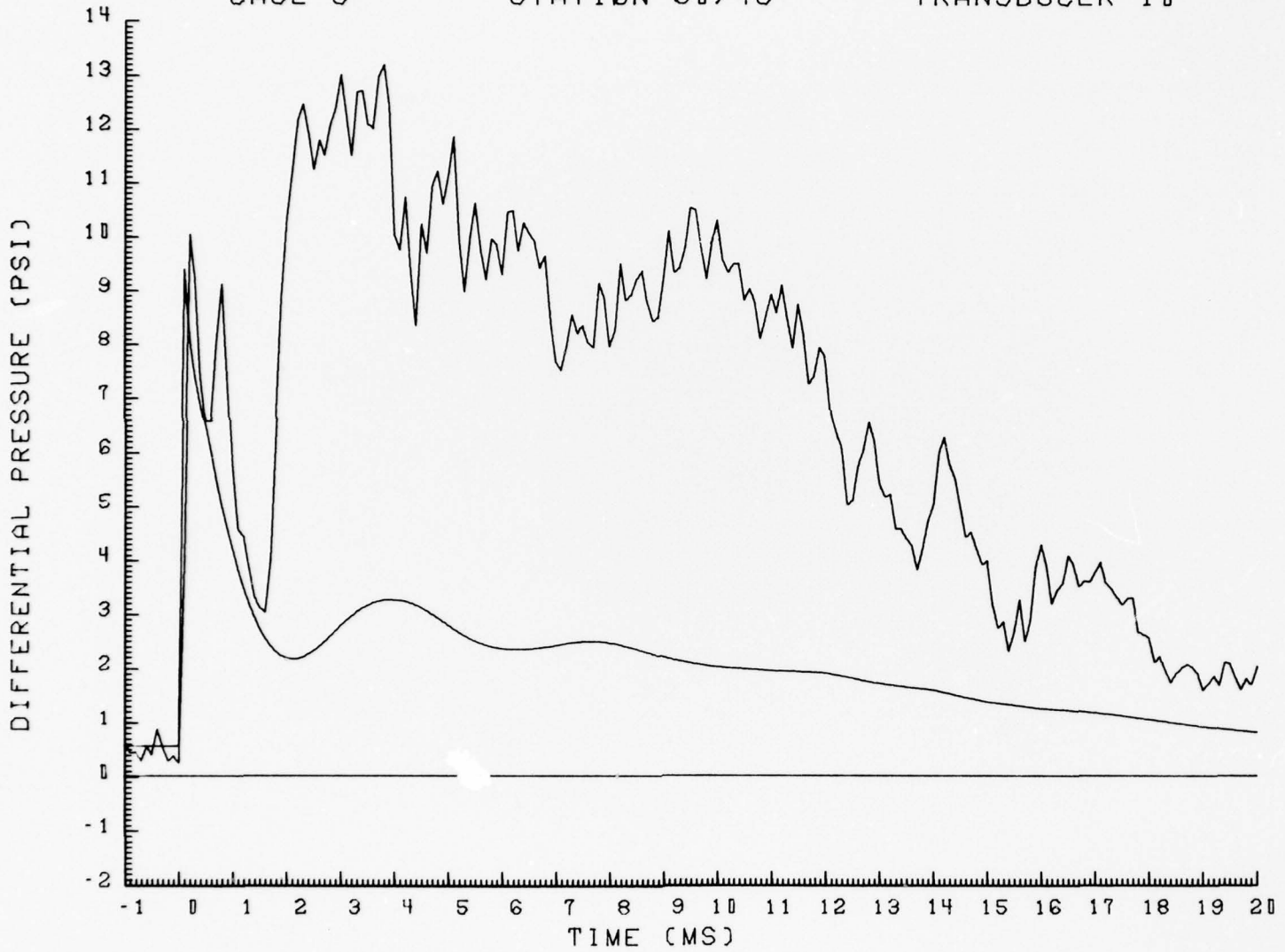


Figure 4. (Continued)

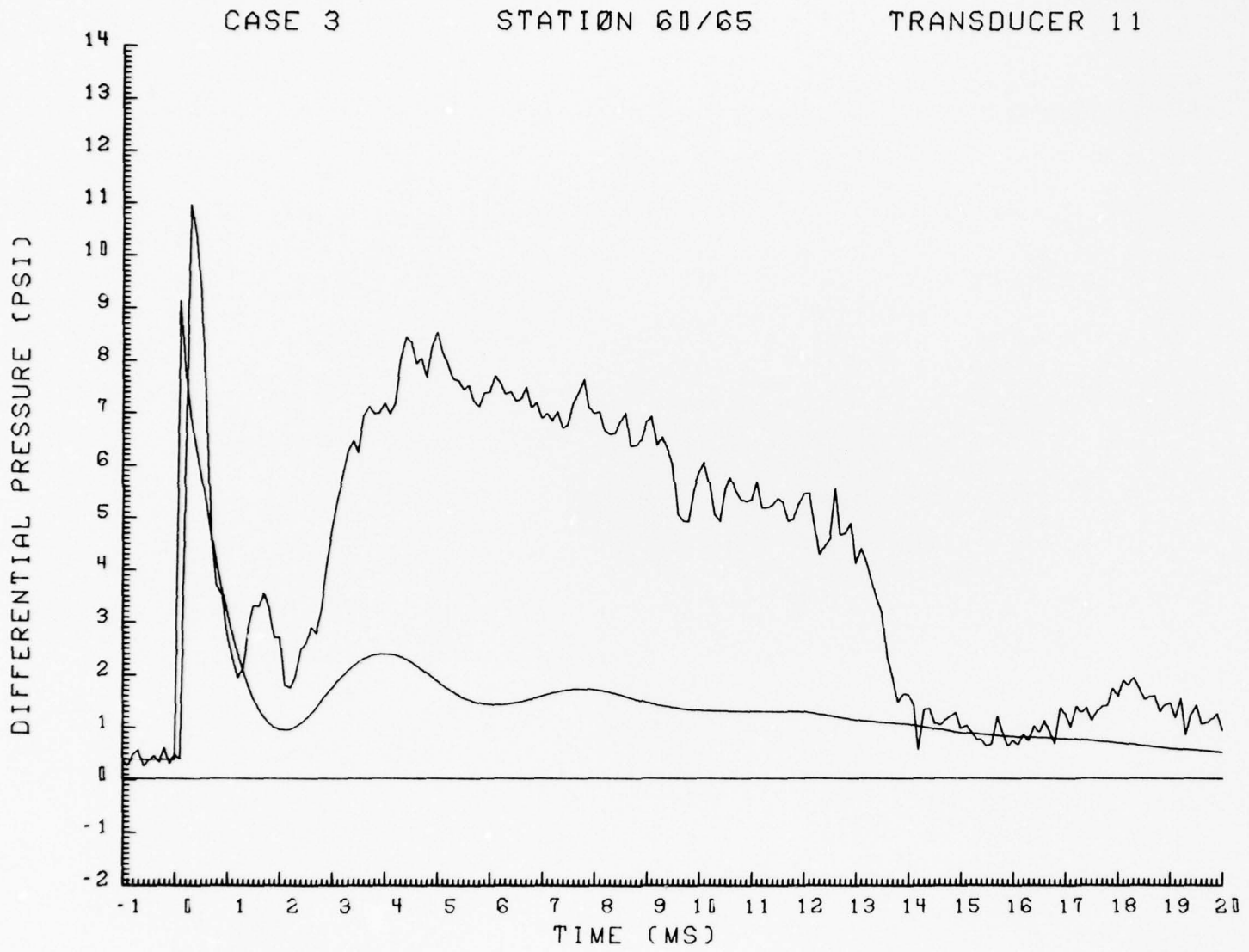


Figure 4. (Continued)

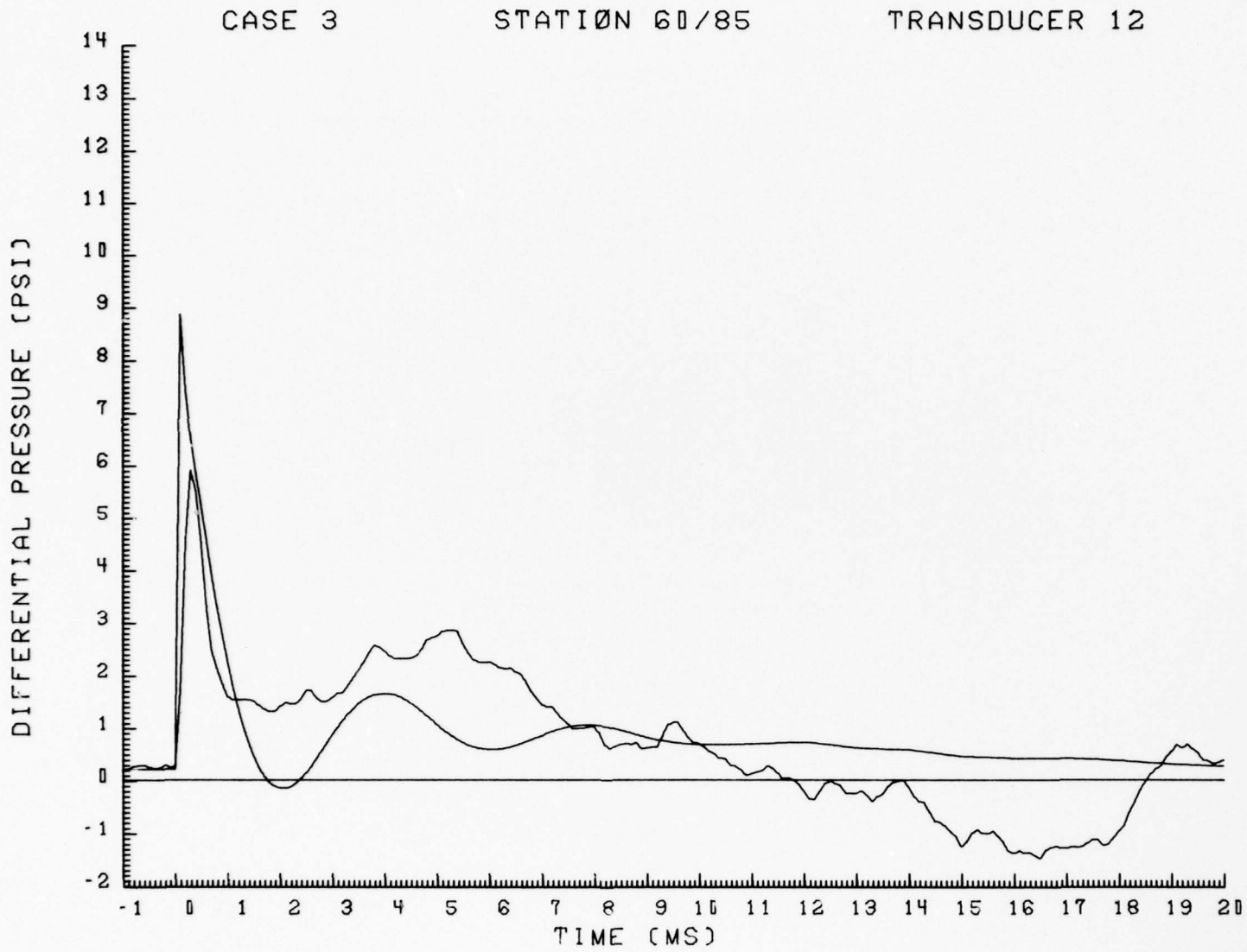


Figure 4. (Continued)

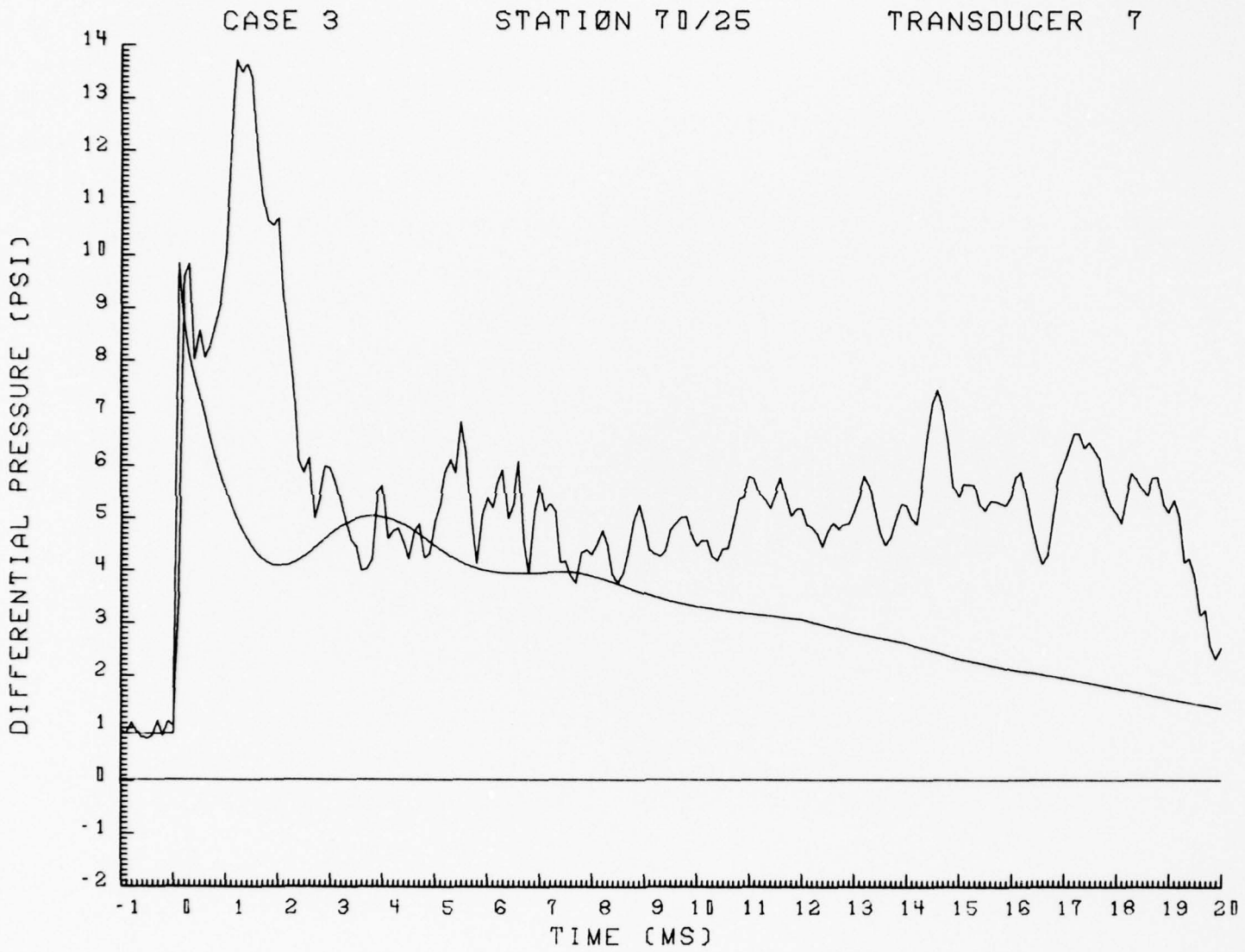


Figure 4. (Continued)

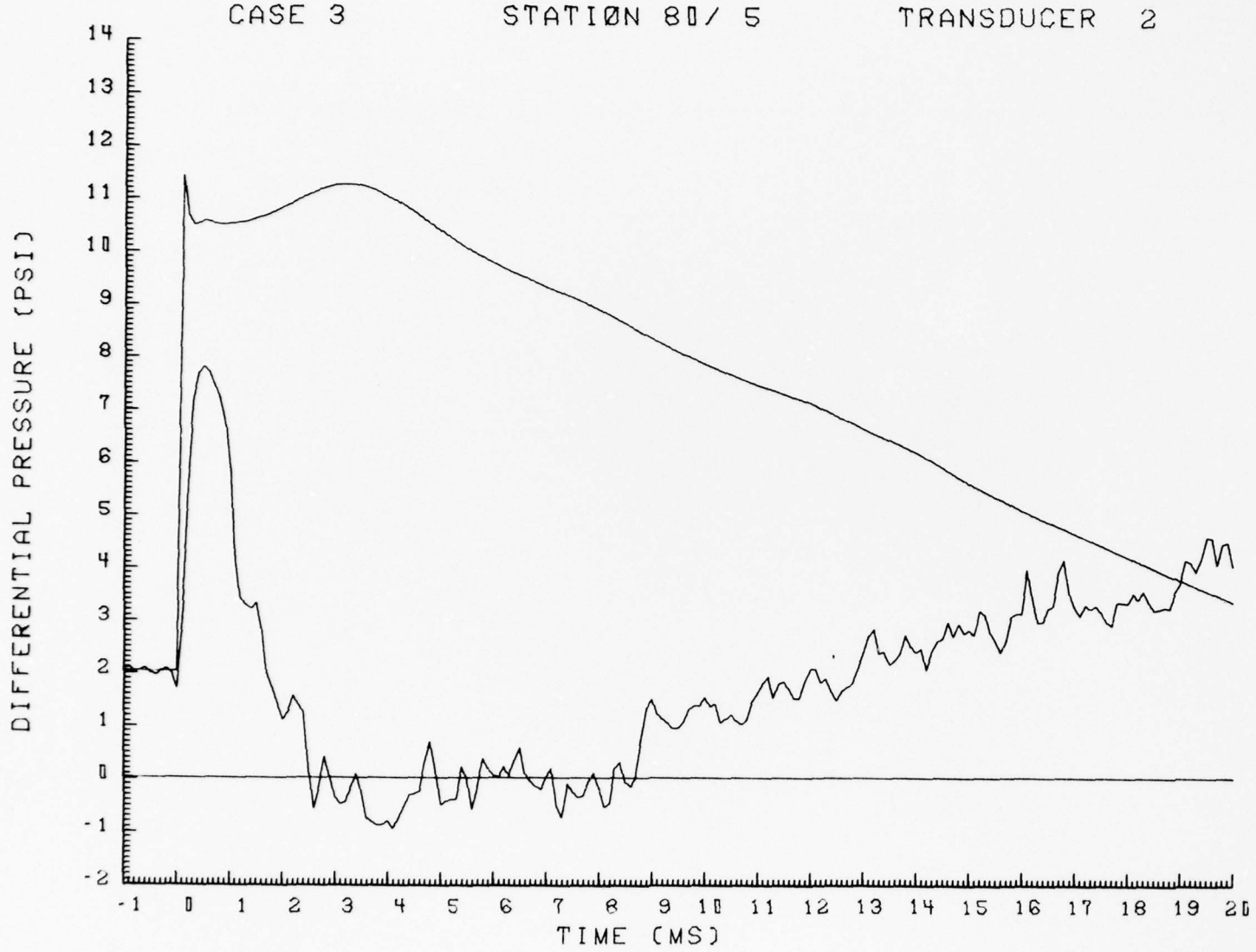


Figure 4. (Continued)

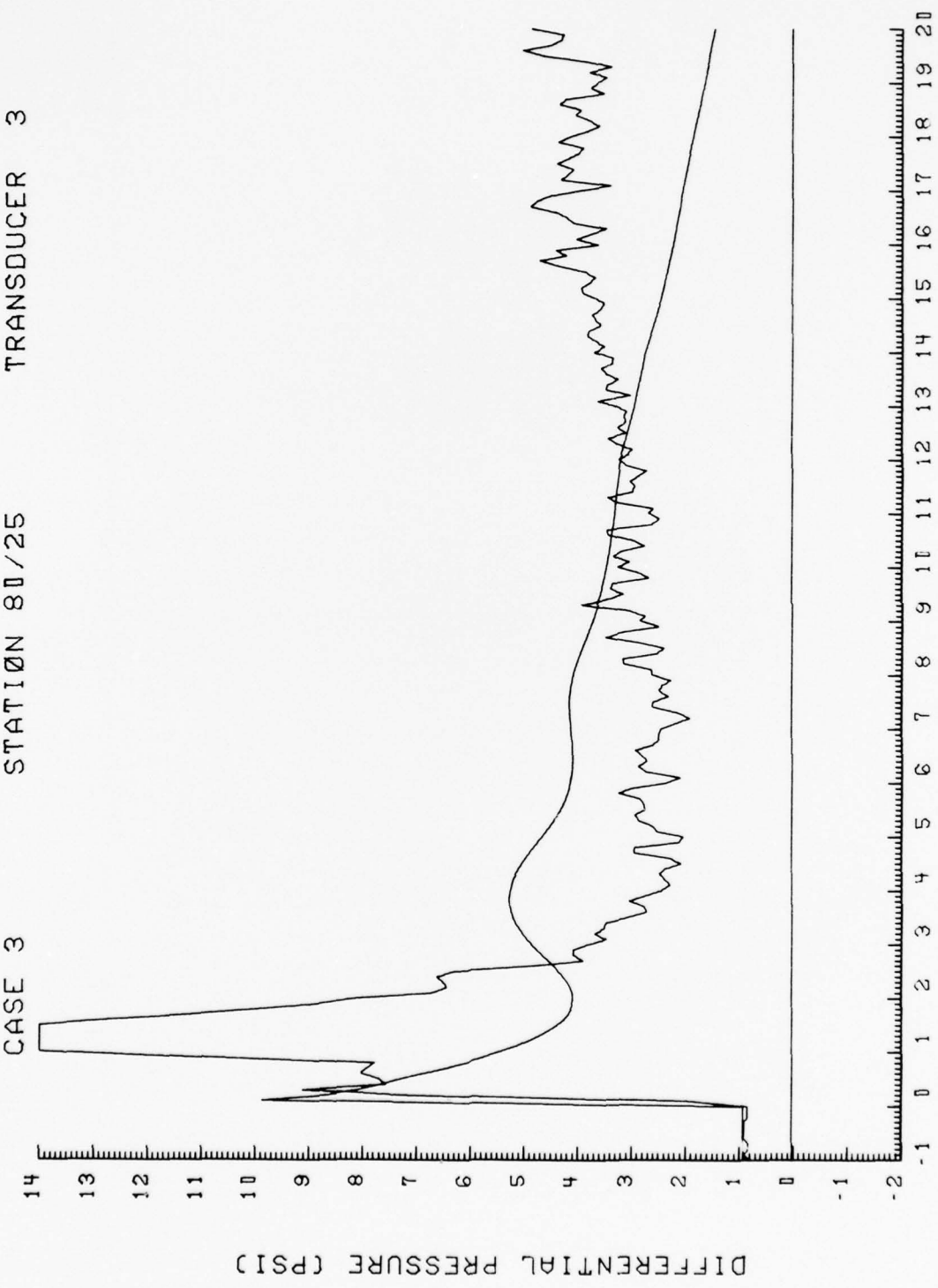


Figure 4. (Continued)

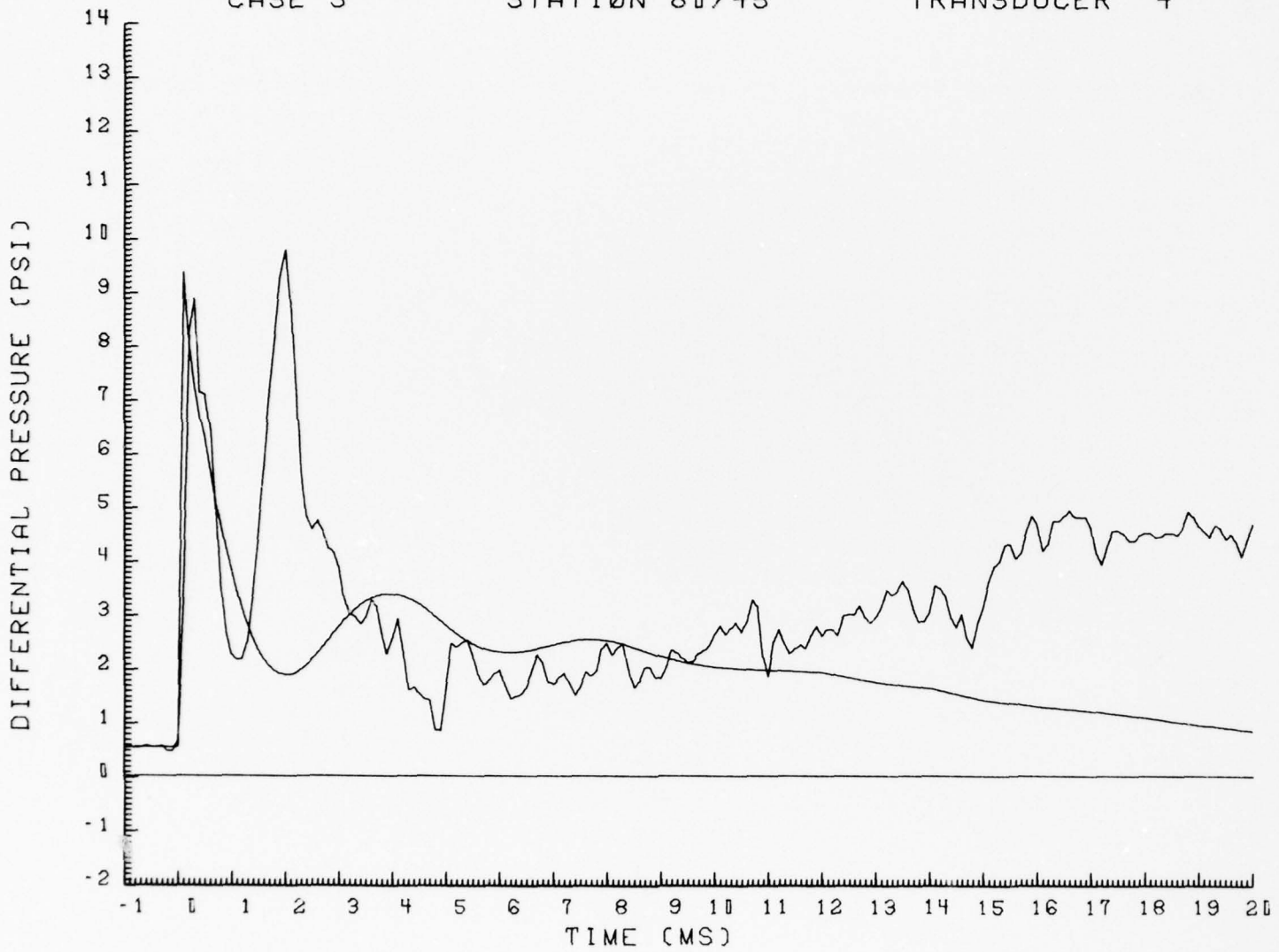


Figure 4. (Continued)

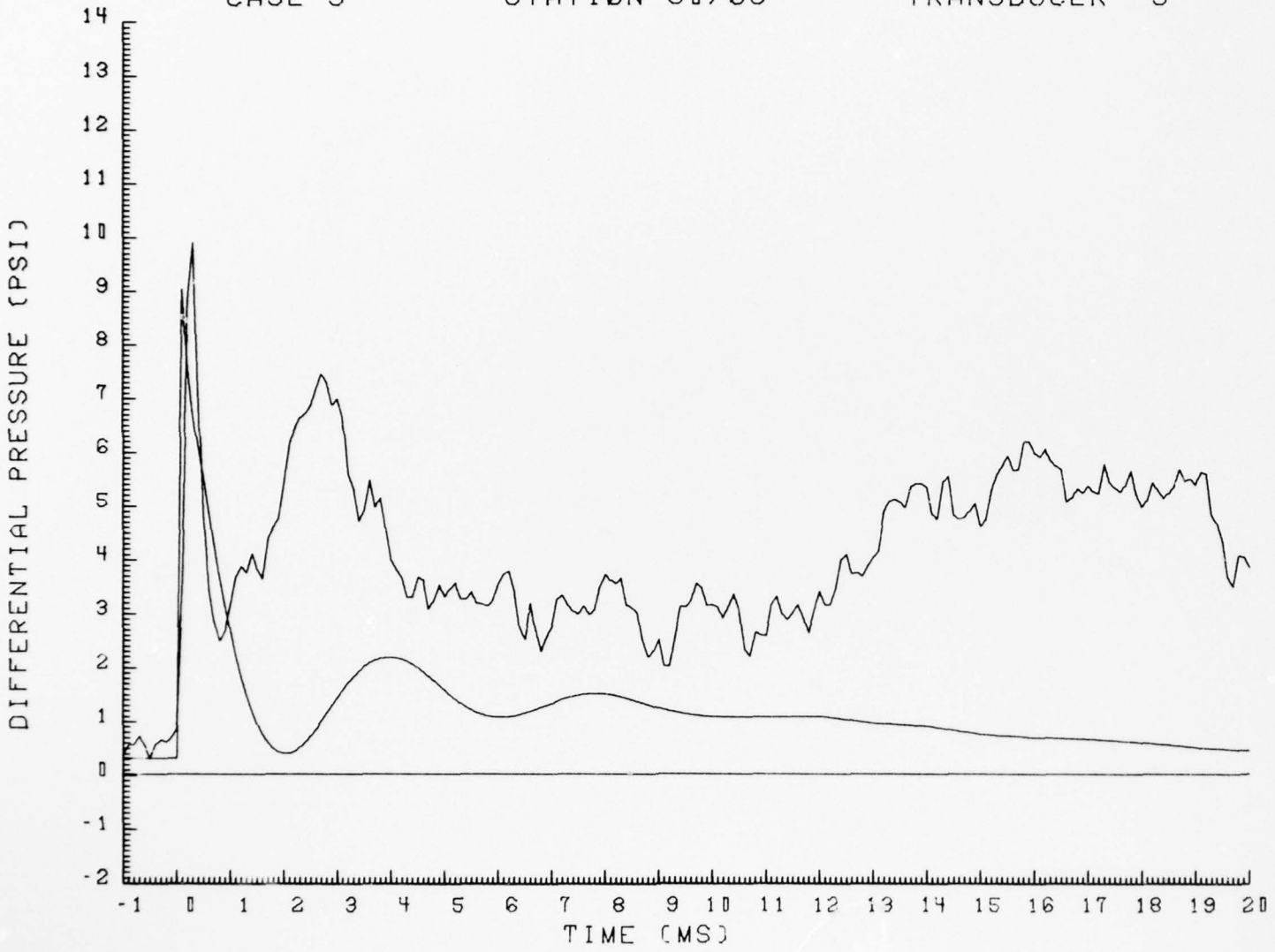


Figure 4. (Continued)

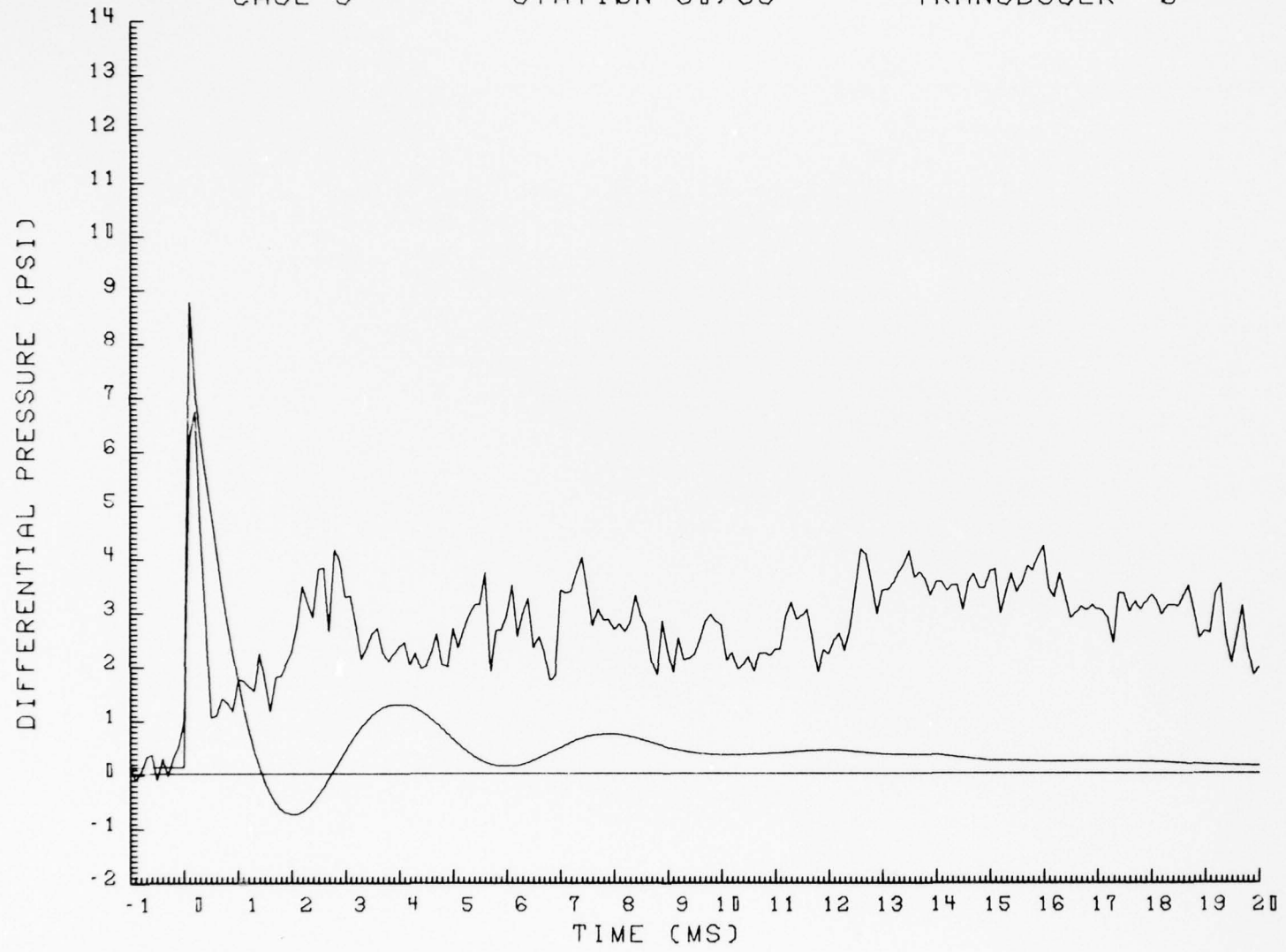


Figure 4. (Continued)

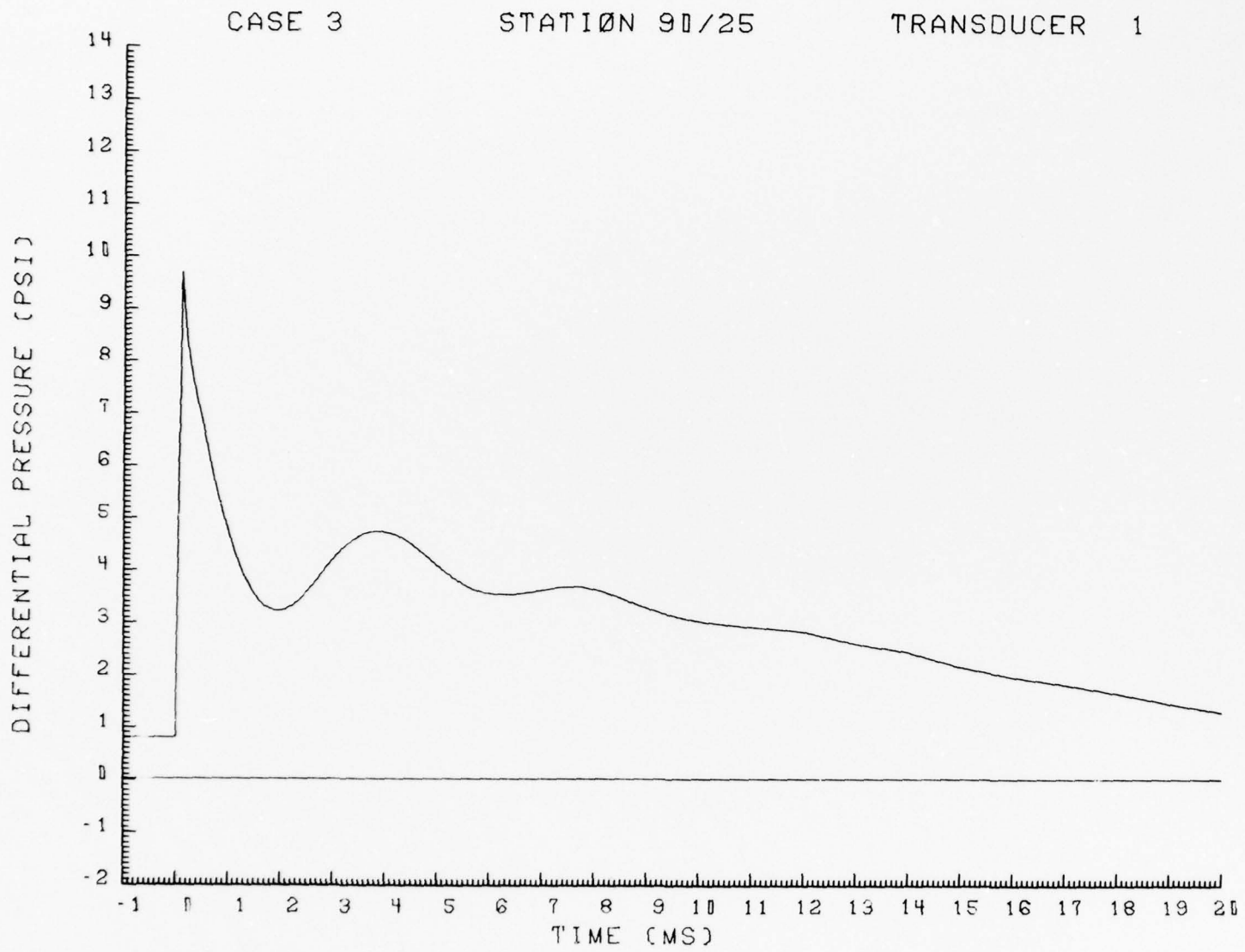


Figure 4. (Concluded)

Figure 5. Time-Variations of Pressure Loadings at Transducer Locations. Predictions From VIBRA-6 Compared With Experiment.

Case 2 - $\phi$ = 20.1 deg, $\Delta p_s$=2.01 psi. (9B-A2-1)

———— VIBRA-6

~~~~~~~~ Test Data
~~~~~~~~

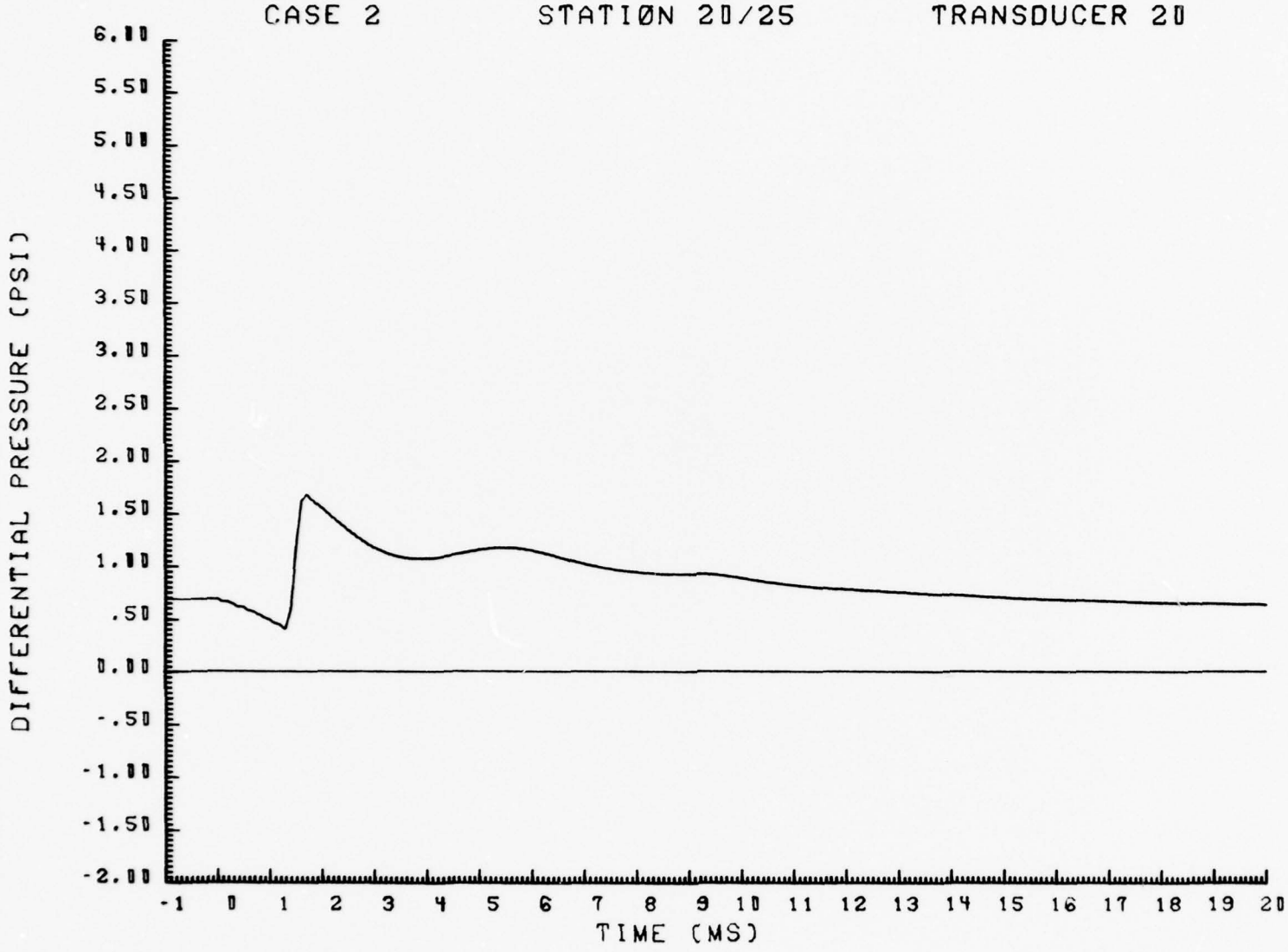
CASE 2
STATIØN 20/25
TRANSDUCER 20
DIFFERENTIAL PRESSURE (PSI)
6.00
5.50
5.00
4.50
4.00
3.50
3.00
2.50
2.00
1.50
1.00
.50
0.00
-.50
-1.00
-1.50
-2.00
-1 0 1 2 3 4 5 6 7 8 9 10 11 12 13 14 15 16 17 18 19 20
TIME (MS)

Figure 5

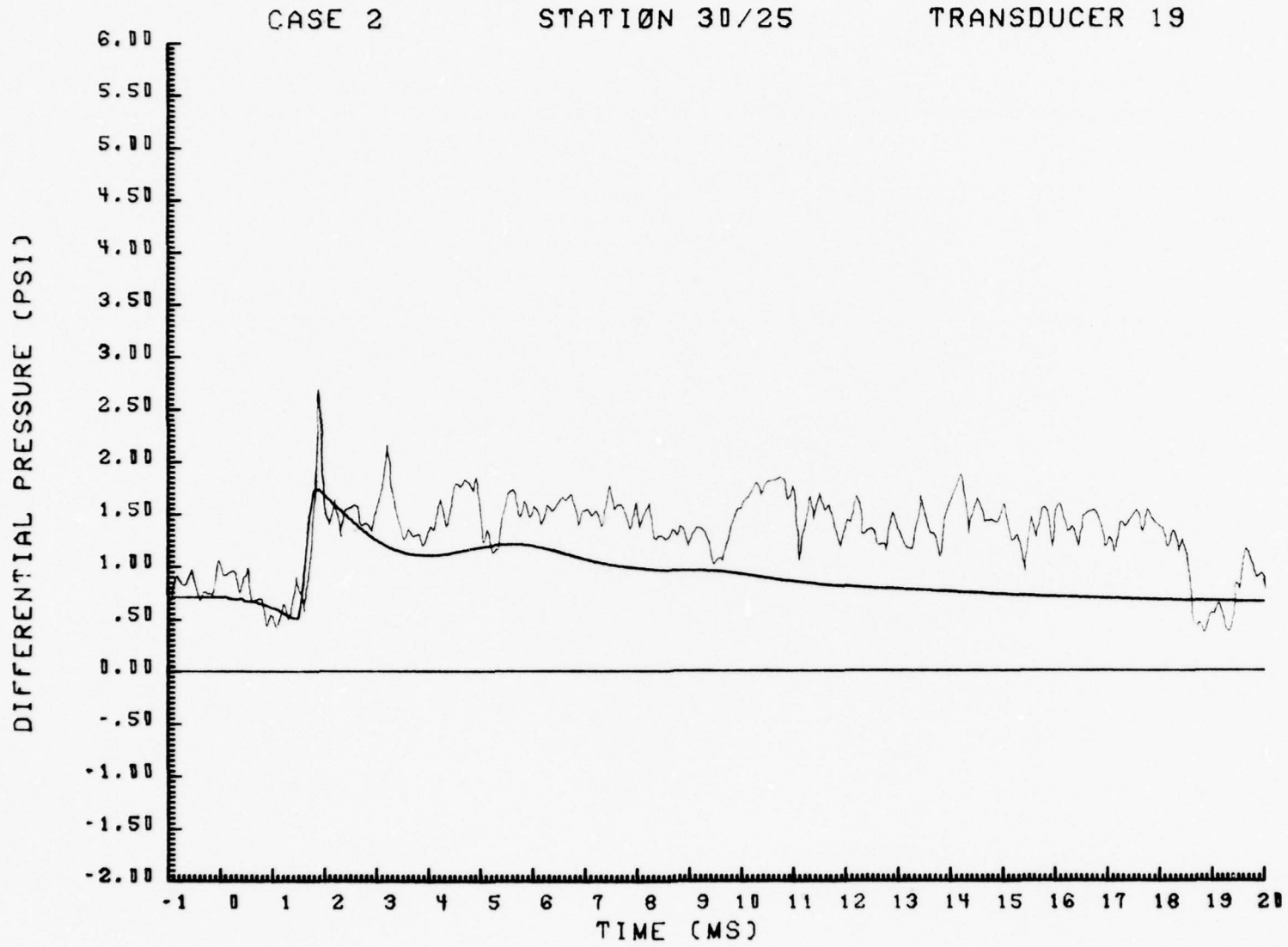


Figure 5. (Continued)

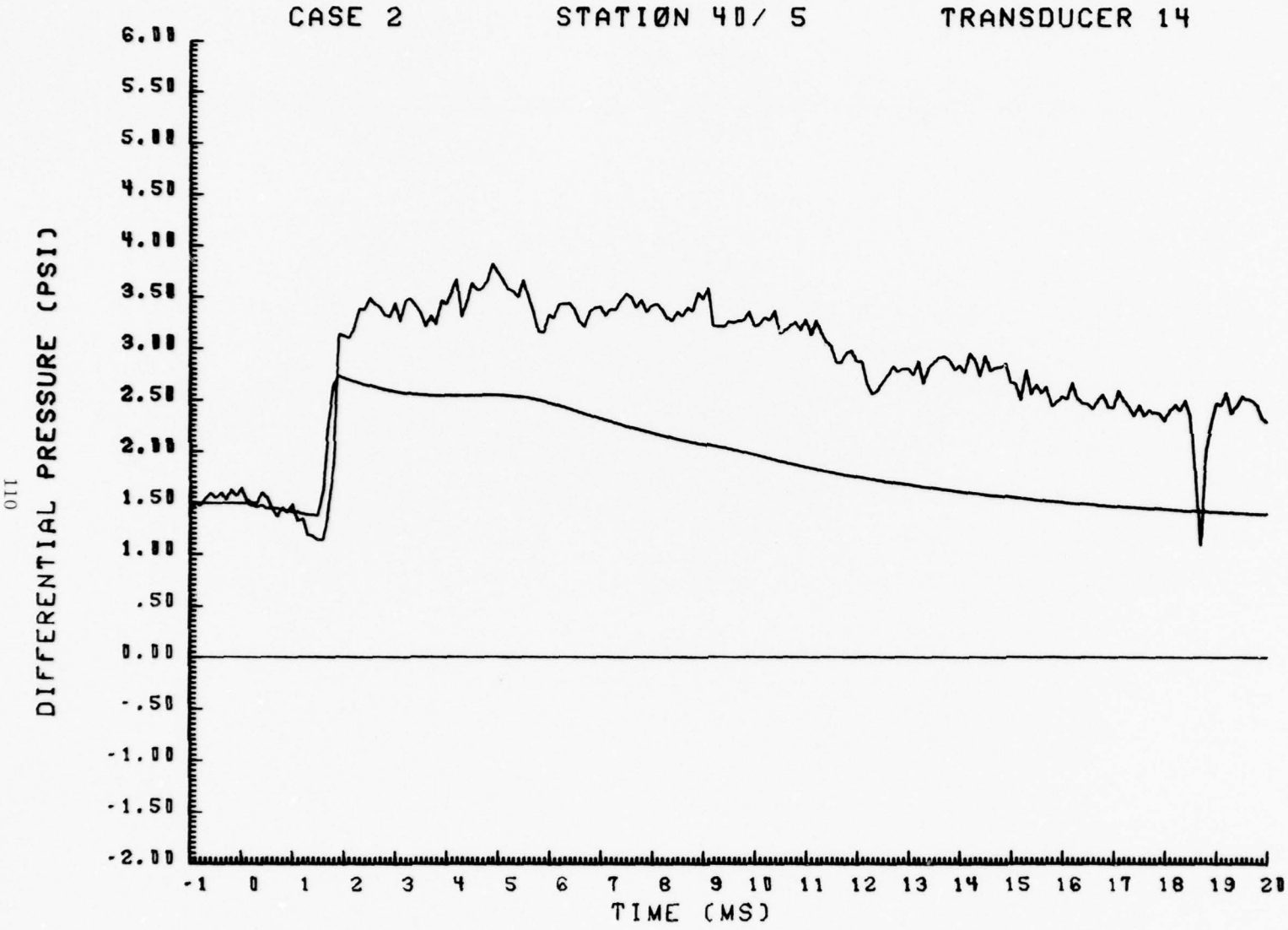


Figure 5. (Continued)

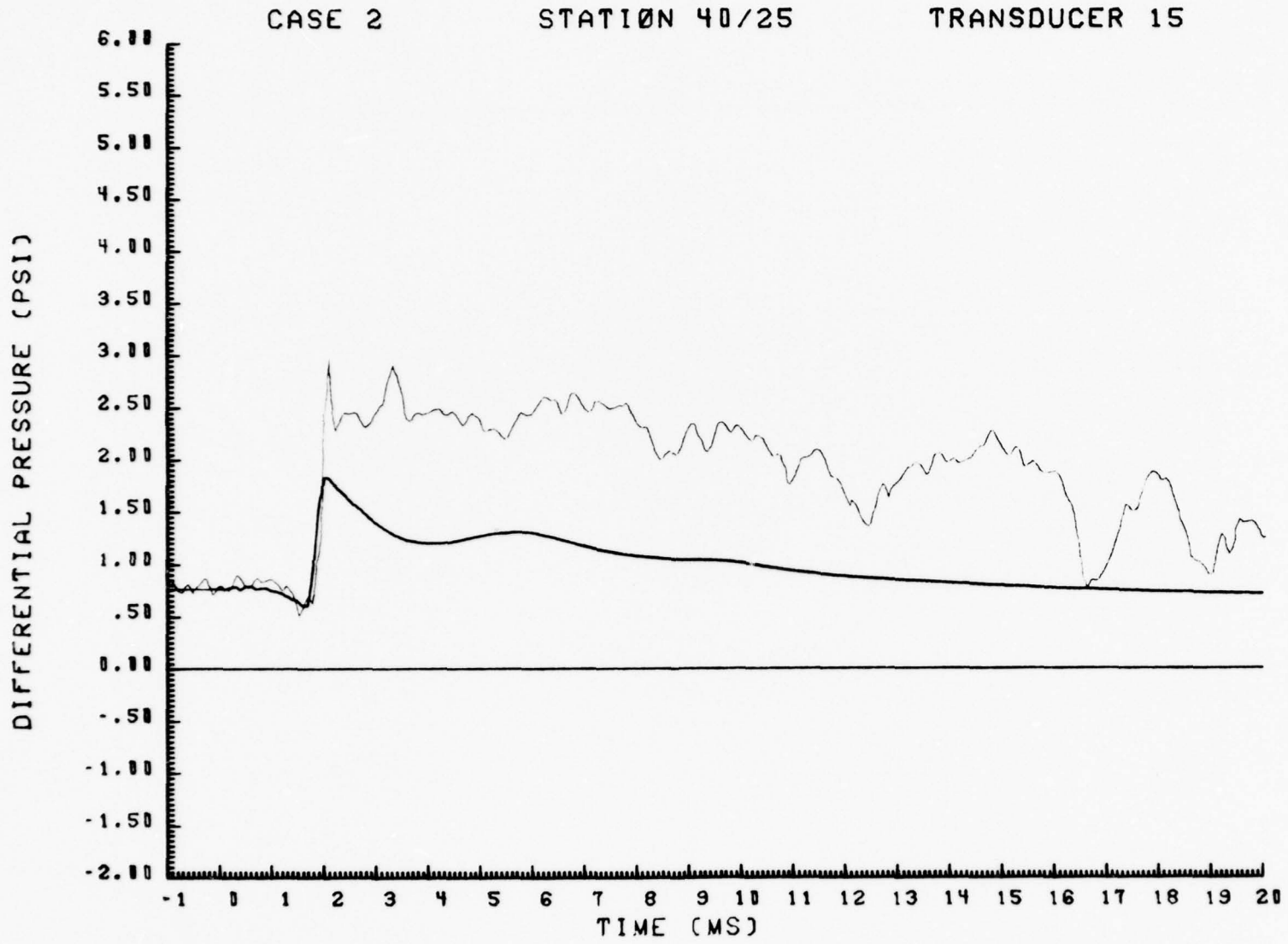


Figure 5. (Continued)

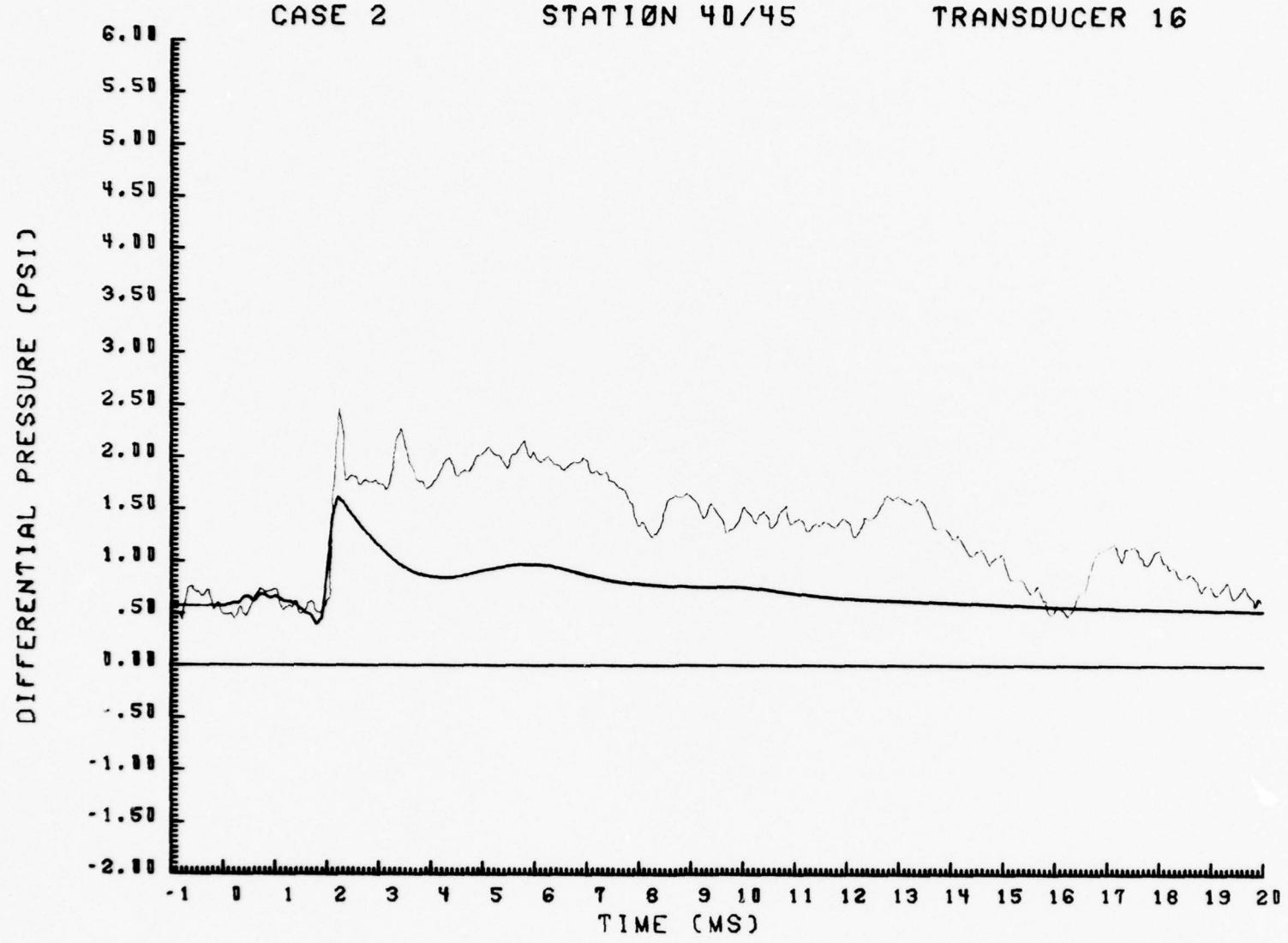


Figure 5. (Continued)

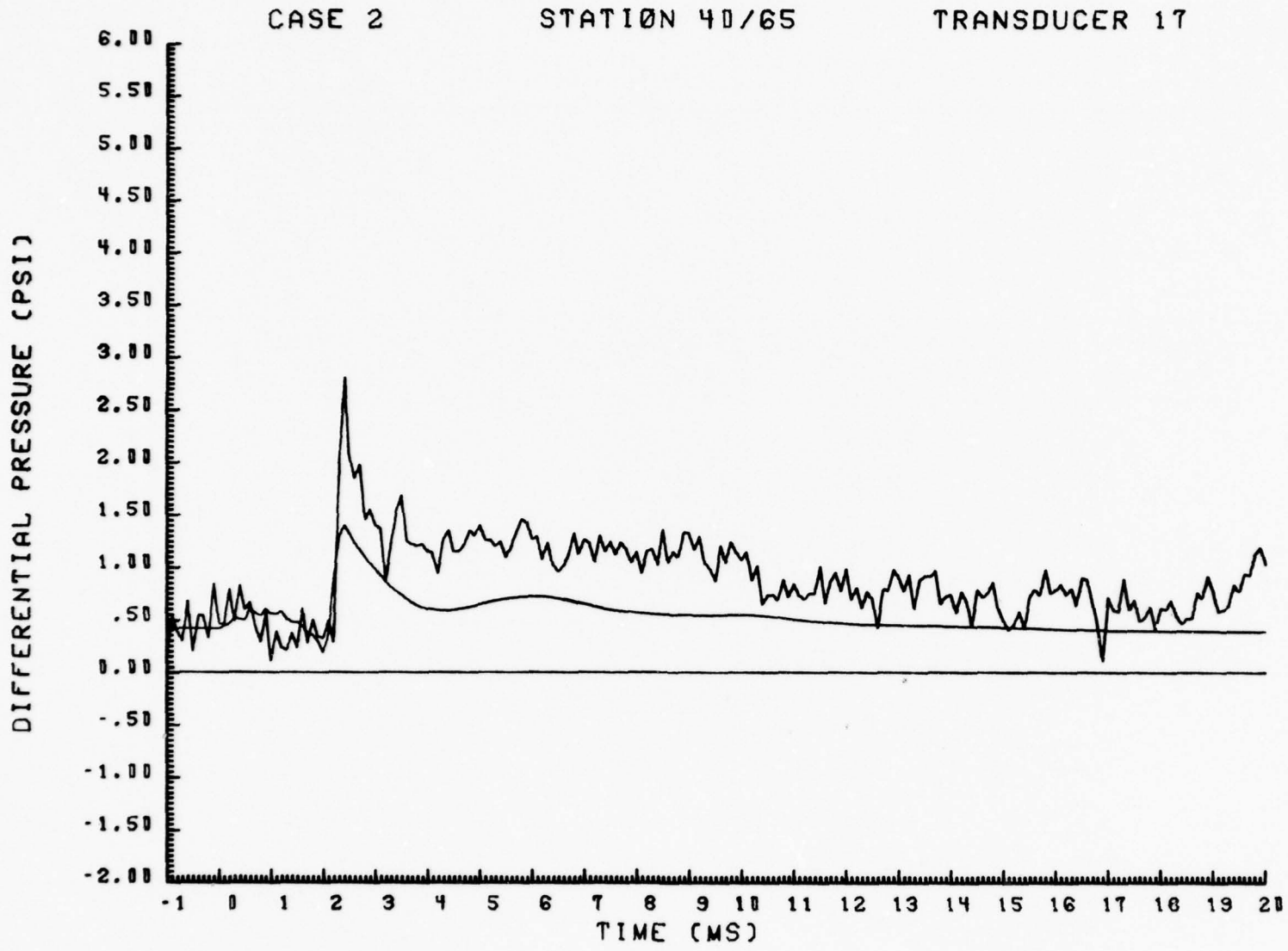


Figure 5. (Continued)

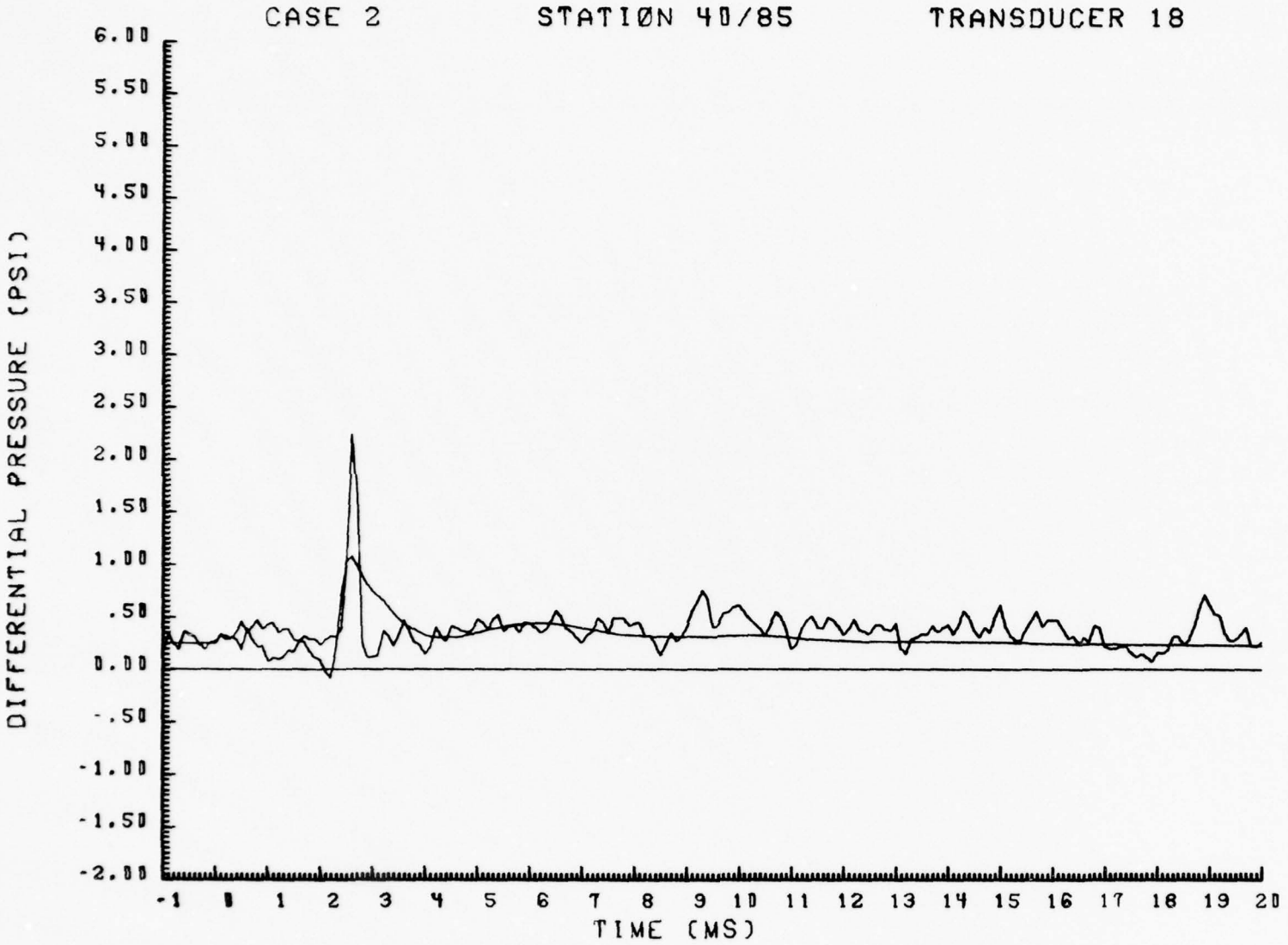


Figure 5. (Continued)

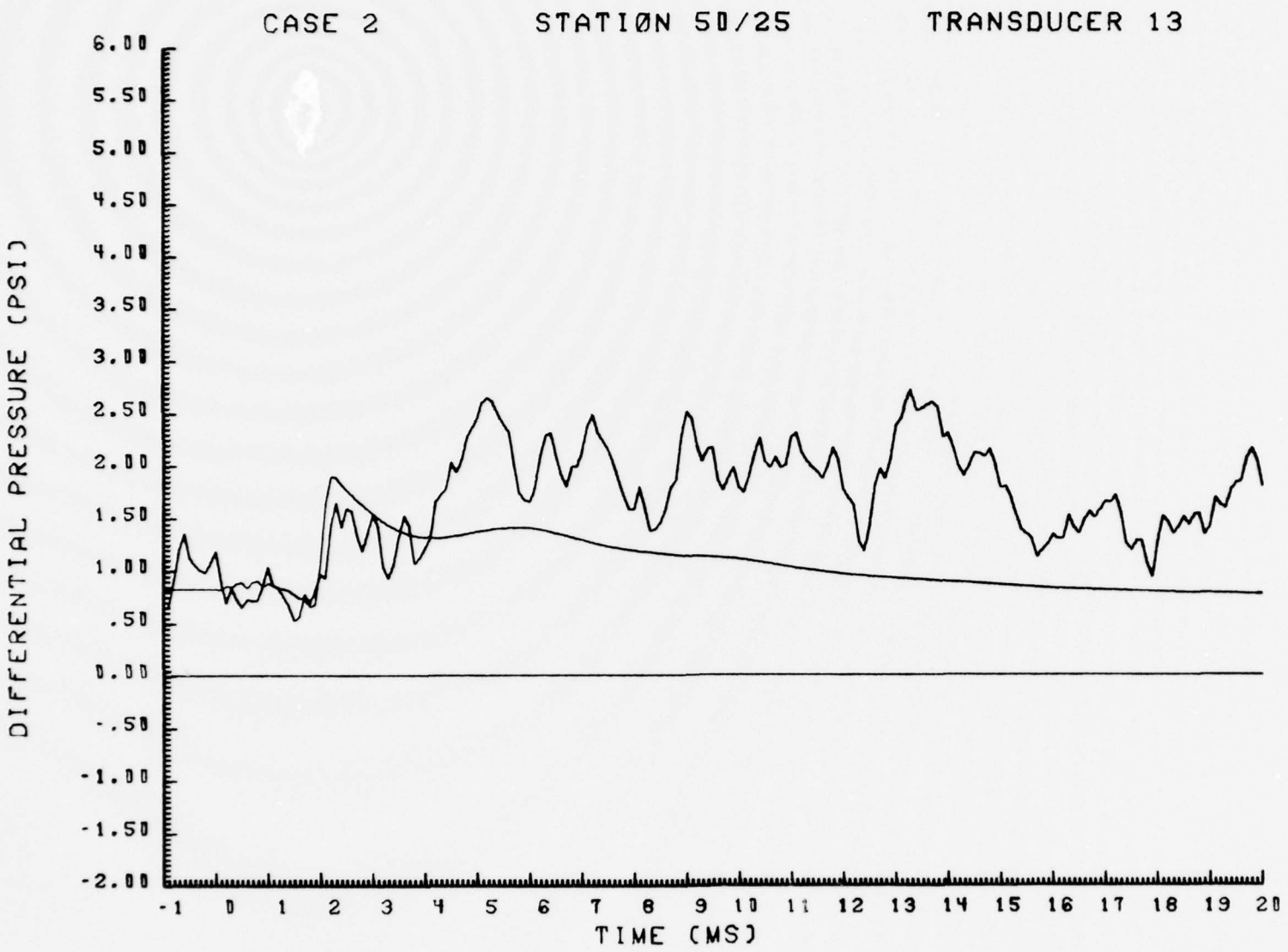


Figure 5. (Continued)

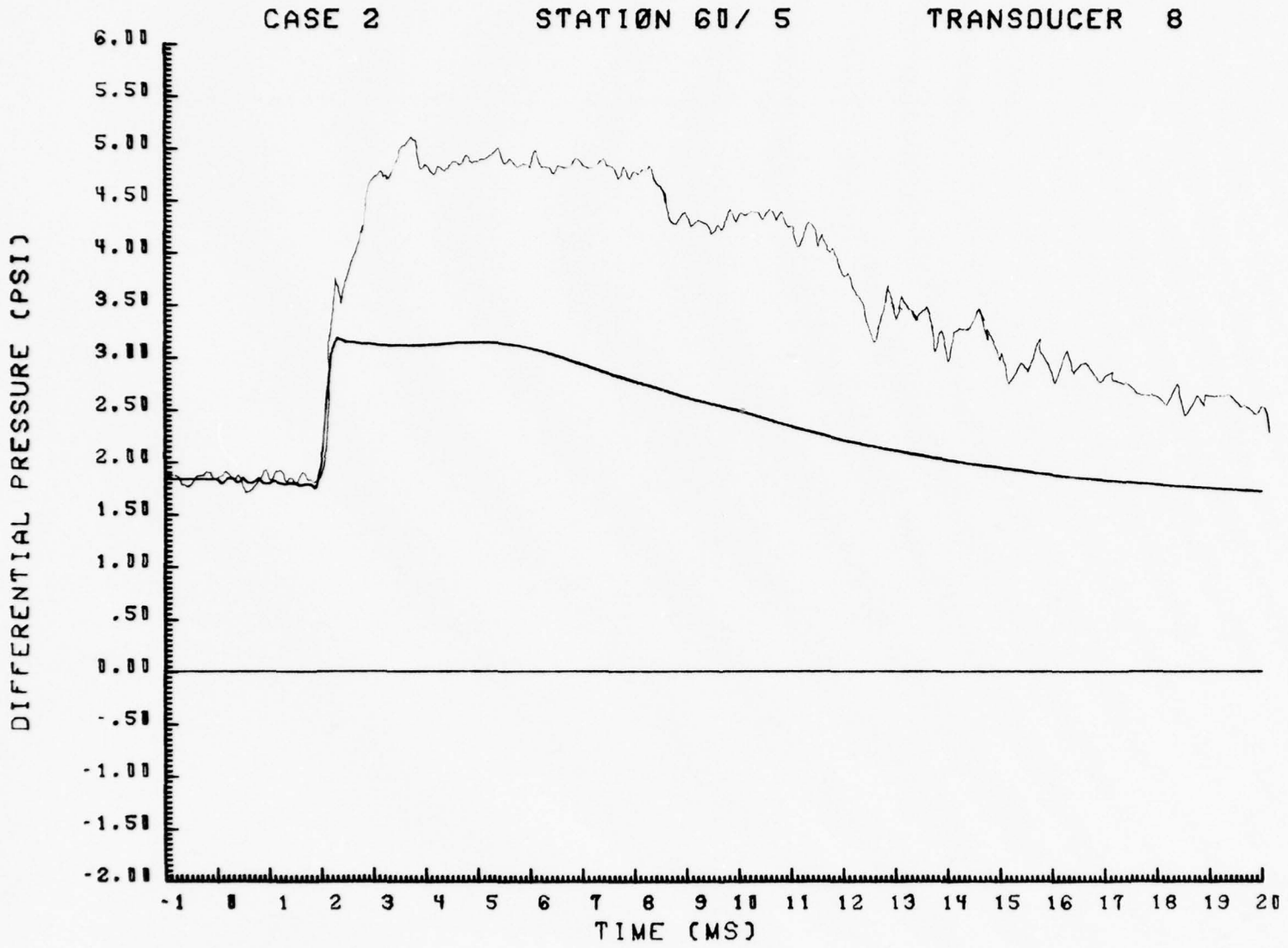


Figure 5. (Continued)

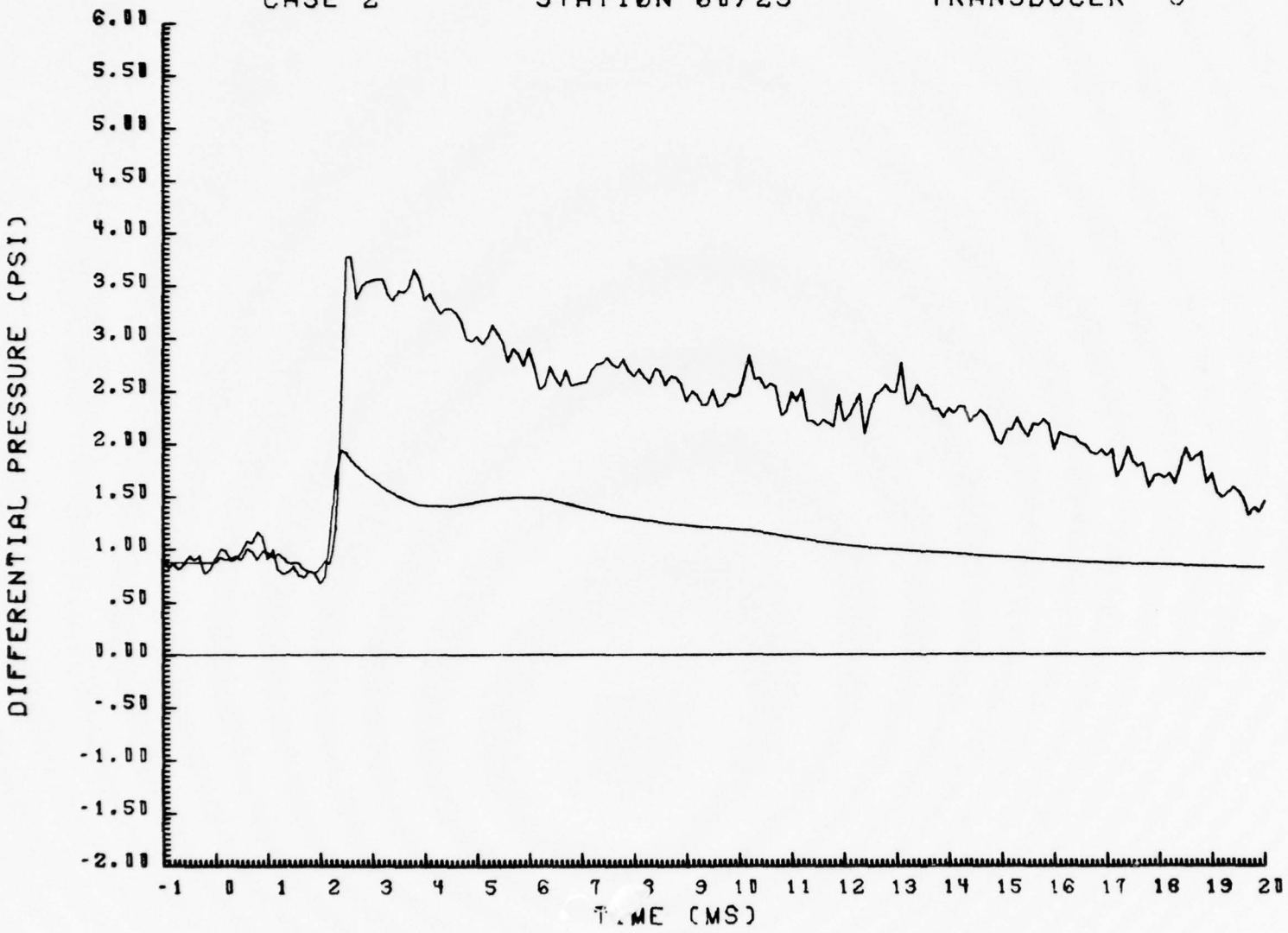


Figure 5. (Continued)

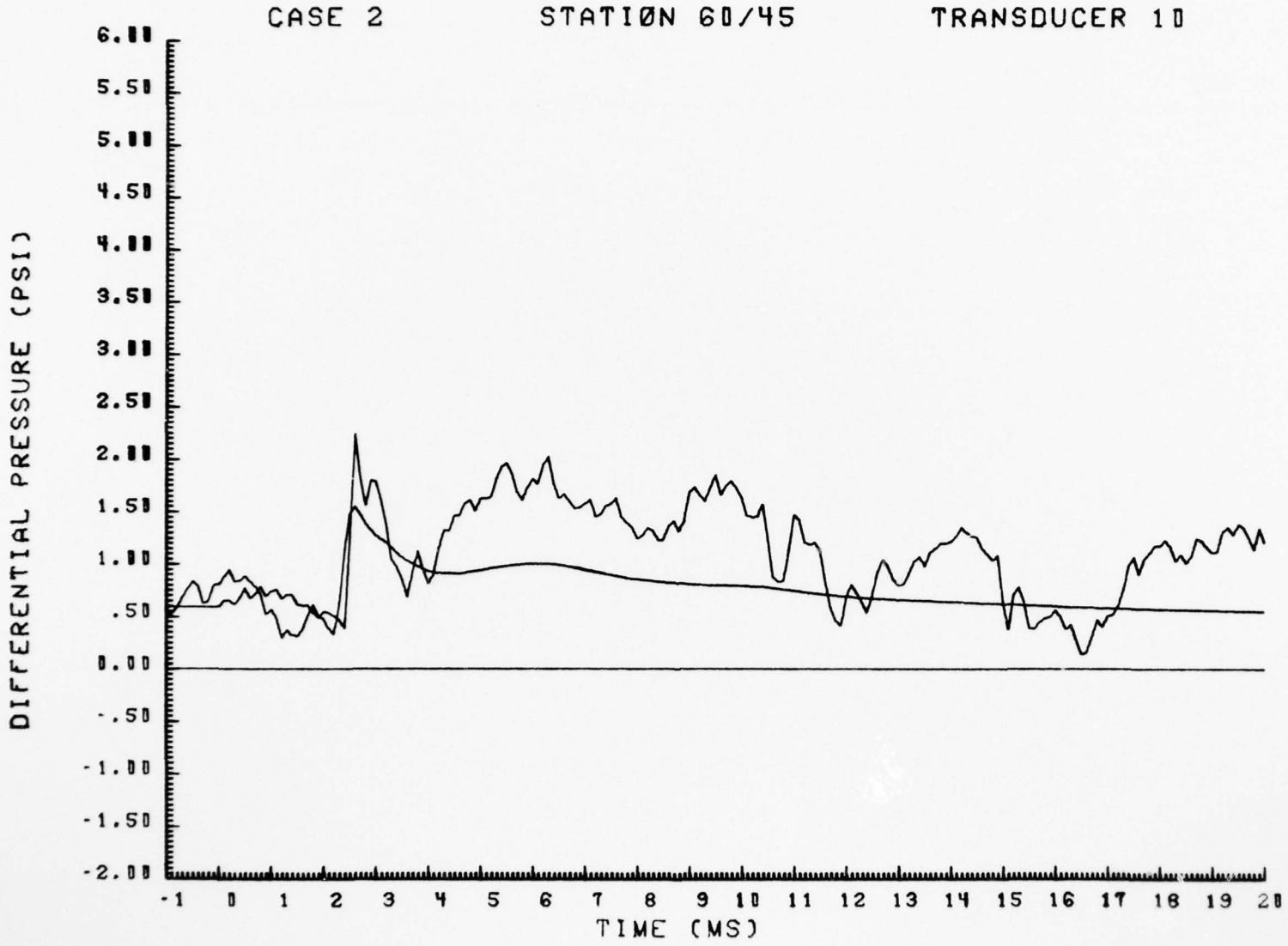


Figure 5. (Continued)

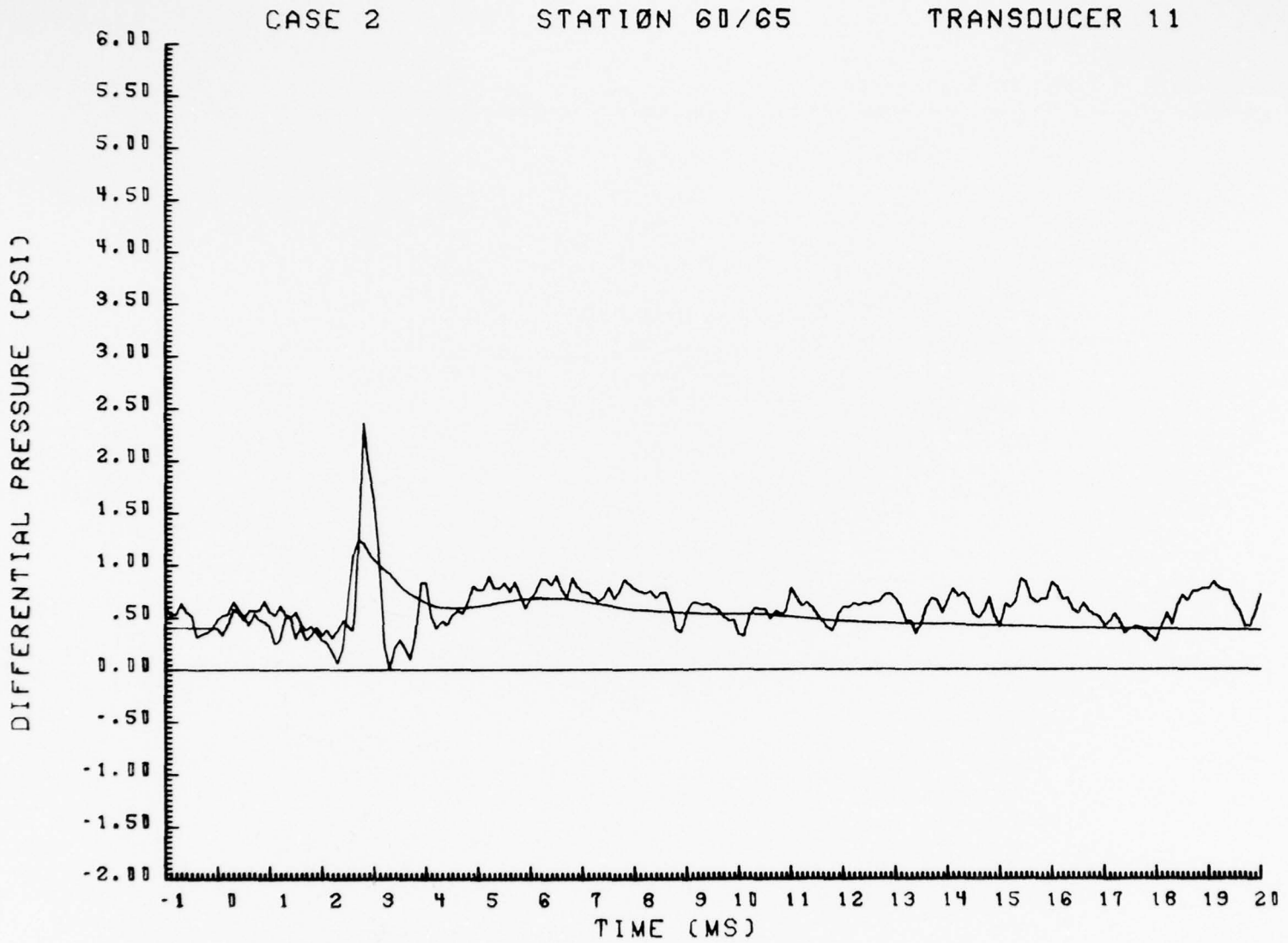


Figure 5. (Continued)

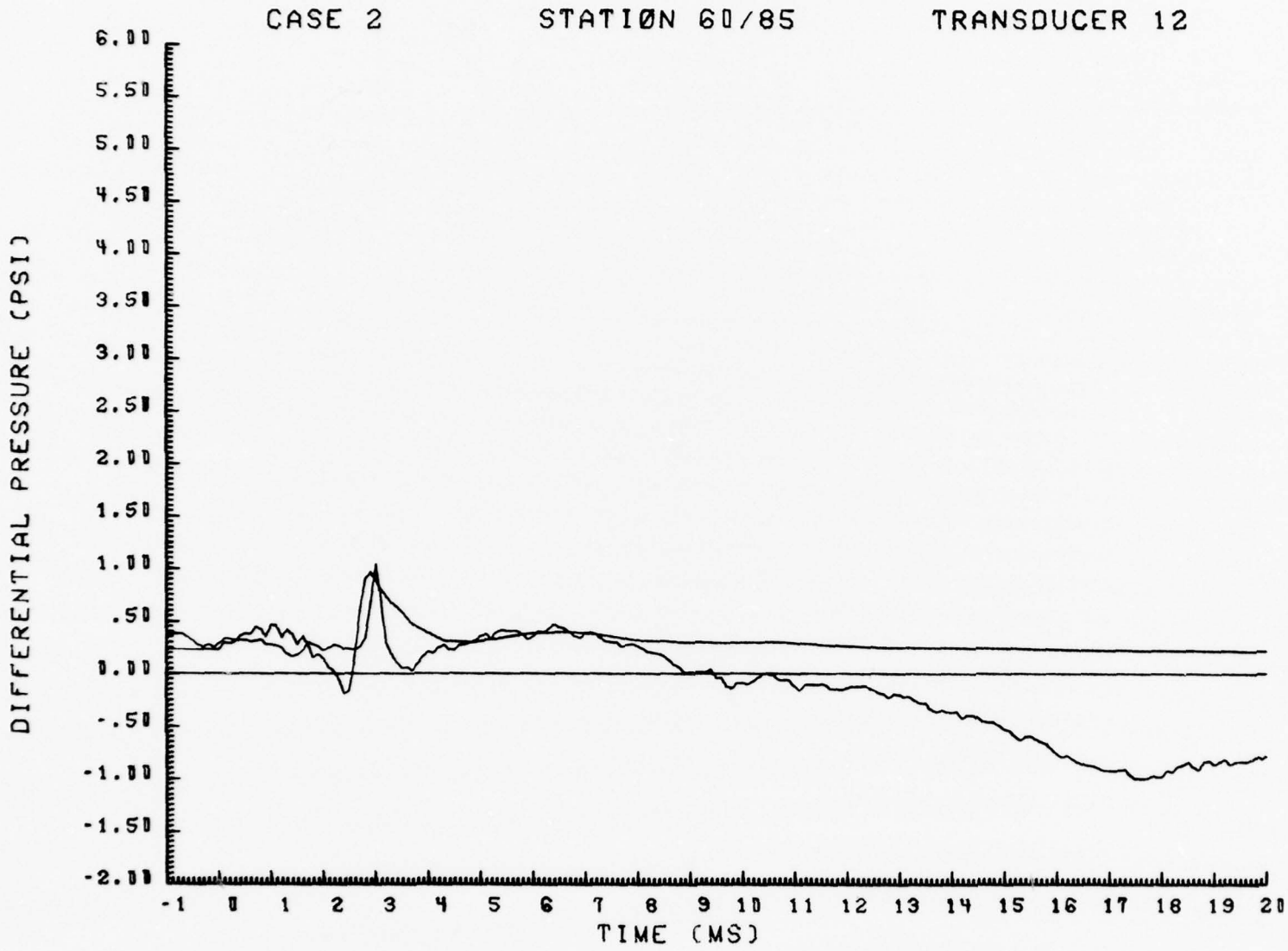


Figure 5. (Continued)

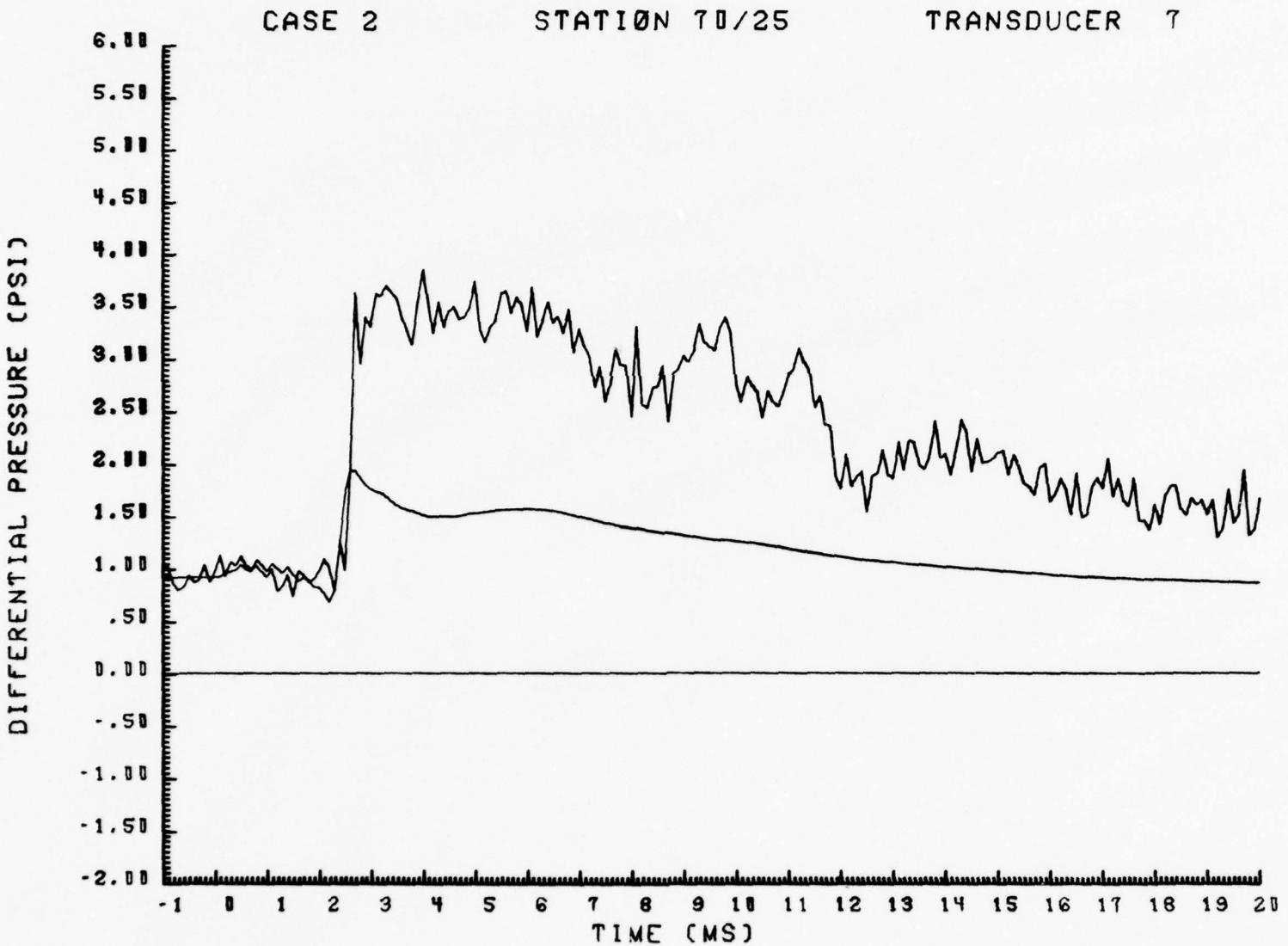


Figure 5. (Continued)

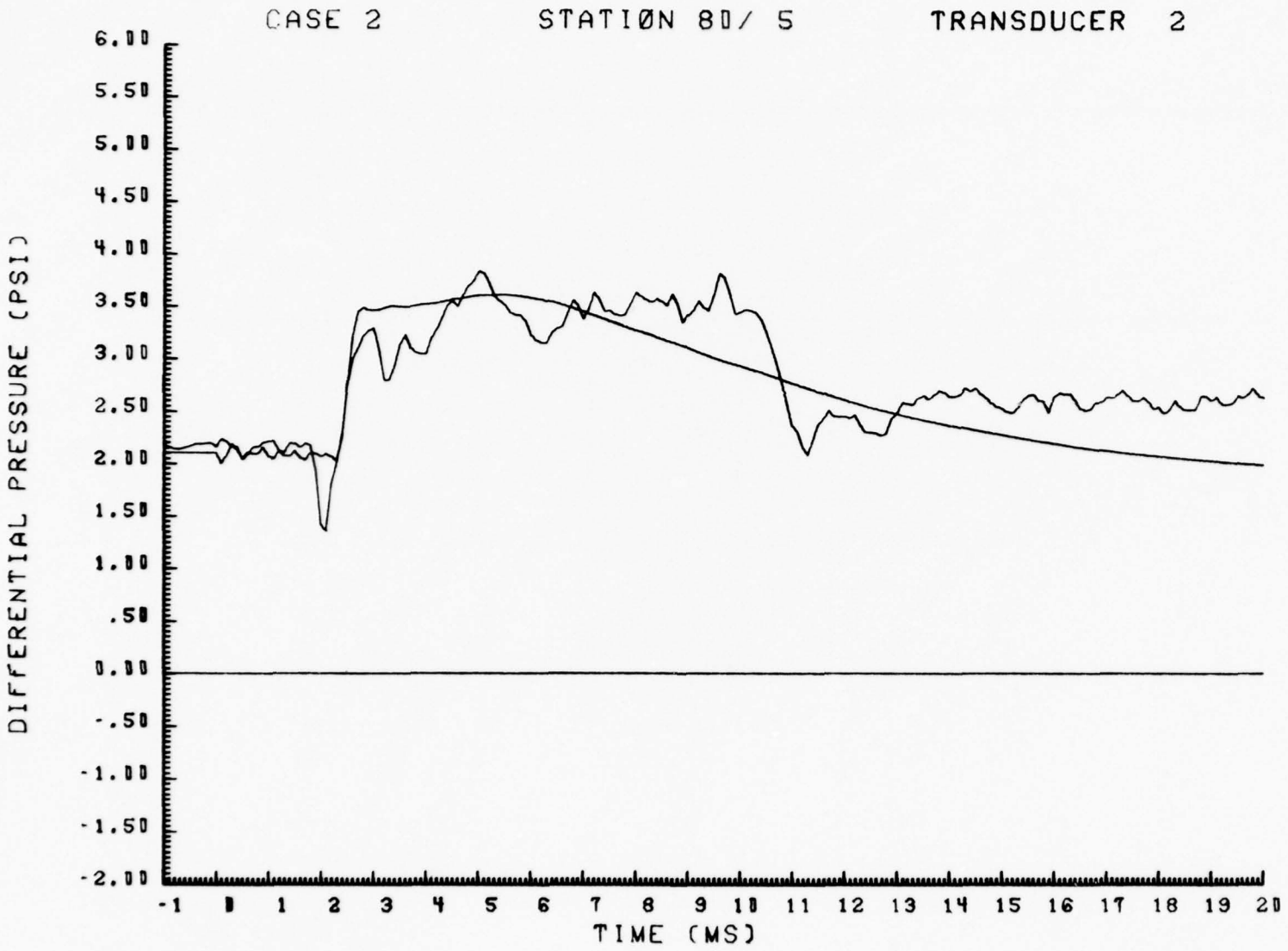


Figure 5. (Continued)

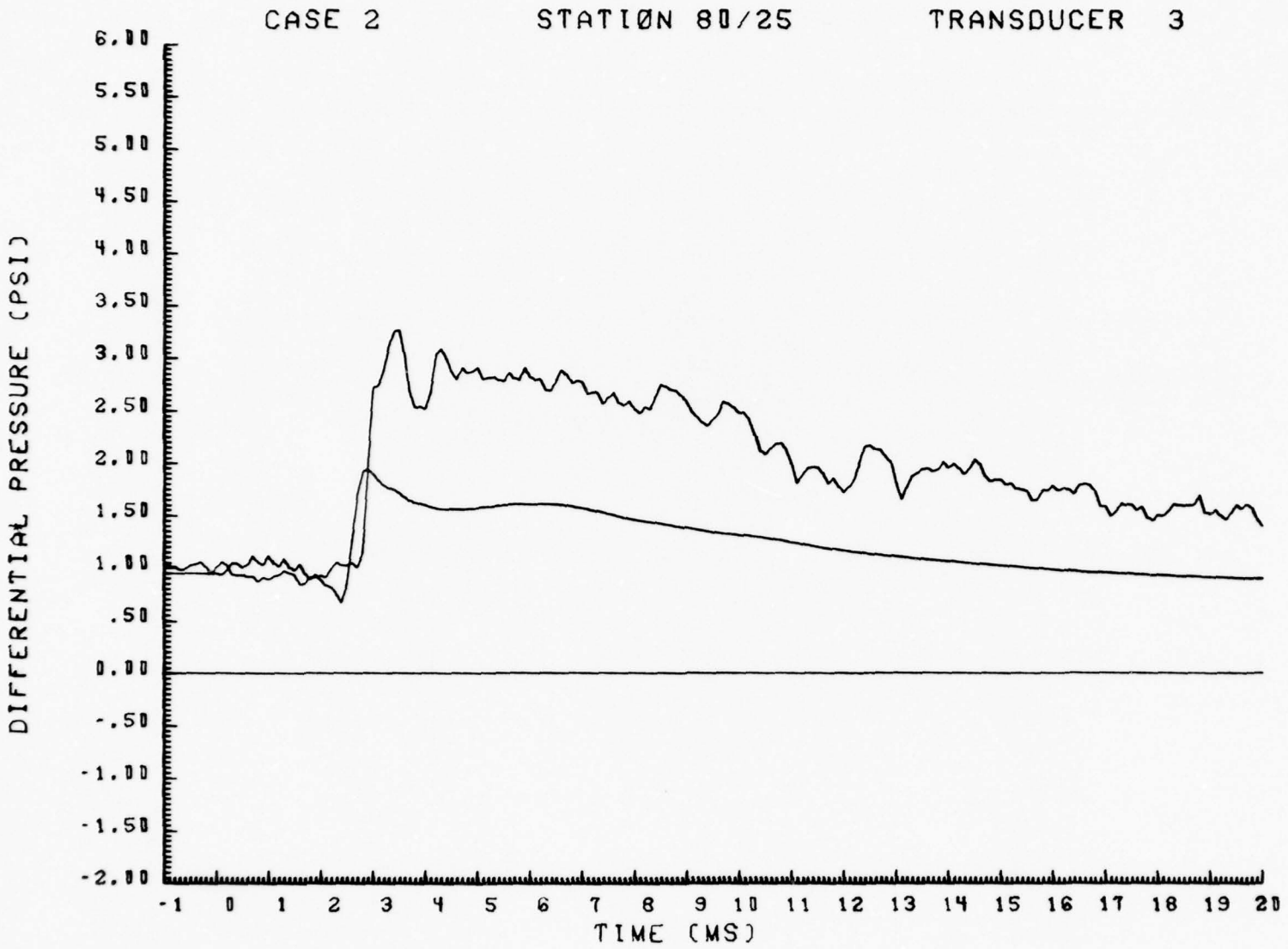


Figure 5. (Continued)

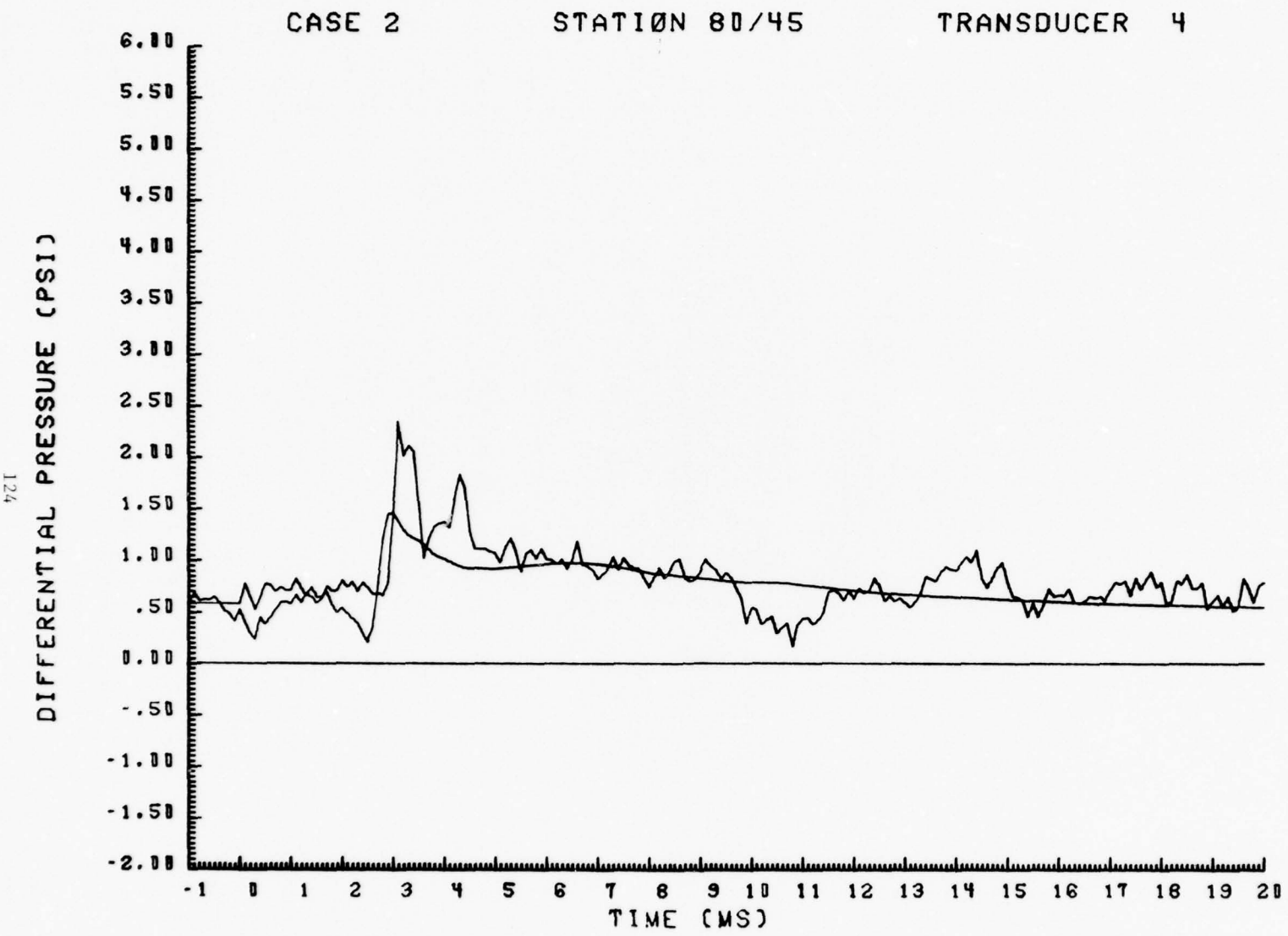


Figure 5. (Continued)

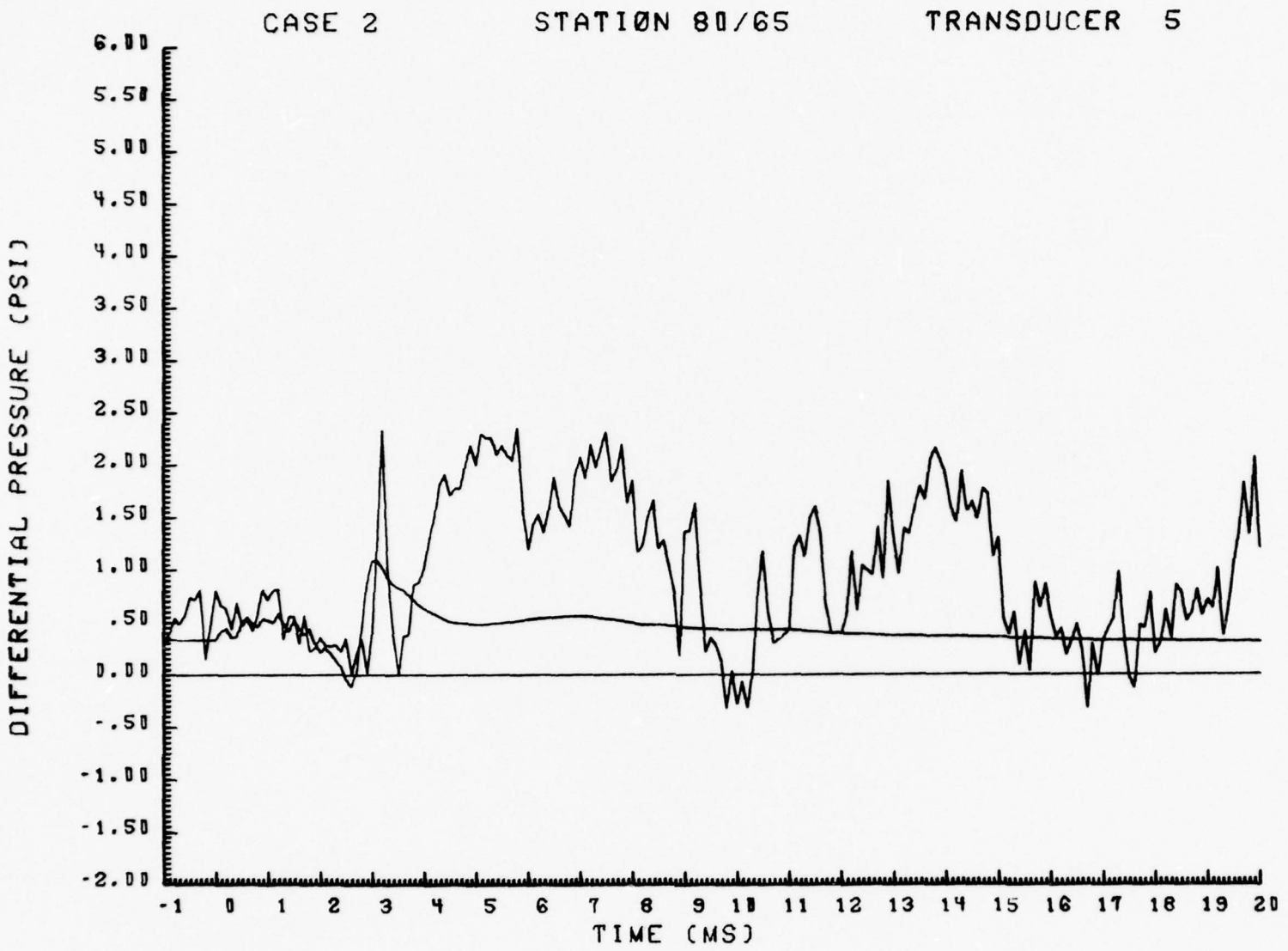


Figure 5. (Continued)

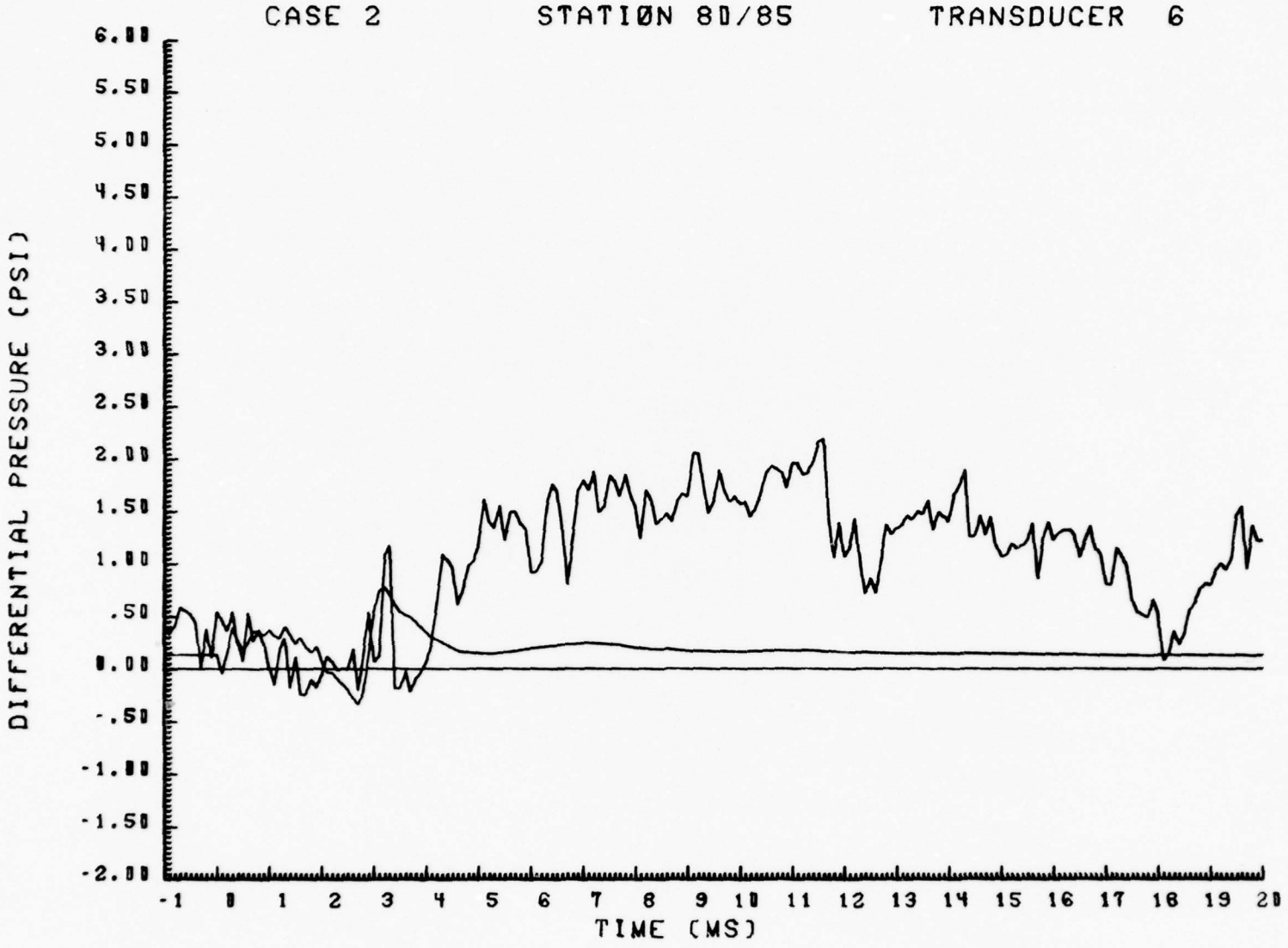


Figure 5. (Continued)

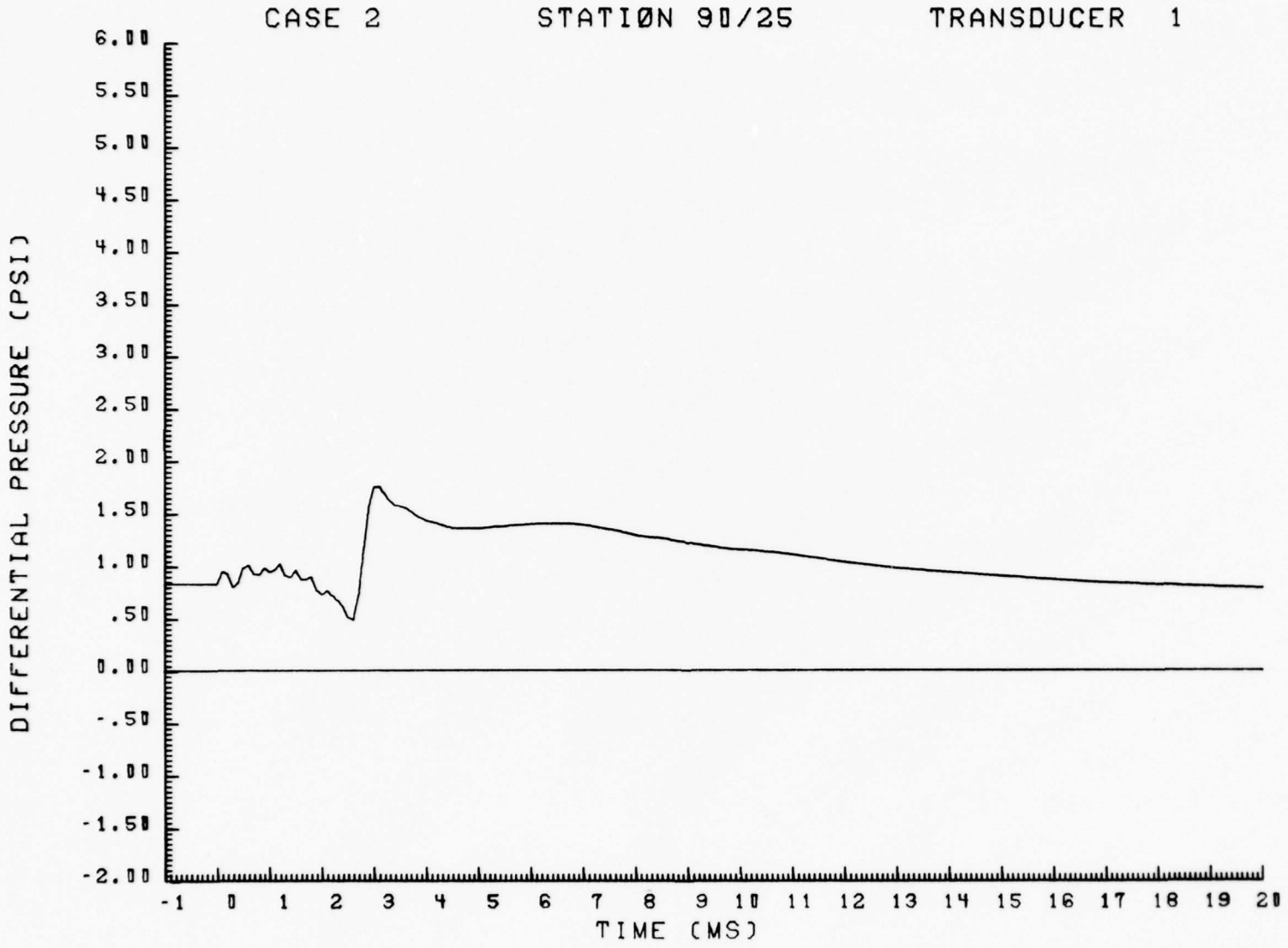


Figure 5. (Concluded)

Figure 6. Time-Variations of Pressure Loadings at Transducer Locations. Predictions From VIBRA-6 Compared With Experiment.

Case 5 - $\phi$ = 20.1 deg, $\Delta p_s$=3.56 psi. (9B-A3-1)

——————— VIBRA-6

~~~~~~~~ Test Data
~~~~~~~~

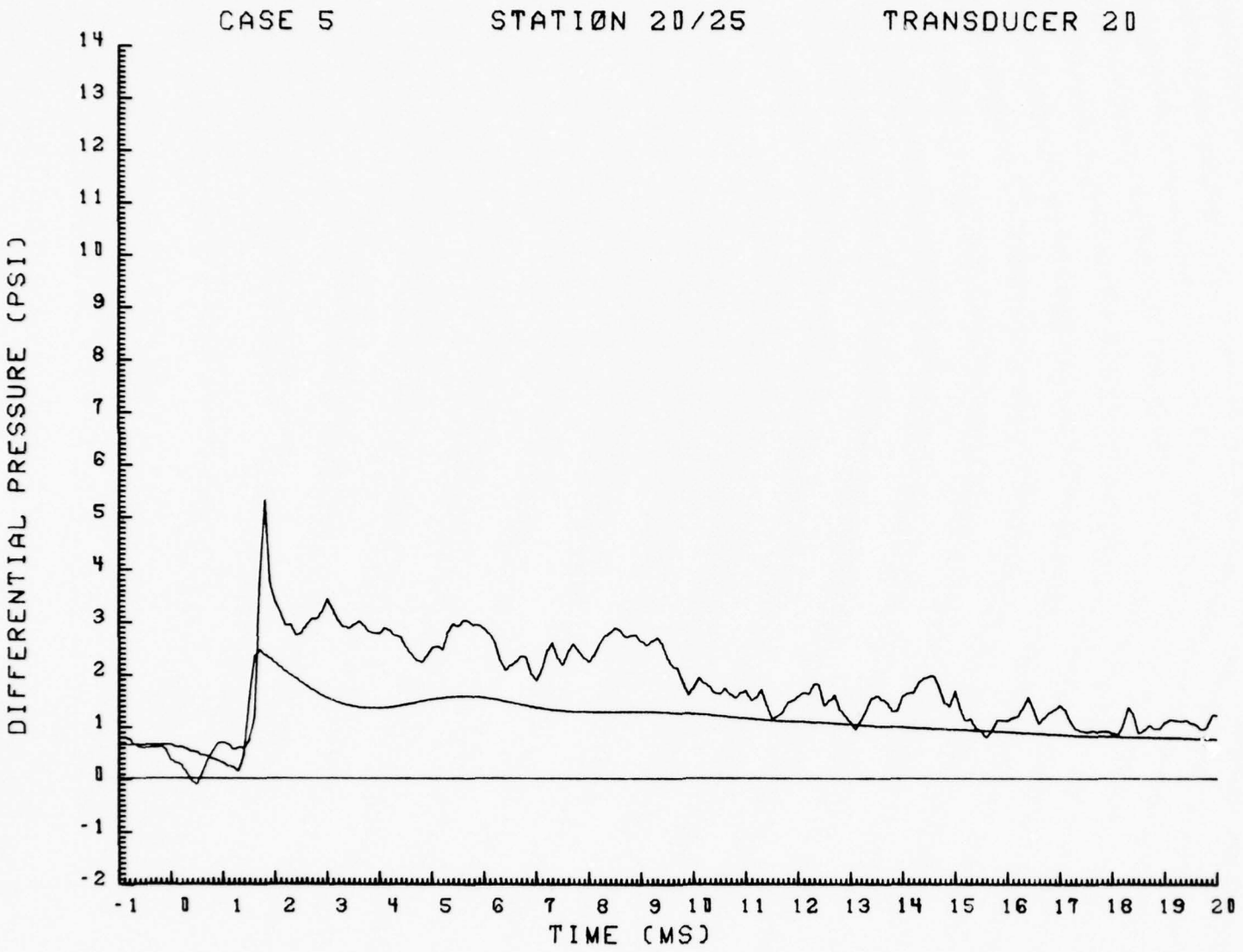
CASE 5
STATIØN 20/25
TRANSDUCER 20
DIFFERENTIAL PRESSURE (PSI)
14
13
12
11
10
9
8
7
6
5
4
3
2
1
0
-1
-2
-1 0 1 2 3 4 5 6 7 8 9 10 11 12 13 14 15 16 17 18 19 20
TIME (MS)

Figure 6

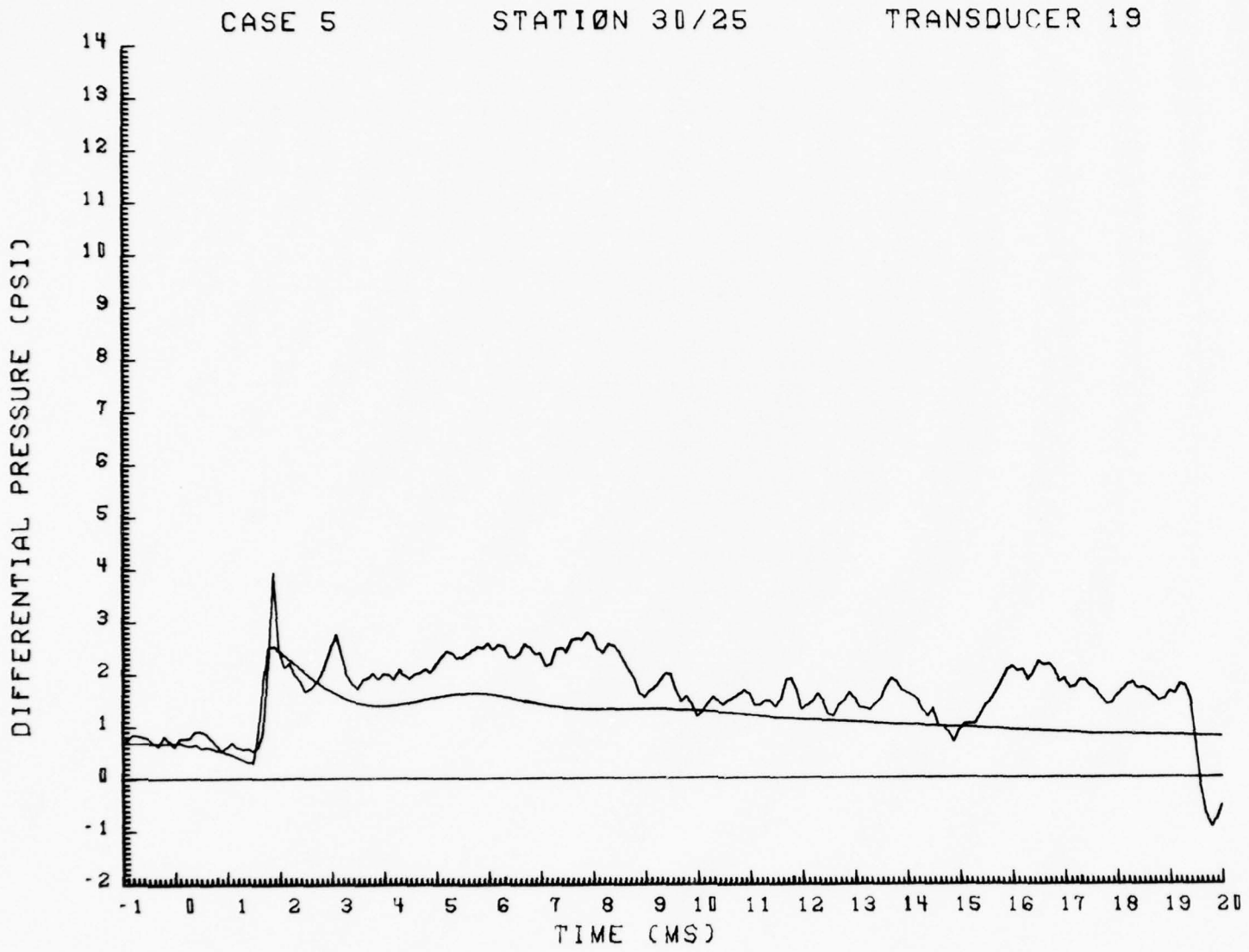


Figure 6. (Continued)

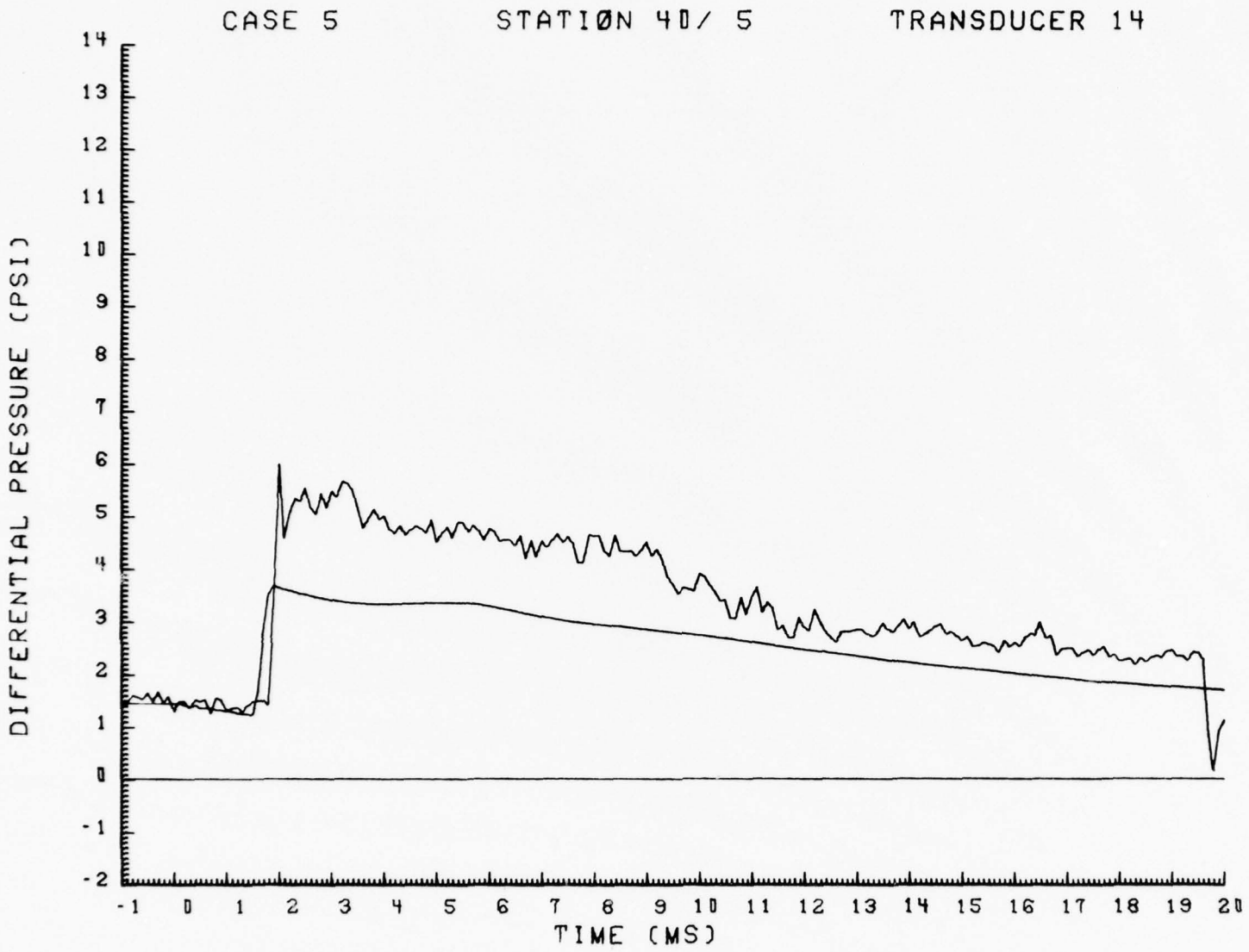


Figure 6. (Continued)

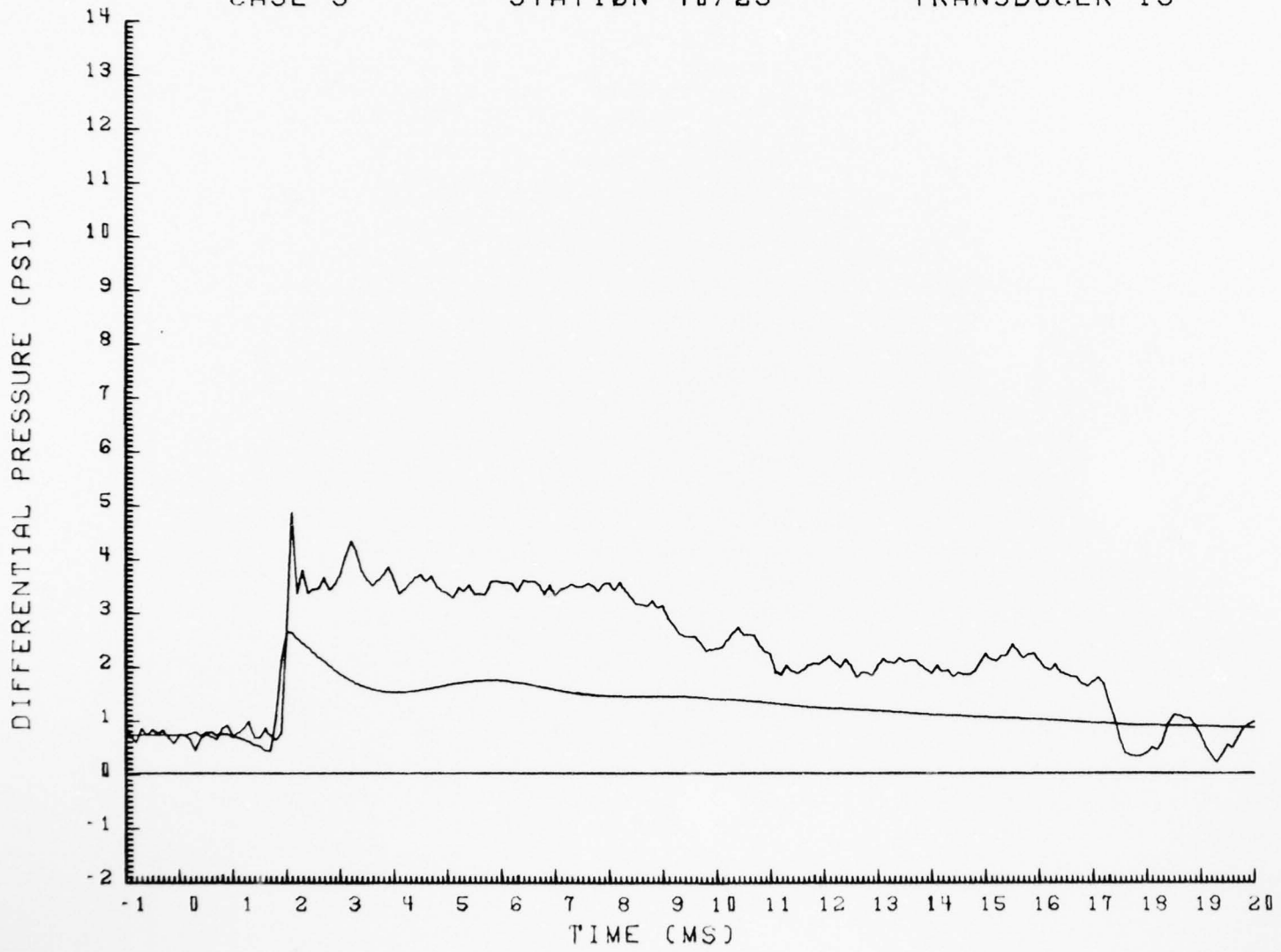


Figure 6. (Continued)

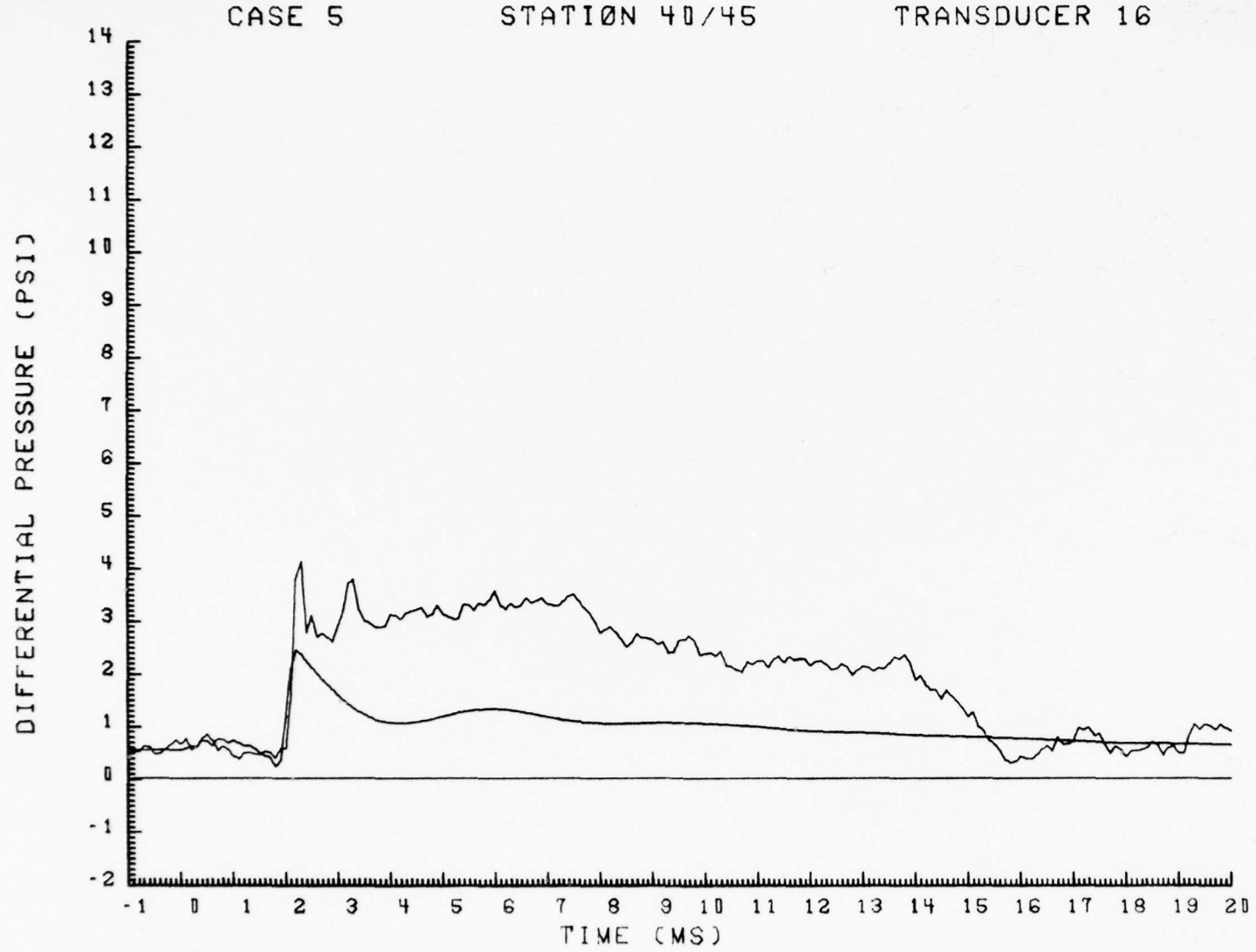


Figure 6. (Continued)

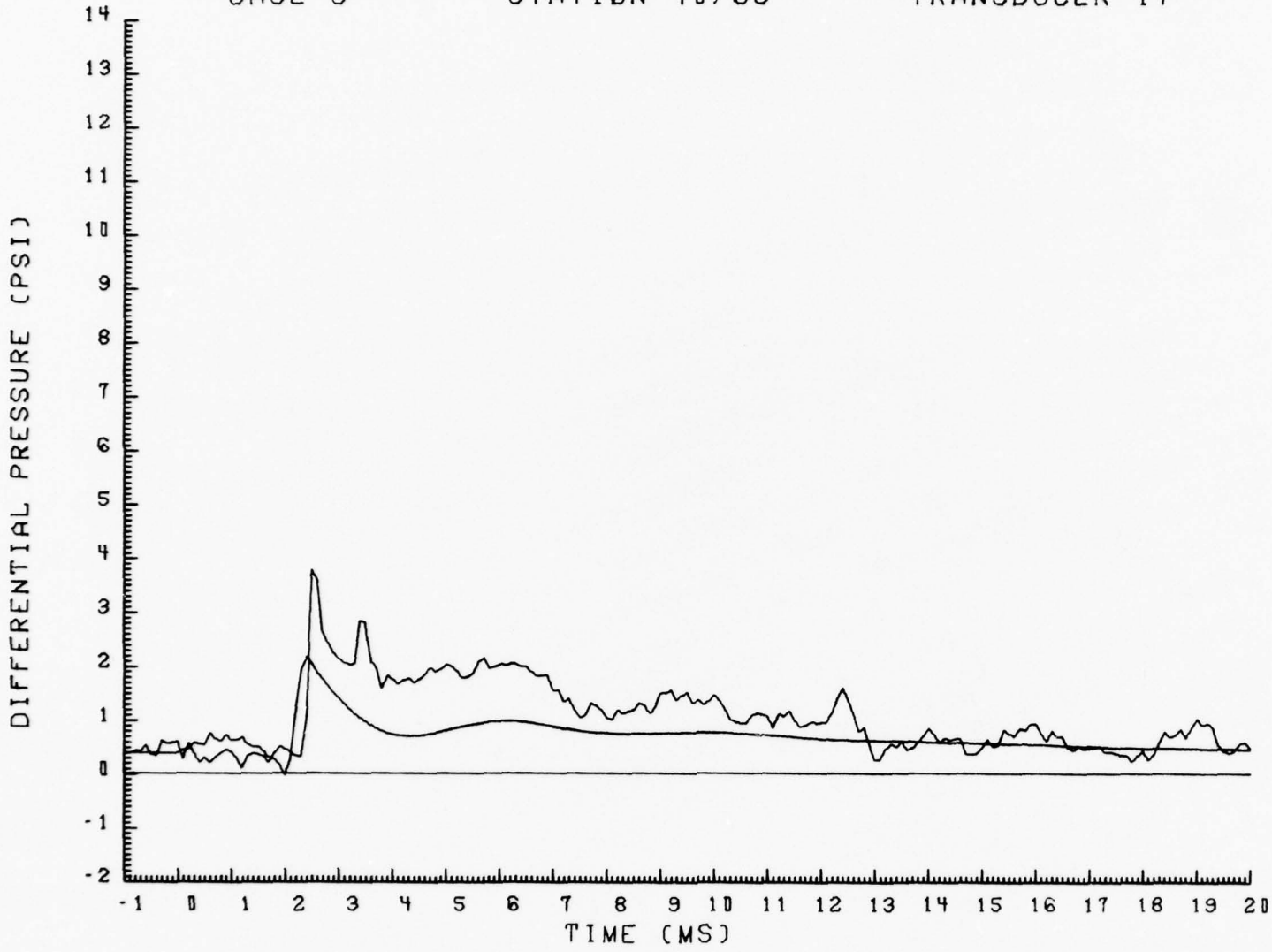


Figure 6. (Continued)

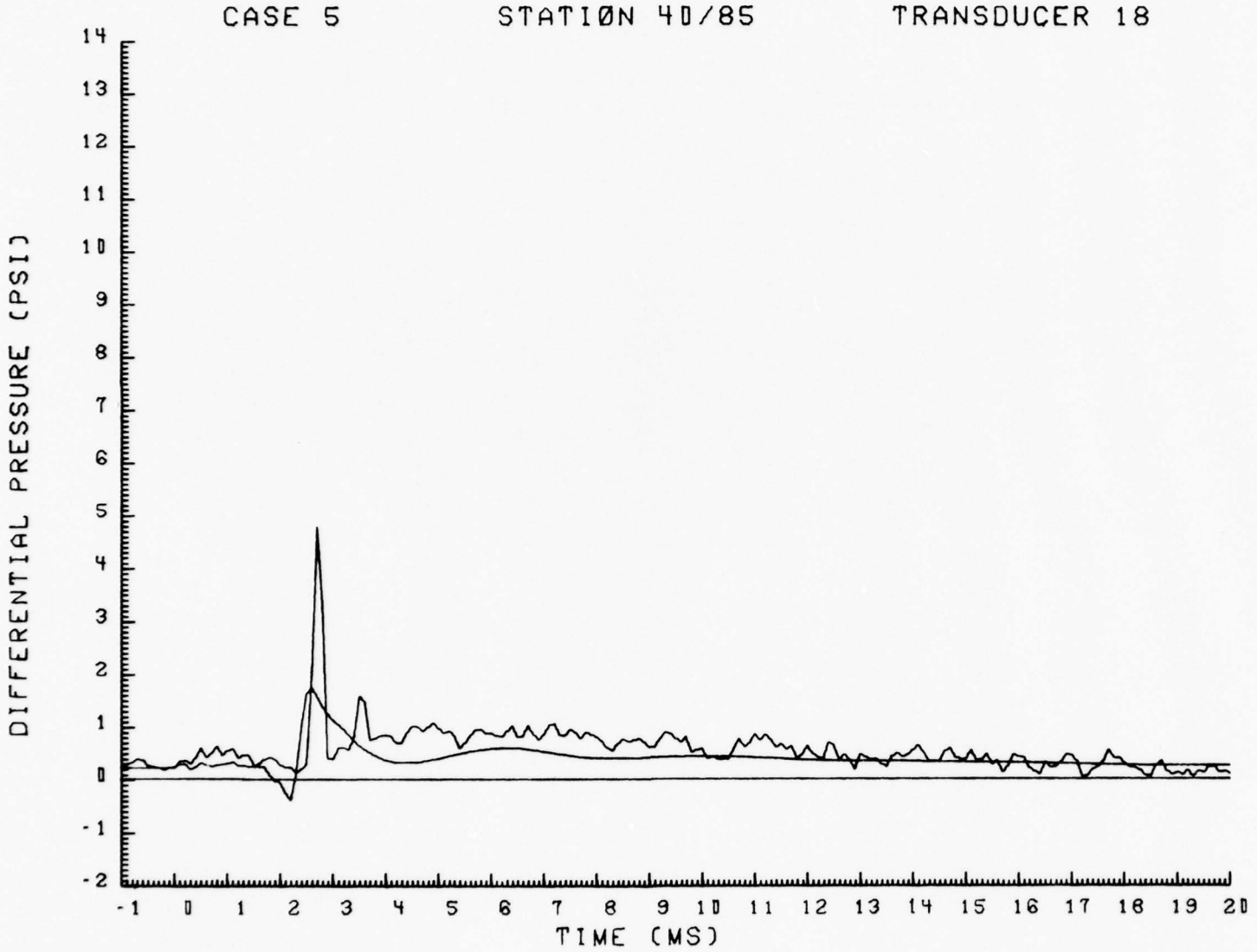


Figure 6. (Continued)

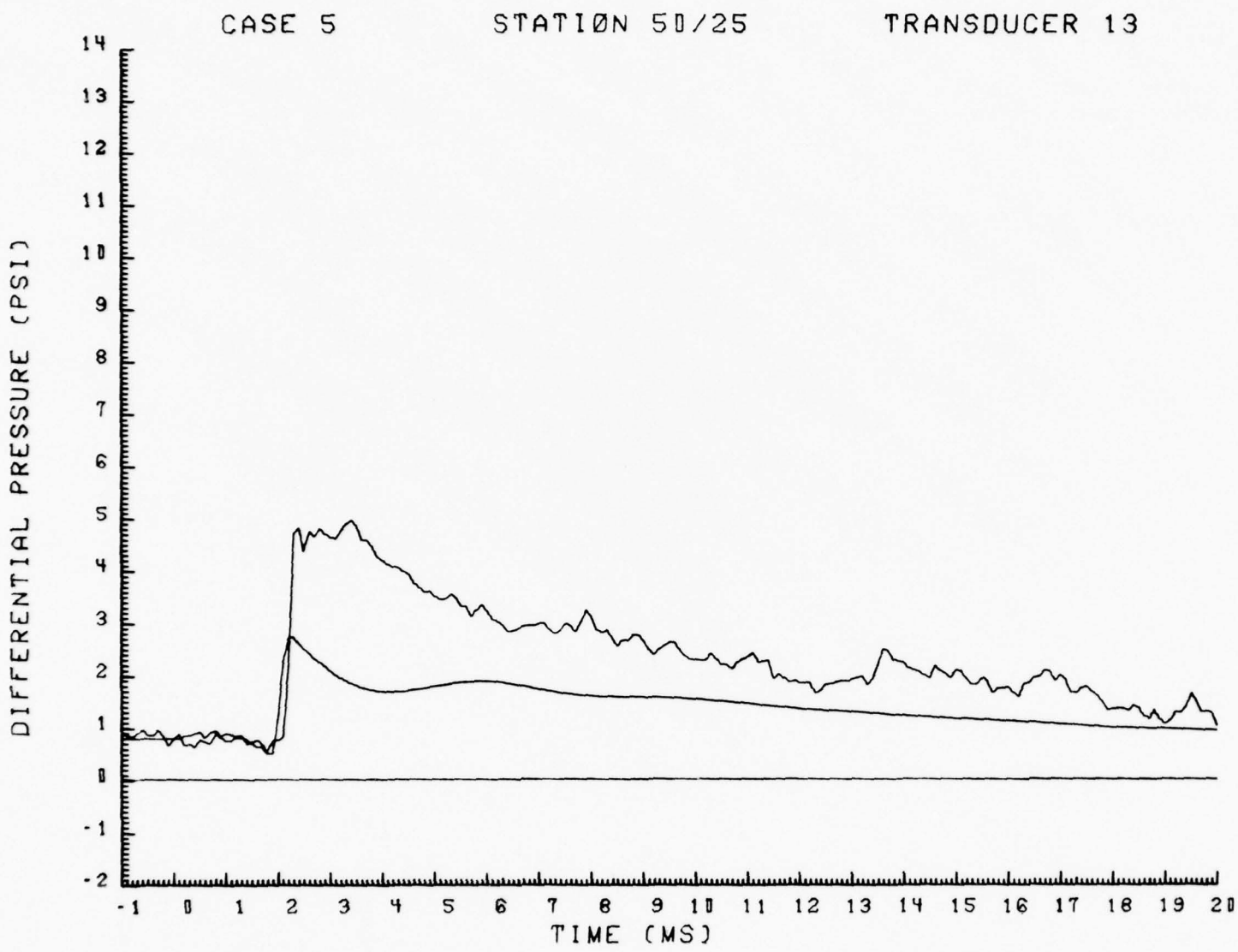


Figure 6. (Continued)

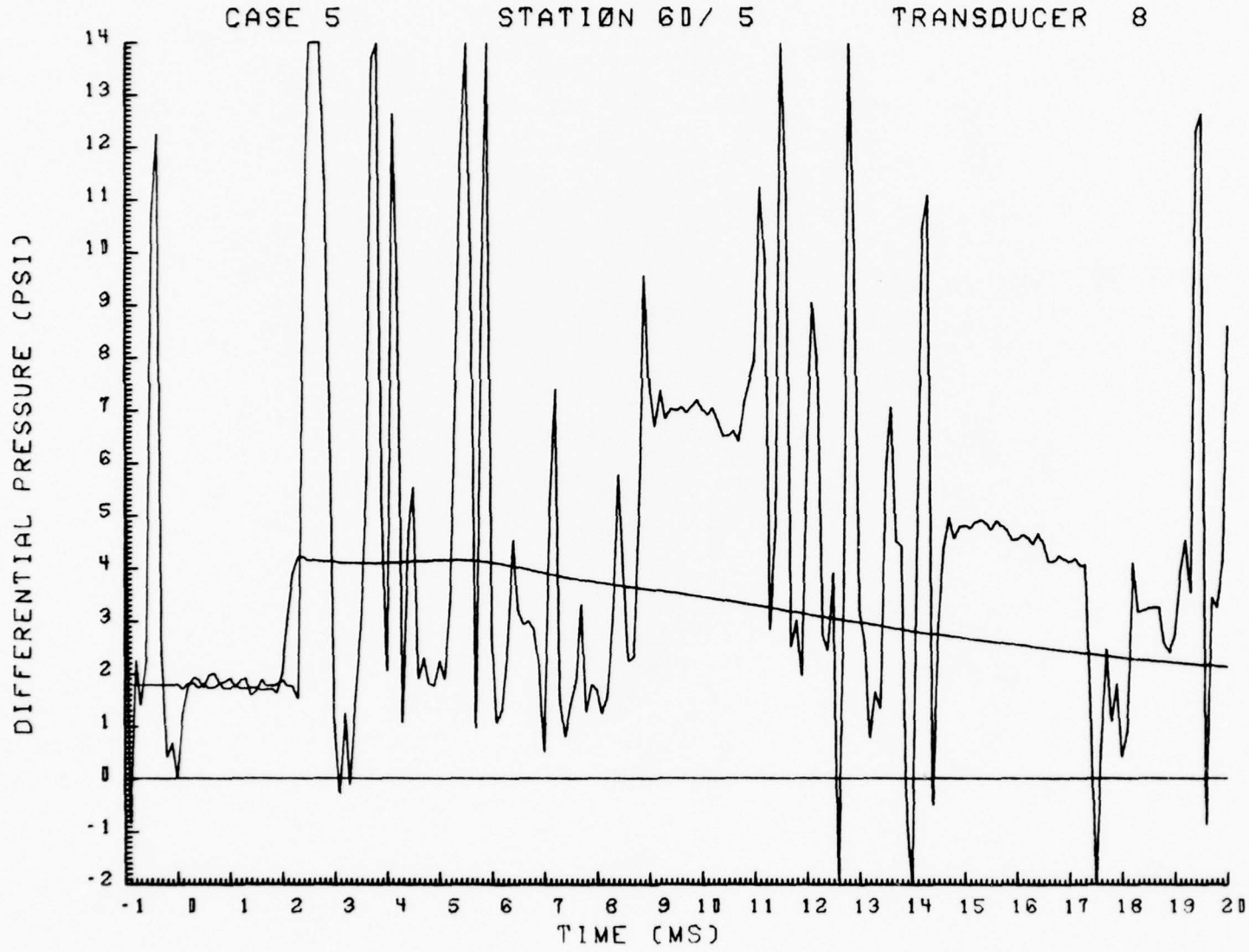


Figure 6. (Continued)

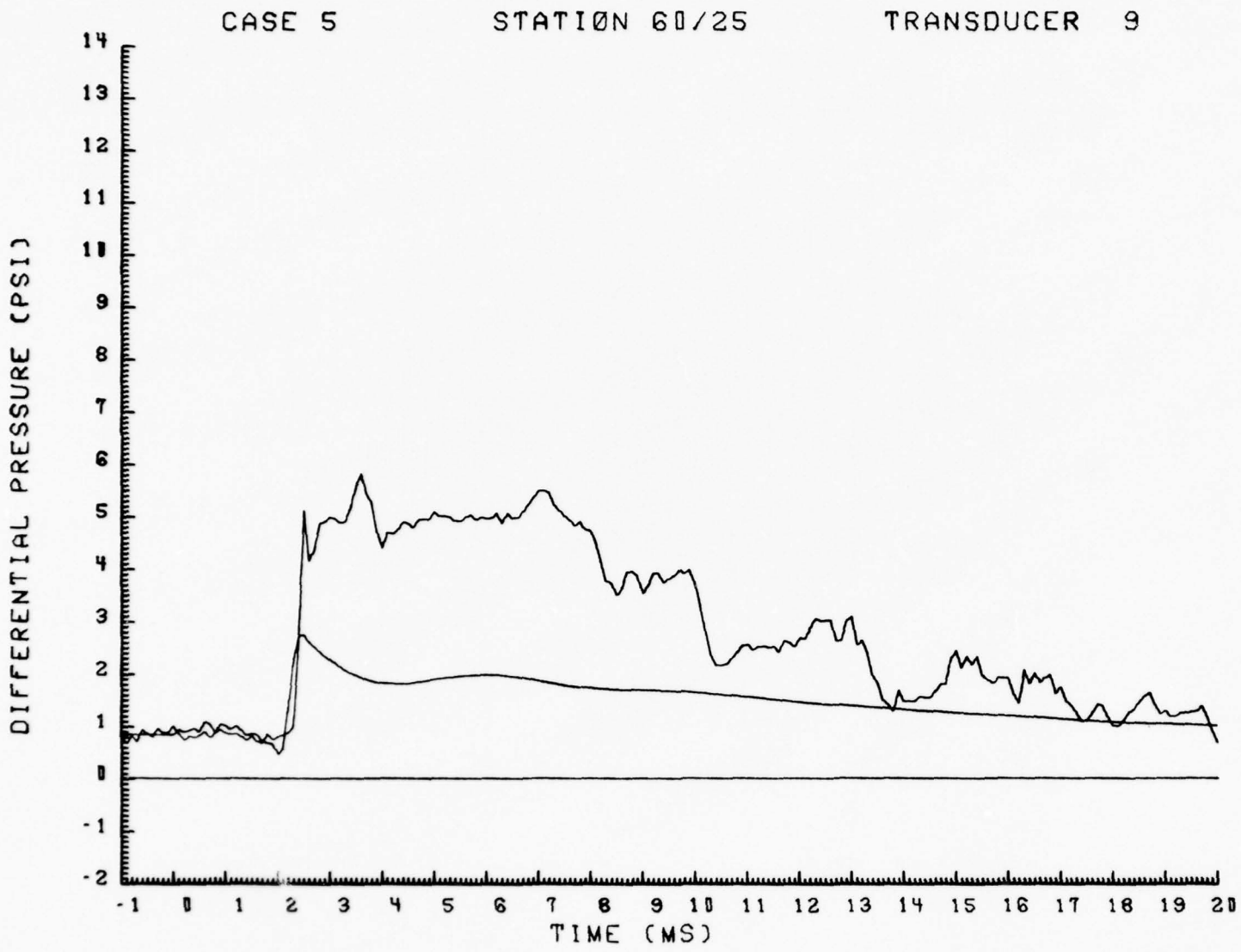


Figure 6. (Continued)

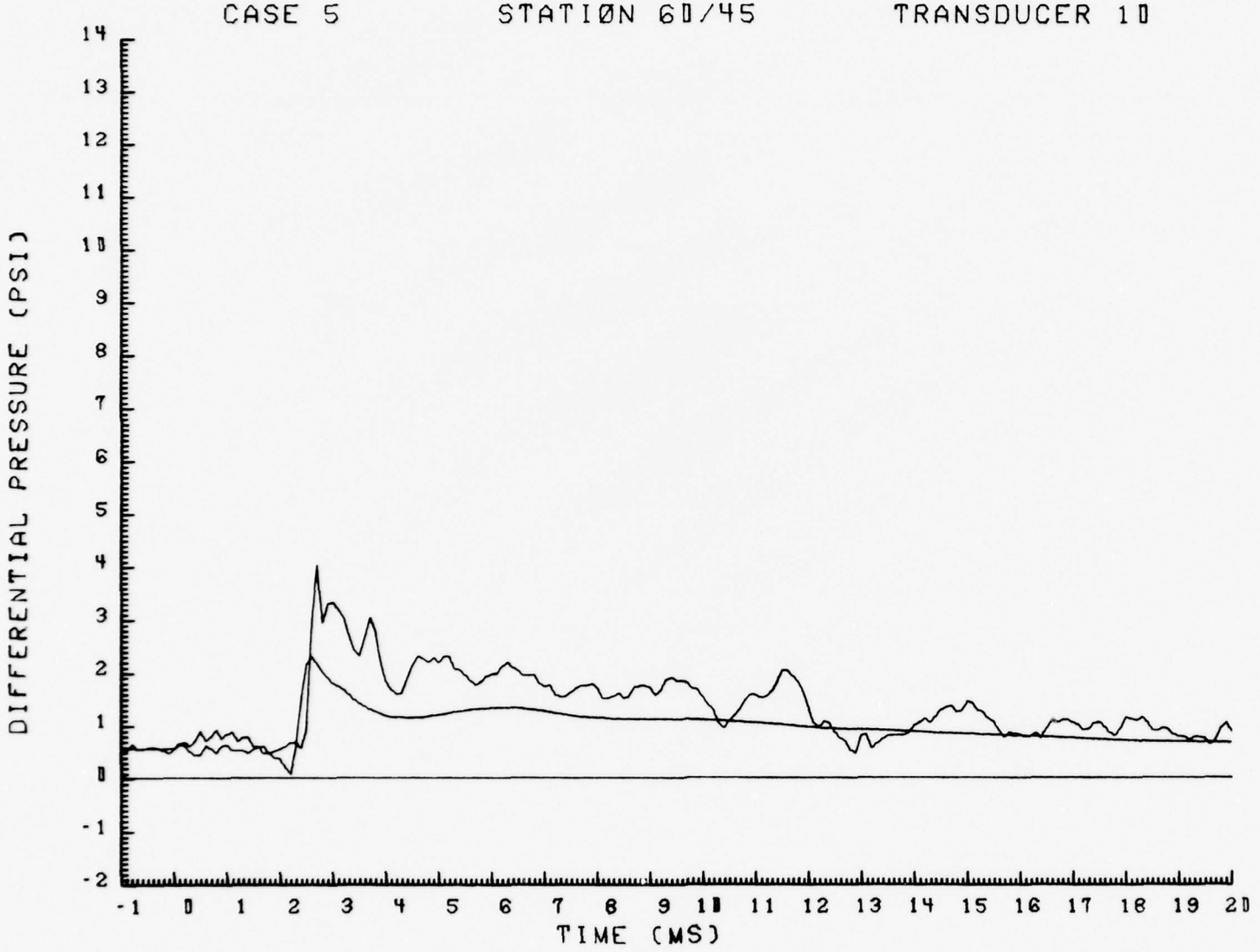


Figure 6. (Continued)

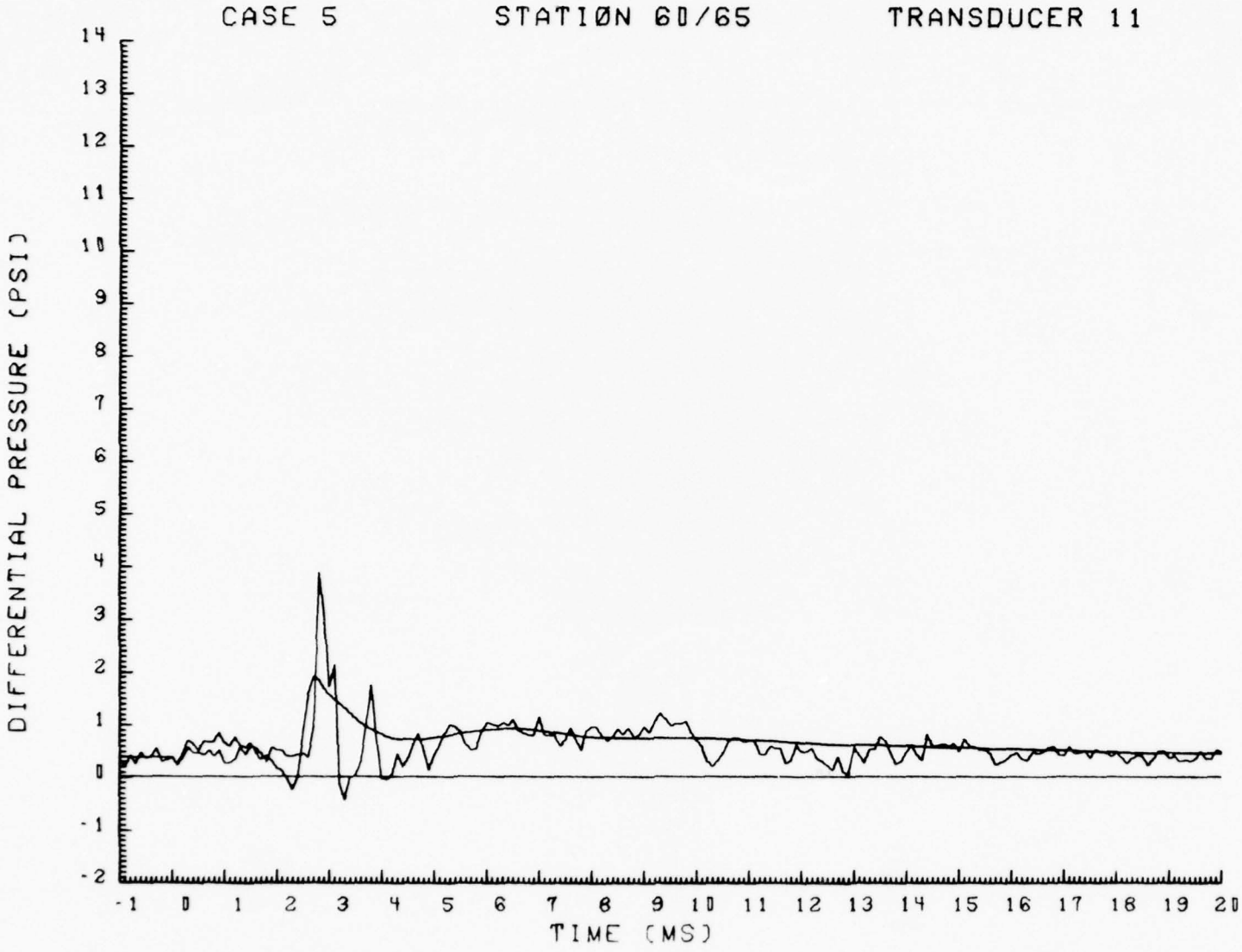


Figure 6. (Continued)

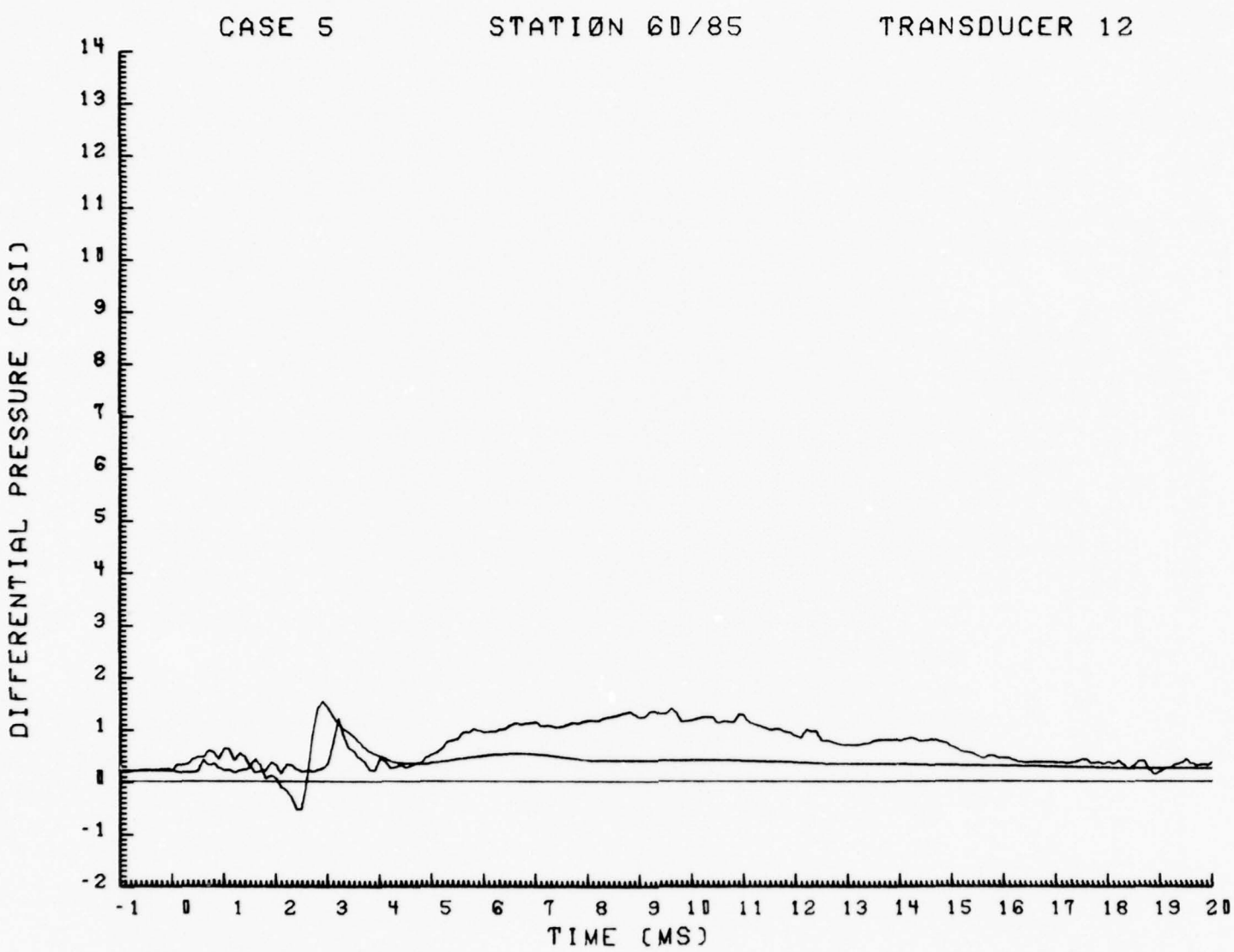


Figure 6. (Continued)

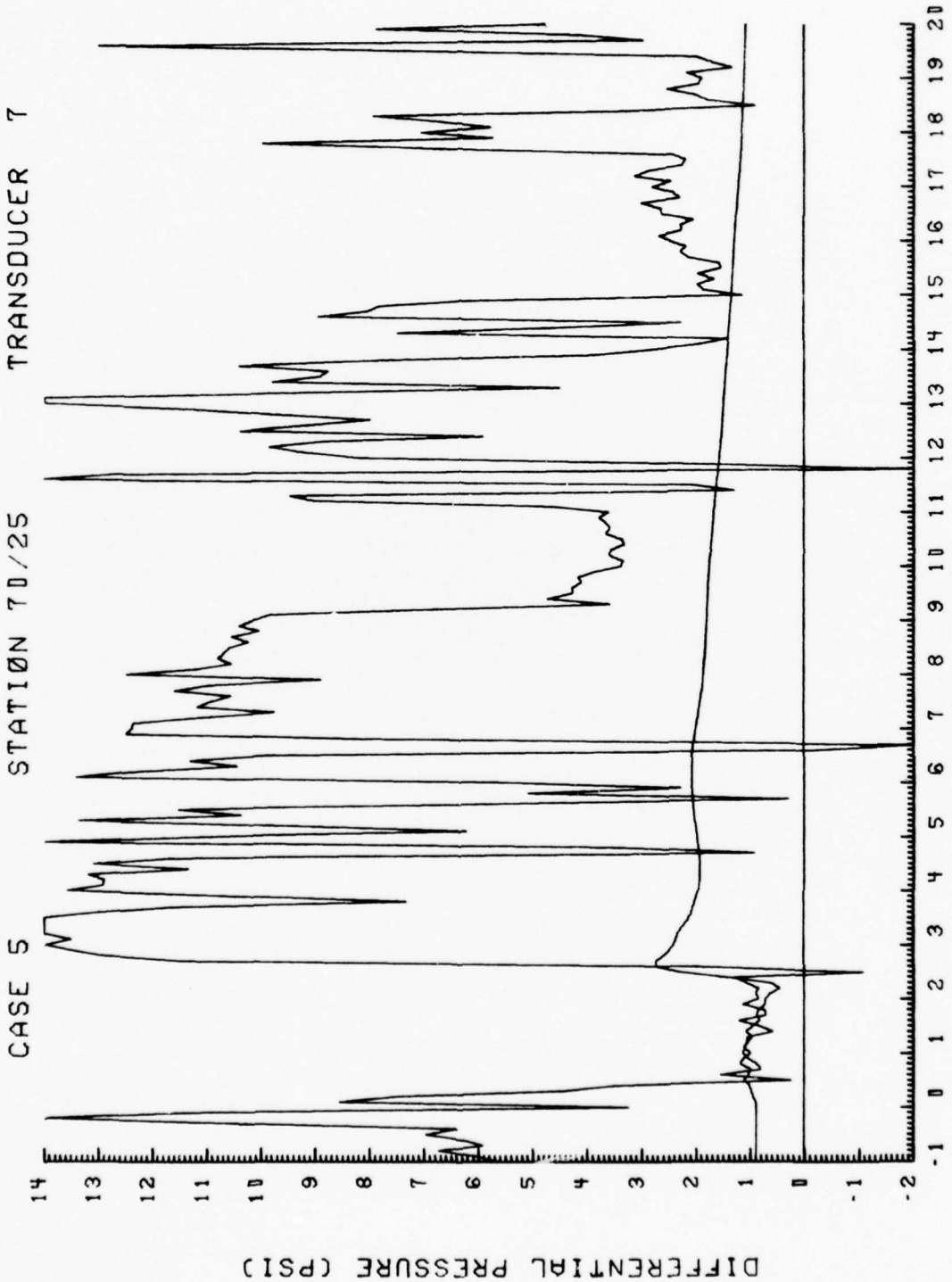


Figure 6. (Continued)

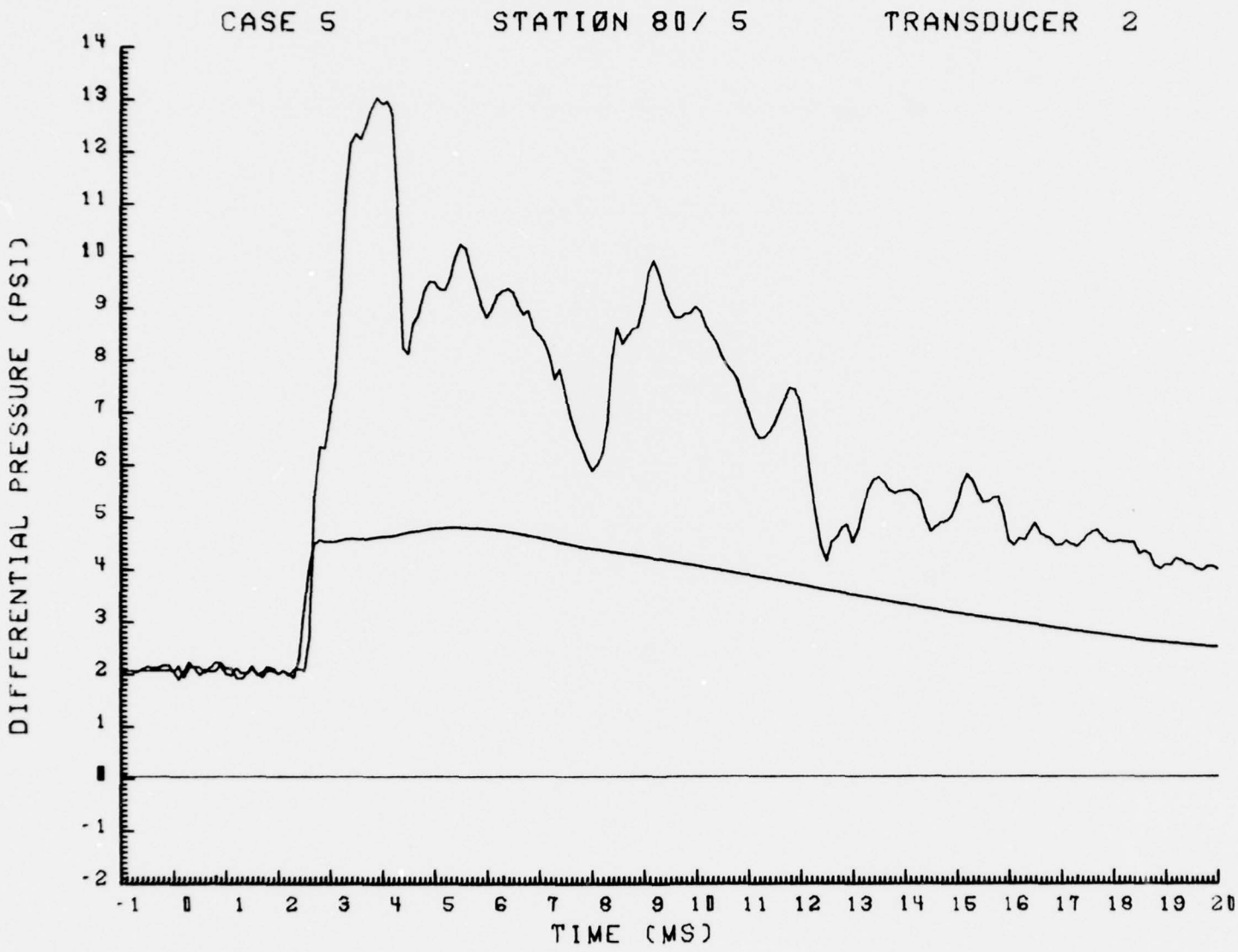


Figure 6. (Continued)

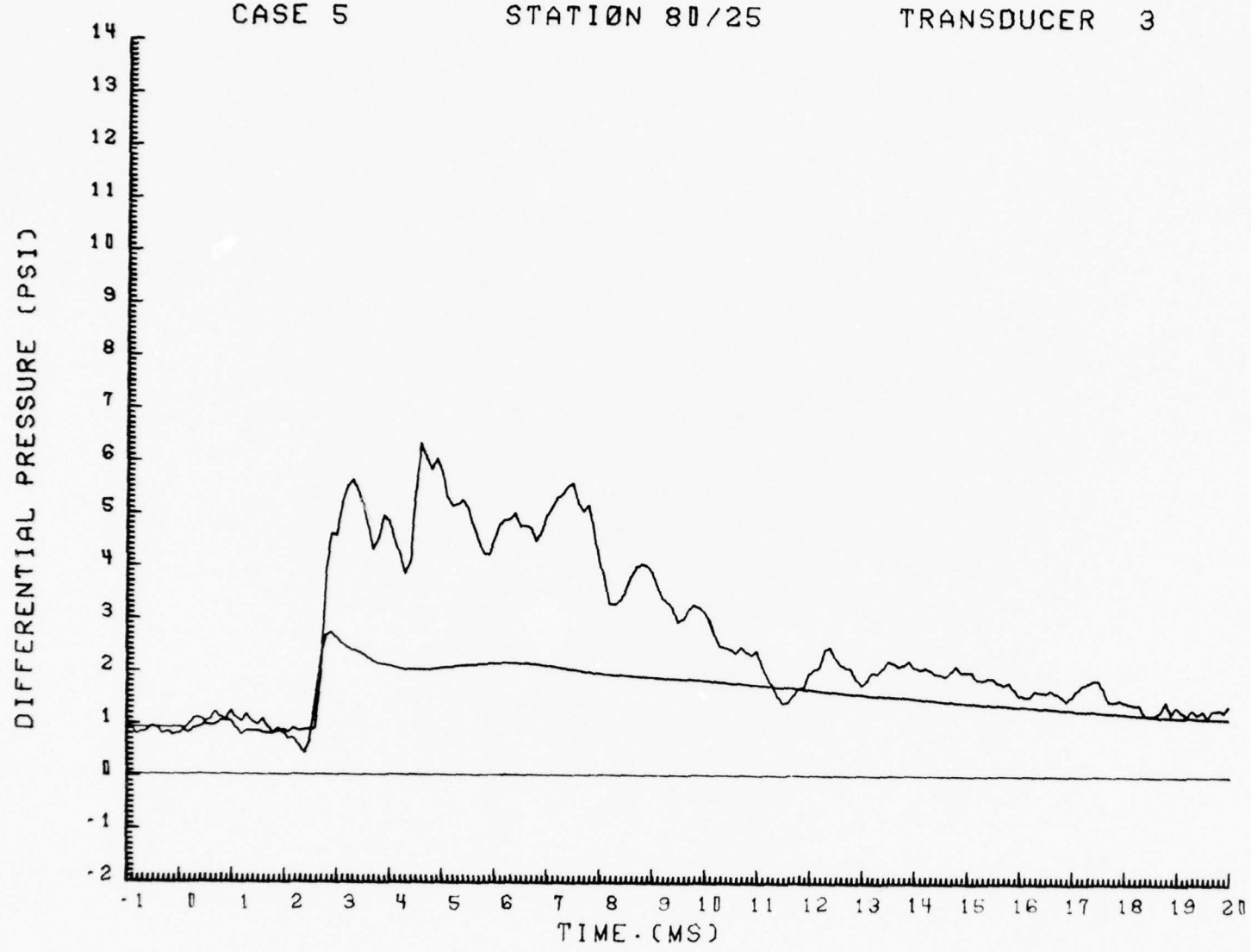


Figure 6. (Continued)

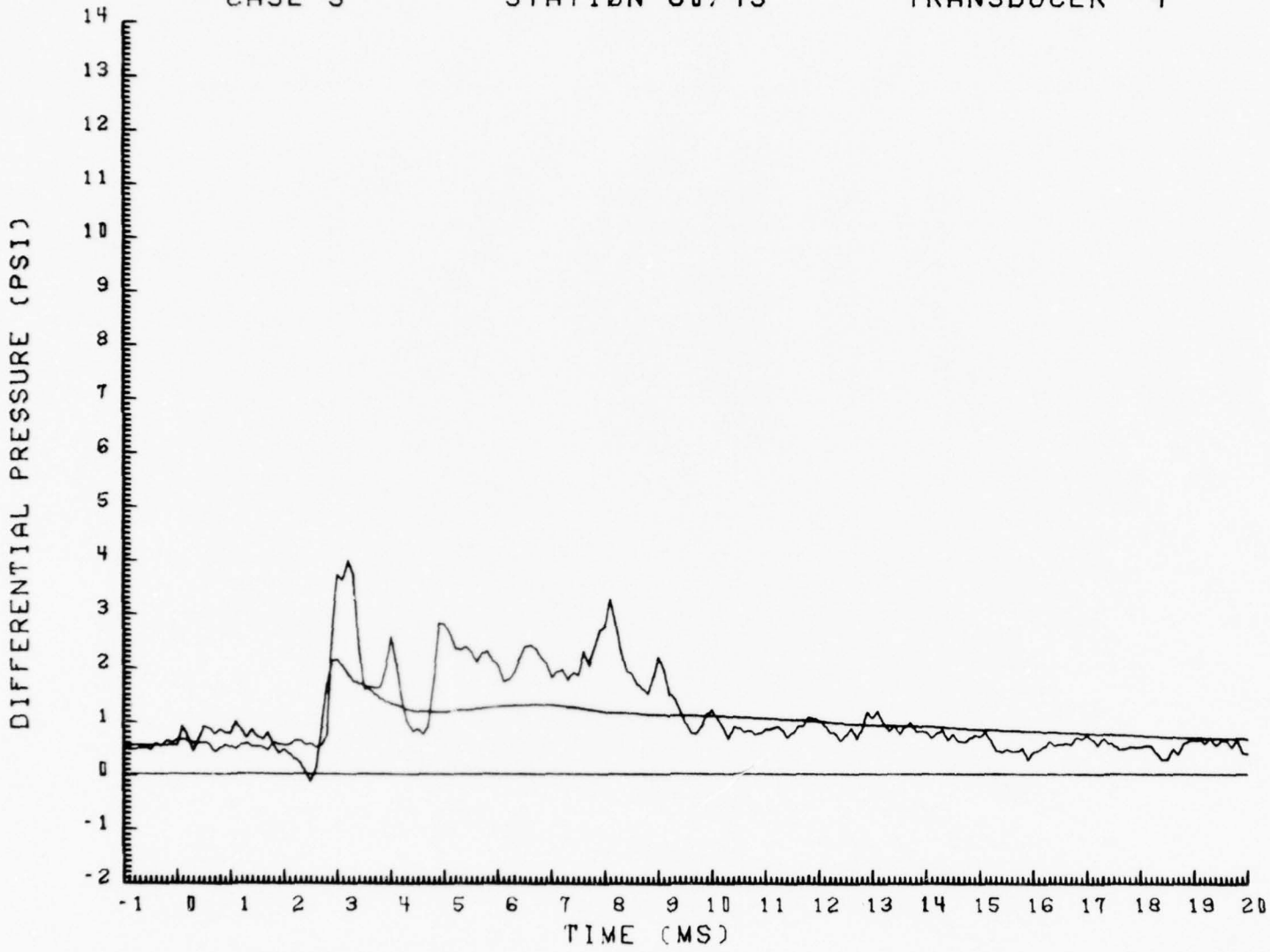


Figure 6. (Continued)

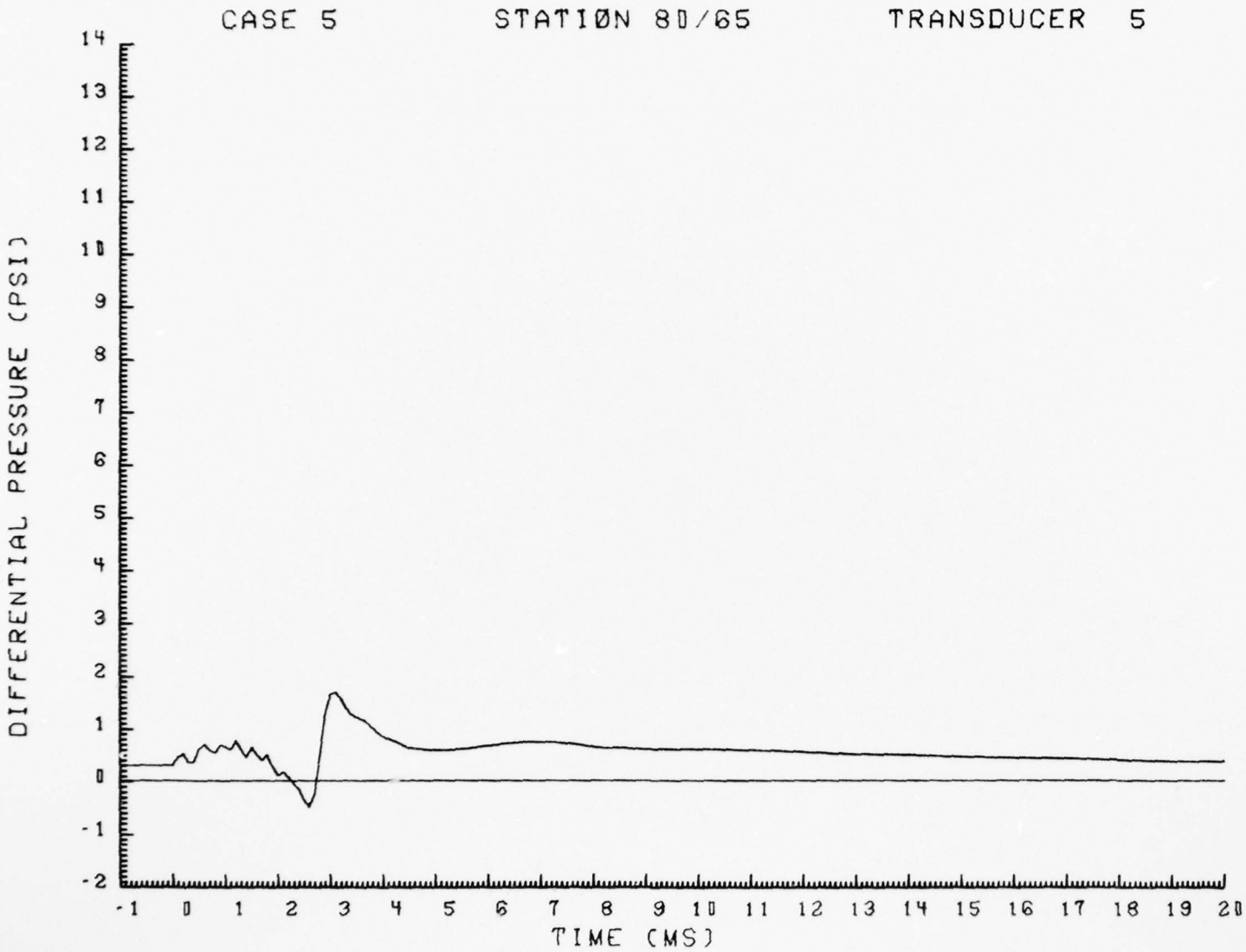


Figure 6. (Continued)

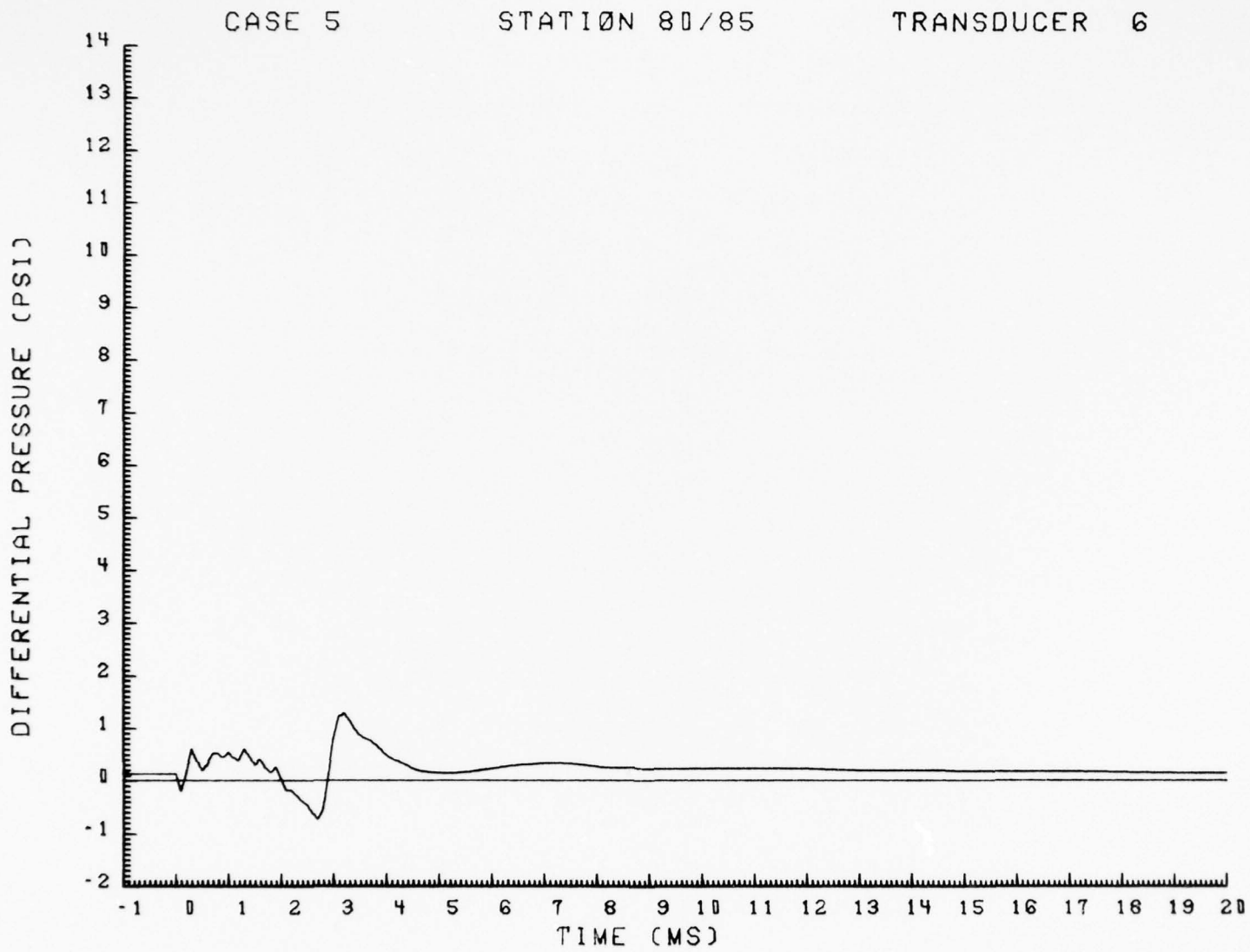


Figure 6. (Continued)

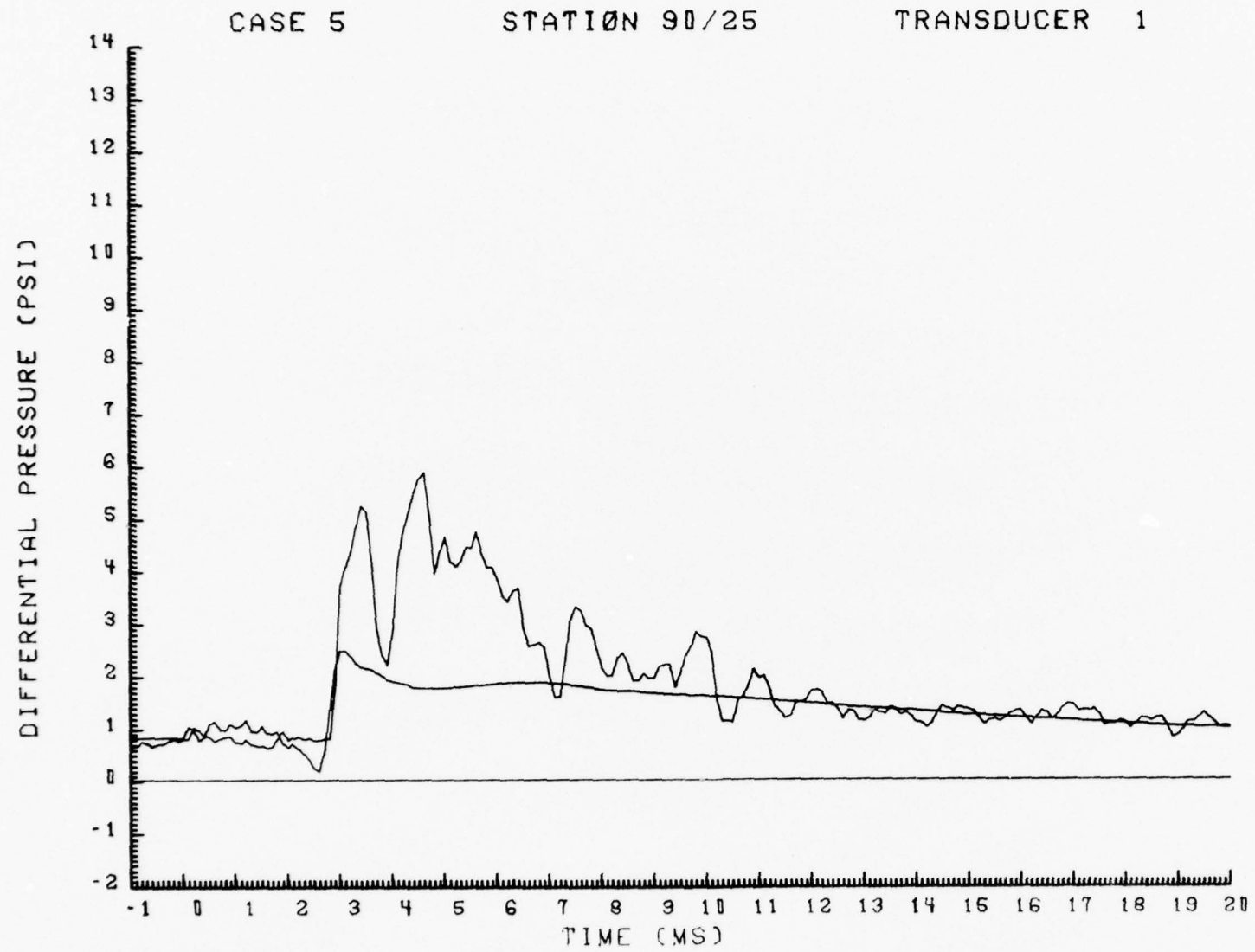


Figure 6. (Concluded)

Figure 7. Time-Variations of Pressure Loadings at Transducer Locations. Predictions From VIBRA-6 Compared With Experiment.

Case 4 - $\phi$ = 134.9 deg, $\Delta p_s$=1.97 psi. (9B-A2-3)

———— VIBRA-6

~~~~ Test Data
~~~~

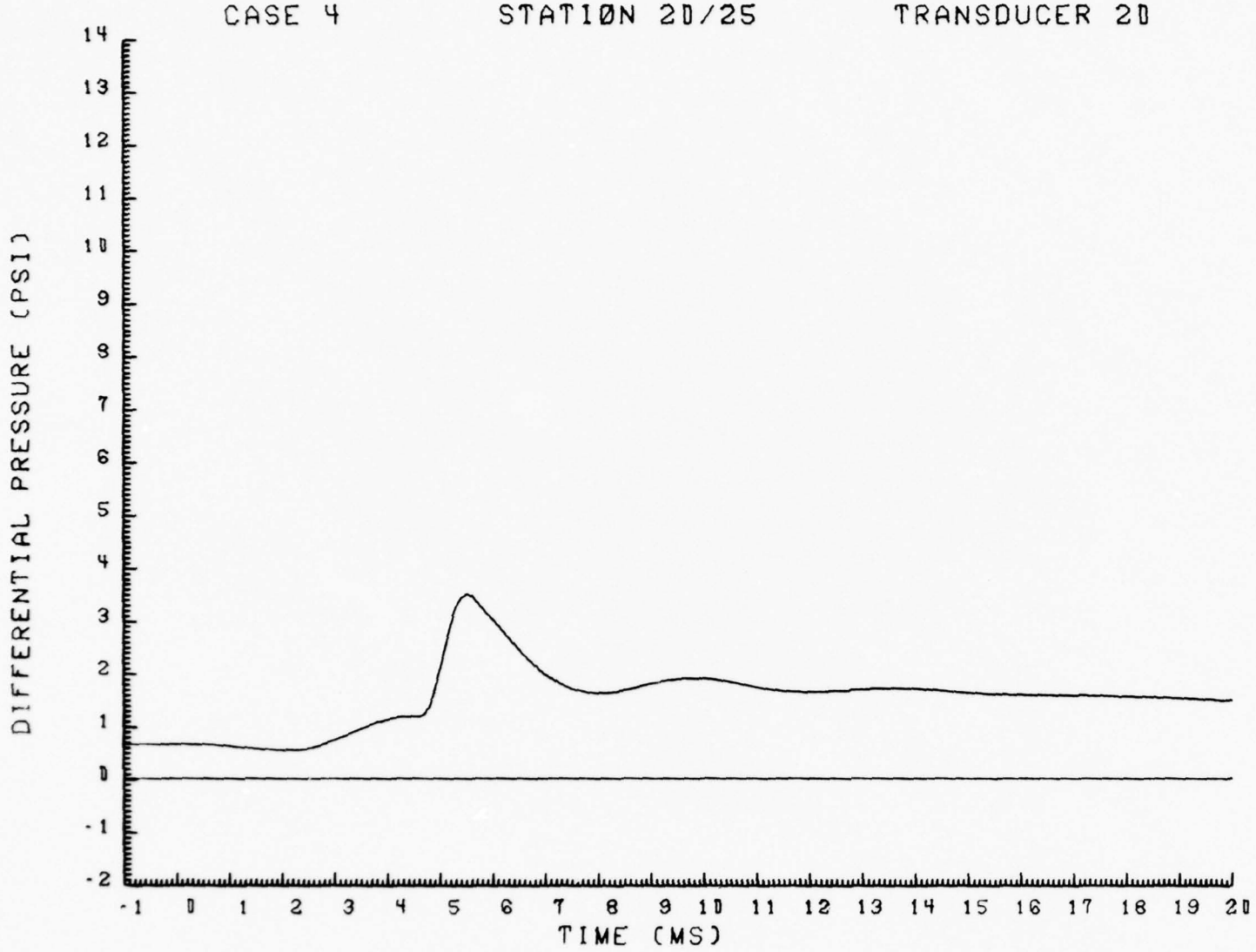
CASE 4
STATIØN 20/25
TRANSDUCER 20
DIFFERENTIAL PRESSURE (PSI)
14
13
12
11
10
9
8
7
6
5
4
3
2
1
0
-1
-2
-1 0 1 2 3 4 5 6 7 8 9 10 11 12 13 14 15 16 17 18 19 20
TIME (MS)

Figure 7

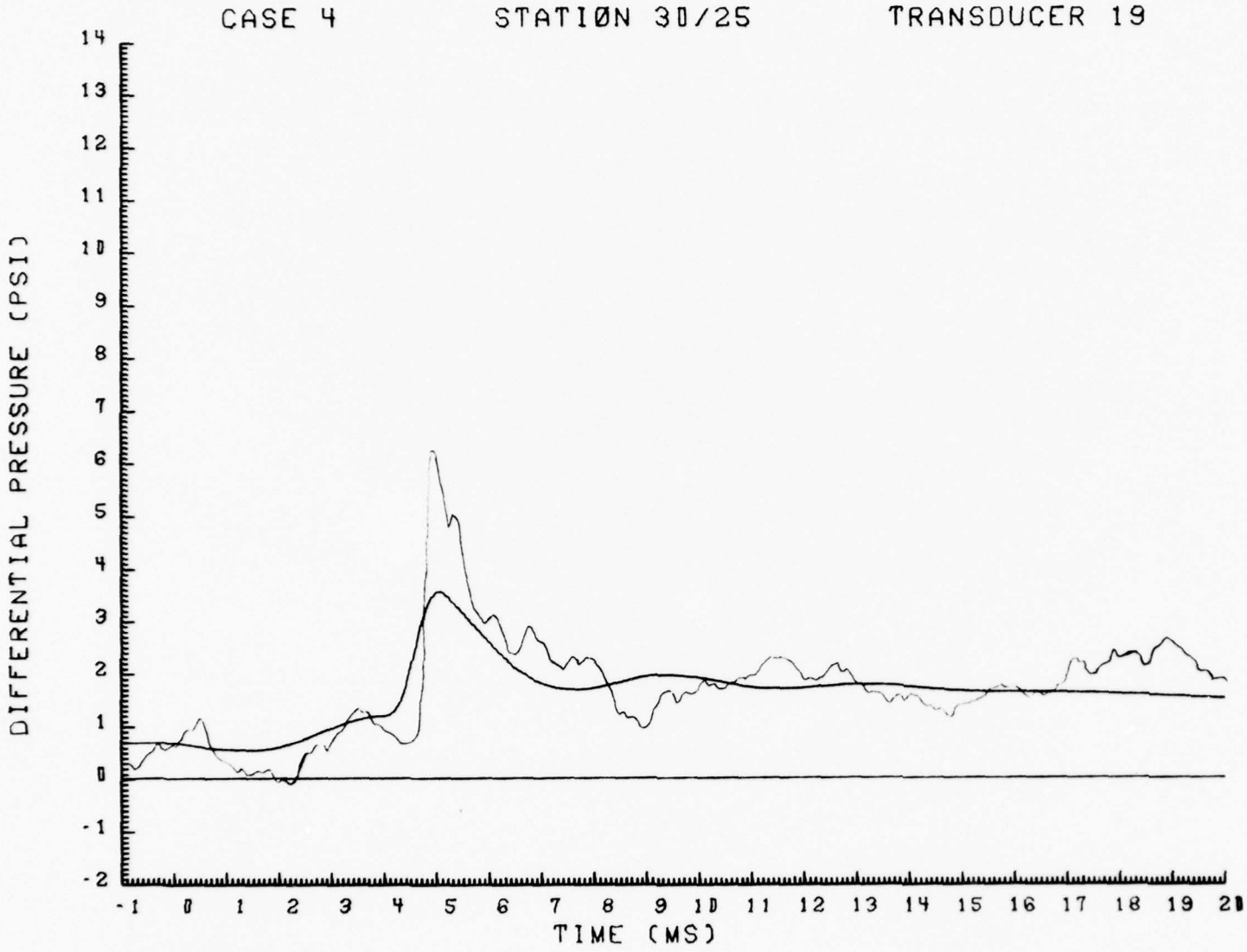


Figure 7. (Continued)

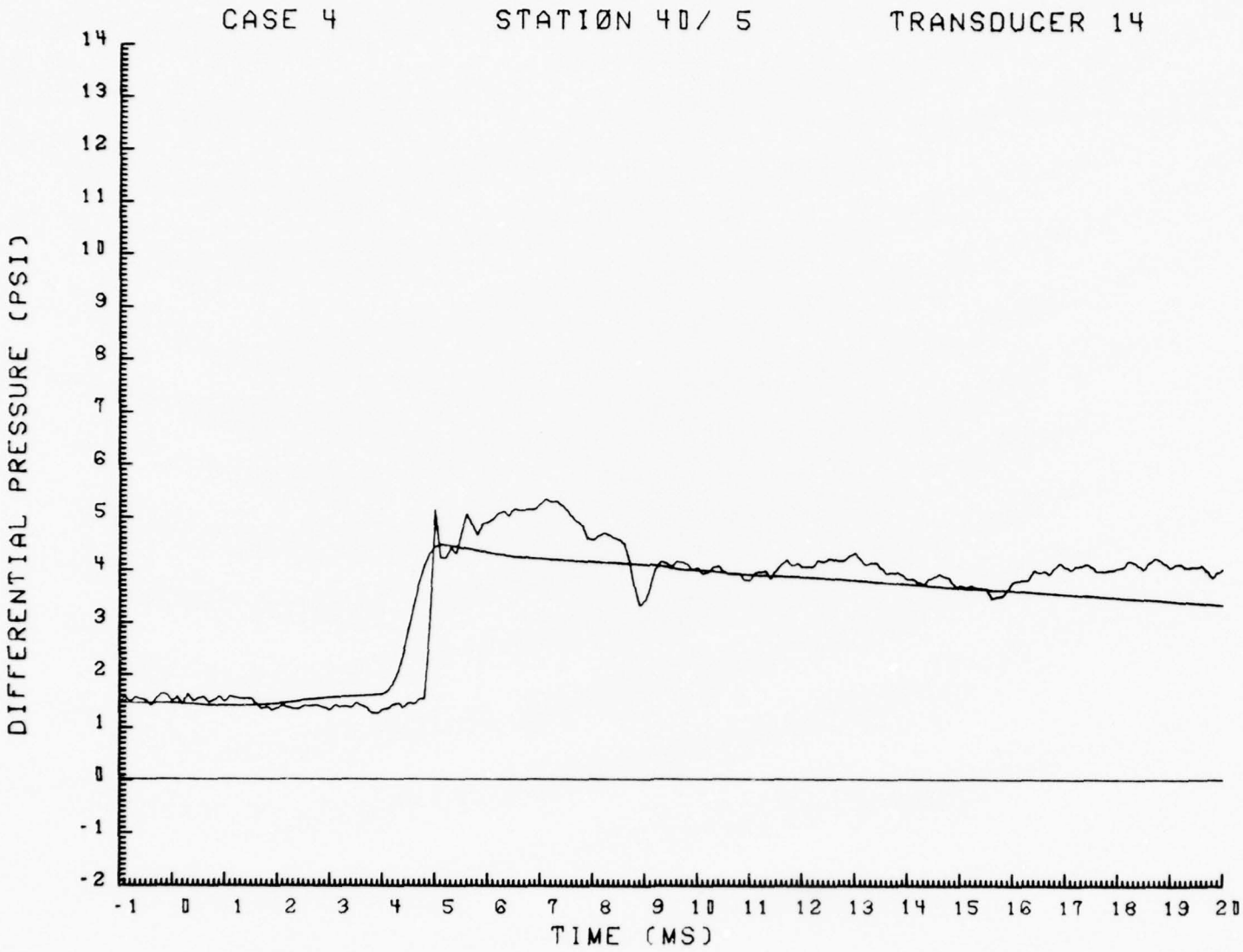


Figure 7. (Continued)

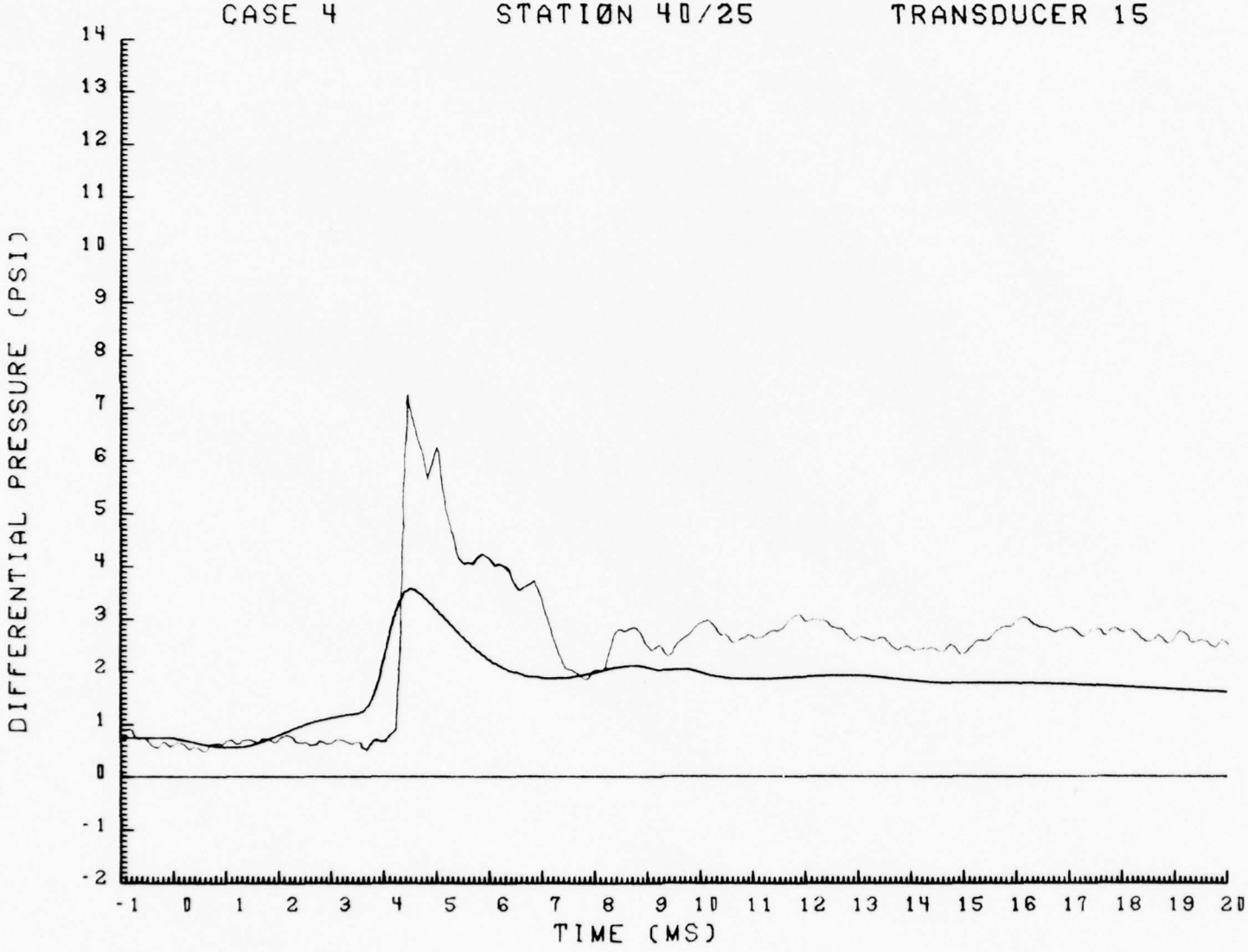


Figure 7. (Continued)

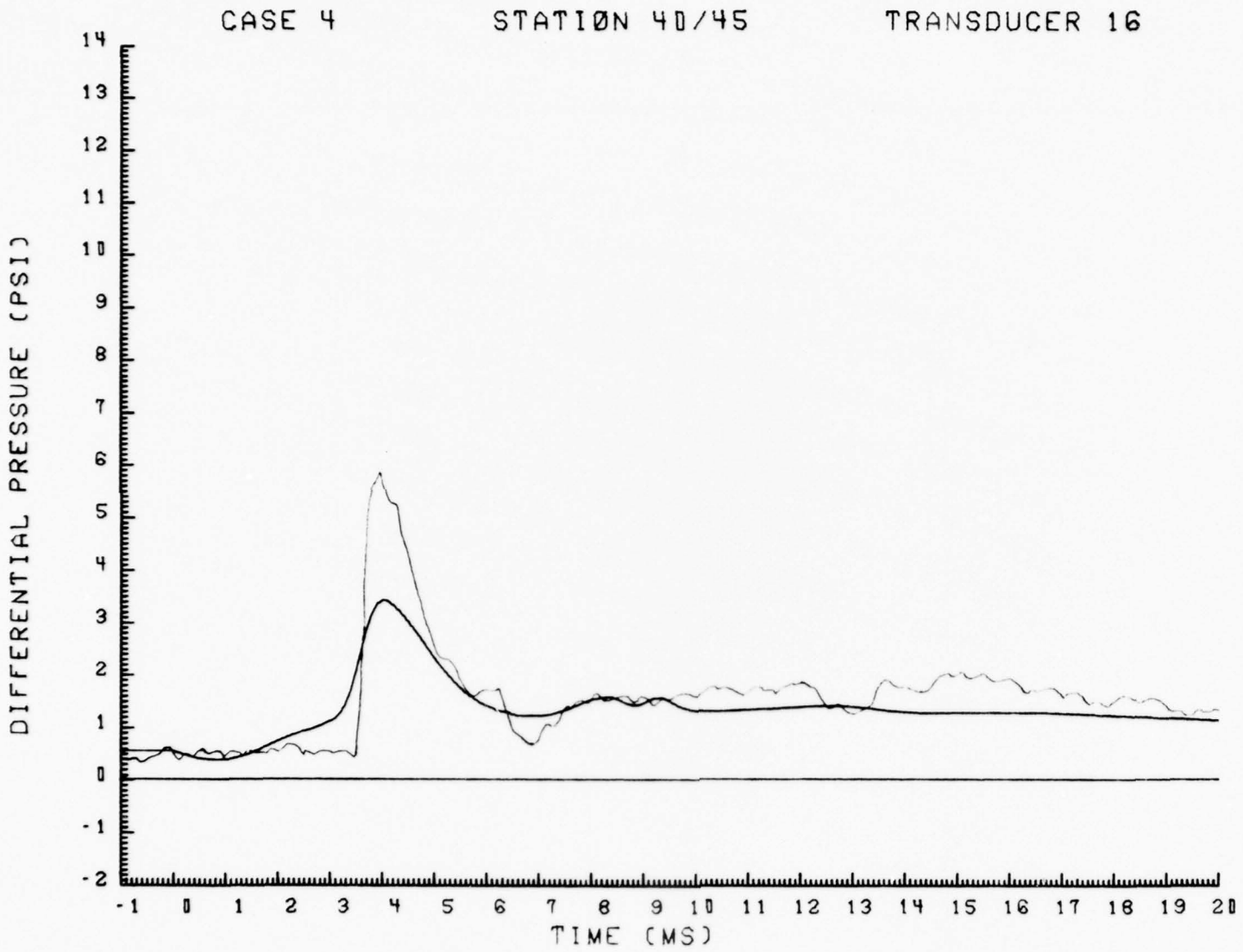


Figure 7. (Continued)

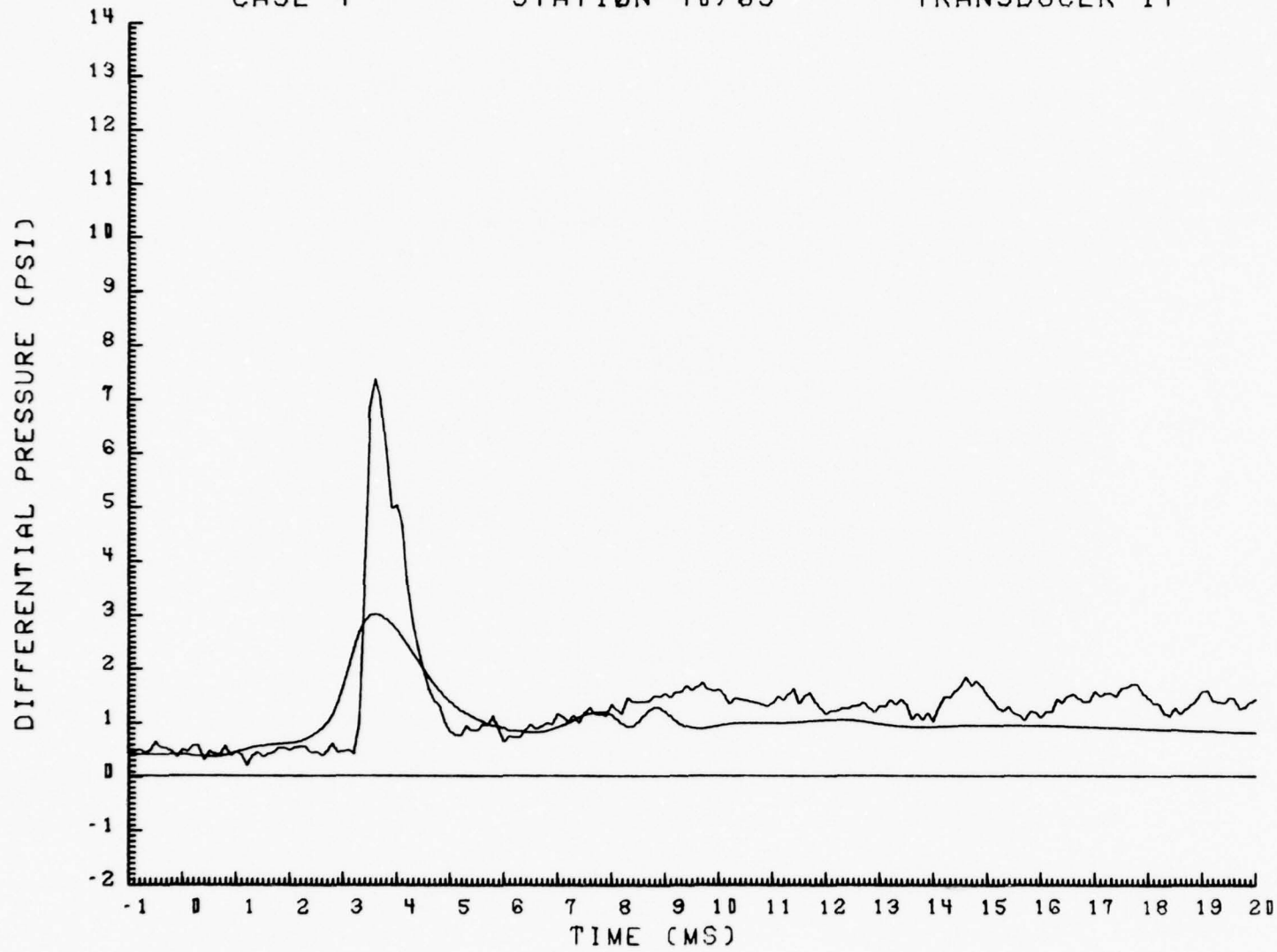


Figure 7. (Continued)

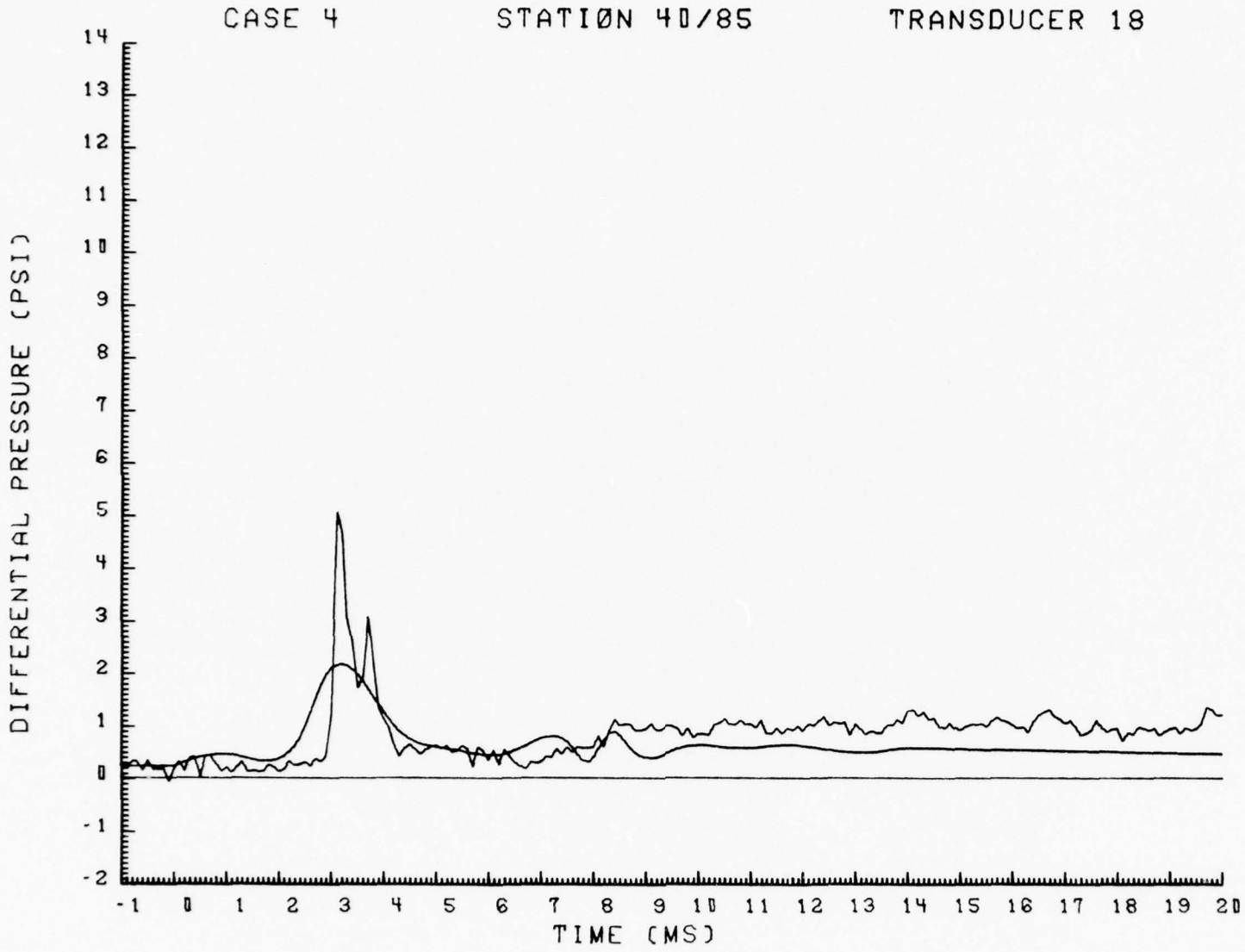


Figure 7. (Continued)

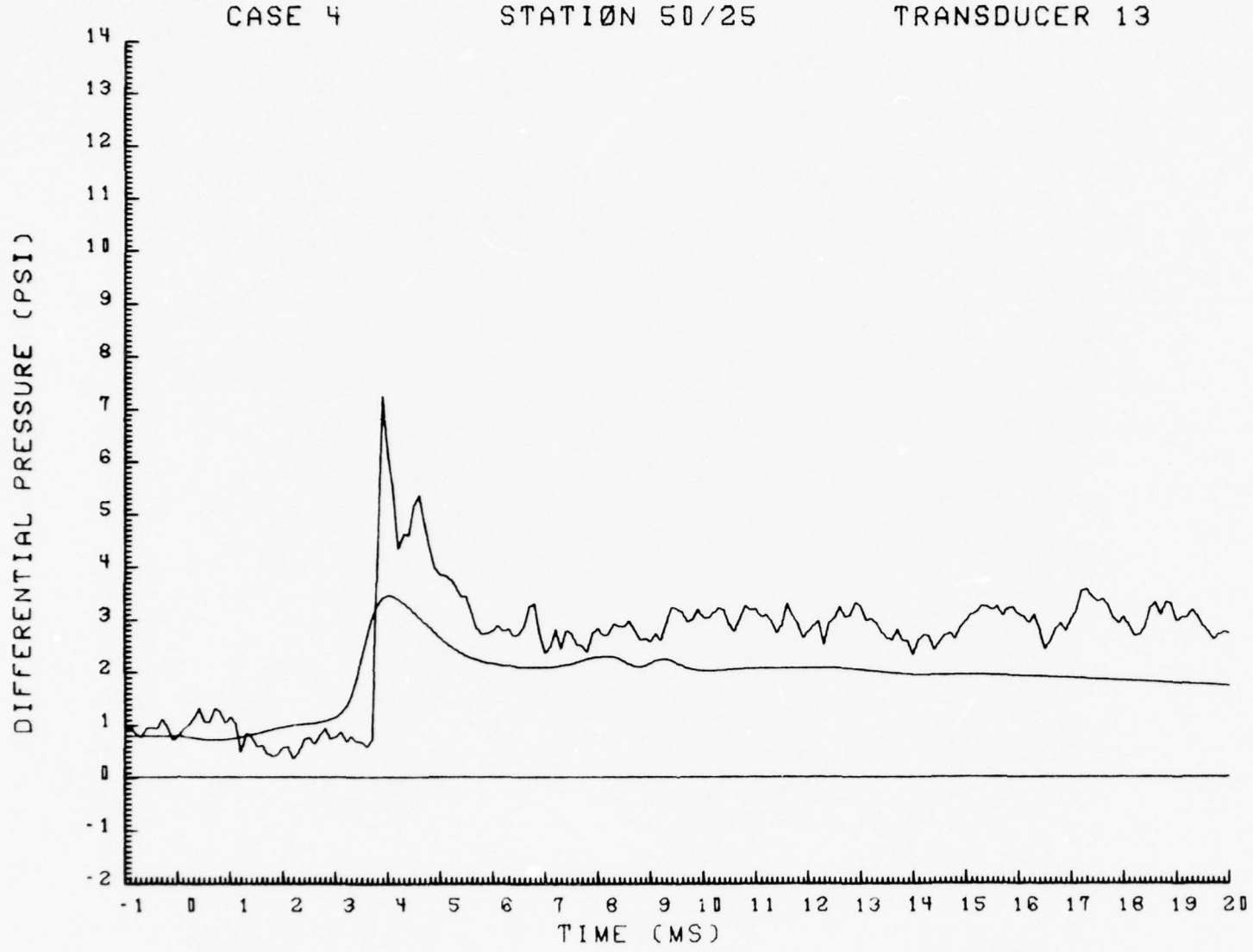


Figure 7. (Continued)

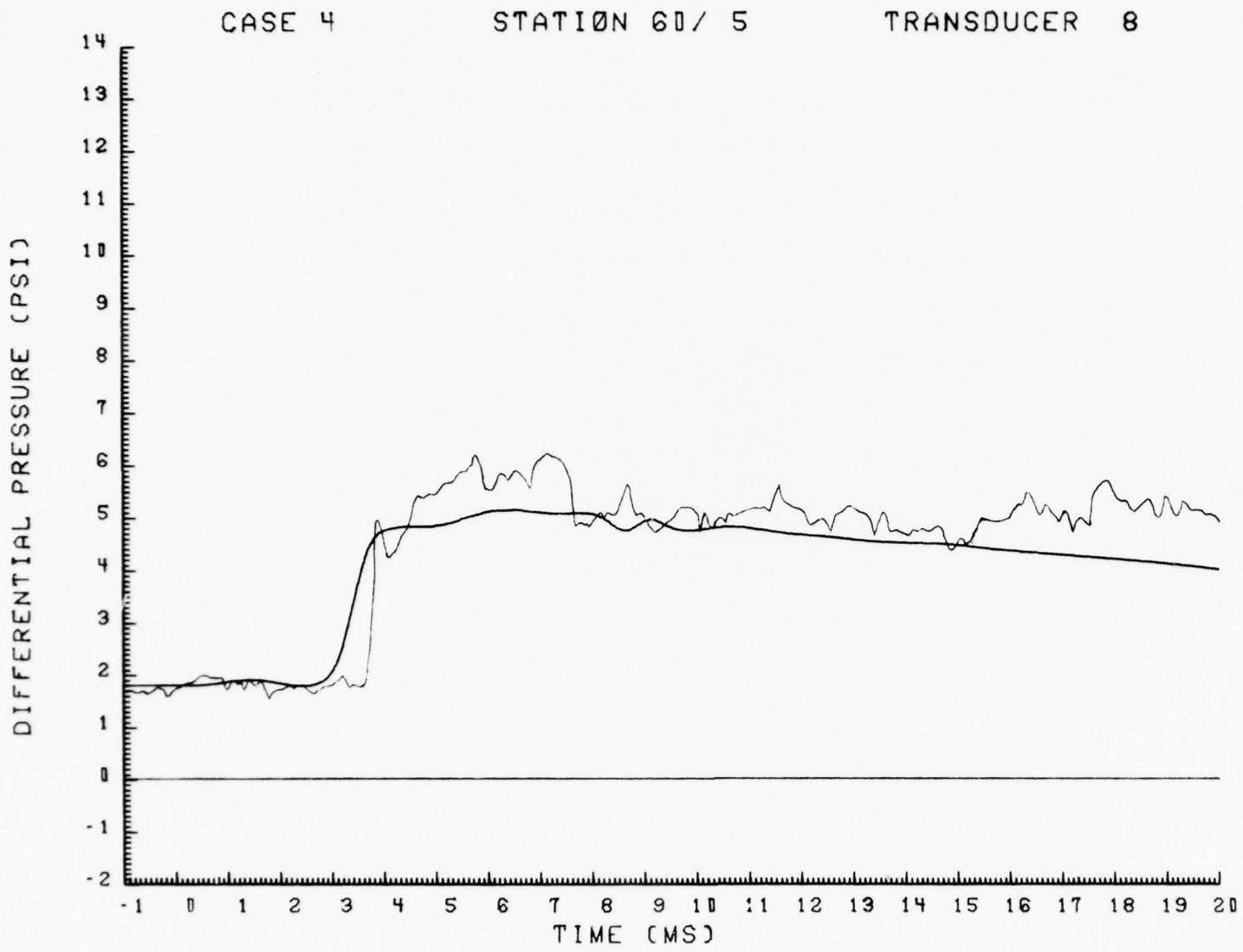


Figure 7. (Continued)

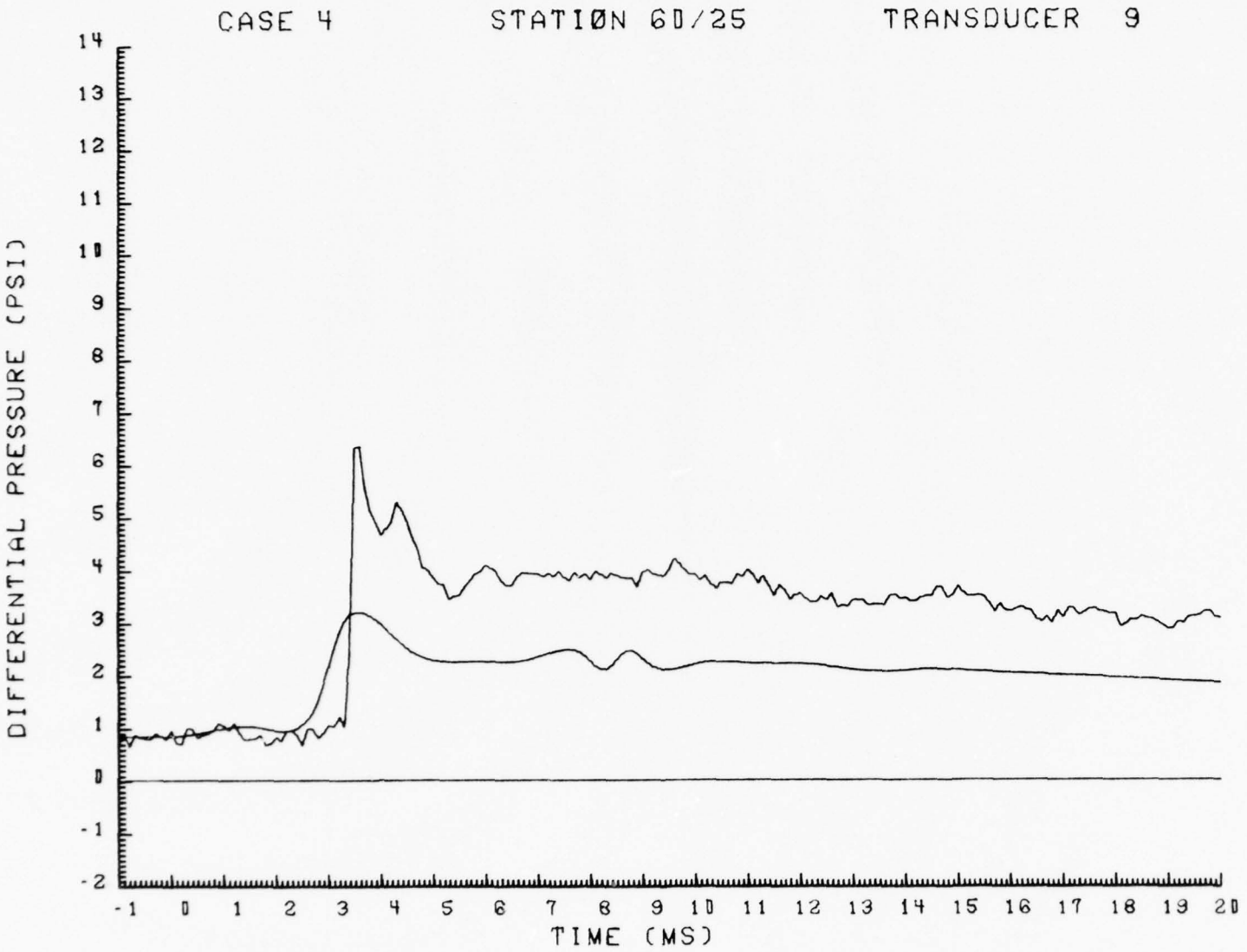


Figure 7. (Continued)

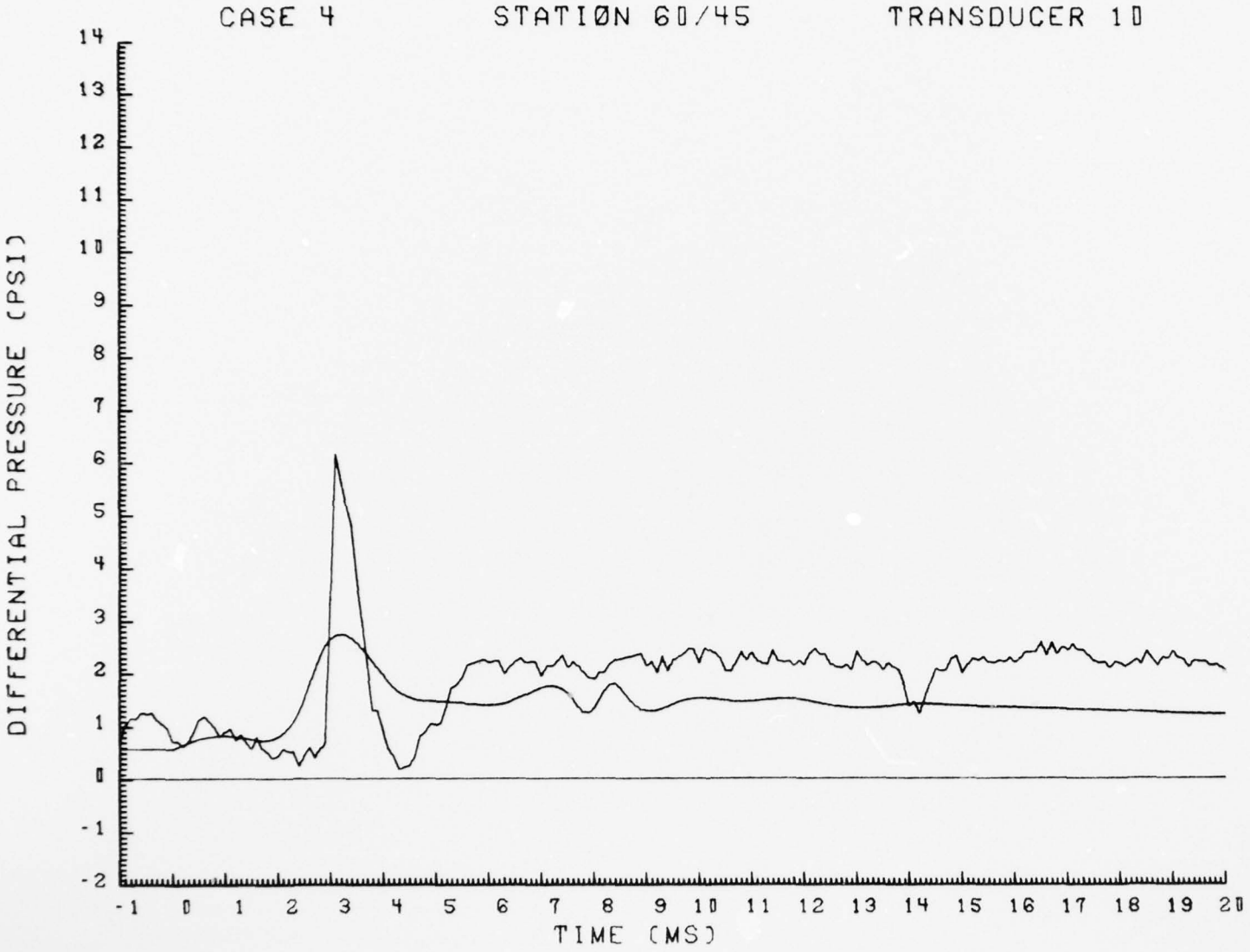


Figure 7. (Continued)

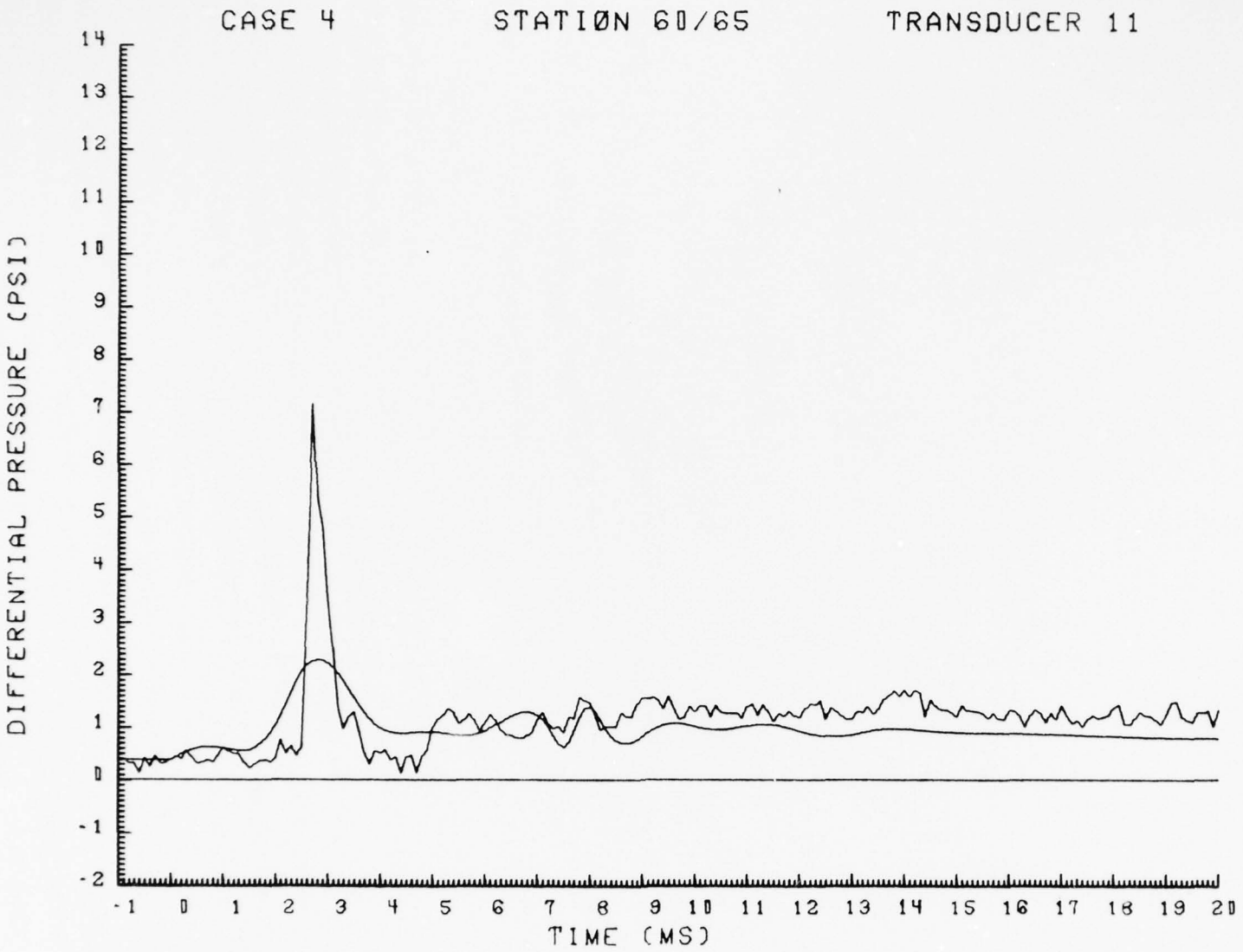


Figure 7. (Continued)

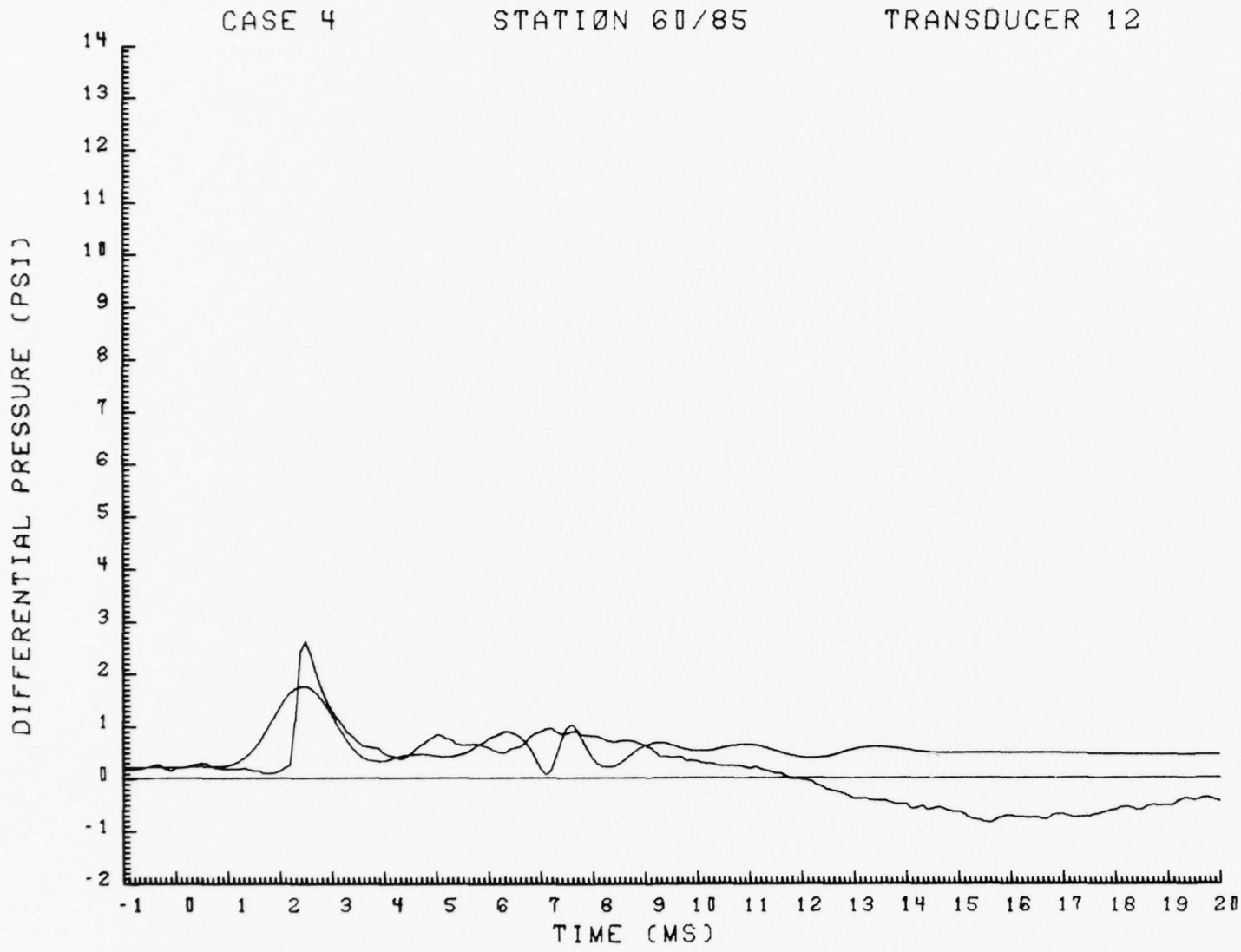


Figure 7. (Continued)

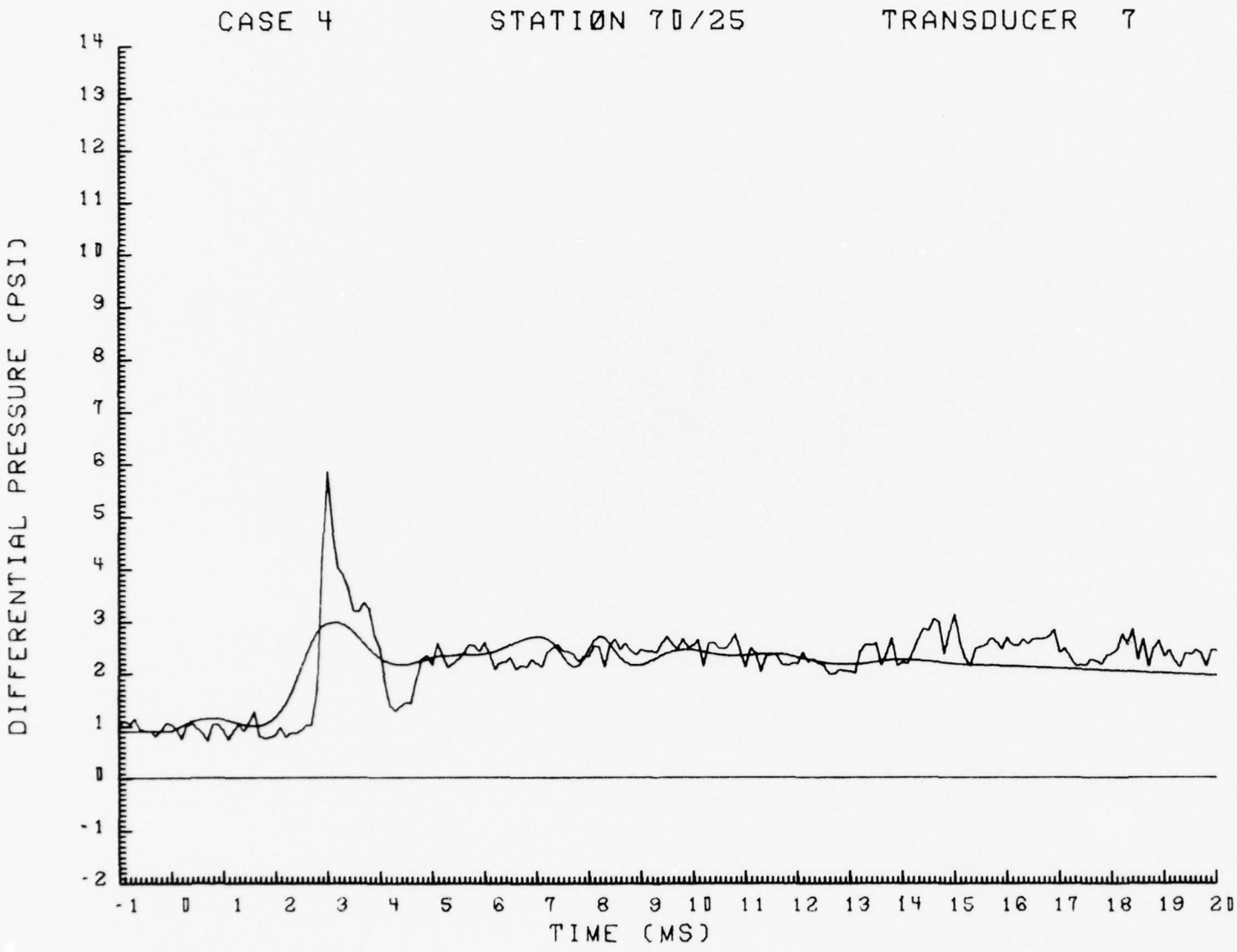


Figure 7. (Continued)

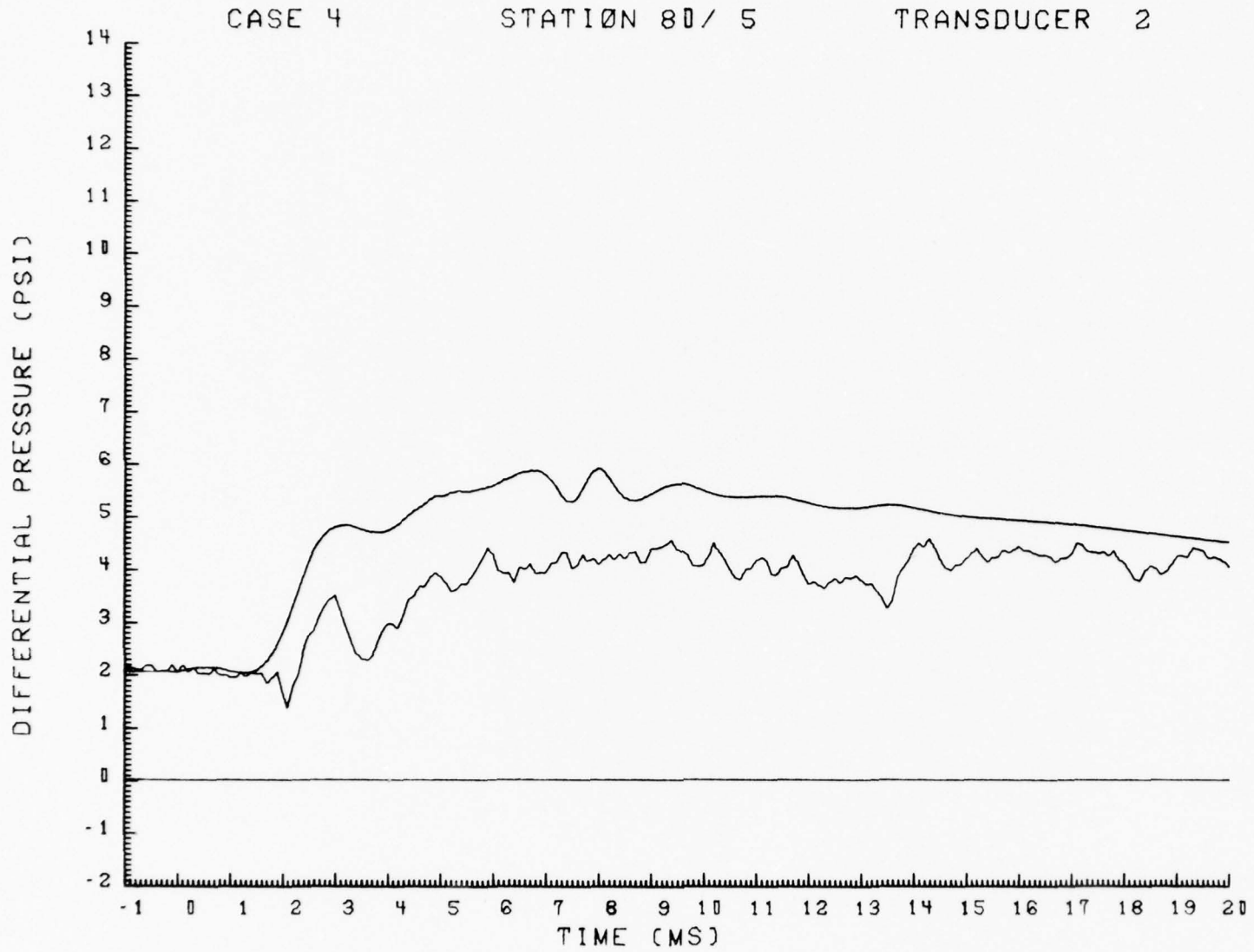


Figure 7. (Continued)

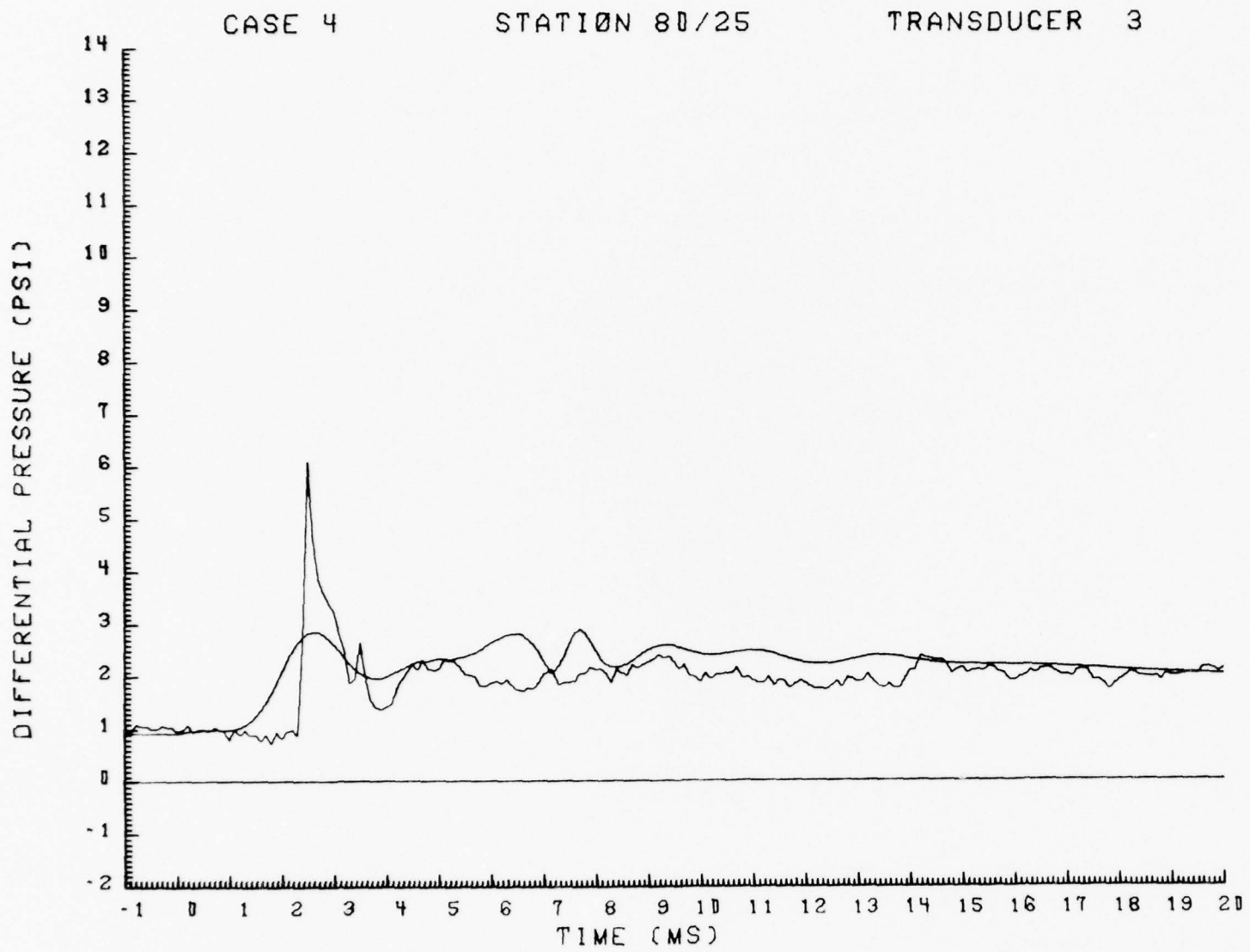


Figure 7. (Continued)

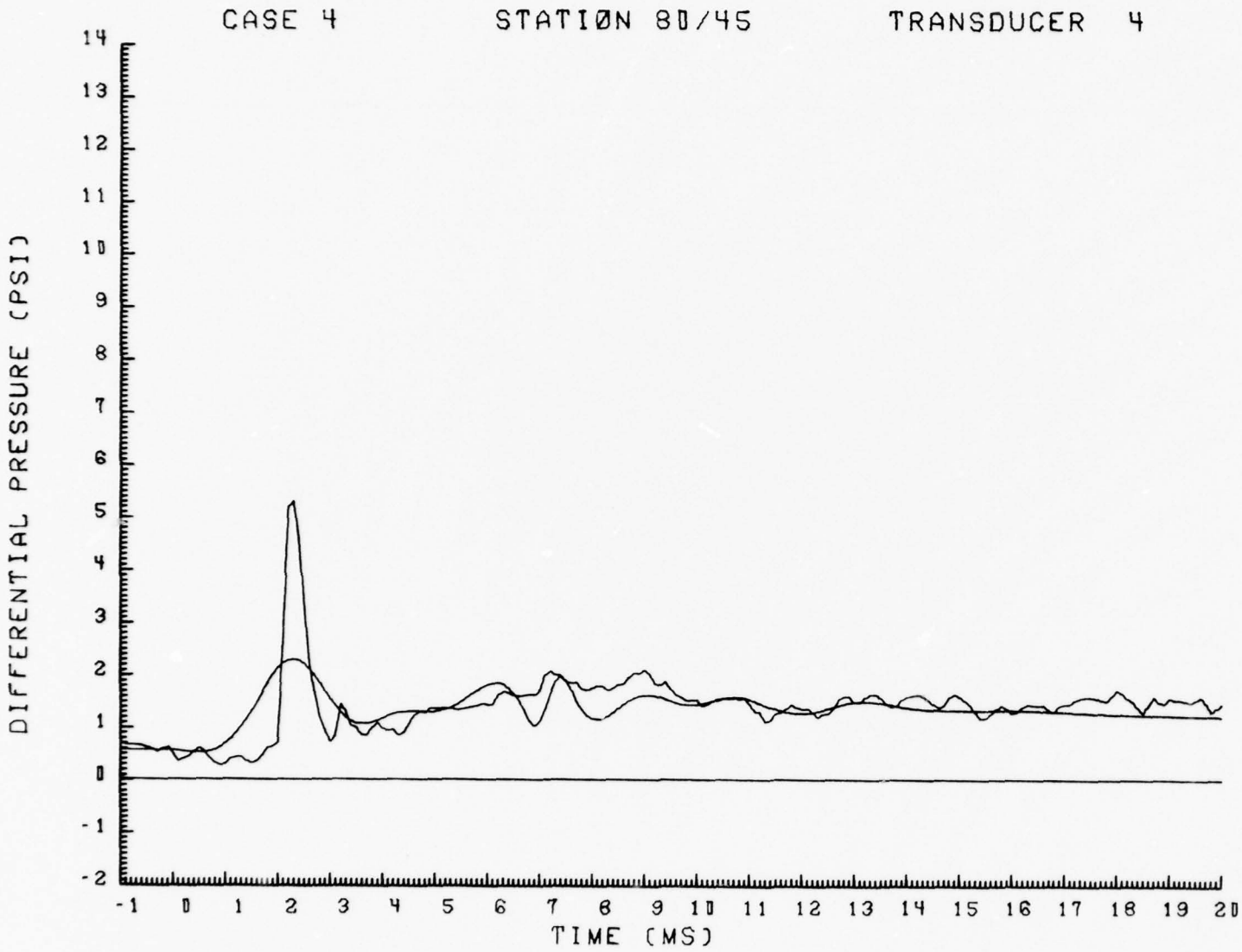


Figure 7. (Continued)

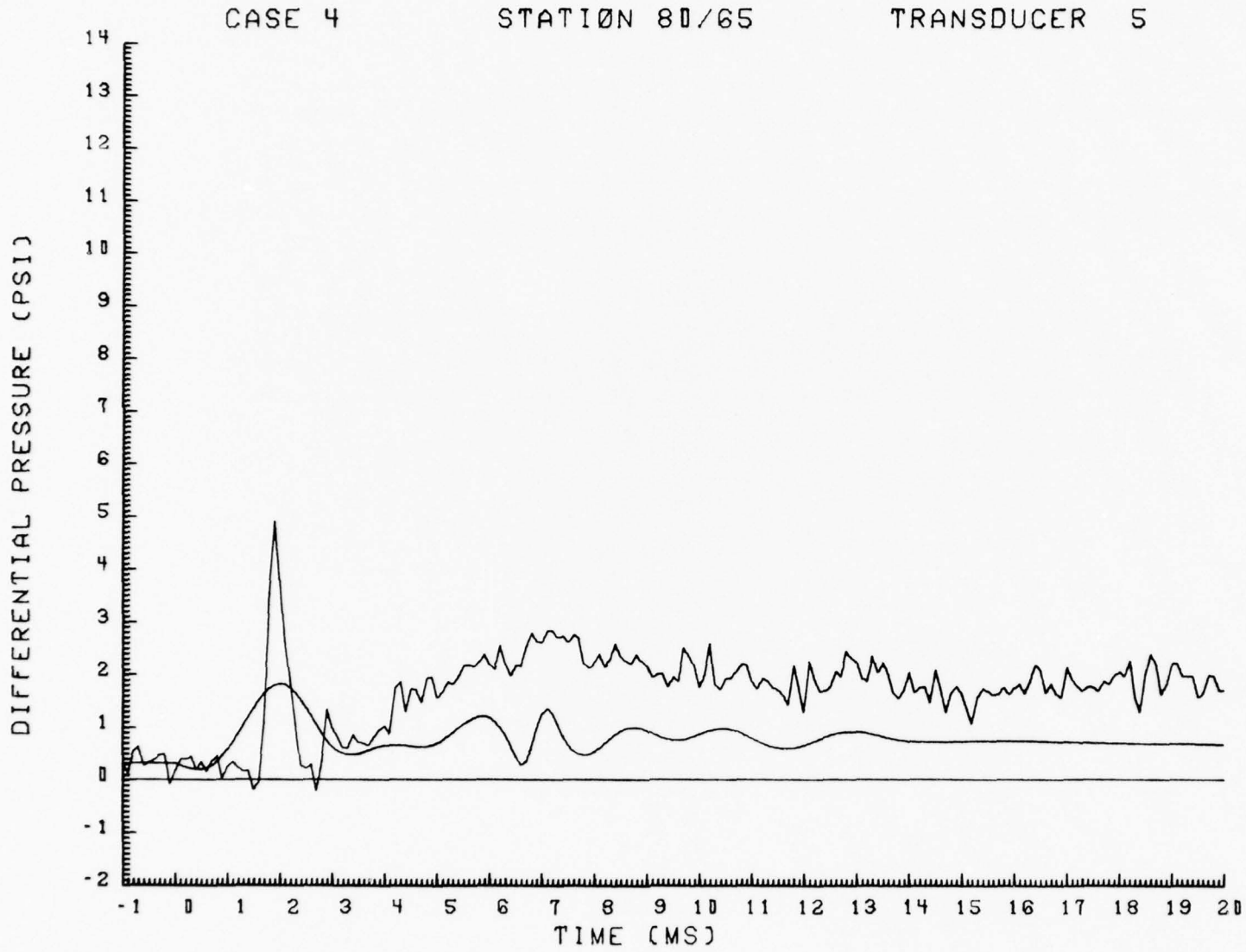


Figure 7. (Continued)

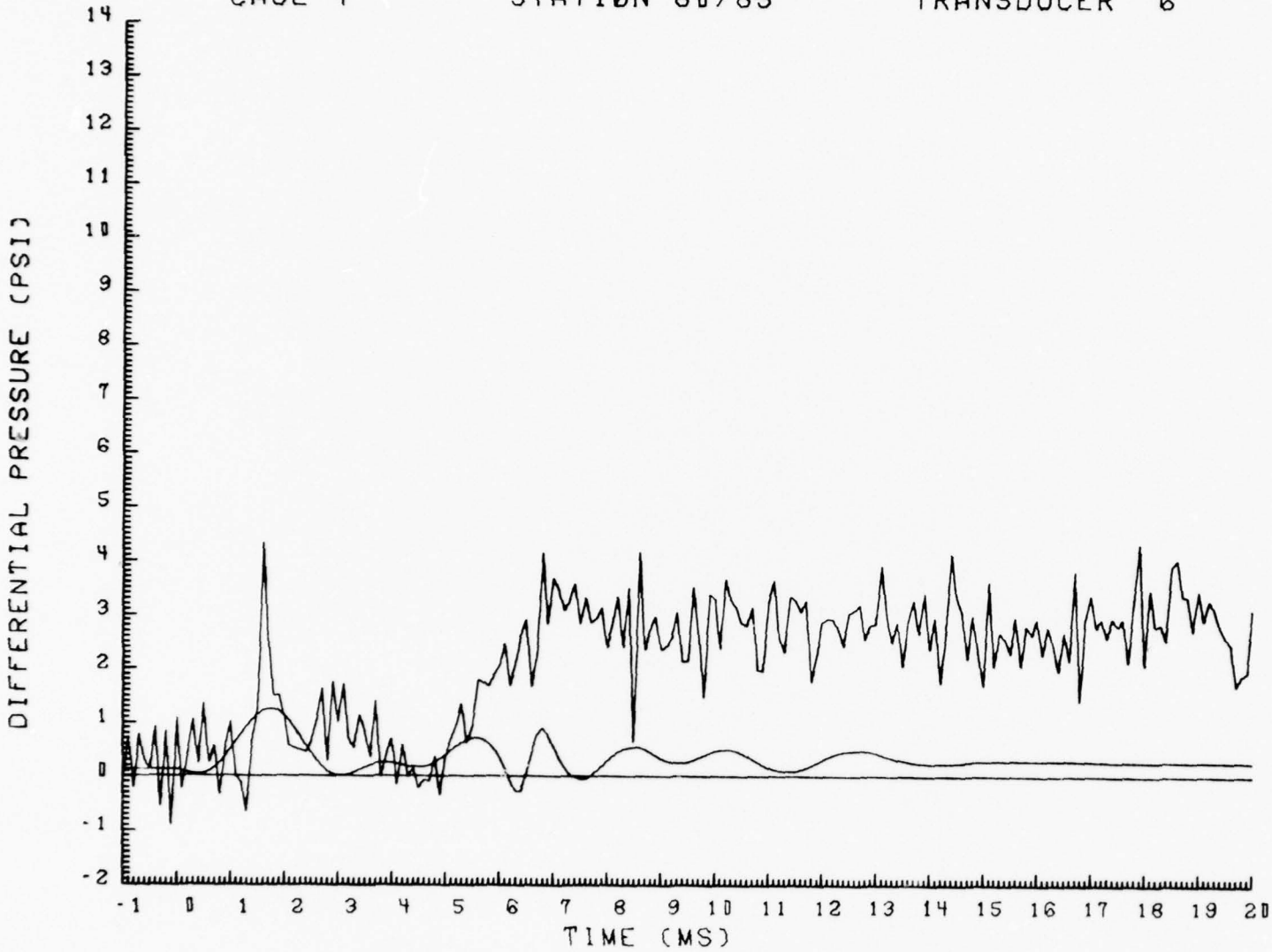


Figure 7. (Continued)

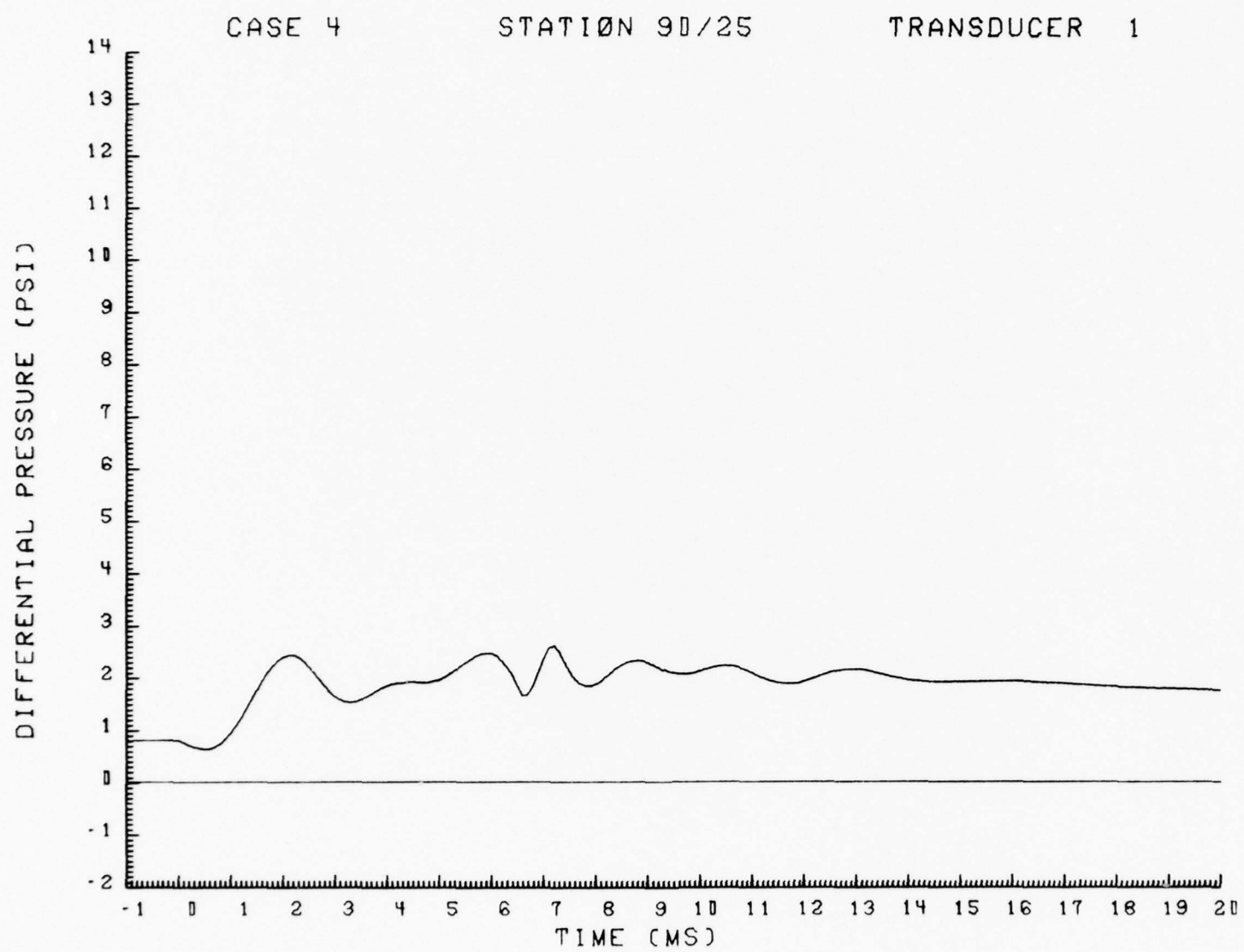


Figure 7. (Concluded)

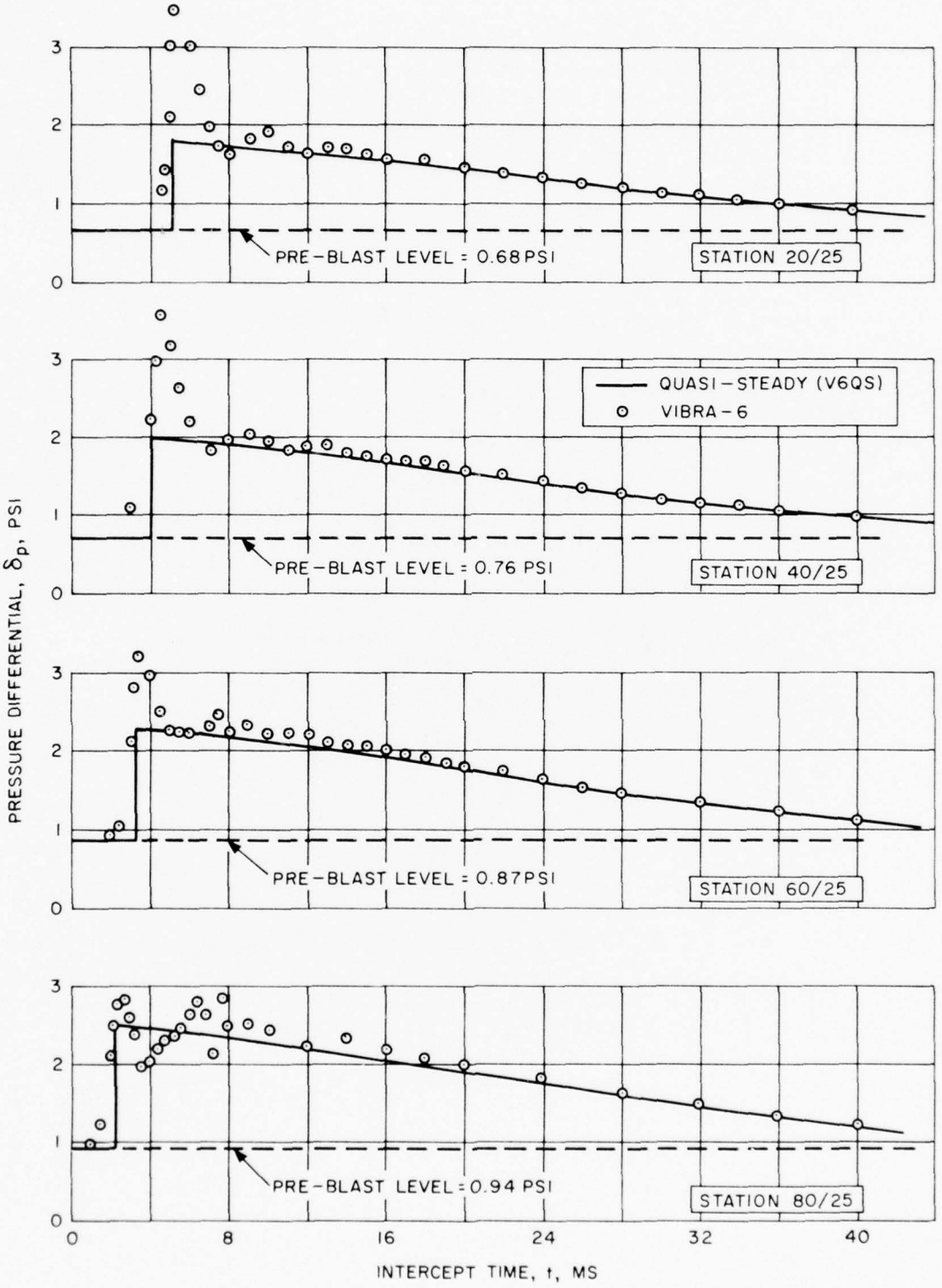


Figure 8. Comparison Between VIBRA-6 (DLM) and Quasi-Steady (V6QS) Predictions for Time-Variations of Differential Pressure. Spanwise Along the Quarter-Chord Line. Case 4

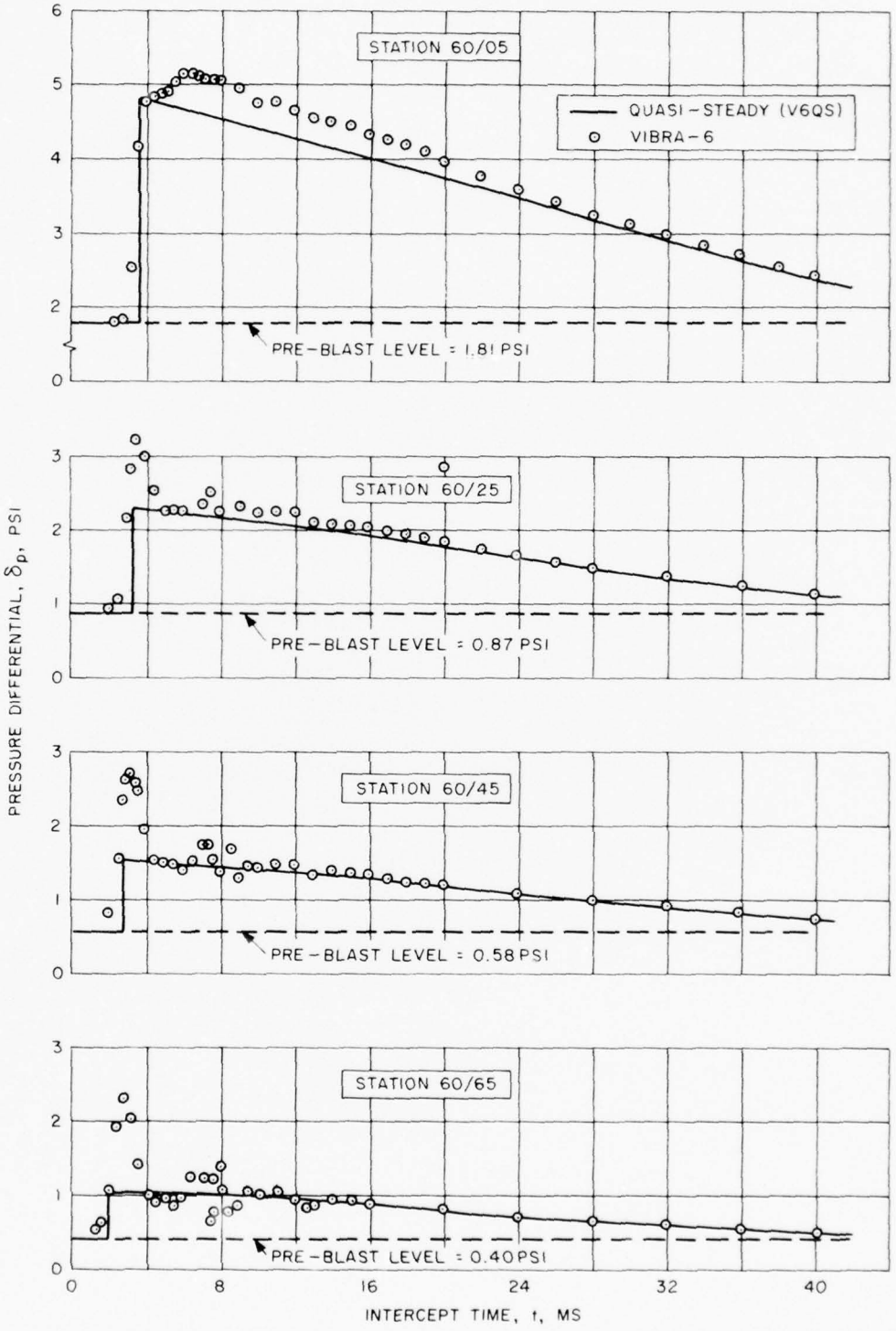


Figure 9. Comparison Between VIBRA-6 (DLM) and Quasi-Steady (V6QS) Predictions for Time-Variations of Differential Pressure. Chordwise Along the 60 Percent Span Station. Case 4

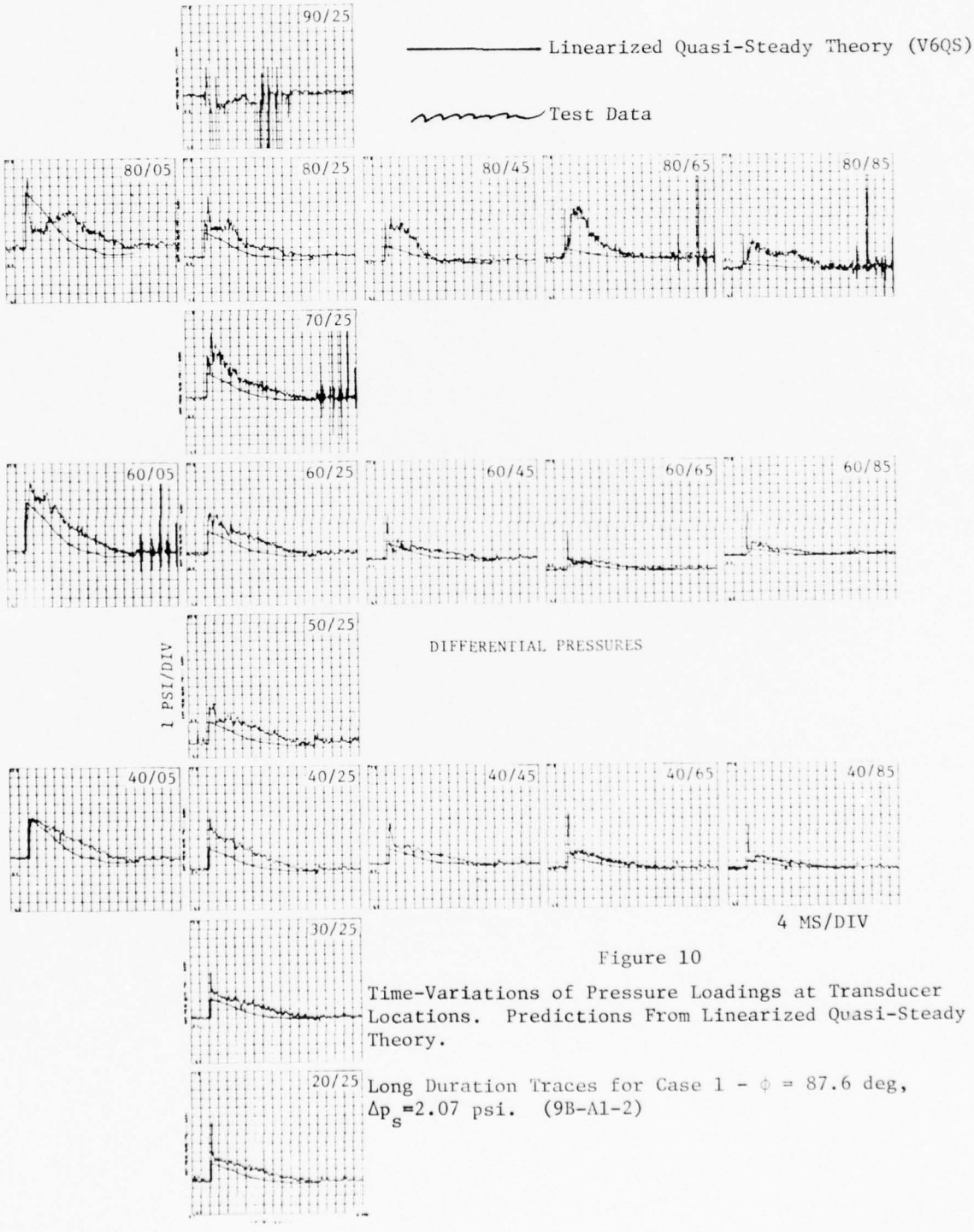


Figure 10

Time-Variations of Pressure Loadings at Transducer Locations. Predictions From Linearized Quasi-Steady Theory.

Long Duration Traces for Case 1 - $\phi$ = 87.6 deg, $\Delta p_s$=2.07 psi. (9B-A1-2)

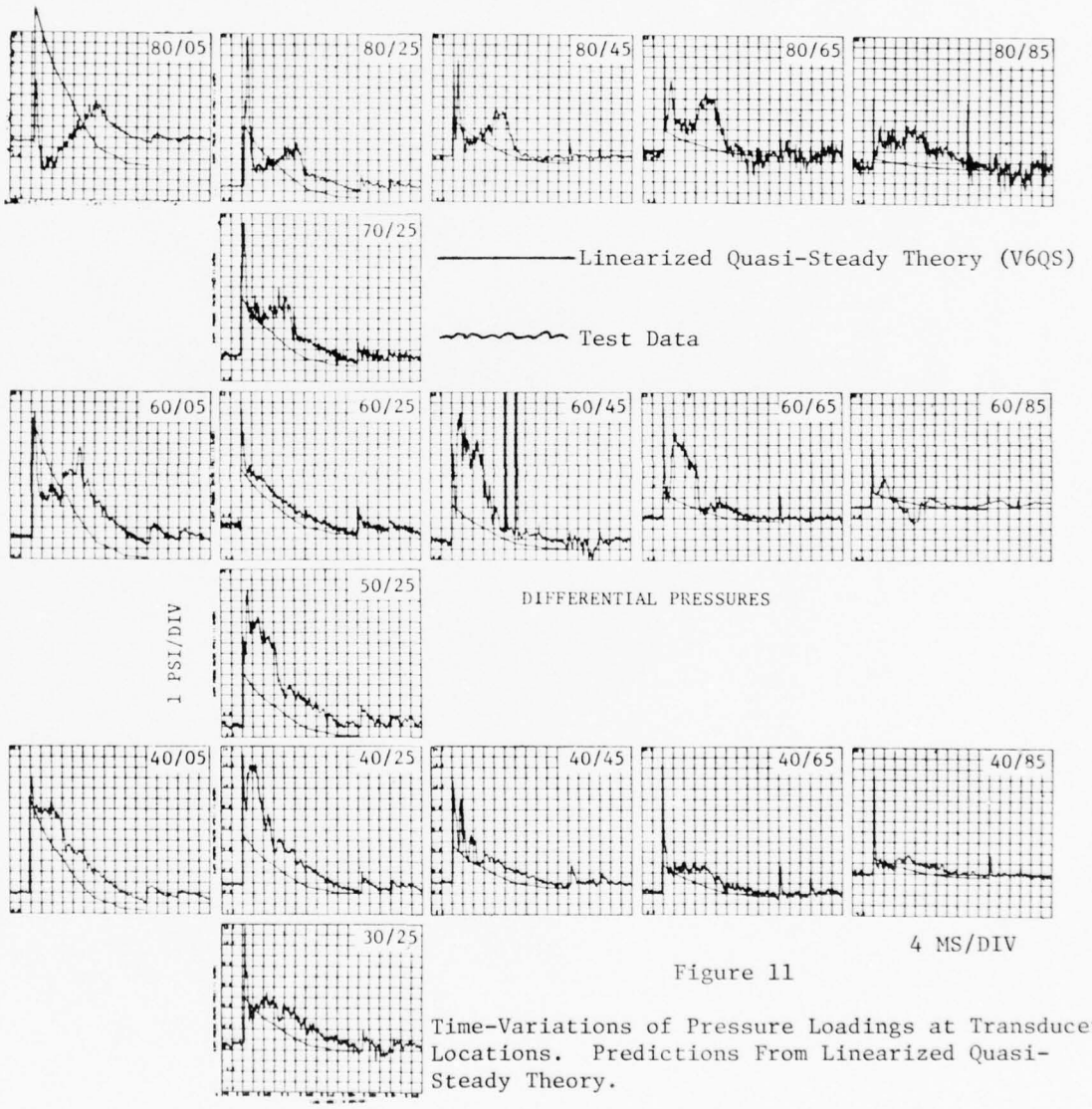


Figure 11

Time-Variations of Pressure Loadings at Transducer Locations. Predictions From Linearized Quasi-Steady Theory.

Long-Duration Traces for Case 3 - $\phi$ = 90.3 deg, $\Delta p_s$=4.02 psi. (9B-A2-2)

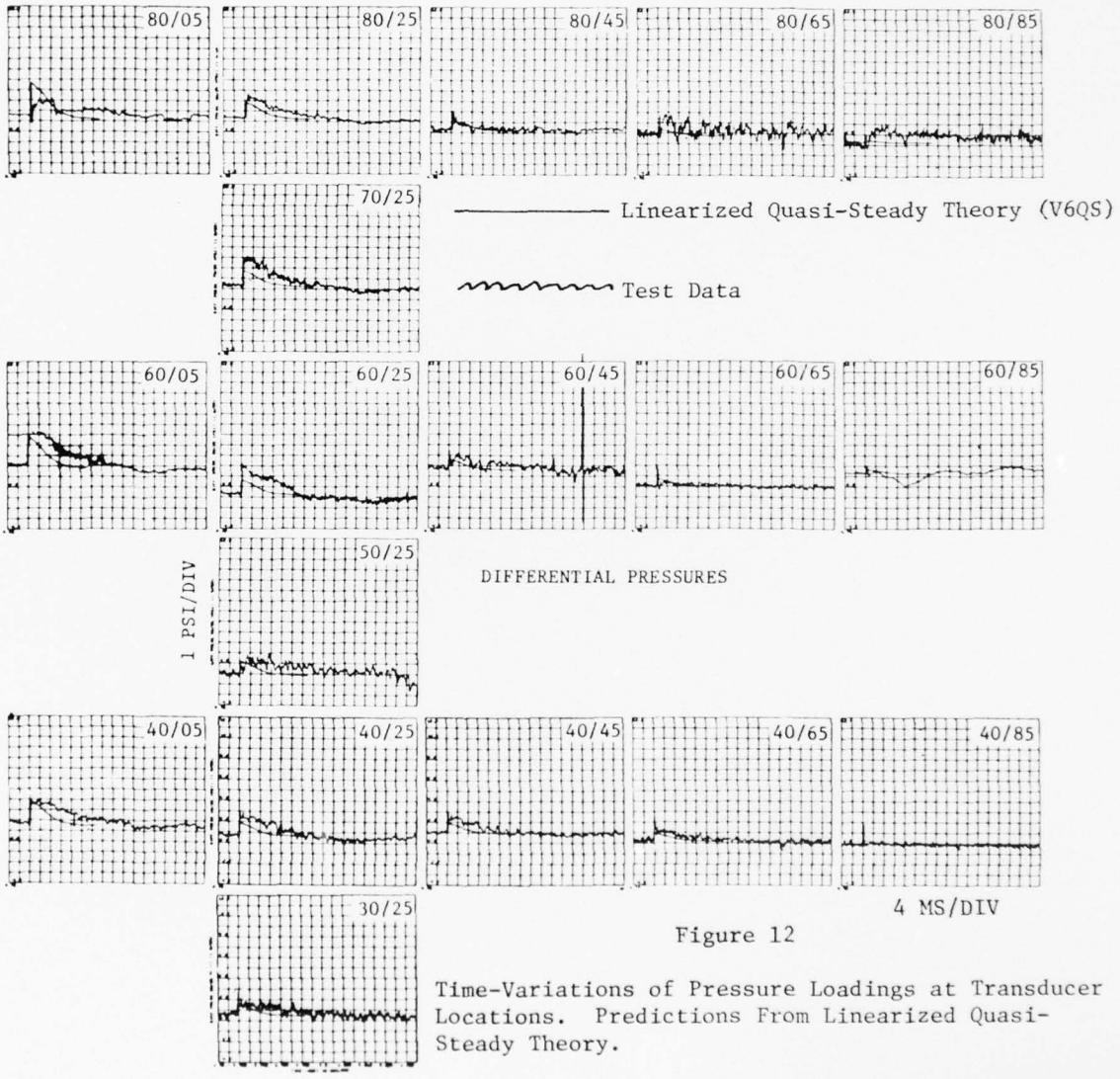


Figure 12

Time-Variations of Pressure Loadings at Transducer Locations. Predictions From Linearized Quasi-Steady Theory.

Long-Duration Traces for Case 2 - $\phi$ = 20.1 deg, $\Delta p_s$=2.01 psi. (9B-A2-1)

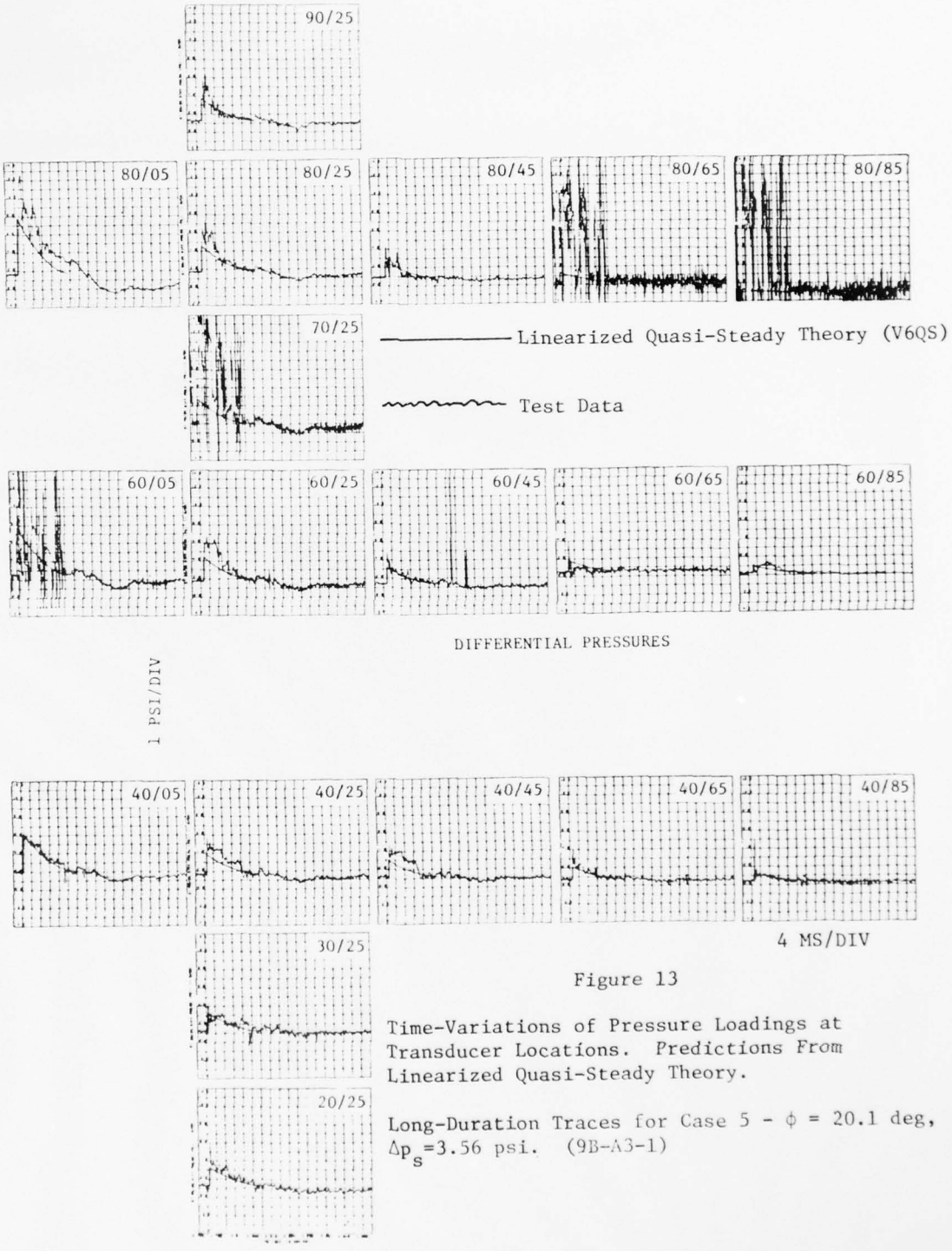


Figure 13

Time-Variations of Pressure Loadings at Transducer Locations. Predictions From Linearized Quasi-Steady Theory.

Long-Duration Traces for Case 5 - $\phi$ = 20.1 deg, $\Delta p_s$=3.56 psi. (9B-A3-1)

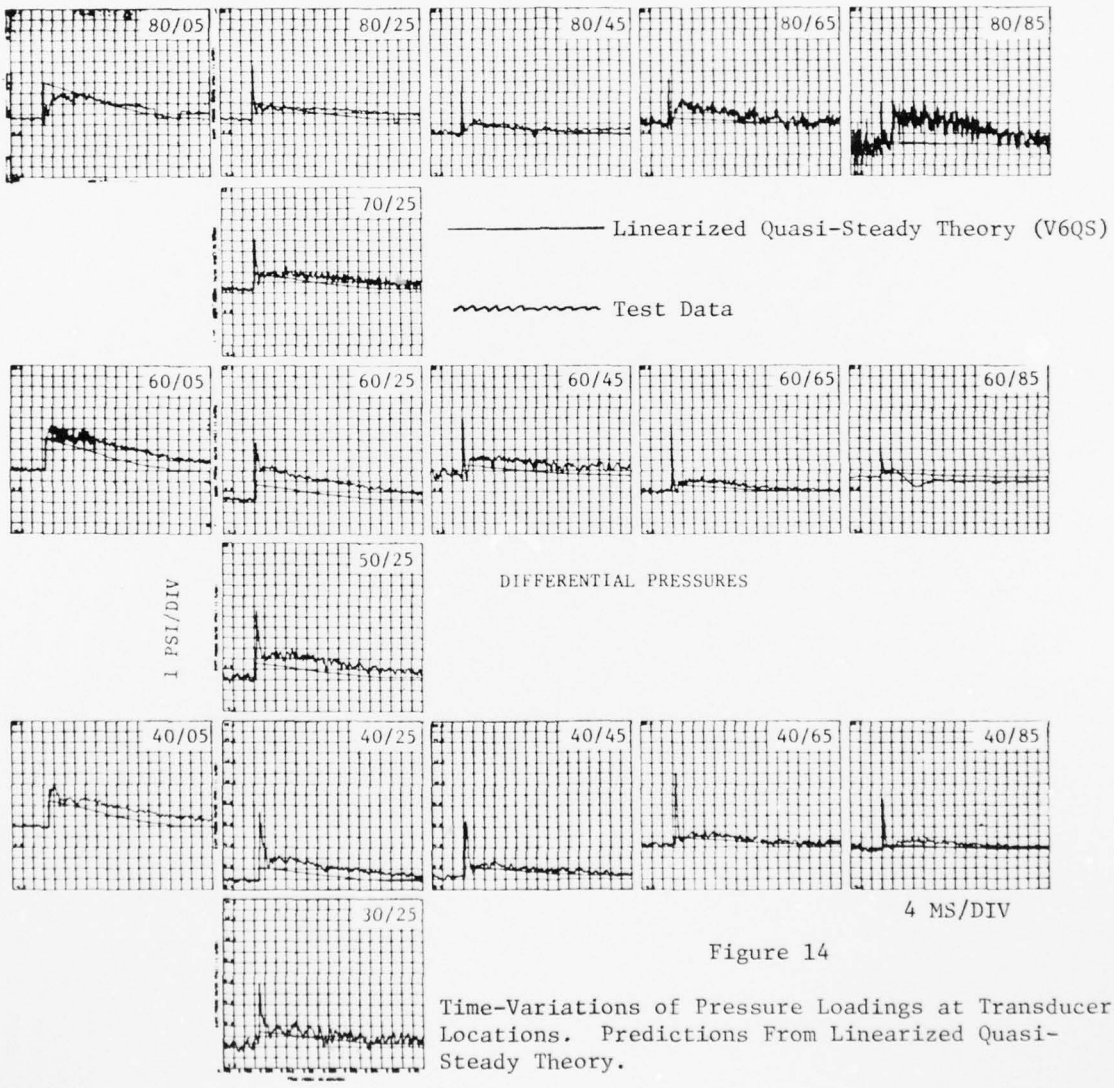


Figure 14

Time-Variations of Pressure Loadings at Transducer Locations. Predictions From Linearized Quasi-Steady Theory.

Long-Duration Traces for Case 4 - $\phi$ = 134.9 deg, $\Delta p_s$=1.97 psi. (9B-A2-3)

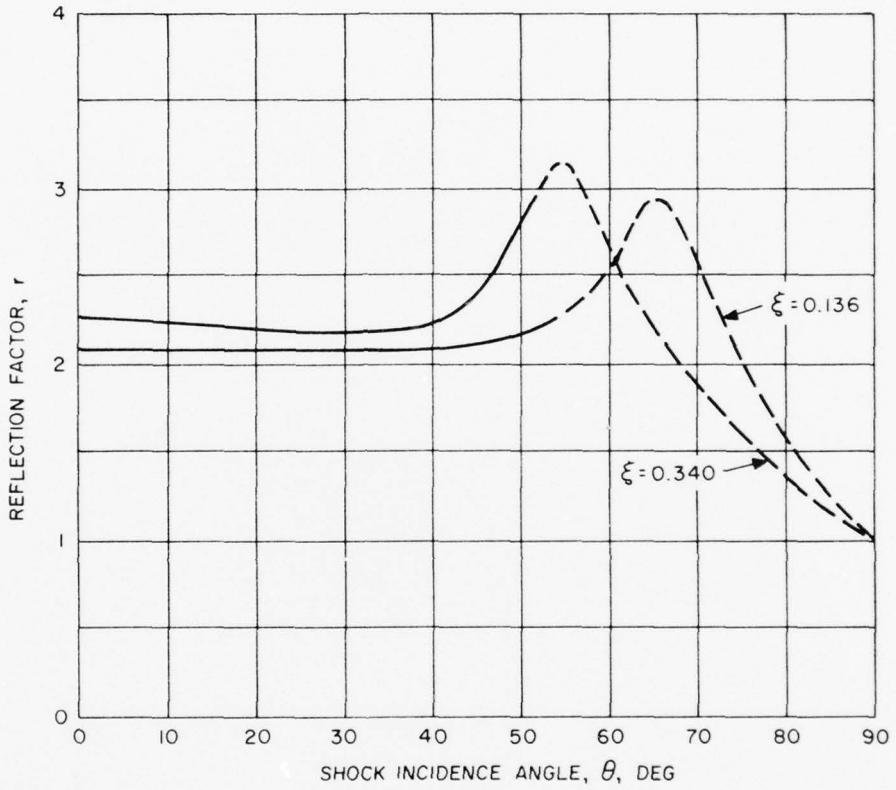


Figure 15. Reflection Factor Versus Shock Incidence Angle For Two Values of Shock Strength Ratio. (From Figure 11.12, Reference 4, Modified to Conform With Present Notation.)

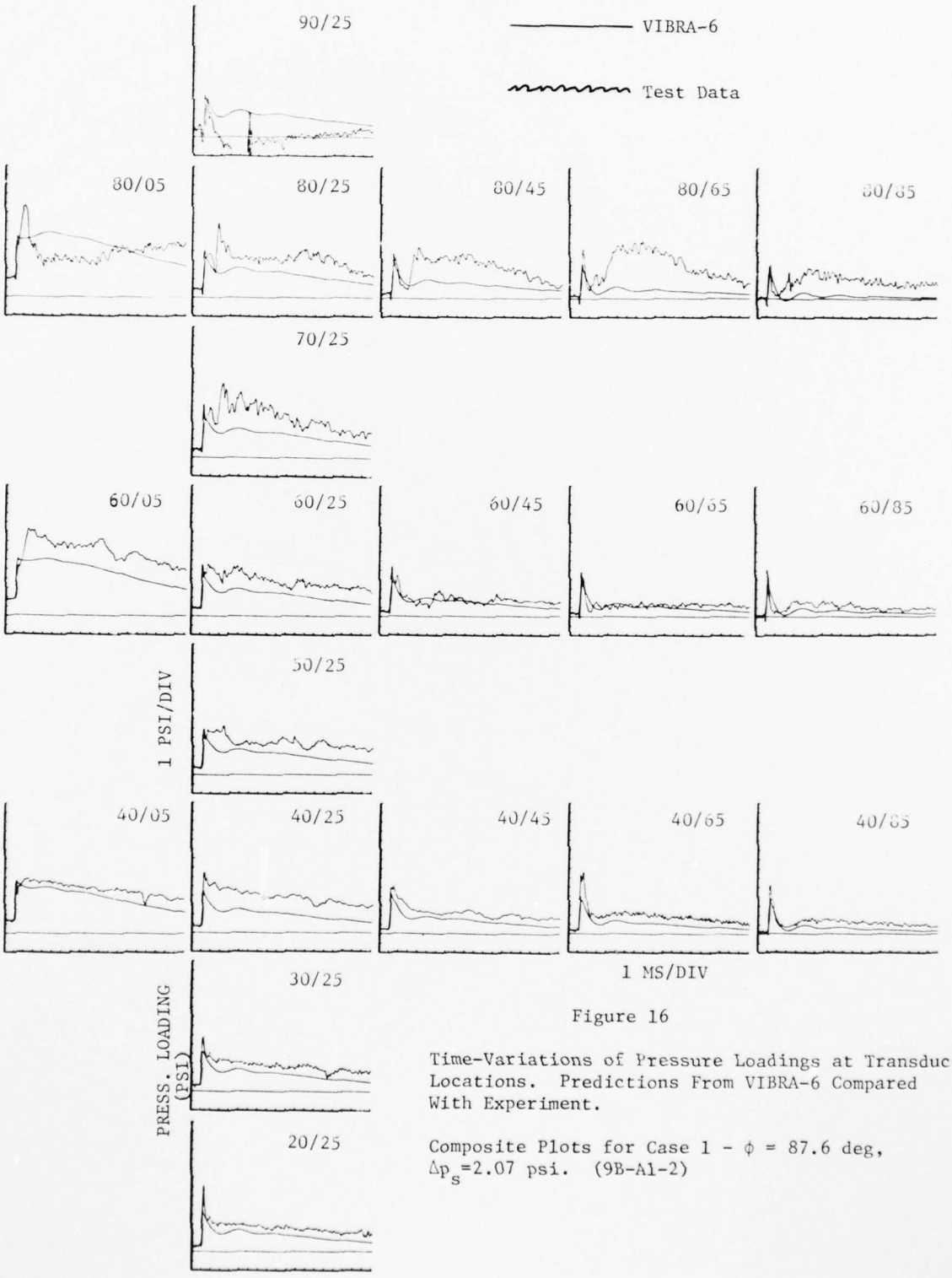


Figure 16

Time-Variations of Pressure Loadings at Transducer Locations. Predictions From VIBRA-6 Compared With Experiment.

Composite Plots for Case 1 - $\phi$ = 87.6 deg, $\Delta p_s$=2.07 psi. (9B-A1-2)

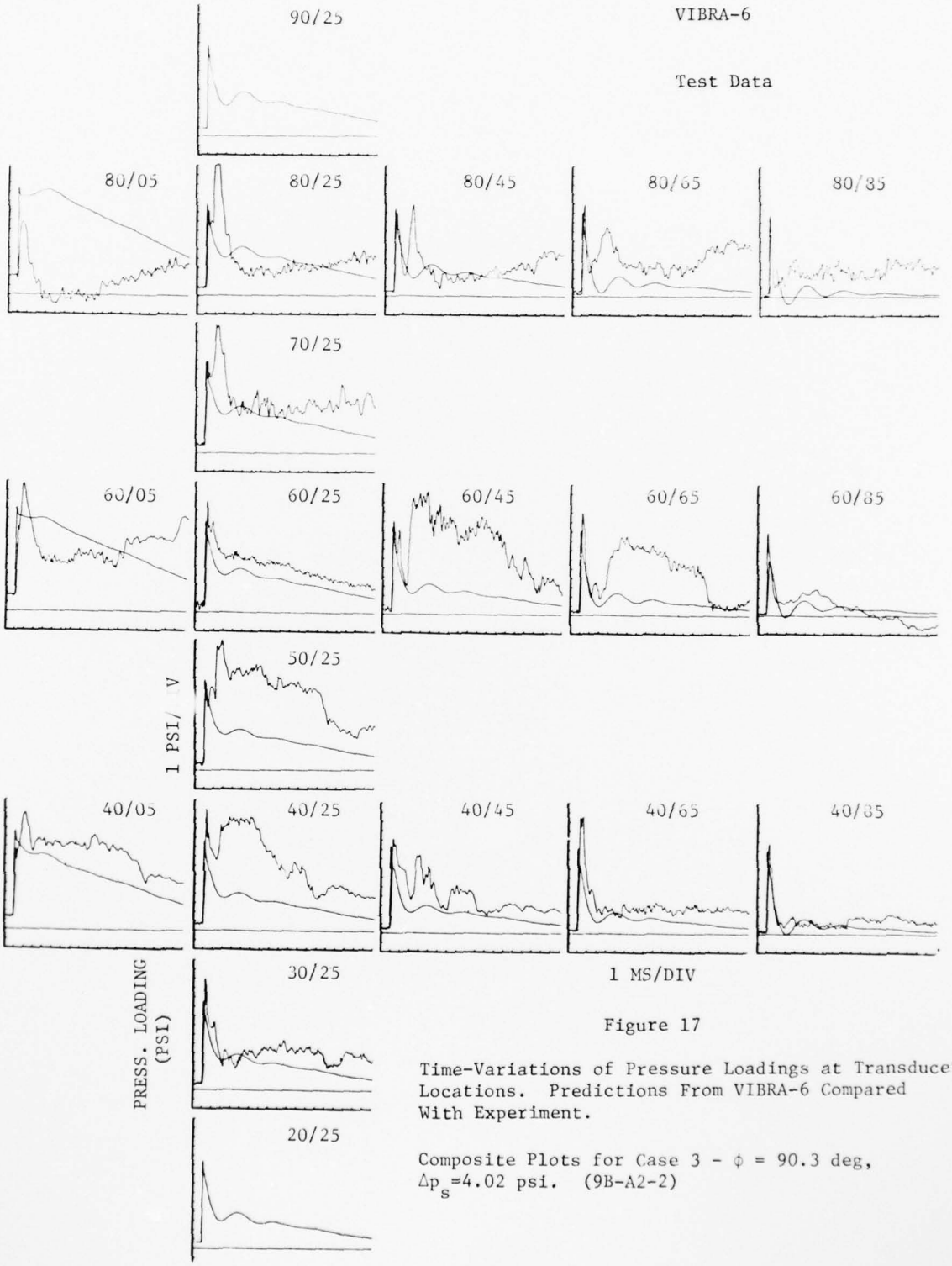


Figure 17

Time-Variations of Pressure Loadings at Transducer Locations. Predictions From VIBRA-6 Compared With Experiment.

Composite Plots for Case 3 - $\phi$ = 90.3 deg, $\Delta p_s$=4.02 psi. (9B-A2-2)

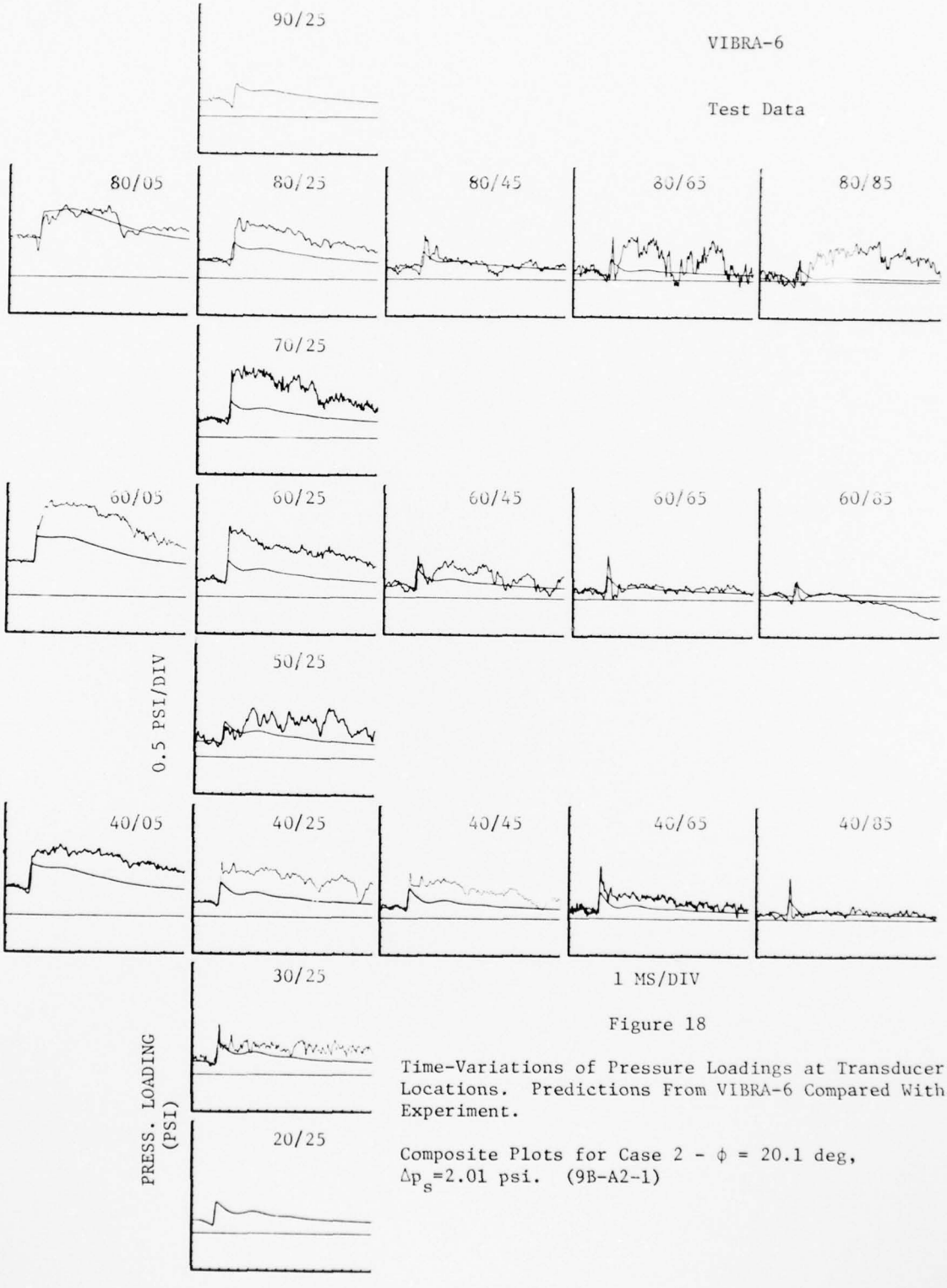


Figure 18

Time-Variations of Pressure Loadings at Transducer Locations. Predictions From VIBRA-6 Compared With Experiment.

Composite Plots for Case 2 - $\phi$ = 20.1 deg, $\Delta p_s$=2.01 psi. (9B-A2-1)

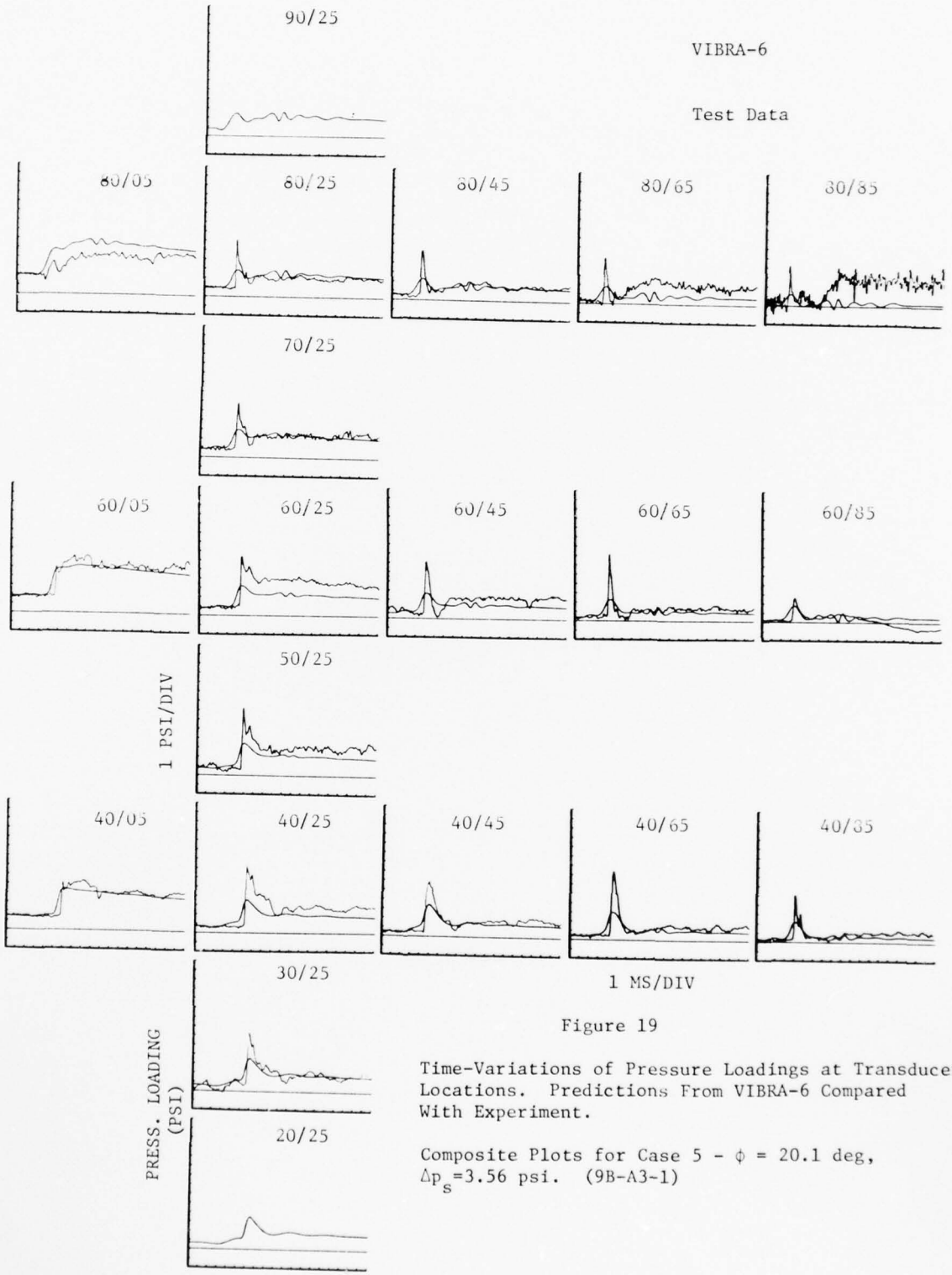


Figure 19

Time-Variations of Pressure Loadings at Transducer Locations. Predictions From VIBRA-6 Compared With Experiment.

Composite Plots for Case 5 - $\phi$ = 20.1 deg, $\Delta p_s$=3.56 psi. (9B-A3-1)

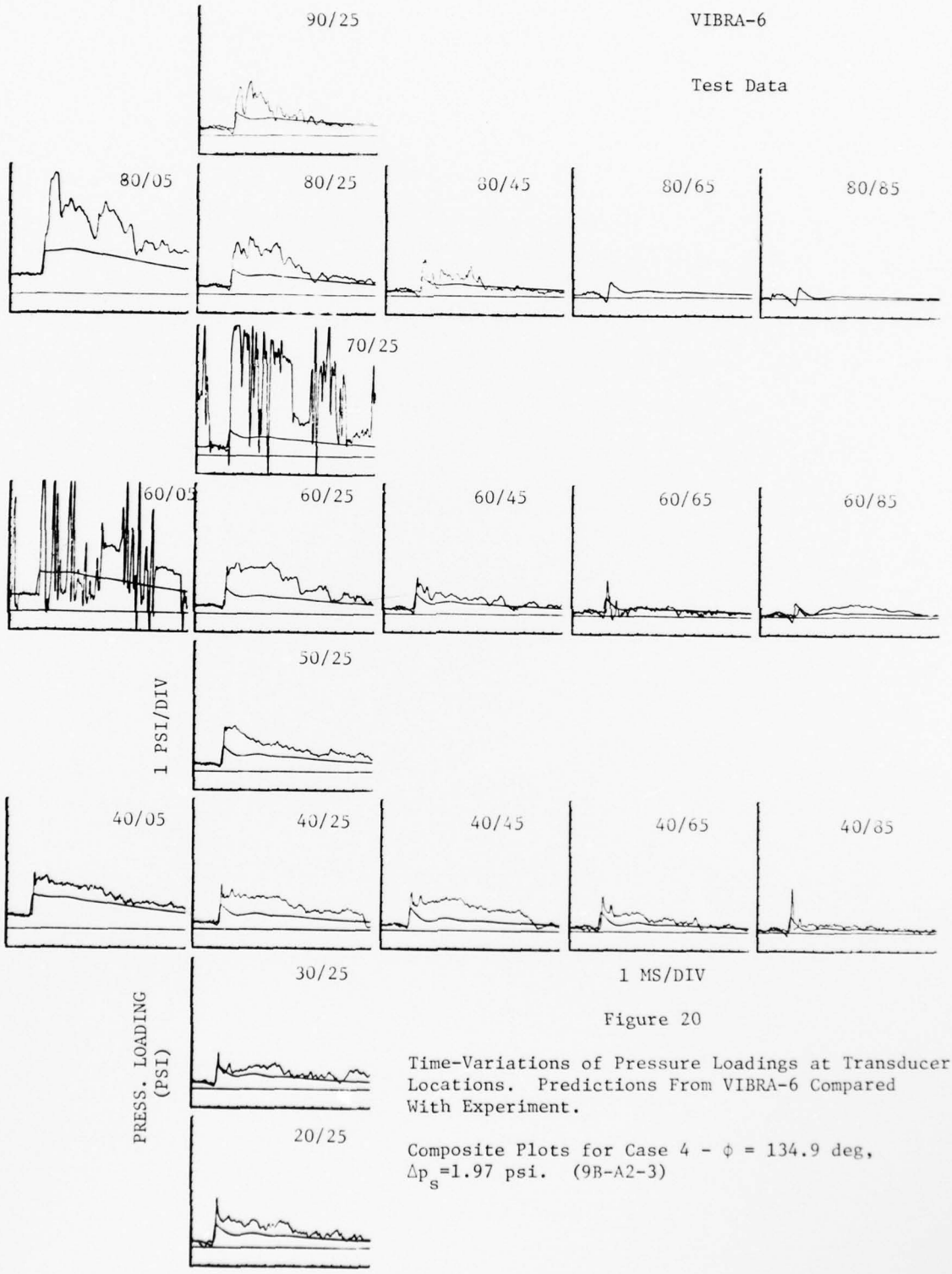


Figure 20

Time-Variations of Pressure Loadings at Transducer Locations. Predictions From VIBRA-6 Compared With Experiment.

Composite Plots for Case 4 - $\phi$ = 134.9 deg, $\Delta p_s$=1.97 psi. (9B-A2-3)

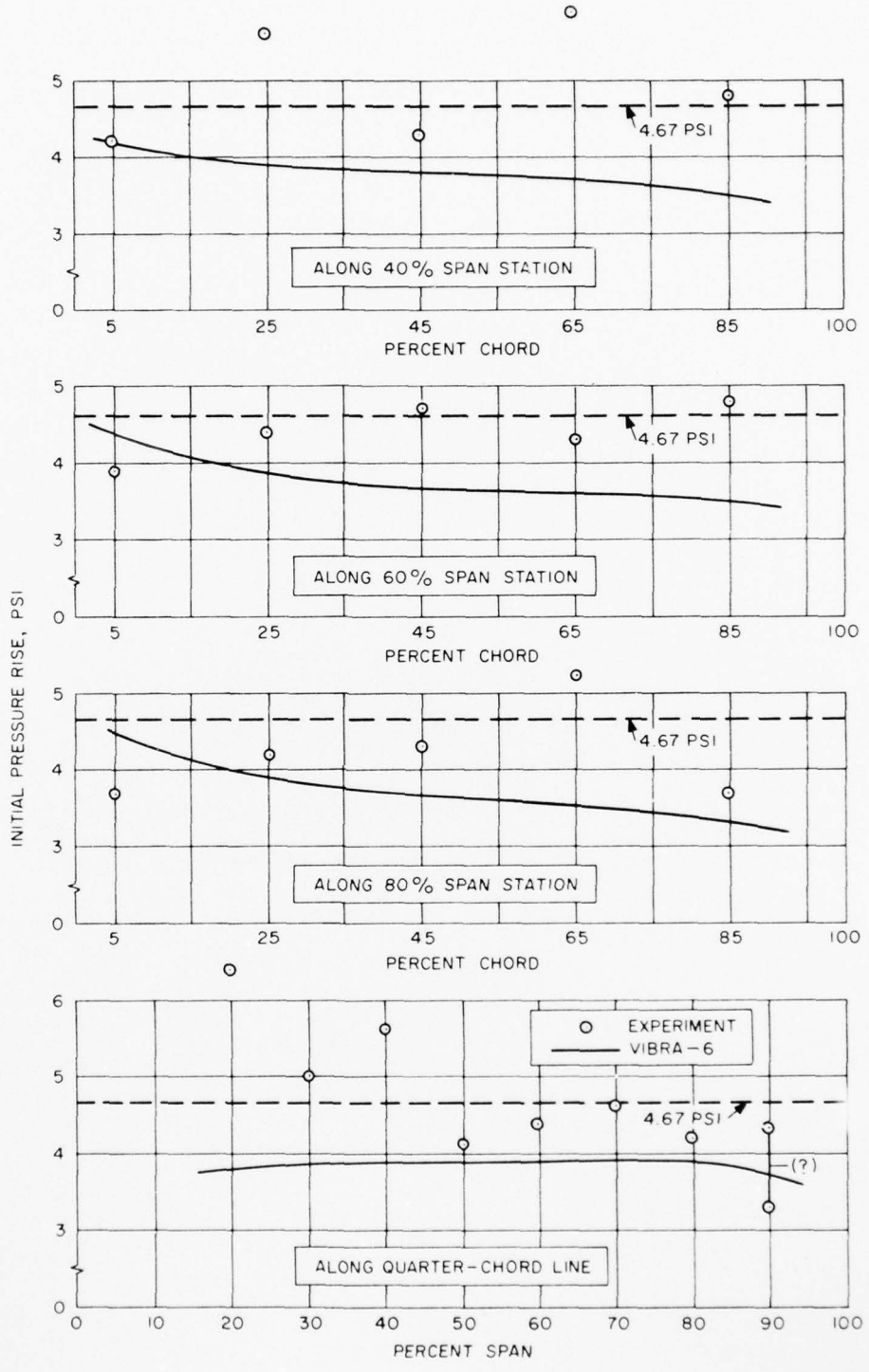


Figure 21. Comparisons Between Experimental and Predicted Initial Pressure Rises - Case 1.

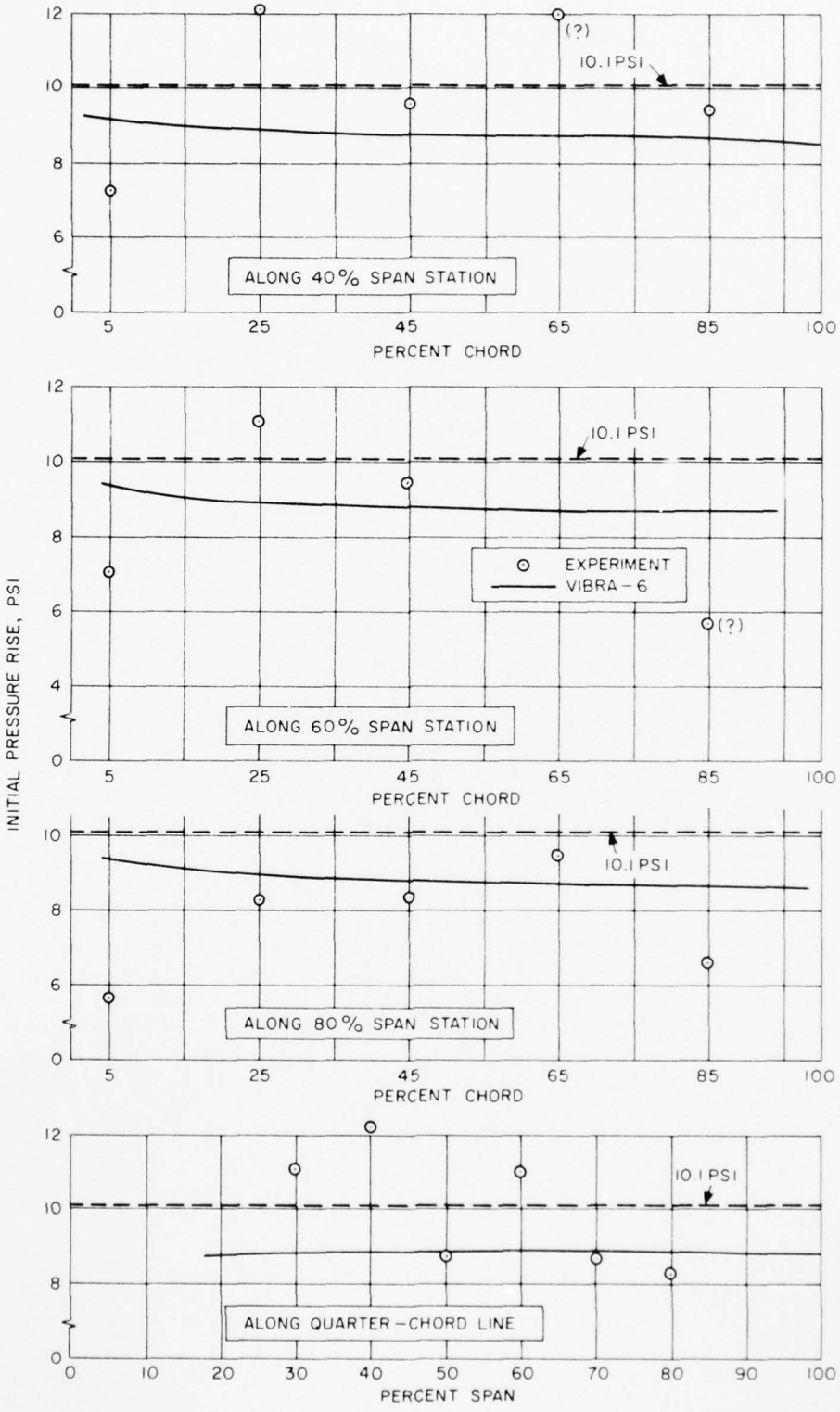


Figure 22. Comparisons Between Experimental and Predicted Initial Pressure Rises - Case 3

## REFERENCES


1. McGrew, J.A., Giesing, J.P., Kalman, T.P., Croxen, H.H., and Rodden, W.P., Nuclear Blast Response Program,

   Vol. I. Program Description

   Vol. II. Doublet Lattice Aerodynamics.

   Douglas Aircraft Company Reports for the Defense Nuclear Agency under Contract DNA 001-75-C-0216, 1976. (To be published.)

2. Hobbs, N.P., Zartarian, G., and Walsh, J.P., A Digital Computer Program for Calculating the Blast Response of Aircraft to Nuclear Explosions, Air Force Weapons Laboratory Report AFWL-TR-70-140, Vol. I., April 1971.

3. Zartarian, G., Application of the Doublet-Lattice Method for Determination of Blast Loads on Lifting Surfaces at Subsonic Speeds, Air Force Weapons Laboratory Report AFWL-TR-72-207, January 1973.

4. Norris, C.H., Hansen, R.J., et al, "Structural Design for Dynamic Loads, McGraw Hill Book Company, Inc., New York, 1959.

5. Manro, M.E., et al., Transonic Pressure Measurements and Comparisons of Theory to Experiment for an Arrow-Wing Configuration, Vol. I: Experimental Data Report-Base Configuration and Effects of Wing Twist and Leading-Edge Configuration, NASA CR-132727, October 1975.

# DISTRIBUTION LIST

DEPARTMENT OF DEFENSE

Assistant to the Secretary of Defense
Atomic Energy
ATTN: Executive Assistant

Defense Documentation Center
12 cy ATTN: DD

Defense Nuclear Agency
ATTN: SPAS
ATTN: DDST
4 cy ATTN: TITL
ATTN: STSP

Field Command
Defense Nuclear Agency
ATTN: FCPR

Livermore Division Field Command DNA
Department of Defense
Lawrence Livermore Laboratory
ATTN: FCPRL

NATO School (SHAPE)
ATTN: U.S. Documents Officer

Under Secretary of Defense for Rsch. & Engrg.
ATTN: Strategic & Space Systems (OS)

DEPARTMENT OF THE ARMY

Harry Diamond Laboratories
Department of the Army
ATTN: DELHD-NP
ATTN: DELHD-RBH, J. Gwaltney

U.S. Army Ballistic Research Labs.
ATTN: DRXBR-BLE, W. Taylor
ATTN: DRXBR-X, J. Meszaros

U.S. Army Materiel Dev. & Readiness CMD
ATTN: DRCDE-D, L. Flynn

U.S. Army Nuclear & Chemical Agency
ATTN: Library for J. Vecke

DEPARTMENT OF THE NAVY

Naval Material Command
ATTN: Mat. 08T-22

Naval Research Laboratory
ATTN: Code 2627

Naval Surface Weapons Center
ATTN: K. Caudle

Naval Weapons Evaluation Facility
ATTN: P. Hughes

Office of Naval Research
ATTN: Code 464

DEPARTMENT OF THE NAVY (Continued)

Strategic Systems Project Office
Department of the Navy
ATTN: NSP-272

DEPARTMENT OF THE AIR FORCE

Aeronautical Systems Division, AFSC
4 cy ATTN: ENFTV, D. Ward

Air Force Materials Laboratory
ATTN: MBC, D. Schmidt
ATTN: MBE

Air Force Weapons Laboratory
ATTN: DYV, Lt. Col. Rensvold
ATTN: SUL

Foreign Technology Division, AFSC
ATTN: PDBF, Mr. Spring

Strategic Air Command/XPFS
ATTN: XPFS

DEPARTMENT OF ENERGY

Sandia Laboratories
ATTN: Doc. Con. for D. McCloskey

DEPARTMENT OF DEFENSE CONTRACTORS

Aerospace Corp.
ATTN: W. Barry

Avco Research & Systems Group
ATTN: J. Patrick
ATTN: W. Broding

Boeing Co.
ATTN: R. Dyrdahl
ATTN: E. York

Boeing Wichita Co.
ATTN: R. Syring
ATTN: D. Pierson

Effects Technology, Inc.
ATTN: R. Parisse

General Dynamics Corp.
ATTN: R. Shemensky

General Electric Co.-Tempo
Center for Advanced Studies
ATTN: DASIAC

Kaman AviDyne
Division of Kaman Sciences Corp.
ATTN: N. Hobbs
ATTN: R. Ruetenik
ATTN: G. Zartarian
ATTN: R. Smiley

Kaman Sciences Corp.
ATTN: D. Sachs

DEPARTMENT OF DEFENSE CONTRACTORS (Continued)

McDonnell Douglas Corp.
ATTN: J. McGrew

Prototype Development Associates, Inc.
ATTN: J. McDonald

R & D Associates
ATTN: C. MacDonald
ATTN: F. Field
ATTN: J. Carpenter
ATTN: A. Latter

Rockwell International Corp.
ATTN: R. Sparling

DEPARTMENT OF DEFENSE CONTRACTORS (Continued)

Science Applications, Inc.
ATTN: D. Hove

SRI International
ATTN: G. Abrahamson

Martin Marietta Corp.
ATTN: G. Aiello

Northrop Corp.
ATTN: D. Hicks



END